

**A DYNAMIC PRESSURE DISTRIBUTION MODEL FOR
ICE PRESSURE LOAD PATCHES USED IN NUMERICAL
SIMULATIONS**

by

© Sthéfano Lande Andrade, B.Eng., M.Eng.

A thesis submitted to the School of Graduate Studies

in partial fulfillment of the requirements for the degree of

Doctor of Philosophy

Faculty of Engineering and Applied Science

Memorial University of Newfoundland

May 2023

St. John's

Newfoundland and Labrador

Canada

Abstract

The work presents a model for ice load pressure patch representation in numerical structural simulation that captures the non-uniform pressure distribution as a function of the ice-structure interface shape.

For this purpose, the first step of the work was the analysis of pressure data from ice impact experiments. This work presents the ice pressure distribution recorded and analysed in high temporal- and spatial-resolutions. The results show regions of high- and low-pressure zones (i.e., HPZ and LPZ) at the ice-indenter interface, which agree with previous works. Furthermore, based on the visual analysis of the pressure maps and ice specimen test faces, it was possible to hypothesise that the pattern assumed by the HPZ could be explained by the shape of the contact area. Based on this observation a geometric model for HPZ and LPZ representation over any contact area was developed and it is presented in this work for the first time. The methodology uses the topological skeleton and distance field information of the ice contact area's shape to define the HPZ and LPZ associated to a contact area from the high-strain-rate interaction between an ice feature and a flat structure. The results from this methodology compare favourably with experimental observations of the HPZ distribution patterns.

Finally, this led to the development of a new energy-coupled ice load model called NILAS (Non-uniform Ice Load Application System). The NILAS is capable of accounting for structural deformation energy during the simulation, while also generating non-uniform ice load pressure patches. The NILAS is designed for use in numerical structural simulations

for the assessment of damage to non-polar class structures and overloaded polar class structures. While simpler methods that use uniform pressure patches with correction factors (e.g., IACS UR I) can approximate the effects of load concentration caused by HPZ, the NILAS model can directly include these regions of pressure concentration into the load patch. Therefore, the new model can account for the path-dependent plasticity associated with localized deformation response to the HPZ, which is of particular importance for non-ice class ships and overloaded ice-class ships.

General Summary

The progressive reduction in polar waters ice coverage during the melt season is leading to an increase in ship traffic in these regions, particularly in the Arctic. Some of the ships navigating in polar waters are non-polar class ships and even non-ice-strengthened vessels. Even though they operate in ice free water or very light pack ice conditions, there is always a risk of accidental impact against multi-year ice floes, which are capable of causing large plastic deformation to the local structure of such vessels. Given this, there is a necessity for a strength limit assessment of these structures under accidental loads. This type of load study often requires numerical structural analysis, but ice is a particularly complex material to model numerically. It is brittle at the speeds at which these impacts are expected to occur, and furthermore, two different ice materials will be present at the interface between ship structure and ice, crushed ice and intact ice. As shown in the current work and previous works, each ice type imparts a different load magnitude to the structure. An alternative to using an ice material model in such numerical structural simulations is to directly apply ice pressure load patches to a structure. Although simpler in approach, this is also not trivial, as the ice pressure distribution is known to be non-uniform and ice is actively crushed and extruded during the impact event, so the contact area, and consequently the idealized load patches, are changing as an interaction proceeds. This work presents a new energy-coupled ice load model called NILAS (Non-uniform Ice Load Application System), that can represent the non-uniform pressure distribution in ice pressure load patches.

Acknowledgements

The following previously published works are used in this thesis:

Chapter 2: R. Gagnon, S.L. Andrade, B. Quinton, C. Daley, B. Colbourne, Pressure distribution data from large double-pendulum ice impact tests, *Cold Regions Science and Technology*, Volume 175, 2020 103033, ISSN 0165-232X, <https://doi.org/10.1016/j.coldregions.2020.103033>.

Chapter 3: Andrade, SL, Quinton, BWT, Daley, CG, & Gagnon, RE. Numerical Study of Large Pendulum Ice Impact Loads. Proceedings of the ASME 2020 39th International Conference on Ocean, Offshore and Arctic Engineering. Volume 7: Polar and Arctic Sciences and Technology. Virtual, Online. August 3–7, 2020. V007T07A017. ASME. <https://doi.org/10.1115/OMAE2020-19068>.

Chapter 4: Sthéfano Lande Andrade, Ahmed Y. Elruby, Evan Hipditch, Claude G. Daley & Bruce W. T. Quinton (2022) Full-scale ship-structure ice impact laboratory experiments: experimental apparatus and initial results, *Ships and Offshore Structures*, DOI: 10.1080/17445302.2022.2032993. © copyright 2022, reprinted by permission of Informa UK Limited, trading as Taylor & Taylor & Francis Group.

The following pre-print work is currently in its second round of reviews for the *Cold Regions Science and Technology Journal*:

Chapter 5: S.L. Andrade, R. Gagnon, B. Colbourne, and B.W. Quinton (2023). Ice Pressure Distribution Model: A Geometry-Based Solution for High-Pressure Zone Representation.

Cold Regions Science and Technology. ISSN 0165-232X,
<https://doi.org/10.1016/j.coldregions.2023.103822>.

I acknowledge the financial support from the Natural Sciences and Engineering Research Council of Canada DND/CRD, and the contributing project partners: Defence Research and Development Canada (Atlantic), Vard Marine Inc., the American Bureau of Shipping (ABS), and the Newfoundland and Labrador Provincial Government & Labrador Provincial Government.

I would like to thank my supervisors for their continual support during my doctoral research: First, I would like to extend my deepest gratitude to Prof. Dr. Bruce W. T. Quinton, my supervisor, who is an incredible mentor, advisor, and professor. Thank you for sharing your extensive knowledge and, as significantly, for the constant support. I had little to worry about besides the doctoral work itself, even during a global Pandemic, and this fact cannot be overstated.

Dr. D. Bruce Colbourne, my co-supervisor, was a source of both levity and focus for this doctoral research. He helped me stay on track with advice plenty and constant encouragement. Thank you for the discussions, stories, and experience sharing.

Dr. Robert G. Gagnon, my co-supervisor. Thank you for sharing your vast knowledge of ice mechanics, and for the patience and time dedicated in all our meetings. Dr. Gagnon has an impressive ability to pass knowledge forward and to incentivize critical thinking.

Dr. John R. Mackay, my co-supervisor, who showed continuous interest and insight into the practicalities of this research. Dr. Mackay advice were crucial in helping the trace the direction of this work.

I would like to thank my office colleagues and friends at the ABS HETC, Dan Oldford, Ed Moakler, and Alessandro Zambon. Thank you for all the lunch time and coffee break discussions. More than once our discussions led to breakthroughs in this research work.

I would like to thank my friend Carla Teodoro, who introduced me to the topological skeleton. When I presented to her my findings and ideas, she was able to guide to the geometric descriptor that I was looking for. It would become one of the pillars of this work.

Thank you to all my friends in Brazil, Canada, and other parts of the world for all the support during these almost 5 years of work. In special, to Lucas Silvestre and Gabriel Lopes, who offered (or were drafted into offering) a friendly ear and shoulder.

Finally, I would like to thank my family, Cláudio, Ana Rosa, Ana Cláudia, Oliver, and Lorelai. They are the most incredible people, full of care, love, and faith, who supported me throughout these years, helping and encouraging me all the way. I am glad that I can share this part of my life with you.

Table of Contents

Abstract	ii
Acknowledgements	v
Table of Contents	viii
List of Tables	xviii
List of Figures	xx
Chapter 1 Introduction	1
1.1 Problem statement.....	1
1.2 Background	2
1.2.1 Ice-ship interaction process.....	2
1.3 Ice load characterization	5
1.3.1 Early ice load measurements during sea trials.	6
1.3.2 In-situ contact area pressure distribution studies – Hobson’s Choice Ice Island and Hokkaido saltwater lagoon	8
1.3.3 Laboratory contact area pressures measured in high resolution	11
1.4 Models for ice loads in numerical structural simulations	12
1.4.1 IACS UR I: A codified approach for polar ship design.....	12
1.4.1.1 Ice material models for FEA simulations	14

1.4.1.2	Direct application of measured ice load.....	15
1.4.2	Summary	16
1.5	Scope and contribution of the research.....	17
1.5.1	Chapter 2 summary description	19
1.5.2	Chapter 3 summary description	20
1.5.3	Chapter 4 summary description	21
1.5.4	Chapter 5 summary description	22
1.5.5	Chapter 6 summary description	22
1.5.6	Summary table	24
1.6	References.....	25
Chapter 2	Pressure Distribution Data from Large Double-Pendulum Ice Impact Tests	33
2.1	Co-authorship statement	33
2.2	Abstract.....	33
2.3	Introduction.....	35
2.4	Description of apparatus and ice samples	35
2.5	Safety considerations	41
2.6	Impact module description.....	42
2.7	Impact speed and ice penetration.....	46

2.8	General notes on the data presentation	51
2.9	Discussion of the pressure-sensing technology and load-cell data ...	51
2.10	Identifying a ‘High-Pressure Zone, HPZ	54
2.11	The three categories of tests.....	56
2.12	Detailed descriptions of typical category I, II and III tests.....	58
2.12.1	Description of the evolving pressure pattern from a typical impact test	58
2.12.2	Average pressures of HPZ’s and LPZ’s, and total-area nominal pressure and average pressure.....	70
2.12.3	Pressure and contact area comparisons with other studies and instrumentation	76
2.12.4	Confining aspects of LPZ’s	81
2.12.5	HPZ load correlation with the total load.....	81
2.12.6	Maximum pressure characteristics.....	84
2.13	Conclusions.....	84
2.13.1	CCD enabled technology	85
2.14	Acknowledgements.....	85
2.15	References.....	85
2.16	Appendix A.....	91

2.16.1	Preparation and conversion of raw images to pressure-distribution patterns	91
2.16.2	Fisheye correction and first image centering	91
2.16.3	Isolation of the pressure information and edge detection	92
2.16.4	Pressure-data determination and presentation	93
2.16.5	Pressure-sensing technology calibration and accuracy	96
2.17	Appendix B	103
2.17.1	(Test: May8_A+B_2014) –	103
2.17.2	(Test: May22_2014).....	105
2.17.3	(Test: Dec10_2015)	107
2.17.4	(Test: June27_2014).....	110
2.17.5	(Test: Oct16_2014).....	112
2.17.6	(Test: Dec15_2014)	114
2.17.7	(Test: Jan20_2015).....	117
2.17.8	(Test: Feb25_2016).....	119
2.18	Appendix C	122
2.18.1	(Test: May8_A+B_2014).....	122
2.18.2	(Test: May22_2014).....	123
2.18.3	(Test: Dec10_2015)	125

2.18.4	(Test: June27_2014).....	126
2.18.5	(Test: Oct16_2014).....	128
2.18.6	(Test: Dec15_2014)	129
2.18.7	(Test: Jan20_2015).....	131
2.18.8	(Test: Feb25_2016).....	132
2.19	Appendix D.....	134
Chapter 3	Numerical study of large pendulum ice impact loads.....	137
3.1	Co-authorship statement	137
3.2	Abstract	137
3.3	Introduction.....	138
3.4	Background	139
3.5	Ice impact experiments	142
3.6	Methodology	149
3.7	Numerical model.....	151
3.8	Results.....	153
3.9	Energy study of the dynamic simulations.....	159
3.10	Conclusion	162
3.11	Future Work.....	163
3.12	Acknowledgements.....	164

3.13	References.....	164
Chapter 4	Full-scale ship-structure ice impact laboratory experiments: experimental apparatus and initial results.....	168
4.1	Co-authorship statement	168
4.2	Abstract	169
4.3	Introduction.....	170
4.4	The Large Double Pendulum Apparatus.....	172
4.5	Ice impact experimental setup	174
4.5.1	Ice cone indenters	175
4.5.2	Panel carriage design	176
4.5.3	Test panel details.....	180
4.5.4	Sensor array	182
4.5.5	High speed imaging	183
4.5.6	Experimental setup summary.....	185
4.6	Load cell, accelerometer and DIC data.....	186
4.6.1	Peak load and accelerations	191
4.6.2	High-speed camera and DIC results.	194
4.6.3	Ex-HMCS IROQUOIS panel deformation	196
4.6.4	Ice behaviour, carriage displacement, and energy analysis	198

4.7	Lessons learned.....	201
4.8	Conclusion	203
4.9	Future work.....	204
4.10	Acknowledgements.....	204
4.11	References.....	204
4.12	Appendix A – Ice cone	207
4.13	Appendix B – Load curves and accelerometer curves.....	208
4.14	Appendix C – ex-HCMS IROQUOIS panel.....	212
Chapter 5 Ice pressure distribution model: A geometry-based solution for high-		
pressure zone representation.....		
5.1	Co-authorship statement	215
5.2	Abstract.....	215
5.3	Introduction.....	216
5.4	The ice feature failure process	217
5.5	Confinement and high-pressure zone formation.....	221
5.6	The importance of the contact area shape for HPZ development...	224
5.7	Geometrical models for HPZ representation	227
5.8	A geometric descriptor for HPZ representation: The topological	
	skeleton	231

5.9	Distance transform to determine confinement levels.....	232
5.10	Methodology for the ice pressure distribution and implementation	235
5.11	Comparison with experimental pressure distribution data	241
5.12	Discussion on limitations of the geometric method for HPZ representation	252
5.13	Application for idealized ice load patches	255
5.14	Discussion and Conclusions	257
5.15	Acknowledgments.....	258
5.16	References.....	258
5.17	Appendix A.....	264
5.18	Appendix B.....	268
Chapter 6	The Non-uniform Ice Load Application System (NILAS) and its use in numerical structural analyses of ice impact	271
6.1	Co-authorship statement	271
6.2	Abstract.....	271
6.3	Introduction.....	272
6.4	A summary of the Popov-Daley (PD) method for ice load patch determination.	273

6.5	A discrete method for the ice load patch creation. Progressive ice load patches	280
6.6	Pressure distribution during ice-structure interaction	287
6.7	A Non-uniform Ice Load Application System – NILAS	288
6.7.1	How HPZs can be integrated into IACS pressure patches for FEA analyses.	289
6.7.2	Defining LPZ and HPZ size and average pressure for the FEA simulations	293
6.8	The numerical simulation setup	297
6.8.1	Structural design of the panel	297
6.8.2	Boundary conditions	300
6.8.3	Meshing.....	303
6.8.4	Material model	305
6.9	Variable parameters of the studied cases	306
6.10	Results and discussion for the simulations	308
6.10.1	Cases solved with PD method.....	309
6.10.2	Cases solved with the PRO method.....	315
6.10.3	Cases solved with the PROWiSE method	324
6.10.4	Cases solved with the NILAS method.	328
6.11	Conclusion	342

6.12	Acknowledgements.....	345
6.13	References.....	345
Chapter 7	Conclusions and recommendations for future work	349
7.1	Conclusion	349
7.2	Limitations of the current work and suggestions for future work ..	353

List of Tables

Table 1-1. Summary of the Research.....	24
Table 2-1. Summary Results from the Impact Tests.....	49
Table 2-2. Summary Results from the Impact Tests (continued).	50
Table 3-1. Integrated impulse and maximum penetration for each experiment.	148
Table 3-2. Structural response parameters for the dynamic simulation scenario.	155
Table 3-3. Comparison of the structural force response between the dynamic and quasi-static simulations.....	157
Table 3-4. Structural response comparison between quasi-static (QS) and dynamic transient (DT) simulations.	157
Table 3-5. Comparison between maximum energy absorbed by the structure in the dynamic and quasi-static simulation scenarios.....	159
Table 3-6. Force comparison between the full impact analysis and the depleted kinetic energy scenario.	161
Table 3-7. Energy comparison between the full impact analysis and the depleted kinetic energy scenario.	162
Table 4-1. Theoretical carriage speed and impact energy versus starting pendulum angle.	173
Table 4-2. Experimental setup summary.	186
Table 4-3. Peak Load and Peak acceleration for the 3 experiments.	192
Table 4-4. Ice cones pre- and post-impact.	207
Table 6-1. PC7 PSV type ship parameters.....	297

Table 6-2. IACS PC7 (bow) design load patch for the studied case.....	298
Table 6-3. Scantlings of the designed PC7 bow panel.....	299
Table 6-4. Table describing the different ice load patch parameters that are studied in this work.	307
Table 6-5. Simulations methods used and parameter variations studied.	308
Table 6-6. Equivalent kinetic energy for the scenario described for each load case.	309
Table 6-7. Load patch parameters for simulations with single loadstep, non-coupled structural energy, rectangular patch, and uniform pressure distribution.....	310
Table 6-8. Deformation energy parameters and maximum plastic strain for the cases: single loadstep, non-coupled, rectangular patch, and uniform pressure.....	312
Table 6-9. Damage done to the framing elements of the structure (not included webframes). Cases: single loadstep, non-coupled, rectangular patch, and uniform pressure.....	313
Table 6-10. Summary of the damage done to the structure for the progressive non-coupled simulations with rectangular patch and uniform pressure distribution.	322
Table 6-11. Table shows the percent change of the damage parameters studied for progressive non couple load cases (PRO, Table 6-10) w.r.t. the base cases (PD, Table 6-8 and Table 6-9).....	323
Table 6-12. Peak load comparison for the non-coupled (PRO) and the coupled (PROWiSE) cases.	324
Table 6-13. Summary of the damage done to the structure for the progressive coupled simulations with rectangular patch and uniform pressure distribution (PROWiSE).....	325
Table 6-14. Relative difference in structural damage between non-coupled (PRO) and the coupled (PROWiSE) simulation approaches.	326

Table 6-15. Summary of the damage done to the structure for the progressive coupled simulations with triangular patch and non-uniform pressure distribution (NILAS).....337

Table 6-16. Percentage comparison of the central main frame damage with relation to the total plastic damage done to the structure in all load cases studied.....338

Table 6-17. Relative difference in structural damage between coupled rectangular patch (PROWiSE) and the coupled triangular patch (NILAS) simulation approaches.....338

List of Figures

Figure 1-1. Illustration of the ice-ship structure interaction process during crushing. The deformed ship structure is represented in red. The original intact structure is represented by the black dashed line. The crushed and intact ice regions observed are represented, by grey and blue colours respectively.....4

Figure 1-2. Peak stress plotted against strain rate for iceberg ice tests (Jones et al., 2003).6

Figure 1-3. Test face from one of the Hobson’s Choice experiments. The dark area that forms a “X” shape shows where intact ice is observed, which is indicated by the red arrows. (Gagnon, 1998; Muhonen, 1991).....9

Figure 2-1. Schematic of the double-pendulum impact apparatus showing the ice holder pendulum (left) and Impact Module pendulum (right) in the raised position for a test. For future impact tests, where actual ship grillage will be used, the Impact Module will be removed, and the grillage will be attached to the box structure that presently houses the Module. A second graphic of the brake device has been inserted to show how it functions.

Note that some vertical structural members have been removed from the schematic to permit unobstructed views of the right and left pendulums.....36

Figure 2-2. Photograph showing a partial view of the double-pendulum impact apparatus with the ice holder pendulum (left) and Impact Module pendulum (right) in the raised position for a test. The ‘toothed’ rail structure directly below the pendulums is the catch mechanism as shown in Fig. 1. Protective netting is visible at the sides and in the background of the image. An overhead crane is used for lifting the pendulum masses to the desired elevation for a test.37

Figure 2-3. Schematic of the pendulum release mechanism.....41

Figure 2-4. Sectional view of the Impact Module. (From Gagnon (2008a)).43

Figure 2-5. Schematic showing how the new pressure-sensing technology functions. Two of the light rays from the source at the left internally reflect off the block’s internal surface where there is no contact with the strips. The center ray illumines the ‘white’ acrylic strip since the internal reflection is frustrated where the strip is elastically flattened against the block due to the pressure. The curvature of the strips is exaggerated for illustrative purposes. (From Gagnon (2008a)). Note: the strips are clear acrylic, however the thin opaque white plastic film (not shown) between the block and the strips essentially behaves as a thin coat of resilient white paint on the strips’ bottom surfaces.44

Figure 2-6. Load sensor comparisons for test May22_2014. Note that integrated pressure-pattern data are only shown for the time during which ice penetration is occurring.53

Figure 2-7. Load sensor comparisons for test June27_2014.....54

Figure 2-8. Pressure patterns illustrating the demarcation pressure boundary (~ 15 MPa, i.e., the mid blue-green color) for a high-pressure zone (HPZ). The left image is the last

one from the Oct16_2014 test and the right image is from early in the same test. Note that the same pressure-color scale applies to all pressure-pattern images throughout this paper.

.....56

Figure 2-9. Sequence of pressure-pattern images from test May22_2014. The images run from left to right in each row from top to bottom. The capture rate was 500 images/s. The width of a blue box is ~ 60 cm.....59

Figure 2-10. Data plots from test May22_2014.....61

Figure 2-11. A histogram of the pressure distribution at peak load for test Dec10_2015. 62

Figure 2-12. Sequence of pressure-pattern images from test Jan20_2015. The images run from left to right in each row from top to bottom. The capture rate was 500 images/s. The width of a blue box is ~ 60 cm. There were originally 24 raw images, but the 17th – 23rd were too blurred to process.65

Figure 2-13. Data plots from test Jan20_2015.....66

Figure 2-14. Sequence of pressure-pattern images from test Feb25_2016. The images run from left to right in each row from top to bottom. The capture rate was 500 images/s. The width of a blue box is ~ 60 cm.....68

Figure 2-15. Data plots from test Feb25_2016.69

Figure 2-16. Test May8_A+B_2014. Recall that this was actually two impacts on the same ice specimen.....71

Figure 2-17. Test May22_2014.....72

Figure 2-18. Test Dec10_2015. A series of moderate spalling events (load drops) is evident in the ‘Total’ and ‘HPZ’ load records.....73

Figure 2-19. Test Dec10_2015. The spalling events evident in Figure 2-18 are also manifested in the ‘Average Pressure’ time series.73

Figure 2-20. Data plot from test May22_2014. The ‘Nominal Pressure’ is decreasing while the actual ‘Average Pressure’ is relatively stable.74

Figure 2-21. Data plot from test May22_2014. The initial ‘Actual Contact Area’ is greater than the ‘Nominal Contact Area’ and becomes less later.75

Figure 2-22. Pressure-plug data for two tests. The horizontal sequence of solid circles correspond approximately to the times when the Impact Module camera captured pressure-pattern images. The inset on the top graph corresponds to the fourth image in the sequence. It shows a HPZ that had developed and the location and sensing area (dark circle) of the central pressure-plug. Peak pressures are indicated on the graphs. The pressure-color scale is the same as for all pressure-pattern images throughout the paper.80

Figure 2-23. Peak Load vs Maximum HPZ Contact Area for all tests.82

Figure 2-24. Maximum LPZ Contact Area vs Maximum Contact Area for all tests.....83

Figure 2-25. Maximum Ice Contact Area vs Impact Speed for the full set of tests.....83

Figure 2-26. The first picture (left) is an untreated sample of an image recorded by the high-speed camera. The second picture (right) is the same image with fisheye effect correction applied. Note that the symmetric array of nine pressure-sensing plugs is visible in the image.92

Figure 2-27. Image preparation required before using the Python™ routine to obtain the width of contact that it then uses to calculate pressure from a calibration curve of pressure vs contact-width. The first image (top-left) shows the negative image obtained by cleaning

the pressure information. The second image (top-right) is the result of subtracting the original (second image of Figure 2-26) from the negative image. The third image (bottom-left) is totally cleaned. The fourth image (bottom-right) is the result of the edge detection step.94

Figure 2-28. Comparison between the integrated-pressure load (solid black circles) and the load from the load cells in the Impact Module. The broad-scale agreement demonstrates the quality of the integrated-pressure data, and the robustness of the techniques used for analysis of the associated raw images. The oscillations in the load-cell data are due to typical resonance of the load-cell system. Note that the integrated-pressure measurements are free from the inherent resonance of the load-cell system.95

Figure 2-29. The output of the procedure is the color-coded version of the pressure distribution measured by the Impact Module.96

Figure 2-30. Two images from a calibration test conducted for the pressure-sensing technology. The image at the left shows the contact patches (white) created by five vertically-oriented pressure-sensor strips at a certain time during the 5 second ramp when an increasing uniform pressure was applied to the strips. The image at the right shows the same situation at a later time during the ramp when the pressure was significantly higher. The horizontal lines at the top and bottom of the strips indicate opposing edges of the square pressure patch that was applied to the strips.98

Figure 2-31. Calibration data (solid circles) and fit curve (solid line) for the pressure-sensing technology. The data were acquired during the ascending linear portion of the loading ramp that was applied during the calibration. The dashed curve corresponds to the output from the pressure-sensor strips during the descending linear unloading ramp.99

Figure 2-32. Sequence of pressure-pattern images from test May8_A+B_2014. The images run from left to right in each row from top to bottom. The capture rate was 250 images/s. The width of a blue box is ~ 60 cm..... 105

Figure 2-33. Sequence of pressure-pattern images from test May22_2014. The images run from left to right in each row from top to bottom. The capture rate was 500 images/s. The width of a blue box is ~ 60 cm..... 107

Figure 2-34. Sequence of pressure-pattern images from test Dec10_2015. The images run from left to right in each row from top to bottom. The capture rate was 500 images/s. The width of a blue box is ~ 60 cm..... 109

Figure 2-35. Sequence of 17 pressure-pattern images from test June27_2014. The images run from left to right in each row from top to bottom. The capture rate was 500 images/s. The width of a blue box is ~ 60 cm. There were 19 raw images, but the 17th and 18th were too blurred to process..... 111

Figure 2-36. Sequence of 17 pressure-pattern images from test Oct16_2014. The images run from left to right in each row from top to bottom. The capture rate was 500 images/s. The width of a blue box is ~ 60 cm. There were 19 raw images, but the 16th and 17th were too blurred to process..... 114

Figure 2-37. Sequence of 19 pressure-pattern images from test Dec15_2014. The images run from left to right in each row from top to bottom. The capture rate was 500 images/s. The width of a blue box is ~ 60 cm. There were 25 raw images but the 19th - 24th were too blurred to process..... 117

Figure 2-38. Sequence of 17 pressure-pattern images from test Jan20_2015. The images run from left to right in each row from top to bottom. The capture rate was 500 images/s.

The width of a blue box is ~ 60 cm. There were 24 raw images but the 17th – 23rd were too blurred to process..... 119

Figure 2-39. Sequence of 17 pressure-pattern images from test Feb25_2016. The images run from left to right in each row from top to bottom. The capture rate was 500 images/s. The width of a blue box is ~ 60 cm. There were 19 raw images, but the 17th and 18th were too blurred to process..... 121

Figure 3-1. Pressure - sensing technology. Figure modified from Gagnon et al. (2020).144

Figure 3-2. Untreated sample image from the high-speed camera. (Gagnon et al. 2020) 145

Figure 3-3. The output of the procedure is a color-coded pressure distribution image. (Gagnon et al. 2020) 146

Figure 3-4. Load comparison for the dec 10 2015 experiment. The integrated pressure pattern only shows data for duration of the penetration. (Gagnon et al., 2020) 147

Figure 3-5. Meshed model with close-up. 152

Figure 3-6. Effective plastic strain color plot relative to the dynamic simulation using pressure data from the dec 10 2015 experiment. 154

Figure 3-7. Force curves, for the simulation using the loads measured during the dec 10 2015 impact test. 156

Figure 3-8. Curves for structural deformation energy (Dec 10 2015 experiment). 158

Figure 3-9. Curves showing the energy evolution in time and the point of total kinetic energy depletion (Dec 10 2015)..... 160

Figure 3-10. Force curves plot (Dec 10 2015) showing the instant of energy depletion (vertical line). 161

Figure 4-1. Large Pendulum schematic with some structure removed to show the carriages.	173
Figure 4-2. Impact 1 pre-damaged “truncated” cone (left), Impact 2 sharp-tipped cone (centre), and Impact 3 re-used cone (right).....	176
Figure 4-3. Panel Carriage.	177
Figure 4-4. ex-HMCS IROQUOIS panel illustration. Perimeter bar is seen represented in the drawing (grey bar with bolt holes around the plate perimeter). The stiffener end plates are also shown (green).	178
Figure 4-5. Corner of the ringframe showing the recess locations where perimeter bar is clamped with bolts (orange) and, similarly, where the stiffener plates are clamped (yellow).	179
Figure 4-6. Cutaway view showing the fitted panel. Note how stiffener end plates and the perimeter bar align with the bolt holes in the ringframe of the carriage.....	179
Figure 4-7. CAD drawing of the ex-HMCS IROQUOIS panel (shown in metres). Perimeter bars and stiffener end plates are not shown.	181
Figure 4-8. The ex-HMCS IROQUOIS panel in the test carriage.....	182
Figure 4-9. Location of the accelerometers and load cells in relation to the pendulum components	183
Figure 4-10. High speed cameras positioned perpendicular on each pendulum side for capturing the test.	184
Figure 4-11. Image showing the movement direction and the laser cut markers for DIC measurements.....	185

Figure 4-12. Experiment phases. A is the swing phase; B is the impact phase; C is the post-impact phase (Impact 2 shown here).	188
Figure 4-13. The 5000g accelerometer data for Impact 2. The instant of contact is also noted.....	189
Figure 4-14. Impact force data for Impact 2.	190
Figure 4-15. Delay difference between the sensors (Impact 2).	191
Figure 4-16. DIC measurements (Impact 2): (a) Panel carriage (b) Ice cone carriage.	195
Figure 4-17. Representation of panel indentation measurement axis and location. Jig “shelves” shown on the left and right faces of the ringframe.	197
Figure 4-18. Representation of the test panel IROQ1 progressive indentation through the impact experiments. The X-axis shows the points where indentation depth measurements were taken on the panel, as illustrated in Figure 4-17. The Y-axis shows the measured displacement of those of points. The different lines illustrate the panel deformation after each impact.	197
Figure 4-19. Carriages separation during impact (Impact 2).	199
Figure 4-20. Ice indentation progression of Impact 2.	200
Figure 4-21. Energy balance for Impact 2.	201
Figure 4-22. Original ballast plate arrangement. A single plate is indicated by the red arrow.	202
Figure 5-1 – Illustration of the ice-ship structure interaction process during crushing. The deformed ship structure is represented in red. The black dashed line represents the original intact structure. Grey and blue colours represent the crushed and intact ice regions, respectively.	218

Figure 5-2 – A thick horizontal slice from the top of an indented specimen (Hobson’s Choice Ice Island experiments). The indenter was acting on the top of the ice, and the base was connected to the multiyear ice wall. Darker coloured regions (grey regions indicated by full red arrows) are intact ice, and milky white regions are crushed ice (regions indicated by dashed yellow arrows). The crushed ice starts at the edges of the intact region and tends to grow in thickness moving away from the intact region. The crushed ice region is not uniform. Larger chunks are visible within it. (Gagnon, 1998)219

Figure 5-3 – Pressure distribution map (left) and the equivalent ice damage (right) (Sopper et al., 2015). The warmer colours from the color-pressure scale (MPa) on the left image represent high-pressure zones (HPZs). These HPZs correlate with the observed relatively intact ice (dark dendritic feature in the contact zone) observed on the image on the right.221

Figure 5-4 – Test face images from three Hobson’s Choice experiments. All these ice features had originally the shape of a square pyramid. TRF 02 and TRF 03 show no signs of catastrophic spallation events and developed X-shaped HPZs (hard zones). TRF 05 shows a significant change in the bulk-ice geometry and a very different HPZ pattern (sickle-shaped hard zone). (Gagnon, 1998; Muhonen, 1991).....225

Figure 5-5 – From left to right, pressures maps #9, #10, #11, and #12 from the Feb25_2016 experiment (Gagnon et al., 2020), the colour temperature correlates to contact pressure intensity (color-bar in MPa). The maps show the sequential progression and HPZ development during the impact experiment, when spallation occurs in #10, indicated by the arrow. The images were recorded at 500 Hz.226

Figure 5-6 – Load curve data for the Feb25_2016 experiment. Marked is the instant a catastrophic spall was observed in the pressure maps indicated in Figure 5-5, pressure map #10.....226

Figure 5-7 – Test face from one of the Hobson’s choice experiments (Gagnon 1998). The dark area that forms an “X” shape shows where relatively-intact ice is observed.228

Figure 5-8 – Spencer and Masterson’s idealized HPZs model (re-drawn from Spencer and Masterson (1993)).....229

Figure 5-9 – Visual exemplification of the HPZ distribution model from Croasdale (2001). Original in (Croasdale, 2001), adapted in (Daley, 2020).....230

Figure 5-10 – Examples of the medial axes of a rectangle (black lines). The picture also illustrates circumferences that are enclosed in the 2D shape, whose centres belong to a point in the medial axis, and that are tangent (red dots) to at least two points belonging to the object’s perimeter.....231

Figure 5-11 – Example of a discretized distance field of a square shape. Numbers describe how many elements there are between it and the perimeter (indicated by the bold line).233

Figure 5-12 – Example of a high-resolution distance field map of a square shape. The colour warmth relates to the distance value to the perimeter, warmer colours correlate to farther regions, i.e., more confined regions.234

Figure 5-13 – Process of combining the topological skeleton with its distance field data (a square is used as example). Above are the discretized matrices. Below are the visual representations of the matrices.....236

Figure 5-14 – Examples of HPZ (yellow) and LPZ (cyan) representation of a square shape using the topological skeleton method. Different HPZ/Total area ratios are shown: (a) shows a HPZ coverage of 5% of the square area, (b) 10%, and (c) 20%.237

Figure 5-15 – HPZ generation methodology diagram.238

Figure 5-16 – Hobson’s Choice Ice Island indented ice test face (right) (Gagnon, 1998; Spencer and Masterson, 1993) compared with the idealized HPZ distribution (HPZ is yellow and LPZ is cyan) of a square nominal contact area predicted by the topological skeleton methodology (left).239

Figure 5-17 – Examples of HPZ distribution patterns (HPZ is yellow, LPZ is cyan, background is dark blue) for idealized nominal contact area shapes. HPZ is assumed to cover 10% of the contact area.240

Figure 5-18 – Oct_16 2014 Large pendulum’s impact ice test face (right) (Sopper et al., 2015) compared with the HPZ distribution predicted by the topological skeleton methodology (left). HPZ is yellow, LPZ is green, and the background is blue.....241

Figure 5-19 – Large pendulum impact ice test face (right) and corresponding pressure map (left), October_16 2014. Red and Yellow arrows show regions of the contact area that have negligible measured contact pressure.242

Figure 5-20 – Large pendulum’s ice impact October16_2014 test face (centre) compared with experimental pressure distribution data, and the HPZ distribution predicted by the topological skeleton methodology (left). Images are not on the same scale.....243

Figure 5-21 – Generated HPZ distribution for Dec15_2014 (Gagnon et al., 2020) test face (centre) using the topological skeleton method (right). It is compared to the pressure map (left). The pressure map is not on the same scale.244

Figure 5-22 – Generated HPZ distribution for Jan20_2015 (Gagnon et al., 2020) test face (centre) using the topological skeleton method (right). It is compared to the pressure map (left). The pressure map is not on the same scale.244

Figure 5-23 – Generated HPZ distribution for Dec10_2015 (Gagnon et al., 2020) test face (centre) using the topological skeleton method (right). It is compared to the pressure map (left). The pressure map is not on the same scale.245

Figure 5-24 – Generated HPZ distribution for Feb25_2016 (Gagnon et al., 2020) test face (centre) using the topological skeleton method (right). It is compared to the pressure map (left). The pressure map is not on the same scale.245

Figure 5-25 – TFR 01 (Muhonen, 1991) test face (left). Generated HPZ distribution using the topological skeleton method (right). The original ice-feature shape was a vertical wedge.246

Figure 5-26 – TFR 02 (Muhonen, 1991) test face and also region selected for HPZ generation (left). Generated HPZ distribution using the topological skeleton method (right). The original ice-feature shape was a truncated square pyramid.247

Figure 5-27 – TFR 04 (Muhonen, 1991) test face and also region selected for HPZ generation (left). Generated HPZ distribution using the topological skeleton method (right). The original ice-feature shape was a truncated square pyramid.247

Figure 5-28 – TFR 05 (Muhonen, 1991) test face and also region selected for HPZ generation (left). Generated HPZ distribution using the topological skeleton method (right). The original ice-feature shape was a truncated square pyramid with base rotated 45 degrees w.r.t TRF 04.248

Figure 5-29 – On the left, picture of the post-indentation test face of a small-scale indentation experiment (reported in Gagnon and Bugden (2022)). In this image it is possible to see relatively-intact ice as translucent grey, which is associated with the HPZ, and crushed ice as a milky white region, which is associated with the LPZ. The test-face contact geometry (outlined in red) is used to predict the HPZ distribution using the present methodology. On the right, the predicted HPZ distribution of the region.249

Figure 5-30 – On the left, picture of the post-indentation test face of a second small-scale indentation experiment. In this image it is possible to see relatively-intact ice as translucent grey, which is associated with the HPZ, and crushed ice as the milky-white region, which is associated with the LPZ. The test-face contact perimeter (outlined in red) is used to predict the HPZ distribution using the present methodology. On the right, the predicted HPZ distribution of the region.250

Figure 5-31 – Idealized example of an ice-structure indentation. The contact area progression is represented on the left. The contact areas (CA's) are represented as idealized squares and the modelled pressure distribution is shown on the right.256

Figure 5-32 – Topological skeleton generation using different MATLAB algorithms: bwskel (left), and bwmorph (right).268

Figure 5-33 – In this image two different contact areas are selected from a test face, the top image shows a more careful selection (the same as the one shown in Figure 5-30), while the second one was drawn more crudely. In both cases the general shape of the HPZs remain very similar.270

Figure 6-1. Representation of design scenario behind IACS UR I ice load determination method: A ship of speed V_s has a glancing impact against an ice floe causing ice to be

crushed. V_n is component of the ship speed normal to the crushing direction. In this work ice is assumed stationary w.r.t the ship and of infinite mass. (Image modified from Daley (1999)).....274

Figure 6-2. Definition of hull angles used in the IACS UR I and PD for ice load determination. (International Association of Classification Societies, 2011).....277

Figure 6-3. General wedge-shaped edge normal to hull. (Daley, 1999).....278

Figure 6-4. Image on the left illustrates the underlying assumption behind the PD method: only the load patch at the point of maximum penetration is considered in the structural design. The right image illustrates the PRO method, which includes the intermediary contact areas before maximum penetration is achieved.....281

Figure 6-5. Example of load patch sizes at different loadsteps of the same simulation. As expected, load patch size increases during the simulation progression. Loadstep #1 is the first loadstep and loadstep #40 is the last. The simulation is implicit with 40 loadsteps.283

Figure 6-6. Methodology framework for numerical structural simulations with coupled progressive ice loads, or PROWiSE approach (Andrade et al., 2022a).....284

Figure 6-7. Pressure distribution map (left) and the equivalent ice damage (right) (modified from Sopper et. al (2015)). The colored-pressure scale is in MPa on the left image, which shows that HPZs (warmer colors) directly correlate with the observed relatively intact ice observed on the image on the right (the darker grey dendritic features in the contact zone, completely enveloped by milky crushed ice).....288

Figure 6-8. Topological skeleton representation for a rectangular shape. The skeleton is formed by the segments AIp1, BIp1, CIp2, DIp2, and Ip1Ip2.290

Figure 6-9. Topological skeleton representation for a triangular shape. The skeleton is formed by the segments AI, BI, and CI.290

Figure 6-10. Representation of the discs enclosed in a triangle (bottom) and rectangle (top) that are tangent to the closest two sides, and that are centred along the topological skeleton.291

Figure 6-11. Illustration for the process of HPZ zone generation for triangles and rectangles. Discs centred at the topological skeleton have their radii as the shortest distance to the closest edge. These radii are fractionized equally for all discs, and the union of discs will form the HPZ. The HPZ sizes in this image are for illustration purposes only.292

Figure 6-12. The same triangular contact area can be represented with different HPZ regions. In this example the ratio, f , is different for the top and bottom figures, with $f_{\text{bottom}} > f_{\text{top}}$. This causes the bottom contact area to have a larger HPZ region than the top contact area.293

Figure 6-13. Example of a non-uniform load that is used in a number of the numerical structural simulations performed in this work. Red regions are HPZ, blue regions LPZ, and the pressure scale bar is in Pa.296

Figure 6-14. Illustrative drawing of the designed PC7 panel structure.300

Figure 6-15. Meshed panel showing clamped BC around its perimeter.301

Figure 6-16. Full structural model (right) and halved structural model (left). Symmetric boundary condition (along YZ plane at the geometric centre of the plate) can be used for triangular load patches (exemplified in blue) to approximately half the number of elements in the model.302

Figure 6-17. Full structural model (right) and quartered structural model (left). Doubly symmetric boundary condition (along XZ & YZ planes at the geometric centre of the plate) can be used for rectangular load patches (exemplified in blue) to approximately quarter the number of elements in the model.302

Figure 6-18. Meshed model with a close-up to show element density.304

Figure 6-19. Measured displacement for 5 meshes with decreasing element size (from left to right: 100 mm, 50 mm, 37 mm, 25 mm, and 20 mm). The point shown as a red triangle shows the mesh size for the chosen element (25 mm) for this study. The load applied is also the largest load in this study, both in force magnitude (7.61 MN) and pressure concentration (HPZs are present).305

Figure 6-20. AH36 Steel true stress-strain curve (American Bureau of Shipping, 2021).
.....306

Figure 6-21. Illustration of the conceptual difference between calculated load patch (represented by the dashed rectangle) and applied load patch in FEA meshes (blue region).
.....311

Figure 6-22. Location of the plate's geometric centre, shown by the red dot indicated by the arrow. It is located behind a main frame, located inside the dashed rectangle. The out-of-plane nodal displacement data depicted in this work were collected from the node coincident to that region.313

Figure 6-23. Sequence of images showing the difference in equivalent plastic strain for the PD load cases. The colour scale for each load case is shown to its right. The top left image shows the entire structure, and square indicates the region where plastic damage is observed.314

Figure 6-24. Design and applied pressure-area curves for the PC7 case with progressive non-coupled loadsteps, rectangular patch, and uniform pressure distribution.....316

Figure 6-25. Design and applied pressure-area curves for the PC6 case with progressive non-coupled loadsteps, rectangular patch, and uniform pressure distribution.....316

Figure 6-26. Design and applied pressure-area curves for the PC5 case with progressive non-coupled loadsteps, rectangular patch, and uniform pressure distribution.....317

Figure 6-27. Design and applied pressure-area curves for the PC4 case with progressive non-coupled loadsteps, rectangular patch, and uniform pressure distribution.....317

Figure 6-28. Curves showing the progression of plastic damage & applied pressure as function of the applied area for the PRO-PC7- and –PC4 simulations.....319

Figure 6-29. Linear interpolation surface for non-zero Plastic Damage vs Pressure-Area from all loadsteps in the PRO-PC7, PC6, PC5, and PC4 cases. Top image shows the 3D surface plot, and the bottom image shows the 2D contour plot. Red dots are the loadsteps with no plastic damage, black dots have non-zero plastic damage. Note that on the bottom image the dots form the four pressure-area curves shown in Figure 6-24 through Figure 6-27. The 2D contour plot shows the plastic deformation energy for the interpolated surface in joules.320

Figure 6-30. Examples of plastic damage of the structure at different simulation stages for different load cases. The images show only the regions where plastic strain is larger or equal 1%. At the centre is the 2D contour plot.321

Figure 6-31. Structural energy for the PC7 load cases: single loadstep (PD), progressive non-coupled (PRO), and progressive coupled (PROWiSE).326

Figure 6-32. Structural energy for the PC6 load cases: single loadstep (PD), progressive non-coupled (PRO), and progressive coupled (PROWiSE).327

Figure 6-33. Structural energy for the PC5 load cases: single loadstep (PD), progressive non-coupled (PRO), and progressive coupled (PROWiSE).327

Figure 6-34. Structural energy for the PC4 load cases: single loadstep (PD), progressive non-coupled (PRO), and progressive coupled (PROWiSE).328

Figure 6-35. Load patches with NILAS method non-uniform pressure distribution. Red regions are HPZs, and blue regions are LPZs. Each image represents a different stage of the ice crushing process (*the top left image shows the second loadstep because the first loadstep contact area had too few elements to properly define a distinct HPZ). The bottom right image shows the last loadstep.329

Figure 6-36. HPZs and LPZs pressure values for the load patches applied in the NILAS method for PC7 load. They are compared to the nominal pressure-area curve.331

Figure 6-37. HPZs and LPZs pressure values for the load patches applied in the NILAS method for PC6 load. They are compared to the nominal pressure-area curve.331

Figure 6-38. HPZs and LPZs pressure values for the load patches applied in the NILAS method for PC5 load. They are compared to the nominal pressure-area curve332

Figure 6-39. HPZs and LPZs pressure values for the load patches applied in the NILAS method for PC4 load. They are compared to the nominal pressure-area curve.332

Figure 6-40. Illustration of the location of the load patch and its pressure zones with relation to the structure geometry and its central main frame.....333

Figure 6-41. Equivalent plastic strain for the PROWiSE-PC4 load case. A cut was performed to hide the top flanges of the stringers and webframes from view. The top image

shows the entire structure, and square indicates the region where plastic damage is observed. The small image on the left illustrates the type of load patch applied to the structure.....335

Figure 6-42. Equivalent plastic strain for the NILAS-PC4 load case. A cut was performed to hide the top flanges of the stringers and webframes from view. The top image shows the entire structure, and square indicates the region where plastic damage is observed. The small image on the left illustrates the type of load patch applied to the structure.336

Figure 6-43. Structural energy for the PC7 load cases of all studied simulation approaches. The three on the left use rectangular uniform patches (i.e., PD, PRO, and PROWiSE), the one on the right use the triangular non-uniform patch (i.e., NILAS).339

Figure 6-44. Structural energy for the PC6 load cases of all studied simulation approaches. The three on the left use rectangular uniform patches (i.e., PD, PRO, and PROWiSE), the one on the right use the triangular non-uniform patch (i.e., NILAS).340

Figure 6-45. Structural energy for the PC5 load cases of all studied simulation approaches. The three on the left use rectangular uniform patches (i.e., PD, PRO, and PROWiSE), the one on the right use the triangular non-uniform patch (i.e., NILAS).340

Figure 6-46. Structural energy for the load cases of all studied simulation approaches. The three on the left use rectangular uniform patches (i.e., PD, PRO, and PROWiSE), the one on the right use the triangular non-uniform patch (i.e., NILAS).341

Chapter 1 Introduction

The reduction of ice coverage during Arctic summers is allowing new trade routes to be used, facilitating mineral exploration in the region, and increasing Arctic tourism. These, and other changes, come with an increasing need to assert sovereignty in the Arctic region. All these factors are increasing ship traffic in northern polar waters (Aksenov et al., 2017), however, ice reduction does not mean ice-free. Even during the summer, multi-year ice presence is still of concern to vessels navigating polar waters. As first year ice cover reduces, it can free multi-year floes, a much harder type of ice. This multi-year ice can potentially move into shipping lanes, where non-polar class ships are navigating. Another concern is that ice cover reduction mostly happens during summer, while winter ice coverage remains mostly the same, so change rates are higher, which can lead to potentially dangerous situations where non-polar class ships can become trapped in a very short amount of time. In November 2021 (Staalesen, 2021), 18 ships were trapped by the rapidly growing Arctic sea-ice.

1.1 Problem statement

It is clear that a ship navigating the Arctic must be prepared to withstand accidental multi-year ice impact loads even when waters are relatively ice free. At the very least, the ship response to such loading should be evaluated. Predicting possible structural damage and capacity to withstand such events is most commonly conducted using finite element analysis (FEA) but the proper characterization of ice loads for such numerical models is still a challenge. The objective here is to better understand and model the nature of ice impact loads and pressures to allow more accurate predictions of ship structural capacity

using FEA. This will include consideration of the role of structural deformation in the ship and the importance of better modeling the non-uniform distribution of ice pressure. Addressing these issues will improve the ability to model ice impacts, particularly for ships that may be subject to overload conditions from such impacts.

1.2 Background

1.2.1 Ice-ship interaction process

At the level of local structural loading, the ice-ship impact scenario can be described as a high strain rate ice crushing event. At high strain-rates ice failure occurs in the brittle regime and it is a dynamic event (Sanderson, 1988). The interaction is a process in which ice is loaded to the point of material failure and converted from solid ice to crushed rubble, which is then extruded from the impact area (Kennedy et al., 1994; Jordaan et al., 1991). This process occurs repeatedly in space and time as an interaction proceeds, resulting in complex variations in load and pressure, also changing in space and time.

Determining a load model for an ice-ship impact scenario is challenging, as the contact loads, or pressures, vary in both space and time and are a function of the changing intersecting geometries of the ice and ship structure at the contact interface (Riska, 2018).

The contact region geometry is a function of the ship's local structural shape and the ice geometry, and it is referred to as nominal contact area. Further complexity in this case comes from the fact that ice is actively deforming during the interaction, and that the structure can also deform locally during their interaction. The ice feature has an initial bulk shape and can fail in a controlled way through smaller scale crushing, thus maintaining its

general 3D shape, which allows the interface geometry to be somewhat predictable. It can also suffer from larger scale spalling events, that may fundamentally change the local ice geometry, and consequently, the shape of the contact area at the ship-ice interface (Daley, 1994). Ship local geometric changes are related to the structural elastic and plastic deformations of the hull (Riska, 1995).

A second level of interaction occurs directly at the ice-ship interface contact region, and it is related to the non-uniformity of the contact. At this interface, the two different forms of ice, crushed ice and relatively intact ice interact with the structure (Daley, 1994; Kennedy et al., 1994; Jordaan, 2001; Gagnon, 1998; Joensuu and Riska, 1989), influencing the magnitude and distribution of pressure. As an illustration, the crushed ice that is extruded from the contact region, is represented in Figure 1-1 by a grey colour and the original hard ice, which remains relatively intact and is in direct contact with the structure, is shown in blue.

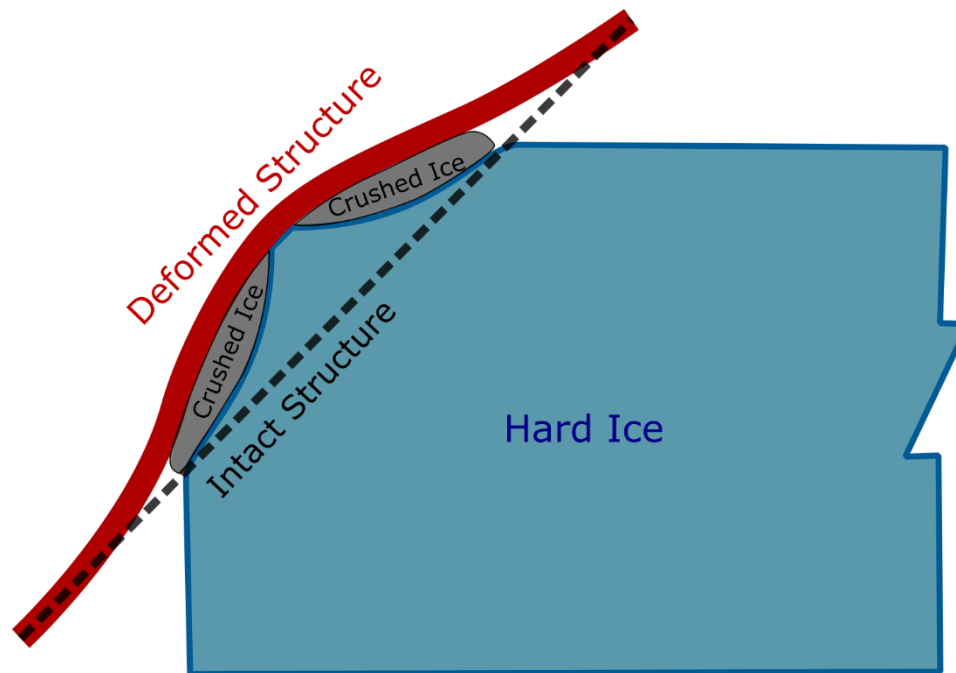


Figure 1-1. Illustration of the ice-ship structure interaction process during crushing. The deformed ship structure is represented in red. The original intact structure is represented by the black dashed line. The crushed and intact ice regions observed are represented, by grey and blue colours respectively.

Crushed ice and intact ice regions have distinct physical properties (Kennedy et al., 1994; Joensuu and Riska, 1989) and thus transmit loads in different ways. While crushed ice is associated with relatively low-pressure zones (LPZs), the intact ice region is associated with localized high pressures that can be almost an order of magnitude larger than that of the LPZs (Gagnon et al., 2020). Due to this fact, intact ice regions are designated as high-pressure zones (HPZs), or hard-zones. The presence of these two different ice types at the ice-indenter interface and their association with non-uniform pressure distribution was initially reported in Joensuu and Riska (1989), whose experiments were later also studied in Daley (1992). Their observations related the high pressures with direct contact between indenter and relatively intact ice. However, very high ice contact pressures had been

reported previously in full scale impacts with the CCGS Louis S. St. Laurent (Glen et al., 1981; Glen and Blount, 1984), but their nature was not entirely understood, since those were very localized measurements. The nature of LPZs and HPZs has subsequently been studied in laboratory experiments (Gagnon et al., 2020; O'Rourke et al., 2016; Gagnon and Daley, 2005; Jordaan et al. 1998) and field experiments (Richard and Taylor, 2014; Frederking, 2004; Kamio et al., 2000; Gagnon, 1998; Jordaan et al., 1991; Frederking et al., 1990; St. John et al., 1984).

In summary, the ice-ship hull interaction is a process that is dependent on the geometry of the indenting ice feature and the indented structure, and the presence of a complex non-uniform pressure interface, which is characterized by the presence of time-varying high- and low- pressure zones (HPZs and LPZs).

1.3 Ice load characterization

Ice compressive strength depends on strain-rate, temperature, the presence of impurities, and crystalline structure. There is a good general knowledge of how each individual parameter influences ice strength, in trend, if not in absolute value. Still, ice compressive strength shows large variation in measured values, even in laboratory settings (Timco and Weeks, 2010). For example, Jones et al. (2003) measured glacial ice compressive strength for different strain-rates, and Figure 1-2 illustrates the large variability in data results for that work.

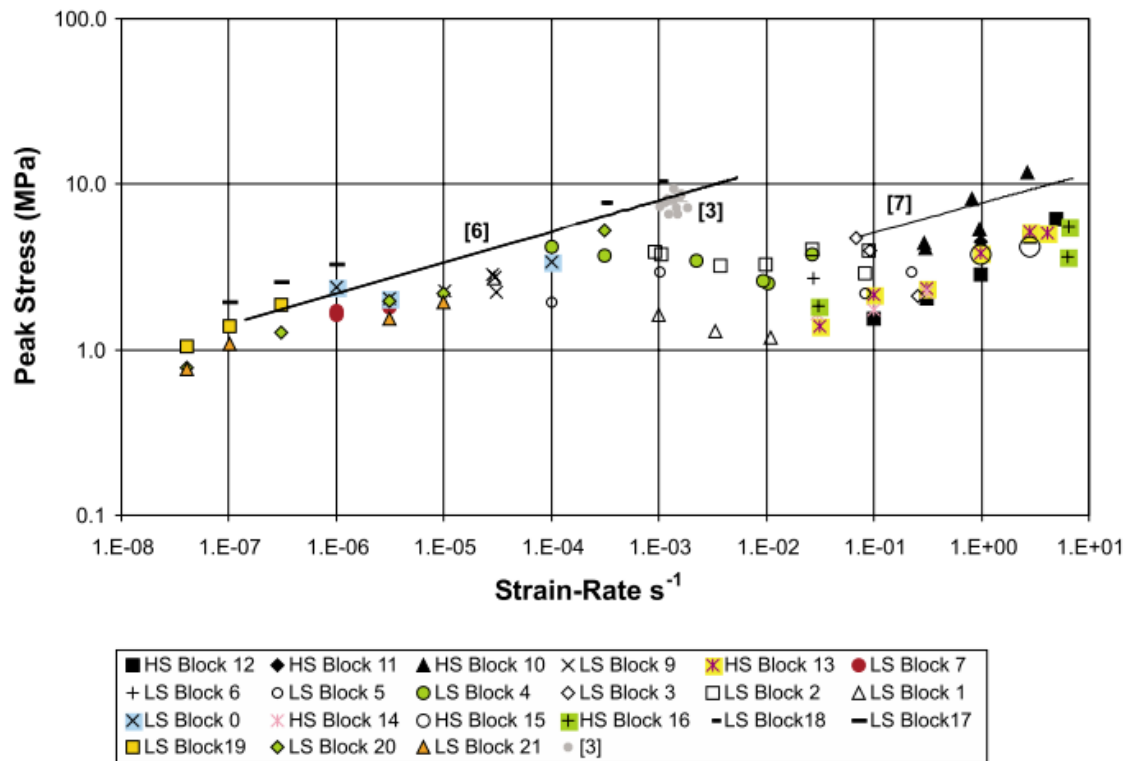


Figure 1-2. Peak stress plotted against strain rate for iceberg ice tests (Jones et al., 2003).

Ice compressive strength variability combined with the complexity of the ice-structure crushing process make the ice load characterization process a significant challenge. Because of this fact, there has been extensive effort in mapping the loads of ice impact events at many experimental scales. In the next section some significant efforts in mapping ice loads are described. These experiments support the results presented in this work.

1.3.1 Early ice load measurements during sea trials.

The icebreaker CCGS Louis S. St. Laurent was fitted with small pressure gauges in 1977. These were unitary load cells, covering a non-continuous contact area. During the trials, pressures of up to 39 MPa were reported (Glen et al., 1981). Such pressures seemed unrealistic and did not agree with available models at that time. It was understood that, if

real, these measurements could only represent a small part of the total pressure distribution over the contact area, otherwise, the local ship structure would have failed during the trials. Notably, these trials were the first attempt to map ice contact area shape and pressure distribution.

In 1978 the MV Sisu icebreaker was fitted with strain gauges attached to hull structural members (Vuorio et al., 1978). This facilitated the measurement of pressure variations over a large contact area. During trials in the Baltic Sea, it was observed that the pressure distribution was not uniform over the entire contact area and that measured pressures (up to 8.5 MPa) were larger than the uniaxial strength of the Baltic ice (about 4 MPa) (Riska, 2018). The ship MV Canmar Kigoriak was built with the intent of being a trial concept for a proposed much larger icebreaking tanker. The vessel was fitted with strain gauges following a similar methodology from the MV Sisu icebreaker. Icebreaking trials were conducted in 1981 and included impacts with old ice (Masterson and Frederking, 1993). These trials confirmed the observations from the icebreakers MV Sisu and CCGS Louis S. St. Laurent regarding non-uniform pressure distributions. A similar system was later used on the USCGC Polar Sea (St. John et al., 1984), which was used to record an extensive dataset of ice loads during ice trials between the years 1982 and 1986. This ice load monitoring system based on measured structural response in the form of strain deformation requires calculating the structure's influence stiffness matrix (Masterson and Frederking, 1993). Thus, it is only valid if the structure deformation is elastic with small deflections. Additionally, its spatial resolution is tied to the ship's structural arrangement, and it is a function of frame spacing, thus it is not fine enough to capture the pressure magnitude

levels observed by the CCGS Louis S. St. Laurent, but the measurements still showed non-uniform pressure distribution. The development of the ice crushing pressure-area theory has its roots in the observations arising from the study of those impact data (Riska, 2018).

1.3.2 In-situ contact area pressure distribution studies – Hobson’s Choice Ice Island and Hokkaido saltwater lagoon

The Hobson’s Choice Ice Island experiments of 1990 were mechanical indenter tests performed at varied strain-rates in situ in Arctic ice. The location was an ice island that had significant multi-year sea ice attached at its perimeter. A trench was excavated in the old ice and actuators (4.5 MN capacity) were placed inside the trench to perform the experiments. The indentation experiments were performed with shaped indenters on flat ice and with flat indenters on shaped ice. In the second case, the ice wall of the trench was sculpted into a convex pyramidal and wedge shapes. The flat rigid indenter was instrumented with an array of pressure-sensor plugs. The pressure-sensor array was not large enough to cover the entire contact area, but it was possible to simultaneously measure pressures over different regions (Frederking et al., 1990). The data from these experiments led to the following observations and conclusions:

- Most experiments were performed in the brittle ice failure regime and force history curves show a clear “saw tooth” pattern.
- Pressure plugs show that the local ice pressures are not uniform.
- Pressures tended to be much higher in the center of the contact area (up to 64 MPa) (Gagnon, 1998).

- It was observed that the contact area consists of a region(s) of relatively intact ice (translucent and blue, due to the natural light conditions in the bulk ice) surrounded by crushed ice (white). (Kennedy et al., 1994; Jordaan, 2001)
- High pressures directly correlate with regions of intact ice.

Figure 1-3 shows a post indentation test face from the TRF 03 experiment (Gagnon, 1998; Muhonen, 1991). It is possible to note the dendritic shapes that coincide with regions of translucent intact ice (darker areas). These regions correlate with higher local contact pressure. They emanate from the center following the diagonals of the contact area. This region is enveloped by crushed ice (white, milky) that correlates with lower local contact pressures.

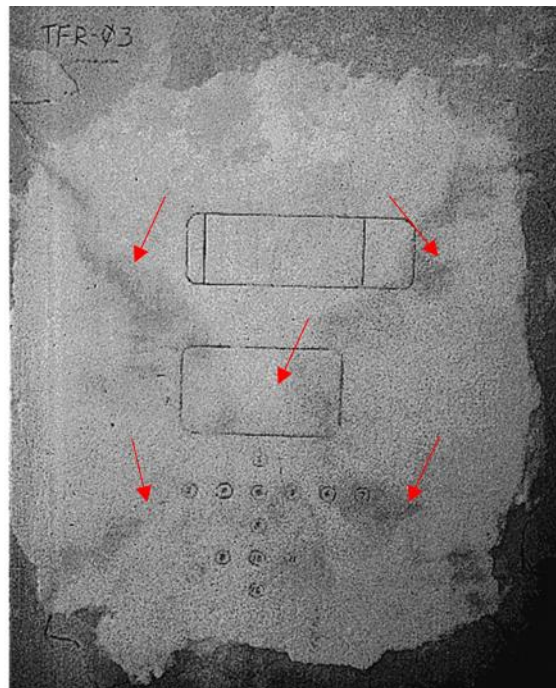


Figure 1-3. Test face from one of the Hobson’s Choice experiments. The dark area that forms a “X” shape shows where intact ice is observed, which is indicated by the red arrows. (Gagnon, 1998; Muhonen, 1991)

Gagnon (1998) argues that regions of intact ice are responsible for bearing much of the load applied to the specimen, an observation that is also presented and discussed in this work, in Chapter 2. A more detailed description of the relevance and relative magnitude of the HPZs contribution to the contact load, based on newer data is described and documented in the current work, presented in Chapter 5.

The Japan Ocean Industries Association (JOIA) medium scale tests were performed in Hokkaido between 1996 and 2000. The tests were carried out in thin first year ice, which was formed in a saltwater lagoon (Kamio et al., 2000). The most interesting aspect of these trials was the use of Tekscan® pressure sensing technology, a tactile pressure measurement system (Sodhi et al., 2006) with spatial resolution of 100 mm² (Frederking, 2004). This fine spatial resolution showed a clear presence of HPZs and LPZs in the ice crushing contact area. The HPZs again were deemed responsible for bearing most of the load while occupying only 10% of the nominal contact area. Interestingly, the highest pressure recorded in these events was 2.55 MPa, after due calibration (Frederking, 2004). This value is much lower than what is seen in other experiments (e.g.: St. John et al. 1984b; Riska 2018; Gagnon et al. 2020). The reason is probably related to ice characteristics and equipment limitations, since Tekscan has coarse time resolution. The tactile sensor manufacturer (Tekscan, 2022) explains that the product is not capable of measuring dynamic loads with rise-time faster than 0.1 - 0.3 seconds. Experimental measurements of ice impact loads are reported to have faster load rise-time than 0.1 seconds (Gagnon et al., 2020; Sopper et al., 2015).

1.3.3 Laboratory contact area pressures measured in high resolution

In 2001 the CCGS Terry Fox icebreaker was instrumented to measure local ice loads from impacts with growlers and bergy bits (glacial ice). The ship was equipped with two different load measurement systems. The first consisted of strain gauges attached to the hull frames/stringers, and the second was an external impact panel with a novel pressure measurement technology (Gagnon et al., 2008). The impact panel was able to record contact pressures with moderate temporal (60 Hz) and high spatial (18 mm × 18 mm) resolution over a relatively large contact area (1.5 m × 2.4 m) (R. Gagnon, 2008). The results showed good agreement between sensor types and validated the impact panel technology. This allowed the changing distribution of HPZs (8 – 20 MPa for these trials) and LPZs (averaging 2.5 MPa) to be tracked, however the instrument was not capable of measuring LPZs during those experiments.

As a follow-on from the bergy-bit impact experiments, a completely new impact panel was designed for future field tests using the CCGS Terry Fox. The panel was modular in design and incorporated 6 Impact Modules, where each of the Impact Modules had new pressure-sensing technology with greater capability than that used in the 2001 bergy bit impact study. One of the Impact Modules was eventually built and used in a series of Large Double Pendulum Ice Impacts performed at Memorial University of Newfoundland. In these experiments, granular freshwater ice cones were impacted against the Impact Module using a double pendulum (Gagnon et al., 2020). The combined spatial and temporal resolution of the pressure distributions is the highest of any known ice pressure sensing device. The current work presents and analyses the results from these experiments in Chapter 2.

Other examples of recent ice crushing experiments that measure pressure distribution using tactile pressure measuring systems include the impact tests between freshwater ice blocks and a floating structure reported in Kim et al. (2017), and ice extrusion crushing experiments presented in Herrnring et al. (2020) and in Kubiczek et al. (2022).

1.4 Models for ice loads in numerical structural simulations

In the following section, some commonly and currently used approaches to modeling ice loads in numerical structural simulations are discussed.

1.4.1 IACS UR I: A codified approach for polar ship design

The IACS UR I (International Association of Classification Societies Unified Requirements I) design rules for ships that operate in polar waters is based on a limited energy impact scenario, where the ship structure is assumed to be rigid, and the impact kinetic energy is exclusively absorbed by the ice crushing process. The underlying methodology behind IACS ice load determination approach is based on the contributions of Popov (1967) and Daley (2000, 1999). Popov et al. (1967) proposed the energy based 1-dimensional ice impact model, while Daley (2000, 1999) proposed the use of pressure-area curves to characterize the ice crushing energy.

The IACS UR I codified design approach defines an ice load patch with uniform pressure and rectangular shape to design local structural scantlings in an ice strengthened vessel (International Association of Classification Societies, 2011). This patch is an adaptation from the nominal contact area defined by the scenario established in the rules (Daley, 2000). The original nominal contact area shape is defined as a function of the ship local geometry

and the ice geometry, which is assumed to be a wedge shape. The nominal contact area (the projection of the wedge on the ship structure at the point of contact) is transformed into an “equivalent” rectangular pressure patch (Area and Aspect Ratio are preserved). The area of this new rectangular patch is then reduced by an area reduction factor, this increases the average pressure when compared to the nominal contact pressure. The function of this factor is to account for the pressure concentration observed in ice impact experiments. This load patch is determined at the point of maximum ice penetration, at the end of the ice crushing process, when all energy of the system is spent.

Although the IACS UR I design ice load patch is sometimes used for numerical structural analysis, it is not an appropriate solution for all cases. The methodology assumes that all energy in the ice-ship system is absorbed by the ice crushing process (assuming that the flexural strength limit of the ice is not reached before that). This means that it ignores energy absorbed by the structure itself during the deformation process. As will be discussed in Chapter 6, this is not an issue for simulations done at the design load of the studied structure (if the studied structure is a polar class vessel), but in overload cases or for non-polar classes, this would not be strictly true. For these cases a method is required to account for the structural losses when defining the load as discussed by Daley and Kim (2010), Liu et al. (2011), Dolny (2017), and Price et al. (2021).

Finally, the codified IACS UR I approach was developed for designing polar-class ship structures quickly and methodically. A single uniform contact patch with constant pressure is not able to represent the dynamism and spatial pressure distribution of the real ice contact

region, thus empirical correction factors are required to address simplifications and uncertainties involved (Kim and Amdahl, 2016).

The Russian Maritime Register of Shipping (RMRS) ice rules and the Finnish-Swedish Ice Class Rules (FSICR) also use a constant pressure load patch to define the contact region. The FSICR ice load value is based on empirical data of ice properties in the Baltic Sea (which is fairly regular first year ice) and studies of ship structural damage for that region (Riska and Kämäräinen, 2011). The RMRS rules ice load determination, although not fully disclosed in scientific literature, can be described as based on the Kurdyumov and Kheisin (1976) hydrodynamic model of ice crushing (Kim and Amdahl, 2016).

1.4.1.1 Ice material models for FEA simulations

There are two main ways to simulate ice-ship dynamic interaction in a finite element simulation. One is using “contactless” loads, which in the context of this work, refers exclusively to the use of user defined load patches to be applied directly to the mesh of the structure in numerical structural analyses. The second approach, which is in contrast with the “contactless” ice load approach, is to model the ice (having realistic material properties) as a deformable body in the simulation environment, and then use a contact algorithm to determine the contact loads applied to the ice and the structure.

Developing a model so that ice can be represented as a body in FEA contact simulations has proven to be difficult. It is not simply a matter of creating an ice material model. Particularly challenging is the modelling of the changes to the ice body’s continuous domain due to spalling events. Capturing the behaviour of ice requires that a continuum be fractured into discontinuous media, which is extremely difficult to properly implement in

FEM (Finite Elements Methods), as FE theory assumes a continuous domain. Another problem is that, after ice fractures/shatters, it remains in the contact region in the form of a new material, the crushed ice, and the material model needs to be able to represent that. Finally, the simulation of ship-ice interaction with an ice material model requires at least two bodies, one for the ice and another for the structure, and the simulation of two deformable bodies in contact is very computer intensive. Still, there are some available ice material models that can be used for specific applications, although some of these are really surrogate models in which an existing material type is provided with a set of property values that allow the existing material to mimic the characteristics of ice over a certain range. These include the viscoelastic material by Xiao (1997), the crushable foam material for glacial ice by Gagnon & Derradji-Aouat (2006), and more recently a Mohr-Coulomb nodal split method developed by Herrnring and Ehlers (2022), and the pressure dependent plasticity model by Mokhtari (2022).

1.4.1.2 Direct application of measured ice load

An alternative to modelling ice as a material is to use experimental data and apply it directly to the studied model as pressure patches. For example, the 4D-Pressure Method (4DPM) is a solution to the problem of performing explicit FE simulations with dynamic ice pressure loads – that vary in space and time – developed by Quinton (Quinton et al., 2013, 2012). The method allows the real-time/real-space full-scale pressures measured from a pressure panel array to be applied, without simplification, to any general FE mesh.

Direct application methods do not modify the loads applied to the hull structure; thus, the ice pressures are applied exactly as they were measured. This is a limitation since the actual

time-varying ice conditions during the trials are seldom reported, and when ice information is available, it is usually generalized, in the form of ice stage of development (e.g., multi-year ice, first-year ice). The problem is compounded further when ice properties (e.g. thickness, strength, density) for any given stage of development can vary widely (Kendrick and Daley, 2011). Another complication is that the rigidity of the apparatus used to measure the ice loads often does not match the rigidity of the studied structure. In other words, the load information is decoupled from structural deformation during the FE simulation. This is a problem for two reasons. One is that the contact area geometry is dependent on the geometry of the bulk ice feature and the ship structure. The second is that the ice-ship impact scenario is usually one of limited energy, and the structure can become a significant energy sink in the system during the ice-ship interaction process. In fact, it is common practice in engineering projects to assume load and structure as decoupled from one another, since in most applications the structural deformation magnitude is not significant enough to require the extra analysis effort. That is, the ship structures are usually designed within the yield limit state. This, however, is not necessarily true for ice loads acting on non-polar class vessels or in overload scenarios, as it is discussed in more depth in Chapter 6.

1.4.2 Summary

This section discussed the main challenges regarding ice load characterization during ice-ship impact events for non-polar class structures and overloaded polar class structures. They can be summarized as follows:

- Measuring pressure distribution at the ice-ship contact interface.

- Modelling the pressure distribution at the contact interface.
- Coupling the ice-load model to structural deformation.

1.5 Scope and contribution of the research

This research addresses the challenges of ice load modelling for ice-ship interaction for non-polar class vessels / overloaded polar class ships, by creating a new “contactless” ice load model. The steps undertaken in this research are as follows:

- **Measuring ice impact pressure distribution (Chapters 2).** The initial stage of the research is data processing and analysis of ice impact experiments recorded in high-temporal and spatial resolution. This work analyzes in detail the results from ice impact experiments performed with the Impact Module developed at NRC (National Research Council Canada) (R. E. Gagnon, 2008a) and Large Pendulum Apparatus at Memorial University (Gagnon et al., 2015). These experiments were done in the Large Pendulum Apparatus between 2014 and 2016, however, the complete dataset had not been processed, analysed, or published prior to the current work. Also in the current work, an original procedure for translating images into a pressure map was revised and updated. The analyses of these data provide a deeper understanding of the relative HPZs / LPZs shape and distribution, and load bearing capabilities.
- **Determining the deformation and energy losses in non-polar class ship structure (Chapter 3 and 4).** In this stage, the ice impact pressure data measured by the Impact Module are applied to numerical models made similar to structural panels from a non-polar class Canadian destroyer, the ex-HCMS IROQUOIS.

These simulations were done in anticipation of a new set of experiments to be performed in the large pendulum apparatus. An energy balance study is performed by comparing the known pendulum energy to the structural deformation energy, and the measured ice crushing energy. This work also presents the initial results from a newer set of impact experiments performed in the large pendulum apparatus using ice cones and stiffened panels from the ex-HCMS IROQUOIS. In this case the loads were measured with piezoelectric load cells. Additionally, local accelerations on the structural panel were measured with accelerometers and the entire impact event was recorded with high-speed cameras. A digital image correlation system (DIC) is used to obtain the pendulums' rigid body displacements, velocities, and accelerations from the high-speed camera recordings. The panels' permanent local deformations were measured after each impact.

- **Modelling ice load distribution (Chapter 5).** The next stage presents a model for representing ice load patches with non-uniform pressure distribution. It is proposed that the topological skeleton and distance field information of an arbitrary contact area can be used to predict the pattern of HPZs. The model is tested against many different test faces recorded from ice impact experiments at different scales including, the Hobson's Choice Ice Island experiments, the large pendulum ice impact experiments, and small-scale ice indentation experiments. Results show excellent prediction capabilities of HPZs shape and distribution.
- **Coupling ice load to structural deformation (Chapter 6).** Numerical and laboratory experiments (Chapter 3 and 4) show that ice loads of the magnitude

generated by the large pendulum are capable deforming the structure plastically and that the structure would be a significant energy sink during an ice interaction event. Following this observation, a procedure is developed to account for structural deformation energies during numerical simulations with “contactless” ice load application. This coupled energy procedure produces significantly different results from a non-coupled single load patch procedure.

- **Application and evaluation of the developed pressure model (Chapter 6).** In the final stage the coupled-energy approach is combined with the geometric model for HPZ generation to develop a new ice load model. The model is capable of recreating pressure distribution patterns observed in experiments, while being coupled to structural deformation. This new coupled ice load model with non-uniform ice pressure distribution shows the importance of modelling load evolution during an impact event, not just at the point of maximum ice penetration (which is the typical codified ice load determination approach), and the importance of using a load model with a more realistic pressure distribution.

The following sub-section provides a summary description of the content in each chapter of the thesis. Each of these chapters is a stand-alone publication and this summary provides the link to the research steps outlined above.

1.5.1 Chapter 2 summary description

In Chapter 2 ice pressure maps obtained from the analysis of the Impact Module experiments are presented. The Impact Module captures non-uniform pressure distribution

during ice impacts with a time resolution of 500 Hz and spatial resolution of roughly 2 cm². The pressure data for 9 medium scale impact experiments are presented. The results show interesting aspects of the pressure distribution during ice impacts including HPZ distribution patterns. It is possible to observe large spalling events and their effects on the pressure distribution. Another significant observation is that LPZ contact areas were generally 2-6 times the size of the HPZ contact areas, while average HPZ pressures were in general almost an order of magnitude higher than average LPZ pressures. This means that in most tests, the time-averaged total load was shared roughly equally between HPZ and LPZ contact areas. Additionally, peak loads are found to be directly proportional to the maximum HPZ contact areas. This work details the importance of HPZ presence in the load characteristics of the pressure patch.

1.5.2 Chapter 3 summary description

Chapter 3 presents the numerical structural simulation of a test panel model acted on by loads measured by the Impact Module. The simulations are done by applying the pressure data to the mesh using the 4DPM (Quinton et al., 2013). The simulation is performed with explicit time integration and both dynamic and quasi-static load application procedures are tested. An energy balance study is performed by comparing the known pendulum energy to the structural deformation energy, and the measured ice crushing energy. The results presented in Chapter 3 show that the non-polar class ship structure is expected to be a significant energy sink during ice impact experiments in the large pendulum apparatus. According to the simulation results, the ice impact experiments recorded with the Impact Module would be capable of causing plastic deformation to the structure, which would

potentially become a significant energy sink for the system (the other sink is the ice crushing process). If the structure becomes an energy sink, then the maximum crushing depth of the ice cones would be reduced, since less energy would be absorbed by the ice crushing process. This was an exploratory study meant to understand how the impact experiments against real panels would behave. It demonstrated that the energy lost to structural deformation should not be neglected in analysis or simulation cases where the ship structure is expected to be loaded past the realm of elastic deformation.

1.5.3 Chapter 4 summary description

Chapter 4 presents the new Large Pendulum ice impacts done using ice cones and a panel from the ex-HCMS IROQUOIS. The data measured by the various sensors is presented, which includes load cells and accelerometers. Additionally, the results from the digital image correlation system are also presented. In this chapter only three initial impact tests are presented. Unfortunately, because of the Pandemic that occurred in 2020-2021, the rest of the experiments were delayed, and the results were not available for inclusion in the current work. The large pendulum was modified in several ways for these experiments, that is, a new carriage was designed, a new brake system was attached, a new release system was installed, and new sensors / high speed cameras were used. The results from the first three impact tests offered learning lessons for the future ice-ship panel impact experiments to be performed with the Large Pendulum. However, because of this, these experiments had to be treated as commissioning experiments, and further improvements for future experiments are outlined in Chapter 4. Still, the load recorded showed magnitudes that were similar or larger than those measured in the ice impact experiments performed against the

Impact Module, discussed in Chapter 2. The work reinforced the conclusions of Chapter 3 – that it is important to consider structural deformation as an energy sink in those interactions where plastic deformation is evident in the structure.

1.5.4 Chapter 5 summary description

In Chapter 5 the development of the methodology for modelling ice pressure zone distributions is presented. The method uses the topological skeleton and distance field information of the ice-indenter contact area to define HPZ and LPZ distribution for that contact area. Results compare favourably with experimentally determined HPZ distributions of varying ice indentation experiments at small, medium, and large scale. This modelling approach proved useful for the representation of non-uniform pressure distribution in ice load patches for “contactless” numerical structural simulations, as is discussed in Chapter 6. This development is the major component of the modeling procedure for “contactless” ice loads that include the effects of HPZ/LPZ during simulated interactions.

1.5.5 Chapter 6 summary description

In Chapter 6 three new different ice load application procedures are presented and studied. The first new method is an approach to apply a series of contact areas based on the progressive ice crushing process. At each loadstep a contact area that is slightly larger than the previous is generated and applied to the structure. The load patches are functions of the calculated indentation depth of the ice feature. In short, the method applies contact areas that represent the nominal contact area at different stages of the ice crushing progression. This is in contrast to the IACS UR I approach that only defines a single load patch at the

maximum ice penetration depth. The second method is an ice-structure coupling approach done by including the structural energy losses in the ice load generation process. This means that the energy spent between load steps is dependent not only on the ice crushing energy, but also the structural deformation energy determined by the numerical structural simulation. The final method presented is the Non-uniform Ice Loads Application System (NILAS), which implements the method developed in Chapter 5 into coupled-load numerical structural simulations. The NILAS not only couples the load but also can represent its non-uniformity with HPZs and LPZs. This replicates the observed variations in real ice crushing experiments. This new method is the final outcome of this work and provides a better alternative to using IACS UR I design load patches in numerical simulations studying the effect of ice loads in non-polar class vessels, or overload of polar class vessels. This method captures the progressive nature of ice interaction, the distribution of pressures induced by HPZ and LPZ, and the effects of structural deformation so as to provide a closer-to-real-life simulation of ship-ice interactions.

1.5.6 Summary table

Table 1-1. Summary of the Research

Research Stage	Chapter / Paper	Objective	Approach	Result
1. Measuring ice impact pressure distribution	2. Pressure Distribution Data from Large Double-Pendulum Ice Impact Tests	Measure pressure distribution during ice impacts	Process images and Analyze Impact Module Data	Accurate pressure distribution maps during small-to-medium-scale ice impact tests
2. Determining the deformation and energy losses in non-polar class ship structure	3. Numerical study of large pendulum ice impact loads	Study energy losses in deformable structure under measured ice loads	Apply loads measured by the Impact Module in a numerical model of a test panel	The panel deforms plastically and to absorb a significant amount of the impact energy
	4. Full-scale ship-structure ice impact laboratory experiments: experimental apparatus and initial results	Study the behaviour of non-polar class ships subjected to ice loads	Perform ice impacts on deformable panels and measure loads and deformation	Because of the Pandemic this stage was not fully completed. Preliminary data from the commissioning impacts were recorded, including load, accelerations, and high-speed videos.
3. Modelling the ice load distribution	5. Ice pressure distribution model: A geometry-based solution for high-pressure zone representation	Develop a model for HPZs / LPZs representation in ice load patches	Use topological skeleton and distance transform to generate the HPZs/LPZs representation	A model that can predict HPZ shape and size for any contact area
4. Coupling ice load to structural deformation 5. Application and evaluation of the ice pressure distribution model	6. The Non-uniform Ice Load Application System (NILAS) and its use in numerical structural analyses of ice impact	Develop a contactless ice load model to study its effect on non-polar class and overloaded polar class ships	Combine the model developed in Chapter 5 with a coupled energy approach	A coupled ice load patch model that can account for structural deformation during simulations with non-uniform pressure distributions

1.6 References

- Aksenov, Y., Popova, E.E., Yool, A., Nurser, A.J.G., Williams, T.D., Bertino, L., Bergh, J., 2017. On the future navigability of Arctic sea routes: High-resolution projections of the Arctic Ocean and sea ice. *Mar. Policy*.
<https://doi.org/10.1016/j.marpol.2015.12.027>
- Daley, C., 2000. IACS Unified Requirements for Polar Ships - Background Notes to Design Ice Loads. IACS Ad-hoc Group on Polar Class Ships and Transport Canada.
- Daley, C., 1999. Energy Based Ice Collision Forces, in: Proceedings of the 15th International Conference on Port and Ocean Engineering under Arctic Conditions. St. John's, Canada, pp. 1–20.
- Daley, C., 1994. Compilation of Medium Scale Ice Indentation Test Results and Comparison to ASPPR. Nepean, Canada.
- Daley, C., 1992. Ice edge contact and failure. *Cold Reg. Sci. Technol.* 21, 1–23.
[https://doi.org/10.1016/0165-232X\(92\)90002-C](https://doi.org/10.1016/0165-232X(92)90002-C)
- Daley, C.G., Kim, H., 2010. Ice Collision Forces Considering Structural Deformation, in: Proceedings of the ASME 2010 29th International Conference on Ocean, Offshore and Arctic Engineering. Shanghai, China.
- Dolny, J., 2017. A Technical Methodology for Establishing Structural Limitations of Ships in Pack Ice. Master thesis. Memorial University of Newfoundland.
- Frederking, R., 2004. Ice pressure variations during indentation, in: International

- Association of Hydraulic Engineering and Research Proceedings IAHR'04, Vol.2. Saint Petersburg, Russia, Russia, pp. 307–314.
- Frederking, R.M.W., Jordaan, I.J., McCallum, J.S., 1990. Field Tests of Ice Indentation at Medium Scale Hobson's Choice Ice Island, 1989, in: IAHR. Espoo, Finland, pp. 931–944.
- Gagnon, R., 2008. Analysis of data from bergy bit impacts using a novel hull-mounted external Impact Panel. *Cold Reg. Sci. Technol.* 52, 50–66. <https://doi.org/10.1016/j.coldregions.2007.04.018>
- Gagnon, R., Andrade, S.L., Quinton, B.W., Daley, C., Colbourne, B., 2020. Pressure distribution data from large double-pendulum ice impact tests. *Cold Reg. Sci. Technol.* 175, 103033. <https://doi.org/10.1016/j.coldregions.2020.103033>
- Gagnon, R., Cumming, D., Ritch, R., Browne, R., Johnston, M., Frederking, R., McKenna, R., Ralph, F., 2008. Overview accompaniment for papers on the bergy bit impact trials. *Cold Reg. Sci. Technol.* 52, 1–6. <https://doi.org/10.1016/j.coldregions.2007.04.015>
- Gagnon, R., Daley, C.G., Colbourne, B., 2015. A large double-pendulum device to study load, pressure distribution and structure damage during ice impact tests in the lab, in: *Proceedings of the 23rd International Conference on Port and Ocean Engineering under Arctic Conditions, POAC*. Trondheim, Norway, pp. 1–10.
- Gagnon, R.E., 2008. A new impact panel to study bergy bit/ship collisions, in: *Proceedings of the 19th IAHR International Symposium on Ice*. Vancouver, Canada, pp. 993–1000.

- Gagnon, R.E., 1998. Analysis of visual data from medium scale indentation experiments at Hobson's Choice Ice Island. *Cold Reg. Sci. Technol.* 28, 45–58. [https://doi.org/10.1016/S0165-232X\(98\)00012-3](https://doi.org/10.1016/S0165-232X(98)00012-3)
- Gagnon, R.E., Daley, C., 2005. Dual-axis video observations of ice crushing utilizing high-speed video for one perspective, in: 18th International Conference on Port and Ocean Engineering Under Arctic Conditions. Potsdam, NY, pp. 271–281.
- Gagnon, R.E., Derradji-Aouat, A., 2006. First results of numerical simulations of bergy bit collisions with the CCGS Terry Fox icebreaker, in: Proceedings of the 18th IAHR International Symposium on Ice. pp. 449–456. <https://doi.org/10.1109/16.987116>
- Glen, I.F., Blount, H., 1984. Measurement of Ice Impact Pressures and Loads Onboard CCGS Louis S. St. Laurent., in: Proceedings of the International Offshore Mechanics and Arctic Engineering Symposium. New Orleans, LA, pp. 246–252.
- Glen, I.F., Blount, H., Comfort, G., Tam, G., 1981. Results of Full-Scale Measurements Aboard CCGS LOUIS S. ST. LAURENT During a 1980 Fall Arctic Probe. Ottawa, Canada.
- Herrnring, H., Ehlers, S., 2022. A Finite Element Model for Compressive Ice Loads Based on a Mohr-Coulomb Material and the Node Splitting Technique. *J. Offshore Mech. Arct. Eng.* 144, 1–9. <https://doi.org/10.1115/1.4052746>
- Herrnring, H., Kubiczek, J.M., Ehlers, S., 2020. The ice extrusion test: a novel test setup for the investigation of ice-structure interaction – results and validation. *Ships Offshore Struct.* 15, S1–S9. <https://doi.org/10.1080/17445302.2020.1713437>

- International Association of Classification Societies, 2011. Requirements concerning Polar Class. IACS Int. Assoc. Class. Soc.
- Jordaan, I.J., 2001. Mechanics of ice–structure interaction, *Engineering Fracture Mechanics*. Volume 68, Issues 17–18, Pages 1923-1960. ISSN 0013-7944, [https://doi.org/10.1016/S0013-7944\(01\)00032-7](https://doi.org/10.1016/S0013-7944(01)00032-7).
- Jordaan, I.J., Matskevitch, D.G., Meglis, I.L., 1999 Disintegration of ice under fast compressive loading. *International Journal of Fracture* 97, 279–300. <https://doi-org.qe2a-proxy.mun.ca/10.1023/A:1018605517923>
- Jordaan I.J., Kennedy, K.P., McKenna R.F., Maes M.A., 1991. Loads and vibration induced by compressive failure of ice. *Cold Regions Engineering. Proc. of the Sixth International Specialty Conference*. ASCE, Hanover, NH, pp. 638-649
- Joensuu, A., Riska, K., 1989. Structure/ice contact, measurement results from the joint tests with Wärtsilä Arctic Research Centre in spring 1988 [in Finnish]. Espoo, Finland.
- Jones, S.J., Gagnon, R.E., Derradji, A., Bugden, A., 2003. Compressive strength of iceberg ice. *Can. J. Phys.* 81, 191–200. <https://doi.org/10.1139/p02-137>
- Kamio, Z., Takawaki, T., Matsushita, H., Takeuchi, T., Sakai, M., Terashima, T., Akagawa, S., Nakazawa, N., Saeki, H., 2000. Medium scale field indentation tests: physical characteristics of first-year sea ice at Notoro Lagoon, Hokkaido. *Proc. Int. Offshore Polar Eng. Conf.* 1, 562–568.
- Kendrick, A., Daley, C.G., 2011. *Structural Challenges Faced by Arctic Ships*, Ship Structure Committee.

- Kennedy, K.P., Jordaan, I.J., Maes, M.A., Prodanovic, A., 1994. Dynamic activity in medium-scale ice indentation tests. *Cold Reg. Sci. Technol.* 22, 253–267. [https://doi.org/10.1016/0165-232X\(94\)90004-3](https://doi.org/10.1016/0165-232X(94)90004-3)
- Kim, E., Storheim, M., Amdahl, J., Løset, S., von Bock und Polach, R.U.F., 2017. Laboratory experiments on shared-energy collisions between freshwater ice blocks and a floating steel structure. *Ships Offshore Struct.* 12, 530–544. <https://doi.org/10.1080/17445302.2016.1183270>
- Kim, E., Amdahl, J., 2016. Discussion of assumptions behind rule-based ice loads due to crushing. *Ocean Eng.* 119, 249–261. <https://doi.org/10.1016/j.oceaneng.2015.09.034>
- Kubiczek, J.M., Herrnring, H., Kellner, L., Ruckert, P., Ehlers, S., 2022. Ice Pressure Measurements With TekScan Sensors - Behaviour, Calibration and Application Limits, in: *Volume 6: Polar and Arctic Sciences and Technology*. American Society of Mechanical Engineers. <https://doi.org/10.1115/OMAE2022-80463>
- Kurdyumov, V.A., Kheisin, D.E., 1976. Hydrodynamic model of the impact of a solid on ice. *Appl. Mech.* 12, 103-109. in Russian.
- Liu, Z., Amdahl, J., Løset, S., 2011. Integrated numerical analysis of an iceberg collision with a foreship structure. *Mar. Struct.* 24, 377–395. <https://doi.org/10.1016/j.marstruc.2011.05.004>
- Masterson, D.M., Frederking, R.M.W., 1993. Local contact pressures in ship/ice and structure/ice interactions. *Cold Reg. Sci. Technol.* 21, 169–185. [https://doi.org/10.1016/0165-232X\(93\)90005-S](https://doi.org/10.1016/0165-232X(93)90005-S)

- Muhonen, A., 1991. Medium scale indentation tests—PVDF pressure measurements, ice face measurements and interpretation of crushing video. Client Report to National Research Council of Canada, Canadian Hydraulics Center by Helsinki University of Technology, Ship Laboratory.
- Popov, Y., Faddeyev, O., Kheisin, D., Yalovlev, A., 1967. Strength of Ships Sailing in Ice.
- Price, A., Quinton, B.W.T., Veitch, B., 2021. Shared-energy prediction model for ship-ice interactions, in: SNAME Maritime Convention 2021, SMC 2021. SNAME, Providence, RI, pp. 27–29. <https://doi.org/10.5957/SMC-2021-033>
- Quinton, B.W.T., Daley, C.G., Gagnon, R.E., 2013. Response of IACS URI Ship Structures to Real-time Full-scale Operational Ice Loads. *Trans. - Soc. Nav. Archit. Mar. Eng.* 120, 203–209.
- Quinton, B.W.T., Daley, C.G., Gagnon, R.E., 2012. Realistic moving ice loads and ship structural response, in: *Proceedings of the Twenty-Second International Offshore and Polar Engineering Conference*. pp. 17–22.
- O'Rourke, B.J., Jordaan I.J., Taylor, R.S., Gürtner A., 2016. Experimental investigation of oscillation of loads in ice high-pressure zones, part 1: Single indenter system. *Cold Reg. Sci. Technol*, Volume 124, Pages 25-39. ISSN 0165-232X, <https://doi.org/10.1016/j.coldregions.2015.12.005>.
- Richard, M., Taylor, R.S., 2014. Analysis of High Pressure Zone Attributes From Tactile Pressure Sensor Field Data, in: *Volume 10: Polar and Arctic Science and Technology*. American Society of Mechanical Engineers. <https://doi.org/10.1115/OMAE2014->

- Riska, K., 2018. Ice edge failure process and modelling ice pressure. *Philos. Trans. R. Soc. A Math. Phys. Eng. Sci.* 376. <https://doi.org/10.1098/rsta.2017.0340>
- Riska, K., Kämäräinen, J., 2011. A review of ice loading and the evolution of the finnish-swedish ice class rules. *Trans. - Soc. Nav. Archit. Mar. Eng.* 119, 265–298.
- Riska K., 1995. Models of ice-structure contact for engineering applications. *Studies in Applied Mechanics*, Elsevier, Volume 42, Pages 77-103. ISSN 0922-5382, ISBN 97804444815835, [https://doi.org/10.1016/S0922-5382\(06\)80007-3](https://doi.org/10.1016/S0922-5382(06)80007-3).
- Sanderson, T.J.O., 1988. *Ice mechanics: Risks to offshore structures*, First. ed. Graham & Trotman, London, UK.
- Sodhi, D.S., Takeuchi, T., Nakazawa, N., Akagawa, S., Saeki, H., 2006. Ice Pressure Measured During JOIA Indentation Tests, in: *Proceedings of the 18th IAHR International Symposium on Ice*. pp. 199–206.
- Sopper, R., Gagnon, R., Daley, C., Colbourne, B., 2015. Measurements of spatial and temporal variations in ice impact pressures, in: *Proceedings of the International Conference on Port and Ocean Engineering under Arctic Conditions, POAC*. Trondheim, Norway.
- St. John, J., Daley, C.G., Blount, H., 1984. *Ice Loads and Ship Response to Ice*. Washington, DC.
- Staalesen, A., 2021. Two icebreakers are on the way to rescue ice-locked ships on Northern

Sea Route. Barents Obs.

Tekscan, 2022. Can I use FlexiForce sensors to measure dynamic loads? [WWW Document]. URL <https://www.tekscan.com/support/faqs/can-i-use-flexiforce-sensors-measure-dynamic-loads> (accessed 1.10.22).

Timco, G.W., Weeks, W.F., 2010. A review of the engineering properties of sea ice. *Cold Reg. Sci. Technol.* 60, 107–129. <https://doi.org/10.1016/j.coldregions.2009.10.003>

Vuorio, J., Riska, K., Varsta, P., 1978. Long term measurements of ice pressure and ice-induced stresses on the icebreaker SISU in winter 1978. Helsinki and Stockholm.

Xiao, J., 1997. Damage and Fracture of Brittle Viscoelastic Solids with Application to Ice Load Models. Doctoral thesis. Memorial University of Newfoundland. <https://doi.org/10.1017/CBO9781107415324.004>

Chapter 2 Pressure Distribution Data from Large Double-Pendulum

Ice Impact Tests

2.1 Co-authorship statement

This chapter has been published as a peer-reviewed journal article: Gagnon, R., Andrade, S.L., Quinton, B.W., Daley, C., Colbourne, B., 2020. Pressure distribution data from large double-pendulum ice impact tests. *Cold Reg. Sci. Technol.* 175, 103033. <https://doi.org/10.1016/j.coldregions.2020.103033>.

R. Gagnon proposed and designed the pressure sensing apparatus and the image processing approach, while S. L. Andrade revised and updated the image processing procedure. R. Gagnon, B. Quinton, C. Daley, and B. Colbourne performed the impact experiments. S. L. Andrade performed the image processing and pressure data collection. R. Gagnon and S. L. Andrade performed the data analysis in collaboration. R. Gagnon wrote most sections of the manuscript, S. L. Andrade authored sections related to the image processing procedure, generated the pressure map images, and graphs of the paper. R. Gagnon, S. L. Andrade, B. Quinton, C. Daley, and B. Colbourne were responsible for the paper editing and revisions. Final note: S. L. Andrade is not the lead author in this research but collaborated closely with the main author. This collaboration was crucial for the publication of this chapter and development of this PhD research work.

2.2 Abstract

Data from ice impact tests using a large double-pendulum apparatus have been analyzed and high spatial resolution pressure-pattern images, recorded at rates of 500 images per

second, are presented. The freshwater ice samples were grown in the lab and were cone-shaped with a base diameter of 1 m and base angle of 30°. Energy of the impacts was controlled by varying the ‘drop angle’ of the pendulum arms. Patterns of high-pressure zones (HPZ’s, consisting of relatively intact ice) that were surrounded by low-pressure zones (LPZ’s, i.e., shattered spall debris), due to spallation of ice from the HPZ’s, were evident. Most of the tests showed consistent results, where the instantaneous average interface pressure of the contact area was relatively consistent (5-8.5 MPa) and found to be constant or slightly increasing with contact area as tests progressed. Maximum pressures (i.e., associated with HPZ’s) were in the 35-52 MPa range and generally increased with contact area as tests progressed. Peak loads during tests were in the 410-630 kN range. LPZ contact areas were generally 2-6 times the size of the HPZ contact areas. In most tests the time-averaged total load was shared roughly equally between HPZ and LPZ contact areas. The peak loads were found to be directly proportional to the maximum HPZ contact areas. The detailed characteristics of the total load time series records were generally reflected in the corresponding HPZ load time series records much more so than in the LPZ load time series records. Average pressures on the HPZ’s and LPZ’s were remarkably consistent, 21 MPa and 3.7 MPa respectively. For all tests the actual average pressure was roughly constant, or slightly increasing, while the nominal pressure followed a decreasing trend.

Keywords: Ice impact tests; high-pressure zones; double-pendulum apparatus; pressure-sensor array.

2.3 Introduction

As activities associated with resource development, tourism, sovereignty, and environmental monitoring continue to increase in cold ocean environments such as the east coast of Canada and the Arctic, the need for updating and improving codes and rules for ships and structures to keep in step with the development is an ongoing issue. While large experiments of various types will have to be conducted, where the greatest emphasis would be on expensive full-scale field studies, there is still much (and less expensive) research that can be done in the controlled environment of the laboratory setting.

In spite of the many laboratory and field studies that have been conducted in the past to investigate ice behaviour during impact and indentation there still remain significant, and at times contentious, topics such as the nature of hard zones and soft zones and how they evolve during ice-structure interaction. Add to this the issue of structure deformation and damage during the course of ice impact and indentation, and how that affects the pressure distribution pattern during the interaction, and one can easily appreciate the need for more study and, in some cases, novel approaches. Here we describe a series of ice impact tests that were conducted using a large double-pendulum impact apparatus that incorporated unique pressure-sensing technology.

2.4 Description of apparatus and ice samples

A double-pendulum design was chosen for the apparatus to enable reasonably high impact loads while minimizing the space requirements since the Structures Lab at MUN is a congested environment with equipment for various types of ongoing experimental studies and student demonstration facilities. Also, the design eliminated the need to have any kind

of force reaction equipment that would ultimately transmit undesirable forces to the floor or walls of the room.

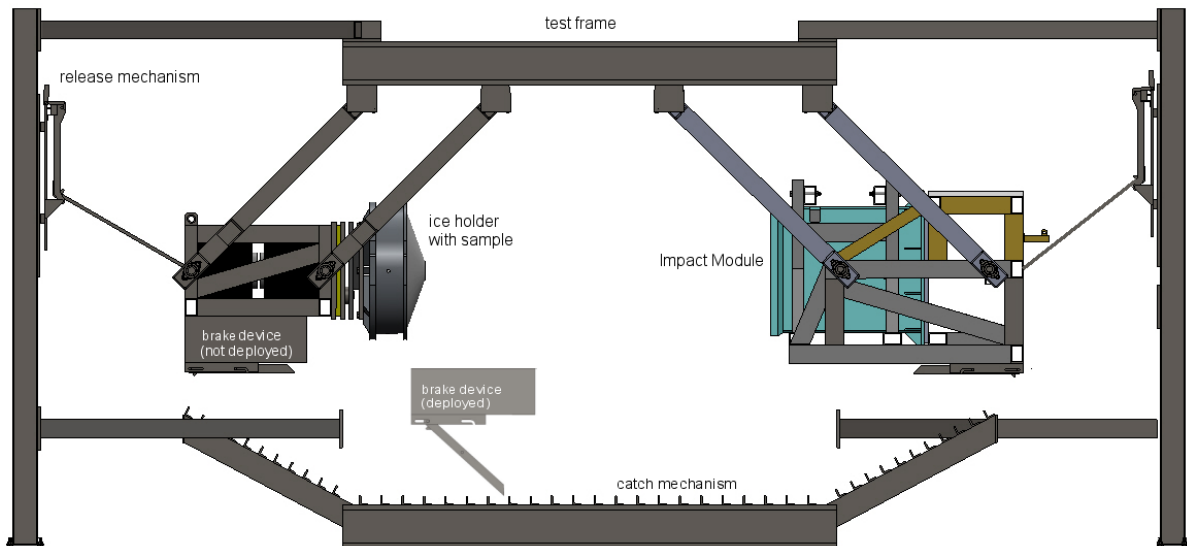


Figure 2-1. Schematic of the double-pendulum impact apparatus showing the ice holder pendulum (left) and Impact Module pendulum (right) in the raised position for a test. For future impact tests, where actual ship grillage will be used, the Impact Module will be removed, and the grillage will be attached to the box structure that presently houses the Module. A second graphic of the brake device has been inserted to show how it functions. Note that some vertical structural members have been removed from the schematic to permit unobstructed views of the right and left pendulums.



Figure 2-2. Photograph showing a partial view of the double-pendulum impact apparatus with the ice holder pendulum (left) and Impact Module pendulum (right) in the raised position for a test. The ‘toothed’ rail structure directly below the pendulums is the catch mechanism as shown in Fig. 1. Protective netting is visible at the sides and in the background of the image. An overhead crane is used for lifting the pendulum masses to the desired elevation for a test.

Figure 2-1 is a schematic of the apparatus that illustrates its essential features. Figure 2-2 is a photograph of the apparatus. An earlier design concept for the apparatus has been published before (Alam et al., 2012). Here we present the full apparatus as fabricated from the final design. Note that the figures show that both sides of the apparatus consist of masses that are supported by four parallel swing arms that attach to the masses through bearings. The tops of the swing arms attach to the apparatus frame via another set of bearings. This configuration enables the pendulum masses to swing freely and maintain a horizontal orientation while doing so. This eliminates undesirable rotation of the masses during impacts. The reader will note the toothed structure at the bottom of the test frame directly underneath the pendulum masses. This is part of the mechanism that prevents multiple hits

of the pendulums that would arise from the masses bouncing apart after the initial impact and then re-colliding. Each pendulum has a brake device that consists of a metal plate, hinged on one end, that is normally held in the horizontal housing. The initial collision causes them to slide forward in the direction of the impact and out of the housing so that the free unhinged end falls down under the influence of gravity to be caught by the teeth of the catch mechanism (the toothed rail at the base of the apparatus) after rebounding.

Figure 2-1 shows the left pendulum of the apparatus with a conical-shaped ice specimen inside the ice holder that is fixed to the box structure at the bottom of the swing arms. The box structure serves as a mounting platform for the ice holder and has three load cells mounted directly behind the ice holder in an equilateral triangular formation. The box structure also serves as a carriage to which mass (in the form of steel or lead plates) may be added behind the ice holder. On the opposite side of the apparatus the figure shows the right pendulum which has a similar box structure at the ends of its swing arms and to which a device called the Impact Module, designed for measuring load and high spatial resolution pressure distributions during ice impacts, is inserted. As with the left pendulum, mass may be added to the box structure to increase impact energy. The intension of the double-pendulum apparatus, as shown in Alam et al. (2012), is ultimately to perform ice impacts against actual ship grillage. The Impact Module experiments are intended to augment the tests using ship grillage by providing detailed information on the ice pressure distribution during impacts. It is understood, of course, that this would likely be a crude approximation of the pressure distribution that would result if an ice impact on a ship occurred that caused the grillage to undergo plastic deformation. With this in mind some design consideration

has been given to incorporating the pressure-sensing technology of the Impact Module into a thin sheet configuration that could be situated between the ice and the grillage during an impact and that could deform along with a grillage if the grillage sustained damage. However, such a thin sheet has not been fabricated yet. To date no grillage impact tests have been performed with the apparatus.

The following expression gives the impact velocity (V) for the mass on a pendulum for any given lift angle (θ) from the vertical

$$V = \sqrt{2gL(1 - \cos\theta)} \quad (2.1)$$

where g is the acceleration due to gravity and L is the length of the pendulum swing arm (2 m). Both pendulums are lifted away from each other to the same angle from vertical so that the relative impact velocity is double the value shown in Eq. 1. The associated impact energy (E) for an impact test where both sides of the pendulum have approximately the same mass (m) is

$$E = mV^2 \quad (2.2)$$

For reasons discussed below, expressions (2.1) and (2.2) should be treated as theoretical since there were practicalities of the apparatus that led to actual relative impact velocities being less than the theoretical values. The Impact Module and ice-mass metallic fixture were ~ 4330 kg each, not including all of the considerable pendulum arm parts and cage support structures.

The ice holder has been described before (Alam et al., 2012). The ice specimens were made of laboratory-grown ice following the procedure given in Gudimetla et al. (2012).

Readily available commercial freshwater ice was crushed into ice chips with sizes up to roughly 12 mm in diameter. The ice seeds were poured into an ice holder set-up and flooded with tap water. After three to four days of uni-directional freezing in a cold room at -10°C , the blank specimen was shaped into a cone (with a 30° base angle) using a purpose-designed shaping apparatus. The final preparation stage before a test is conducted involves transporting the ice (frozen into the ice holder) from a freezer at -10°C into the testing area using a forklift and then attaching the ice holder to the left pendulum. The test would ensue shortly afterwards. Some unavoidable heating of the ice surface would occur during the wait period ($\sim 15 - 45$ minutes).

Note that the Impact Module was originally designed to test a concept for a large impact panel to be installed on a vessel's bow intended for bergy bit impact experiments. Due to the mass of the vessel, it would not be expected that there would be significant decelerations of the vessel and impact panel during the bergy bit collisions. So, one would only have to prevent shock vibration from the ice hitting the front of the Module and transmitting to the high-speed imaging camera that would cause blurring of images. This is easily done by having the camera rest of on soft rubber pads that enable the camera to 'float' while the pads absorb the shock vibrations. The present application, however, does entail fairly high decelerations of the Impact Module during tests and this causes the camera to move substantially on the rubber pads. This necessitates adjusting the images after each test to center, rotationally orient and scale them to compensate for this movement. The procedure (including all aspects of image preparation before processing) that was used for the test data presented here is described in detail in section 2.16 Appendix A. An earlier description

of a less-developed procedure was given by Sopper et al. (2015) with respect to a preliminary analysis of one of the tests.

2.5 Safety considerations

Due to the size of the apparatus frame and the massive components of its pendulums, considerable energy is stored in the equipment just prior to a test when both pendulums have been elevated to the desired height. To ensure the safe operation of the system a number of safeguards and procedures are in place. First, as shown in Figure 2-1, the high-capacity release mechanisms can be seen for the two pendulums.

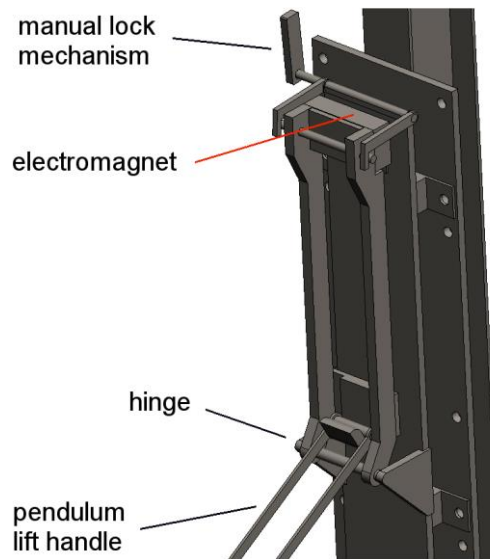


Figure 2-3. Schematic of the pendulum release mechanism.

Conceptually these are similar in design to quick release shackles used in marine applications that provide easy and safe release of heavy loads. Figure 2-3 shows details of the release mechanism. The design involves the use of a relatively small magnetic force to keep the free end of a hinged arm in place, where the pendulum mass is supported at the

other end of the arm near the hinge. The pendulum is released by de-energizing the electromagnet. In addition to the electromagnet there is a manual lock mechanism that is always engaged until shortly before a test.

Before arming the system by raising and locking the pendulum arms in place for a test all secondary staff and spectators are required to move away from the immediate vicinity of the device. Then, after the manual locks on the release mechanisms have been opened the remaining staff move away from the apparatus. Additionally, the frame of the apparatus is fully encompassed by a polypropylene net to prevent ice chunks from flying away from the impact zone that might cause damage to computer and camera equipment near the apparatus or possibly harm the staff that are located at a farther distance.

2.6 Impact module description

The Impact Module and its unique pressure-sensing technology have been described before and we include the description here. The central component of the Impact Module is a thick transparent block of acrylic measuring 1 m x 1m x 0.46 m (Figure 2-4).

mock-up for lab testing

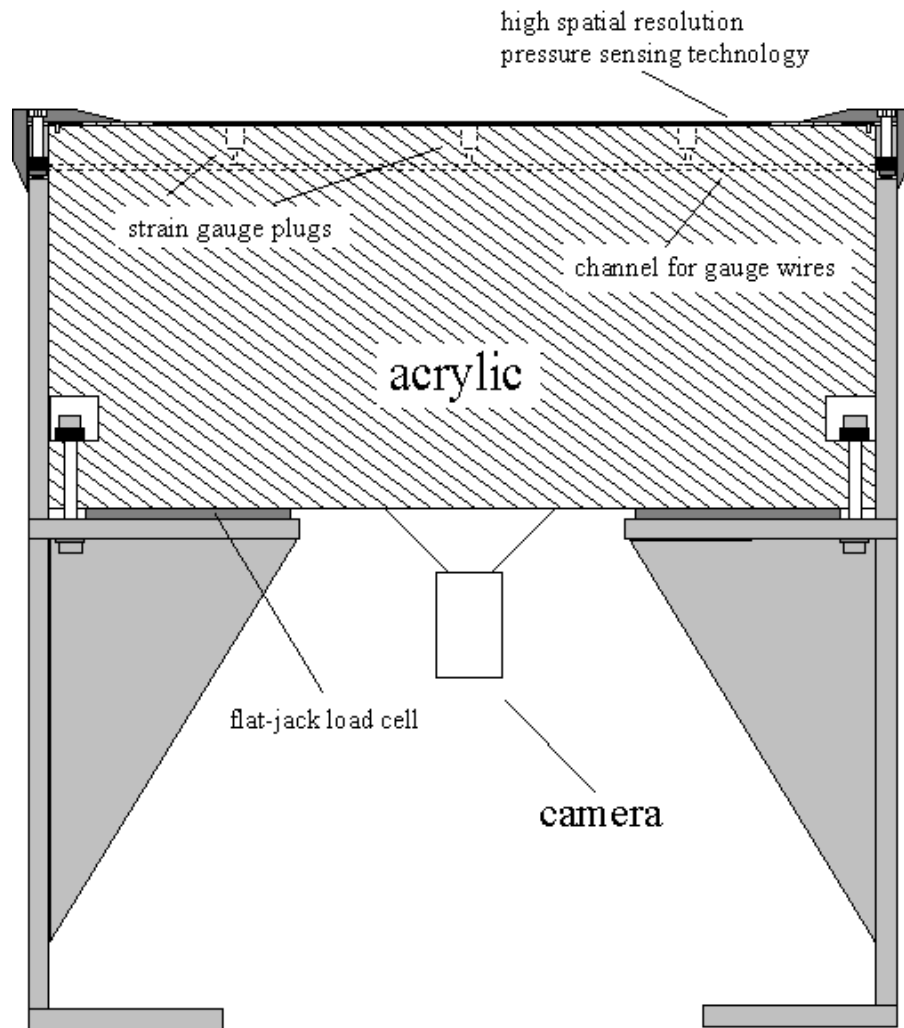


Figure 2-4. Sectional view of the Impact Module. (From Gagnon (2008a)).

The block rests on four flat-jack type load cells. These load cells are metallic envelopes filled with hydraulic fluid. Load applied to the surface of the cell translates into pressure in the fluid, which is monitored by a pressure gauge. The thickness of the acrylic block gives it the flexural strength to withstand high loads while supported at its four corners. The block is held firmly against the load cells by two bolts that pass part-way through opposing

corners of the block and that are secured with nuts and strong springs. Also, around the top edge of the block there is a securing plate that bolts to the steel side plating of the Impact Module with nuts and springs. This protects the edges of the block where a thin (1 mm thickness) stainless steel sheet, that covers the new pressure-sensing technology, is screwed to the block while enabling the load from an ice impact to transfer to the flat load cells.

The top surface of the block is covered by new pressure-sensing technology. This new technology consists of many strips of acrylic, 13 mm wide and ~ 4 mm in thickness and ~ 0.9 m in length, mounted side-by-side on the block's surface. Each strip has a gentle curvature (0.23 m radius) across its width on the face that touches the large acrylic block (Figure 2-5).

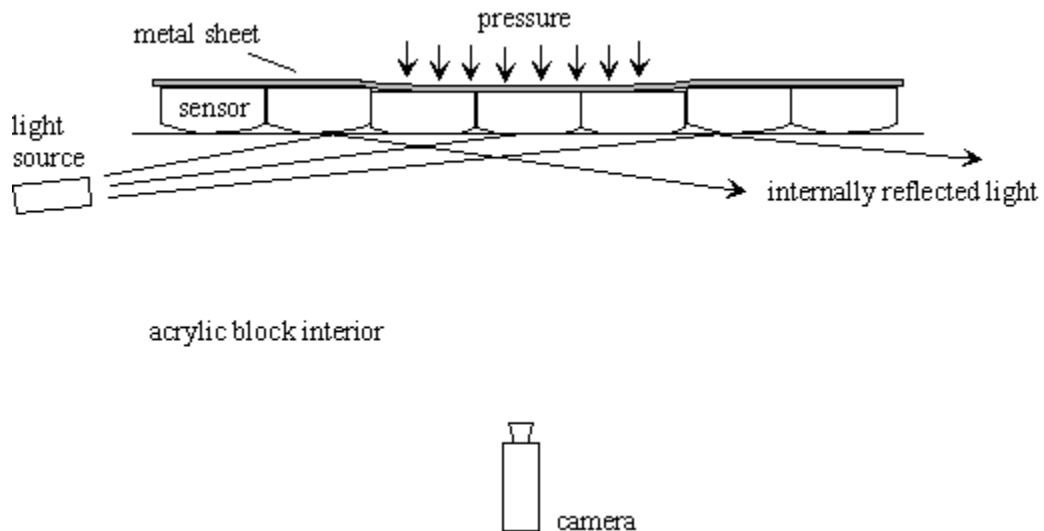


Figure 2-5. Schematic showing how the new pressure-sensing technology functions. Two of the light rays from the source at the left internally reflect off the block's internal surface where there is no contact with the strips. The center ray illuminates the 'white' acrylic strip since the internal reflection is frustrated where the strip is elastically flattened against the block due to the pressure. The curvature of the strips is exaggerated for illustrative purposes. (From Gagnon (2008a)). Note: the strips are clear acrylic, however the thin

opaque white plastic film (not shown) between the block and the strips essentially behaves as a thin coat of resilient white paint on the strips' bottom surfaces.

Pressure applied to the opposite side of the strips causes them to flatten against the block's surface. The degree of flat contact, i.e., the width of the contact, is a direct measure of the pressure applied and can be calibrated. This type of sensor is very robust and has been used successfully in a number of ice crushing studies (Gagnon and Bugden, 2007; Gagnon and Bugden, 2008; Gagnon and Daley, 2005), in single and multiple strip configurations. Its range of sensitivity is about 0-60 MPa. The pressure sensor strips are covered by a thin sheet of stainless steel that is the contacting surface with the ice during impacts. The unit sensing area for this technology is roughly 2 cm², hence the top surface of the block is effectively covered by roughly 3800 pressure-sensing units. The data acquisition system for the pressure-sensing strips is a fast high-resolution imaging camera (AOS S-PRITM), generally operating at 500 images/s with a resolution of 1280 x 1024 pixels, located at the bottom of the block as shown in Figure 4. When not pressed against the acrylic block the strips make very little contact, and when pressure is applied more contact occurs due to elastic flattening of the strips' curved surfaces (Figure 2-5). To enhance the visibility of the flattened areas of the strips a thin sheet of opaque white plastic film (MonokoteTM) is loosely situated between the acrylic strips and the large acrylic block. This thin sheet provides a bright white representation of the flattened areas of the acrylic strips where they are pressed against the acrylic block during loading. The only light source inside the acrylic block is from a large number of horizontally oriented LEDs located around the block perimeter near the top. Light from these LED's normally internally reflects off the top inner block surface. When an acrylic strip is flattened against the film-covered block the internal

reflection is frustrated, and the light passes through the block's surface to illuminate the white plastic film where the strip makes contact. Hence the portion of strip contact, appearing as white, becomes visible to the camera.

In addition to the pressure-sensing strips the top surface of the block has an array of 9 strain-gauged pressure-sensing plugs recessed in it. These are small cylinders of acrylic (2.5 cm diameter) that are located and secured in flat-bottomed holes (with slightly larger diameter) machined in the surface to the exact depth corresponding to the height of the plugs. The end of each cylinder is glued to the acrylic at the bottom of the hole with Loctite 5900™ glue. Each plug has two strain gauges attached at opposite sides with sensitivity along the axis of the plug. Load applied to the top of a plug causes it to contract in length and this registers on the strain gauges. The plugs are essentially pressure transducers that have the same mechanical properties as the block itself. The sensors are useful both for corroborating the output from the pressure-sensing strips and as backup sensors in the event there is a problem with the strip sensors.

The methods used to prepare and convert the raw images from the Impact Module to pressure distribution patterns are described in section 2.16 Appendix A. The calibration procedure and data for the pressure-sensing strip technology are also presented there.

2.7 Impact speed and ice penetration

In Table 2-1 and Table 2-2 below, HPZ refers to a high-pressure zone where ice is relatively intact and interface pressure is above 15 MPa. An LPZ is a low-pressure zone consisting of crushed ice where the interface pressure is less than 15 MPa. The HPZ/LPZ pressure

boundary is discussed in section 2.10. The HPZ contact area is the total actual area of contact where the interface pressure at all points is greater than 15 MPa. The LPZ contact area is the total actual area of contact where the interface pressure at all points is less than 15 MPa. Also note the date-related names of the tests. We have named the tests in this manner to give the reader a little insight into the planning/effort/time required for sample preparation and the conduct of each test. Additionally, the double-pendulum equipment underwent a few minor changes during the course of the tests over the two-year period. Some of the variation in test results might be, in part, due to things such as the seasonal temperature effect on ambient temperature (due to door openings) and inconsistencies in the overall preparation, test conduct and staffing due to the time span between tests. The latter items make the establishment of a rigorous test routine challenging.

No special instrumentation was used for all tests to determine impact speed and ice penetration. The drop angle was set and recorded for each test (Table 2-1, Table 2-2), however the impact speed could not reliably be determined from that because later it was determined that the pendulum release mechanism slowed the initial motions of the pendulum arms, and furthermore the releases for the right and left pendulum arms were slightly out of sync. That is, the Impact Module pendulum always released before the ice mass pendulum by roughly 2 NTSC video image intervals (1/15) s. Fortunately there was a high-speed video record of one experiment (35° drop angle, 400 images/s) from which impact speed and ice penetration could be reasonably estimated. Also, there were regular NTSC video records of two experiments from which reasonable estimates of the impact speed could be determined for 20° and 35° drop angles. Additionally, there were pre-test

and post-test NTSC video and photographic data that enabled the determination of ice penetration in one case. With this limited information we assumed that the impact speed, and ice penetration vs time curve, was the same for all tests conducted with a drop angle of 35°, and we had estimates for the test where the drop angle was 20°. Note that we have combined the two tests that were conducted on May 8, 2014, since the second test was actually a second impact on the same test specimen that had been initially impacted. This was an interesting thing to do because it showed that the ice behaved as though it had experienced a single impact test at a drop angle of 35°. That is, the energy associated with each of the two tests was determined by the impact speed (3.0 m/s in both cases). The combined energy was roughly similar to the energy of any test conducted with a drop angle of 35°, where the impact speed was determined to be 4.7 m/s. Hence, a similar amount of energy was dissipated in the two combined May 8, 2014 tests as was dissipated for any of the tests using a drop angle of 35°. The ice behavior during the second test apparently picked up from where it left off at the end of the first impact it had experienced. This was evident in the pressure pattern that occurred at the end of the first test and that was re-established at the beginning of the second test (see section 2.17 Appendix B (Test: May8_A+B_2014)). The first eleven images are from the first impact and the remaining five images are from the second impact. The recording rate was 250 images/s. All other subsequent tests were recorded at 500 images/s.

Table 2-1. Summary Results from the Impact Tests.

Test	Category	Drop Angle	Peak Load	Maximum Pressure	Max. Average Pressure	Maximum Contact Area	Maximum HPZ Contact Area	Maximum LPZ Contact Area	Time to Peak Load	Impact Duration
	I, II, III	Degree	kN	MPa	MPa	cm ²	cm ²	cm ²	s	s
May8_A+B_2014	I	20	580.6	51.8	10.5	563.0	239.5	396.4	.056	.083
May22_2014	I	30	547.5	51.8	8.7	673.4	224.7	480.3	.020	.039
Dec10_2015	I	35	540.8	35.1	6.6	976.6	210.1	828.6	.028	.058
June27_2014	II	35	451.5	51.8	8.7	880.3	166.7	836.6	.025	.079
Oct16_2014	II	35	466.5	51.8	9.0	890.9	175.1	763.1	.015	.052
Dec15_2014	II	35	426.6	51.8	9.9	926.0	106.1	917.1	.019	.060
Jan20_2015	II	35	415.8	51.8	10.6	781.1	113.0	712.8	.015	.058
Feb25_2016	III	35	621.5	51.8	11.4	862.2	243.4	727.7	.017	.048

Table 2-2. Summary Results from the Impact Tests (continued).

Test	HPZ Average Pressure	LPZ Average Pressure	Time-Averaged Pressure over the Total Area***	Impact Speed	Ice penetration to time of last pressure pattern	Time-Averaged HPZ Load	Time-Averaged LPZ Load
	MPa	MPa	MPa	m/s	cm	kN	kN
May8_A+B_2014	21.62 ±1.84	4.31 ±0.83	7.51 ±1.57	3.0	12.8*	117.1	109.1
May22_2014	21.72 ±1.38	4.04 ±0.57	7.08 ±1.14	4.1†††	10.1	159.1	145.5
Dec10_2015	19.85 ±1.09	3.65 ±0.48	5.04 ±0.86	4.6† (4.7)	11.1	94.7	171.5
June27_2014	20.82 ±2.56	3.71 ±0.97	7.54 ±0.80	4.7	12.2	114.1	138.4
Oct16_2014	21.61 ±2.36	3.52 ±0.74	7.88 ±0.71	4.7	12.2	127.7	152.6
Dec15_2014	21.50 ±3.26	3.16 ±0.93	7.99 ±1.37	4.7	12.6	87.5	123.6
Jan20_2015	22.41 ±2.44	3.54 ±0.83	8.54 ±1.23	4.8†† (4.7)	12.7	114.3	113.4
Feb25_2016	22.09 ±2.12	3.39 ±0.88	Anomalous	4.7	11.5**	153.8	146.7

* Note that the top ~ 2 centimeters of the cone-shaped ice sample was misshaped.

** Note that the top few centimeters of the cone-shaped ice sample was probably damaged/weakened during preparation and handling.

*** This refers to the time-averaged pressure up to the time when a ‘Major Failure’ occurs for the cases where that happens. Also, the first data point is not always used for the calculated average value.

† Relative speed as determined from the NTSC video record of the Impact Module movement, assuming the Ice Holder is moving at the same speed.

†† Relative speed as determined from the high-speed video record of the Ice Holder movement, assuming the Impact Module is moving at the same speed. Hence, the average value from the Ice Holder and Impact Module movements gives the actual relative speed (4.7 m/s).

††† This value was obtained from the theoretical value, associated with a pendulum arm with a drop angle of 30°, suitably adjusted for the actual values that were obtained at the 20° and 35° drop angles.

2.8 General notes on the data presentation

Here we present the pressure pattern images (section 2.17 Appendix B, and included AVI files: May8_A+B_2014.avi, May22_2014.avi, Dec10_2015.avi, June27_2014.avi, Oct16_2014.avi, Dec15_2014.avi, Jan20_2015.avi, Feb25_2016.avi) and the associated data plots (section 2.18 Appendix C) for the set of raw images for each test that were acquired using the pressure-sensing technology. In most cases we have presented the images and data for the portion of the tests where ice penetration was occurring during the impact. Following that point in time there is only elastic rebound/relaxation in the ice and apparatus when the kinetic energy has been dissipated and the ice and Impact Module no longer exert substantial force on one another. In some cases (Oct16_2014, Dec15_2014, Jan20_2015, Feb25_2016) there are a few missing images, either at the end of the sequence or that form a gap near the end of the sequence, of pressure-pattern images. In those tests the unused raw images were excessively blurred by the motion of the high-speed imaging camera that sat on soft rubber pads to isolate it from high-frequency vibration of the apparatus resulting from the impulsive nature of the impacts.

For the Load vs Actual Contact Area plots and the LPZ Area vs HPZ Area plots in section 2.18 Appendix C, linear fits have been applied to the data where the trends show statistical significance (i.e., where $R^2 > 0.5$). Also note that tests where a ‘Major Failure’ had occurred at some point during the ice penetration have an indicator on the load time-series.

2.9 Discussion of the pressure-sensing technology and load-cell data

The commercial product known as ‘TekScan’ has been used by several researchers to study ice interaction (e.g., Izumiyama et al. 1998, Määttänen et al. 2011, Sodhi et al. 2001), but

that technology is quite limited in its response time (~ 0.25 s, as acknowledged by the manufacturer, and shown in independent testing (e.g. Sumiya et al. 1998)). That is, it is incapable of accurately capturing the rapidly changing pressure patterns that are characteristic of ice crushing at the structure/ice interface at rates in the brittle regime of ice. Obviously, some information is captured by the TekScan technology, but one has to be very careful about how it is interpreted. Recall that in these cases pressure spikes and fluctuations during ice crushing often occur on the scale of milliseconds (Gagnon, 1999). Also note that the impact events documented here lasted for durations ≤ 0.08 s (Table 2-1). Traditional arrays of pressure transducers are limited by the number and extent that can be practically installed and monitored on impact and indentation equipment (e.g., Gagnon and Sinha, 1991; Gagnon, 1994). In contrast, the present technology is equivalent to having thousands of pressure sensors on the impacting surface. Another aspect of the present technology worth noting is its accuracy, as borne out by how well the integration of the whole pressure pattern at any point in time during an impact event generally agrees fairly well with the broad features of the load-cell data, i.e. the load cells in the Impact Module and also those located behind the ice holder, for the event. This raises the interesting concept of an essentially ‘massless’ load sensor. Generally, to study and monitor ice/structure interaction at intermediate and large scales, load cells are installed behind heavy metal panels or segments of panels. Furthermore, as noted by Jefferies et al. (2011), surface-mounted ‘Medof’ load panels, configured as two metal plates (sealed at the edges) with polyurethane ‘springs’ and fluid inside, have been used on the Molikpaq structure. Indeed, a whole structure, if outfitted with strain gauges and tilt-meters, can itself function as a ‘load cell’ (Jefferies et al., 2011; Gagnon, 2012). These methods, however, often suffer

from frequency-response limitations and resonance associated with the masses and ‘springs’ involved. Indeed, the load cell measurements in the present case, from both the ice side of the double-pendulum apparatus and the Impact Module side, suffer from these issues since there is significant resonance exhibited in the load records for both cases. The present pressure-sensing technology, on the other hand, has virtually no associated mass, relatively speaking, at the sensing face. This enables it to act as a ‘honest’ load cell that exhibits the load (and nothing but the load) that is present at the ice/structure interface, regardless of stresses, strains and resonances in the surrounding structures and the bulk ice-mass itself.

These issues are illustrated in Figure 2-6 and Figure 2-7, where the load records from the Impact Module, the Ice Holder and pressure-sensing technology are presented together for two test cases that were conducted on May 22 and June 27, 2014.

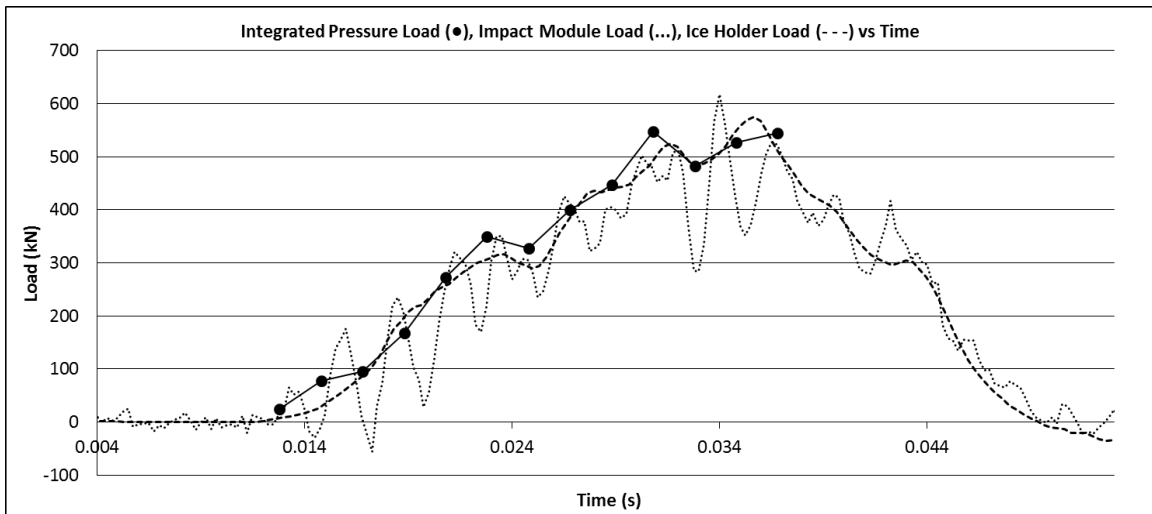


Figure 2-6. Load sensor comparisons for test May22_2014. Note that integrated pressure-pattern data are only shown for the time during which ice penetration is occurring.

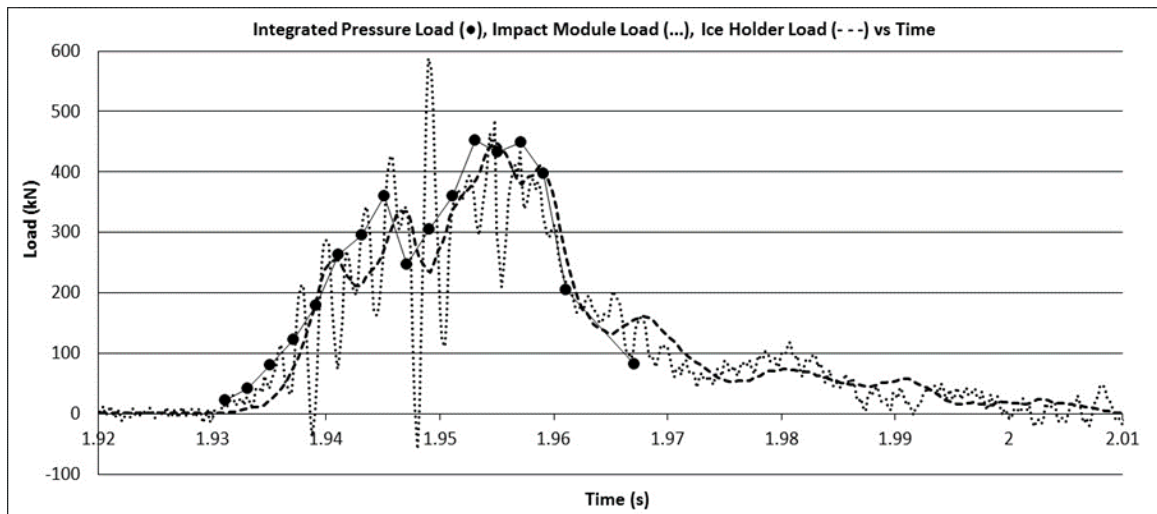


Figure 2-7. Load sensor comparisons for test June27_2014.

For both cases the sets of load-cell data broadly agree with each other, but resonant oscillations are present that mask fine features of the actual load exerted on the Impact Module face. The Impact Module load cells exhibit higher frequency resonance (roughly 390 Hz) and higher amplitude than the Ice Holder load cells (roughly 240 Hz). The load from the integrated pressure data, however, is free from the resonances and reflects spalling events that occur in the ice contact region, such as those which occur between images 6-7 and 10-11 of the May 22 test, and images 8-9 of the June 27 test. This is easier to see in the plots from section 2.18 Appendix C that do not have the load cell data overlapping the integrated pressure-pattern results. The full set of comparative plots from load cells and the integrated pressure patterns are given in section 2.19 Appendix D.

2.10 Identifying a ‘High-Pressure Zone, HPZ

In the introduction we briefly discussed the physics of ice crushing, including the phenomena of high-pressure zones (HPZ’s) and low-pressure zones (LPZ’s). Here we

explain our choice of the ‘boundary pressure’ that distinguished a HPZ from an LPZ in these ice impact experiments. Essentially, we chose the approximate pressure that defined a boundary around the central region of the ice contact where the pressure gradient was the highest. In a few instances we also had the corroborating benefit of post-test photos that showed the relatively intact ice that makes up the HPZ within the general contact area at the ice/impactor interface (Gagnon et al., 2015). In those instances, the peripheral extent of the relatively-intact ice reasonably matched the peripheral extent of the pressure demarcating ~ 15 MPa that was evident on the pressure-pattern record for the last (or close to last) pressure-pattern image that was acquired. Many locations at the pressure boundary exhibited instances where the pressure immediately outside the boundary was 5 MPa or lower (Figure 2-8, left image). The surrounding low-pressure ice contact is crushed ice (the shattered remnants of prior spallations from the HPZ). The fairly distinct HPZ/LPZ pressure boundary is usually evident in pressure patterns both at the early stages of impacts (e.g., Figure 2-8, right image) and throughout the whole of the tests.

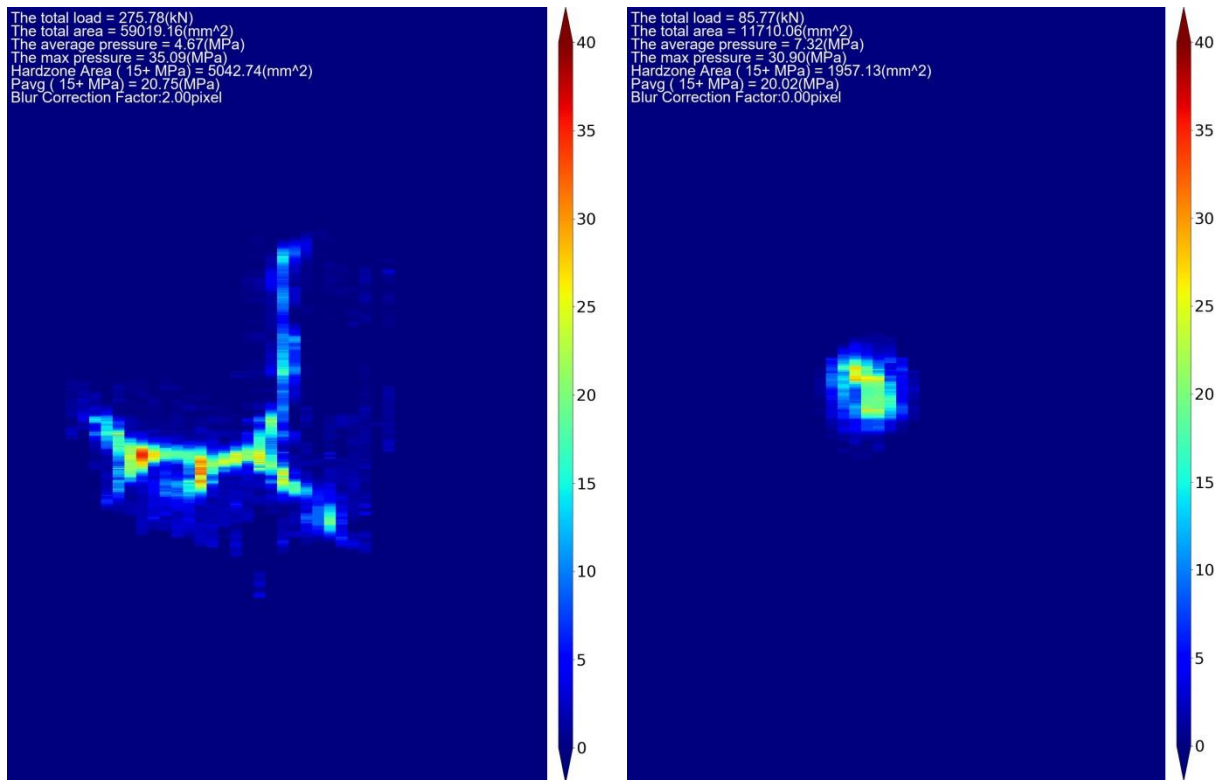


Figure 2-8. Pressure patterns illustrating the demarcation pressure boundary (~ 15 MPa, i.e., the mid blue-green color) for a high-pressure zone (HPZ). The left image is the last one from the Oct16_2014 test and the right image is from early in the same test. Note that the same pressure-color scale applies to all pressure-pattern images throughout this paper.

2.11 The three categories of tests

The tests fall into one of three categories (Table 2-1): Category I corresponds to tests that proceed in a relatively consistent set of non-catastrophic spallations (evident in the load and pressure time series and pressure patterns) during penetration of the ice until the penetration reaches the maximum value, followed by elastic stress relief and consequent drop in load to zero at the end of the test. Tests May8_A+B_2014, May22_2014 and Dec10_2015 fall into this category. Category II tests start out similar to Category I tests and exhibit the same type of consistent spallation events up until a certain time in the tests (occurring between 20-40% through the test, but more so towards the latter), where a

catastrophic spallation event occurs (hereafter referred to as ‘major failure’ in the text, and in the figures). The major failure is obvious in the HPZ load and pressure time series. In these cases, at least half, and sometimes all or almost all, of the HPZ shatters to become LPZ material. We cannot say with certainty if both Categories I and II types of behavior are to be expected, statistically speaking, with ice that is not subject to artificial confinement in the field. That is, as discussed by Daley (1990, 1991), there may naturally be classes of spall sizes and orientations that occur during penetration of any given ice feature. On the other hand, we cannot rule out the possible influence of the ice holder itself on the behavior of the ice confined within it. Category III is for tests that are generally quite different from the other categories. There is only one test in this category, i.e., Feb25_2016. Oddly enough this test exhibited the highest peak load of all the tests. The most unusual characteristic of the test was that the pressure buildup at the initiation of contact was quite slow compared to the other tests. Following this unusual initial behavior, it exhibited somewhat similar behavior to tests in Category II for the rest of the record. We can speculate that the top part of the conical ice specimen may have been flawed or damaged during the growth and/or shaping and handling process. That would be consistent with the fact that the greatest peak load occurred in this test since, and if our speculation is correct, less impact energy would have been expended in the earlier stage of the test than in the other tests. This would leave more energy in the later stage of the test to generate a higher load once the flawed weakened ice had been cleared out of the way. This reasoning is further supported by the fact that the ice specimens tested on May 8 and May22, 2014 were misshaped at the top ~ 2 cm of the cone so that there was significantly less ice present there

than was normally the case, and those two tests had the next highest peak loads of all tests other than the Feb25_2016 test.

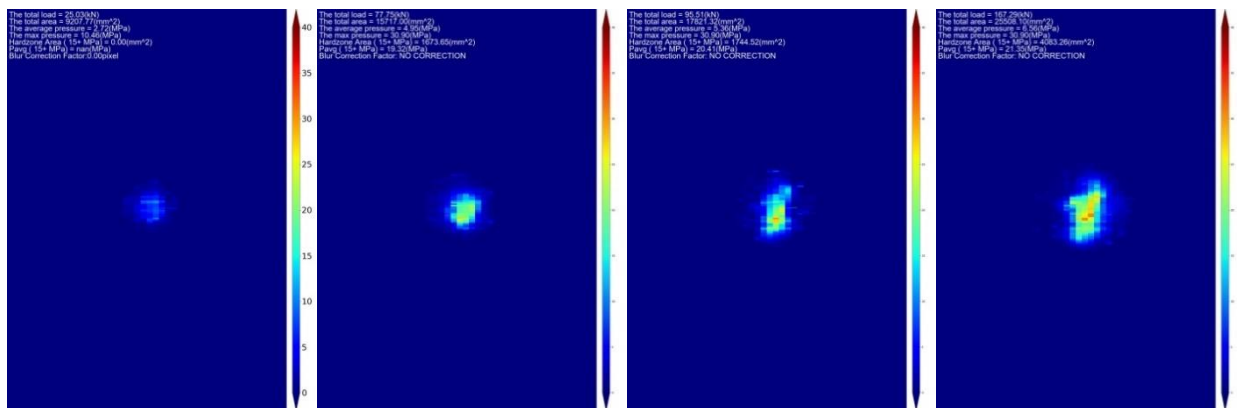
Note that here while we are primarily pointing out the distinguishing characteristics of the three categories, it is also true that all tests share some characteristics, such as the LPZ/HPZ boundary pressure, distinct spallation events, similar average HPZ and LPZ pressures, etc.

2.12 Detailed descriptions of typical category I, II and III tests

2.12.1 Description of the evolving pressure pattern from a typical impact test

The physics of ice crushing during impact and indentation in the brittle regime has been discussed in detail before (e.g., Gagnon, 1999; Spencer and Masterson, 1993; Evans et al., 1984; Frederking, 2004) and is not necessary to include here. In the discussion below, nominal contact area refers to the theoretical contact area derived from the original geometry of the impacted ice feature (a cone in the present case) and the penetration depth.

Figure 2-9 and Figure 2-10 show data for a typical Category I test, in this case May22_2014.



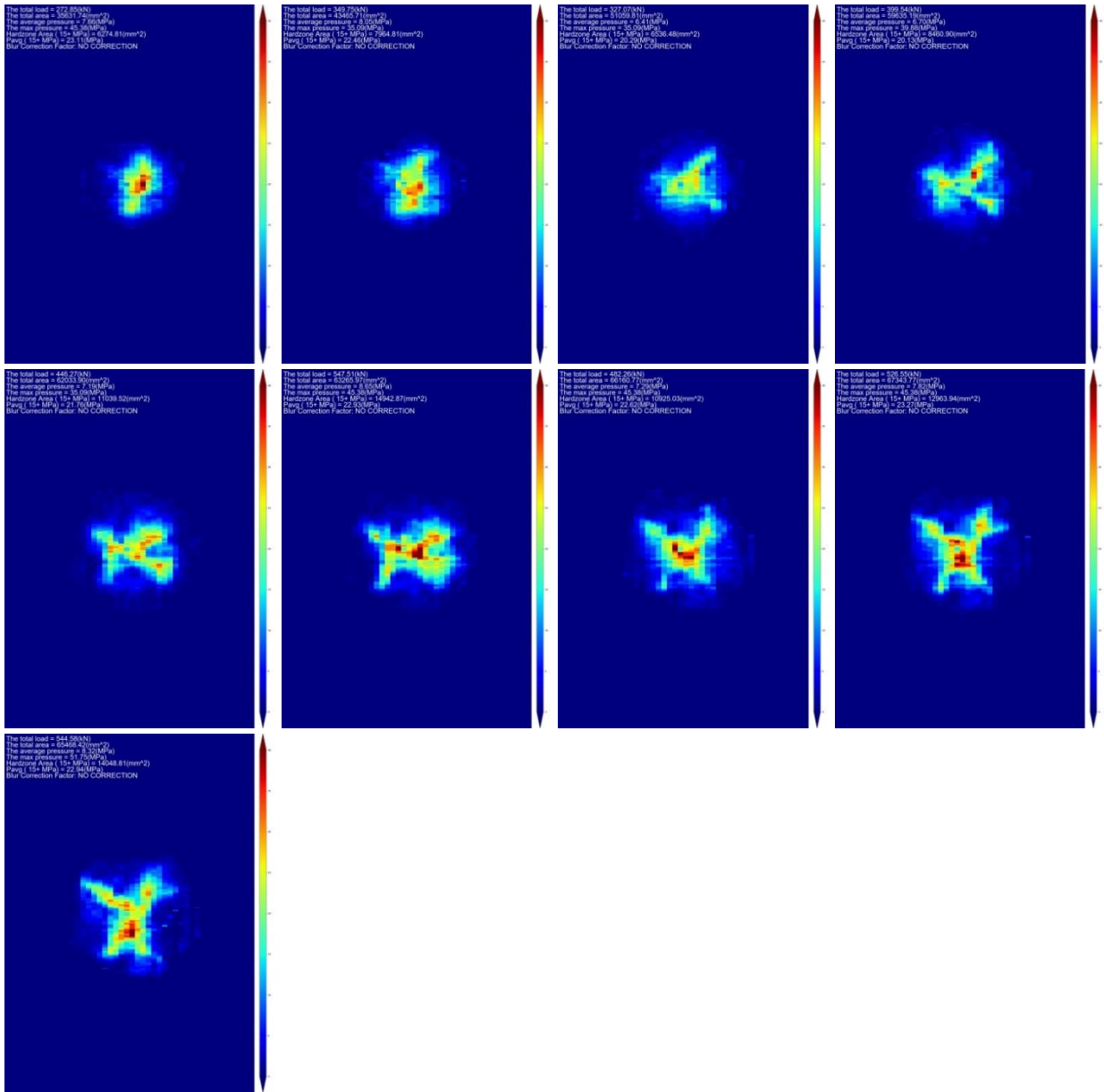
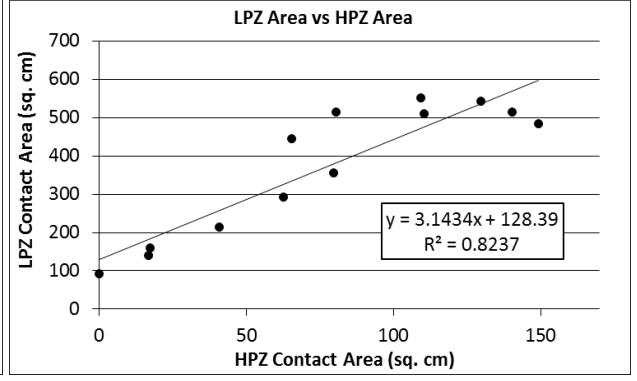
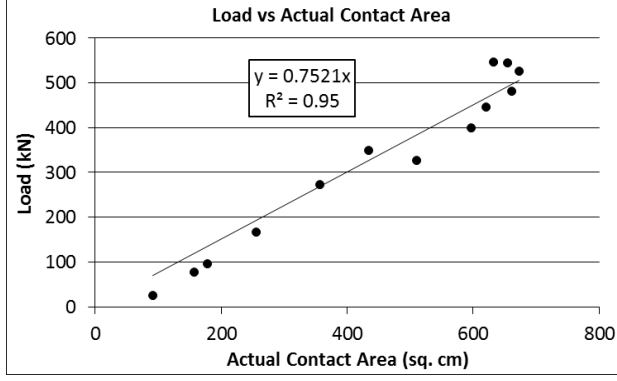
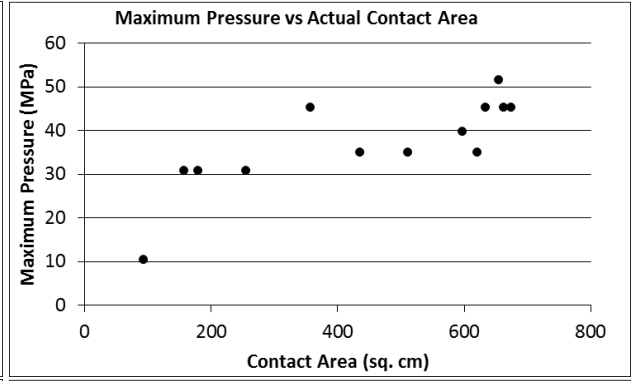
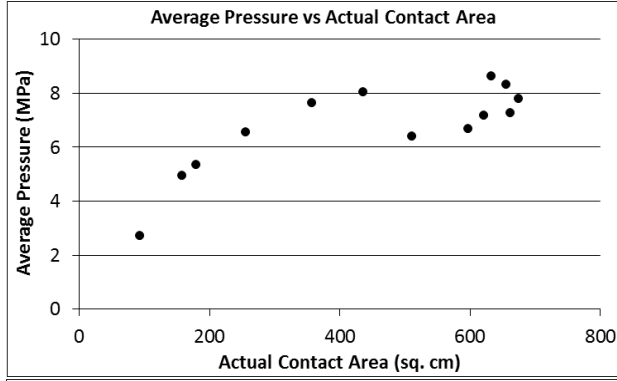
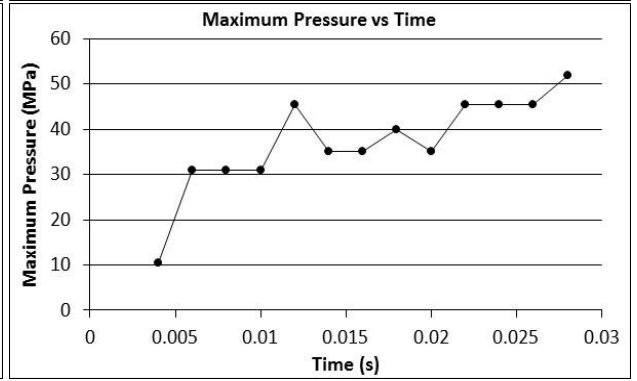
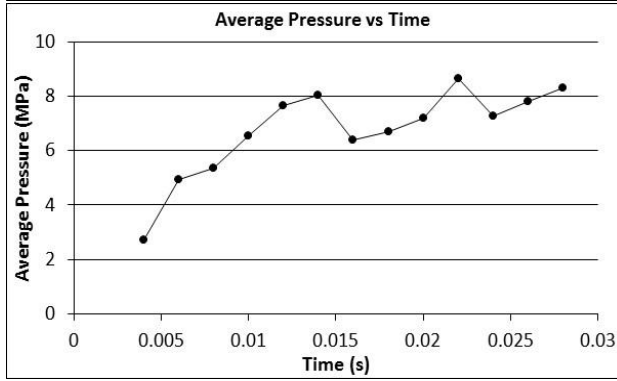
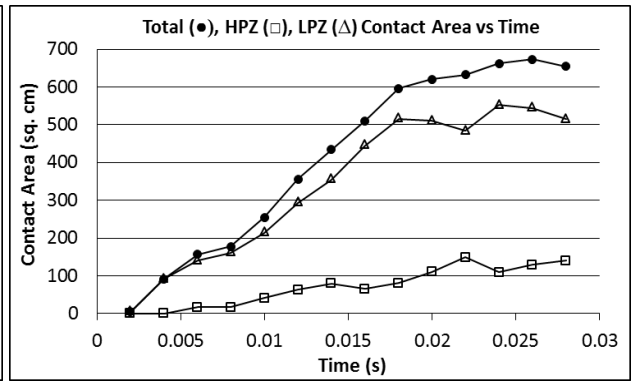
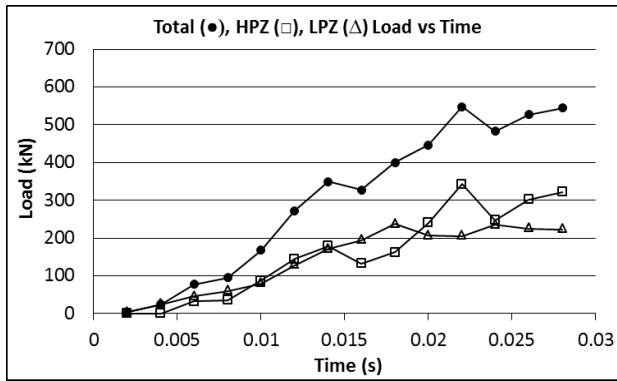


Figure 2-9. Sequence of pressure-pattern images from test May22_2014. The images run from left to right in each row from top to bottom. The capture rate was 500 images/s. The width of a blue box is ~ 60 cm.



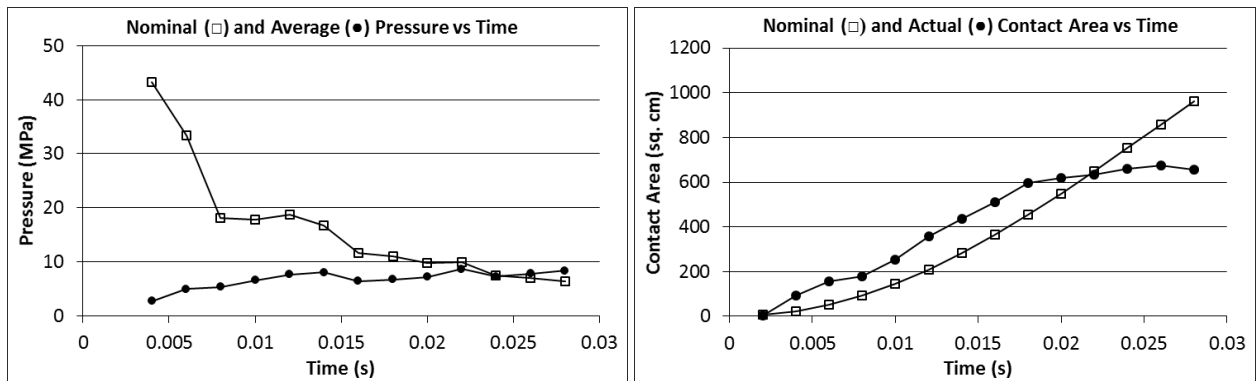


Figure 2-10. Data plots from test May22_2014.

The first few pressure pattern images (Figure 2-9) show where the ice cone top makes initial contact in the central area of the Impact Module face. The HPZ boundary pressure is evident even in the early images. Generally, the pattern grows in size as the load increases but the pattern also undergoes radical changes in shape due to spallations of ice from the HPZ that shatter to become low pressure crushed ice (LPZ) that accumulates around the HPZ. The LPZ material is mobile and extrudes and flows away from the HPZ as the impact penetration progresses (visible in some animations of the pressure-pattern images, see AVI's). Spallation events are not only visible in the pressure patterns but are also manifested in the total load data, the HPZ load data, HPZ contact area data and the average pressure data (Figure 2-10). For example, note the prominent spallation that occurs between the tenth and eleventh images in Figure 2-9 and between the eleventh and twelfth data points in Figure 2-10 (load and average pressure time series). For clarification, we could not include in Figure 2-9 the image showing the first ice contact with the Impact Module because it was obscured by the central pressure-sensing plug.

The reader may note in Figure 2-10 that data points in the plot of maximum pressures occur in a somewhat stepwise fashion. This is due to the non-linear calibration curve of pressure

versus contact width, and the fixed pixel dimensions in the images that show the contact widths of the pressure-sensing strips. More discussion on this effect is given in section 2.16 Appendix A.

Figure 2-11 shows a histogram of the pressure distribution at peak load for a Category I test (Dec10_2015). Other than a roughly diminishing trend with pressure there is no good standard fit (such as exponential) to the data. The same was true for histograms at other points in the load record for the test. The histograms do not have any particular impact on our discussion of HPZ's and LPZ's.

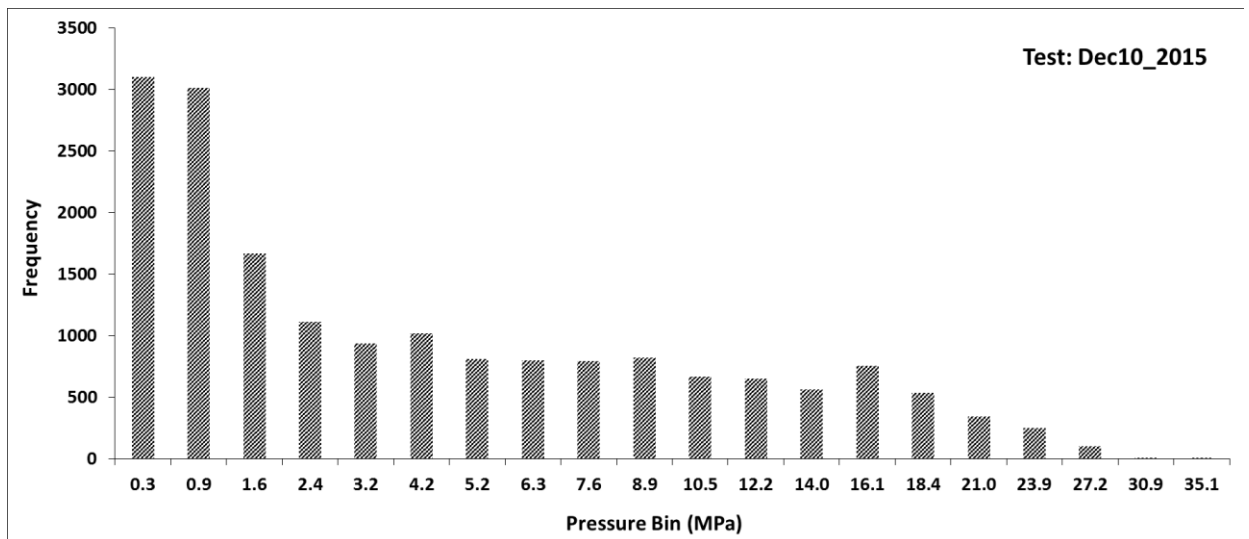
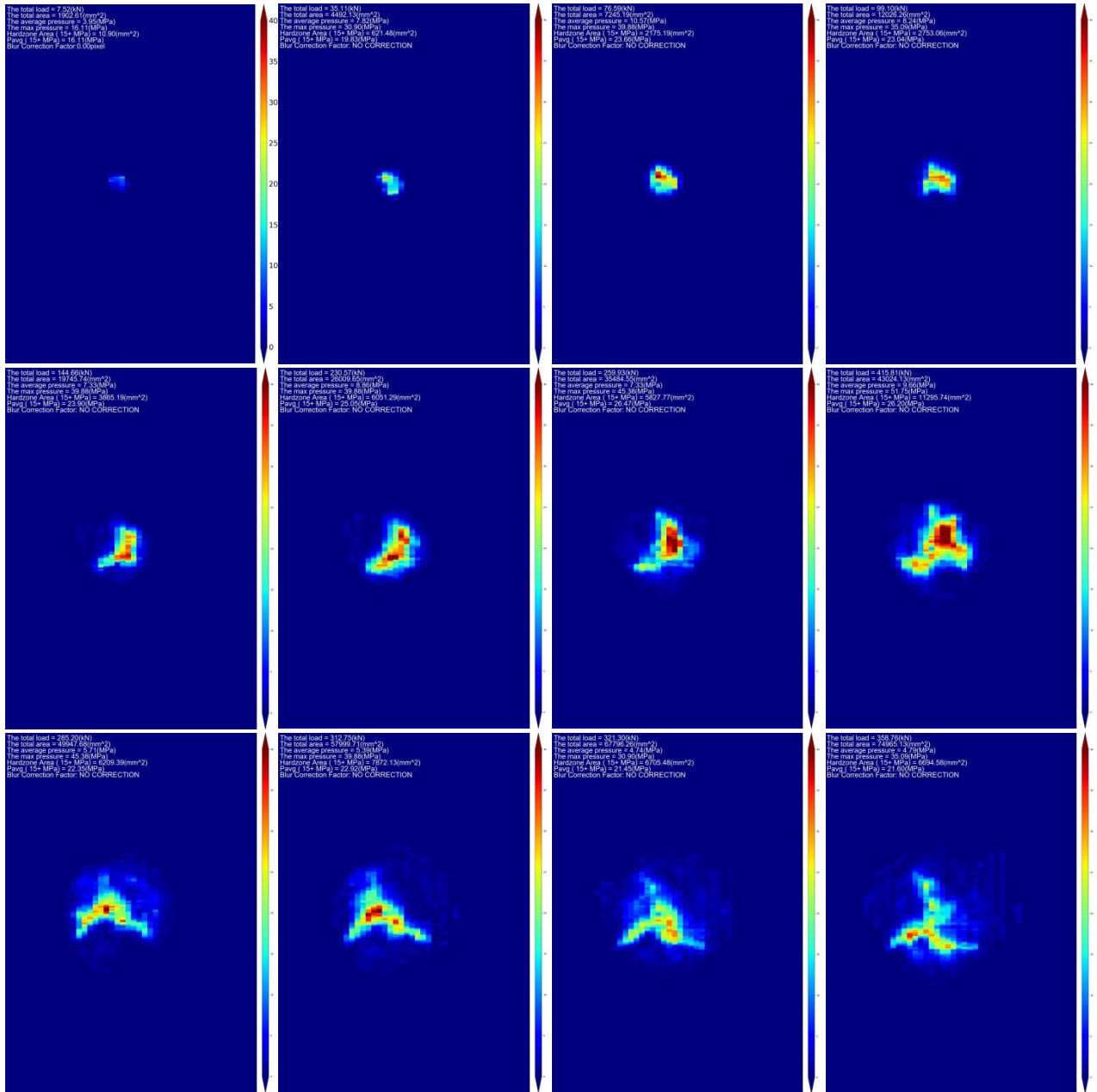


Figure 2-11. A histogram of the pressure distribution at peak load for test Dec10_2015.

If we now consider a Category II test (i.e., Jan20_2015), the first few images of the pressure pattern (Figure 2-12) show the initial contact with the Impact Module, similar to the case of the May22_2014 test. The growth and size evolution of the pressure pattern is similar to May22_2014 up until about 0.018 s (image 9 of the pressure patterns), at which point a major failure occurs. Consequently, the size of the HPZ abruptly decreases, since a large

spallation has happened. This is evident in the load time-series record of the HPZ (Figure 2-13) and is similarly reflected in the total load, average pressure and HPZ contact-area time-series records. Following the major failure event, the pressure pattern continues to evolve in shape as before, with a general growth in size up to 0.026 s as the ice penetration increases. A secondary significant spalling event occurred at 0.026 s (between the 13th and 14th pressure-pattern images) and is similarly reflected in the total load and HPZ load. Ice penetration finishes at around 0.048 s. Category III refers to the behavior of test Feb25_2014. Unlike all other tests the early stages of this test show a slow development of the HPZ (Figure 2-14), that is, the pressure characterizing the HPZ/LPZ boundary doesn't appear until the fourth image, at time 0.008 s (Figure 2-15, maximum pressure time series). The ice contact area (and total load) continues to grow until a major failure at 0.02 s (Figure 2-15). The average pressure also rises during this period, in contrast to the other tests where the pressure becomes roughly stable after the first or second images. The maximum pressure follows a similar trend except that it does roughly stabilize at a maximal value. Unlike other tests, the total load does not appear to recover much after the major failure. On the other hand, the HPZ and total load time series records closely follow one another in characteristics, similar to the other tests.



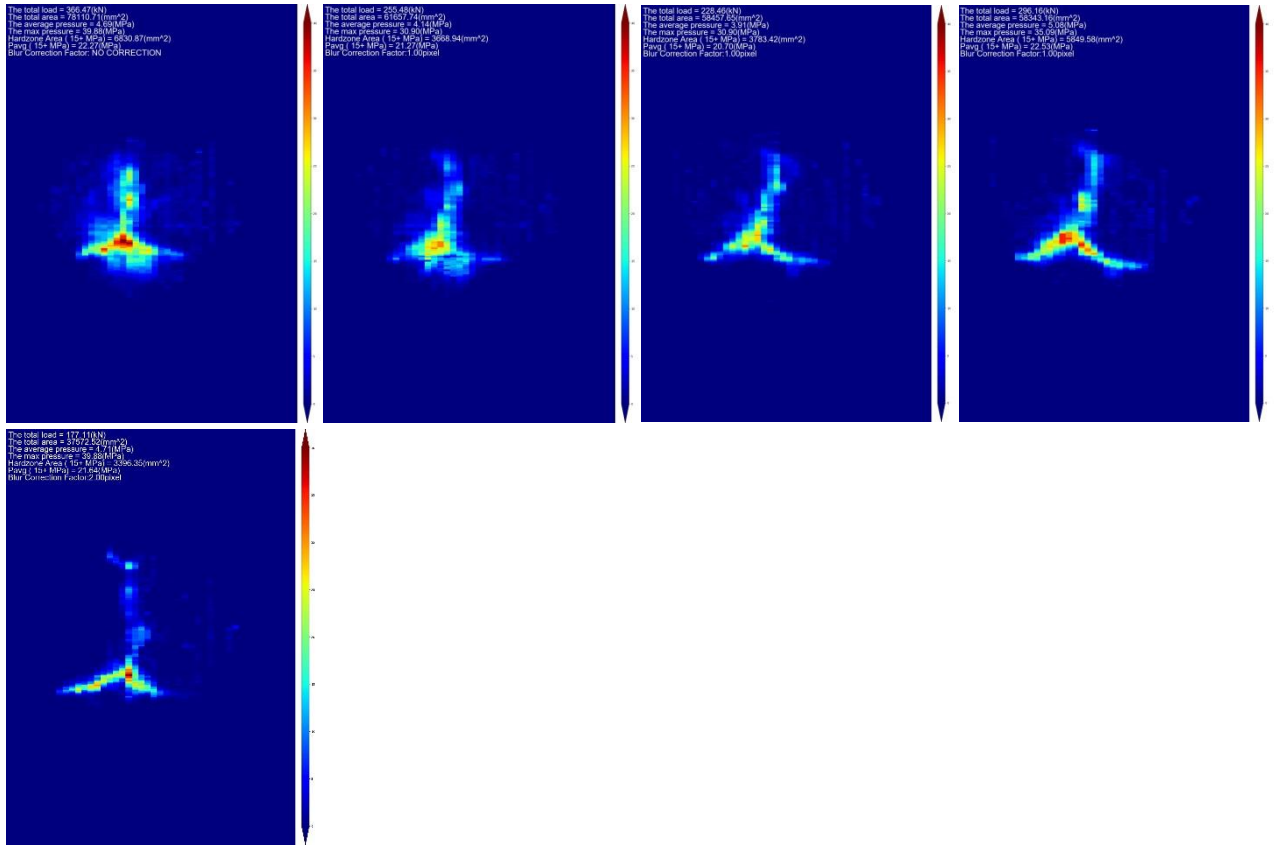
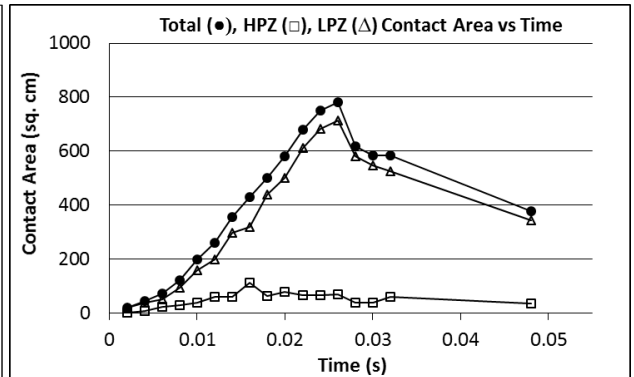
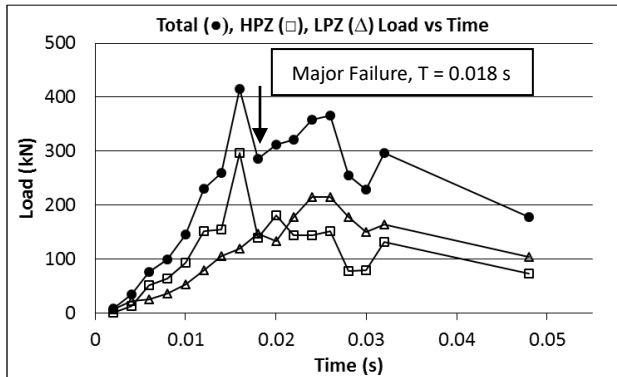


Figure 2-12. Sequence of pressure-pattern images from test Jan20_2015. The images run from left to right in each row from top to bottom. The capture rate was 500 images/s. The width of a blue box is ~ 60 cm. There were originally 24 raw images, but the 17th – 23rd were too blurred to process.



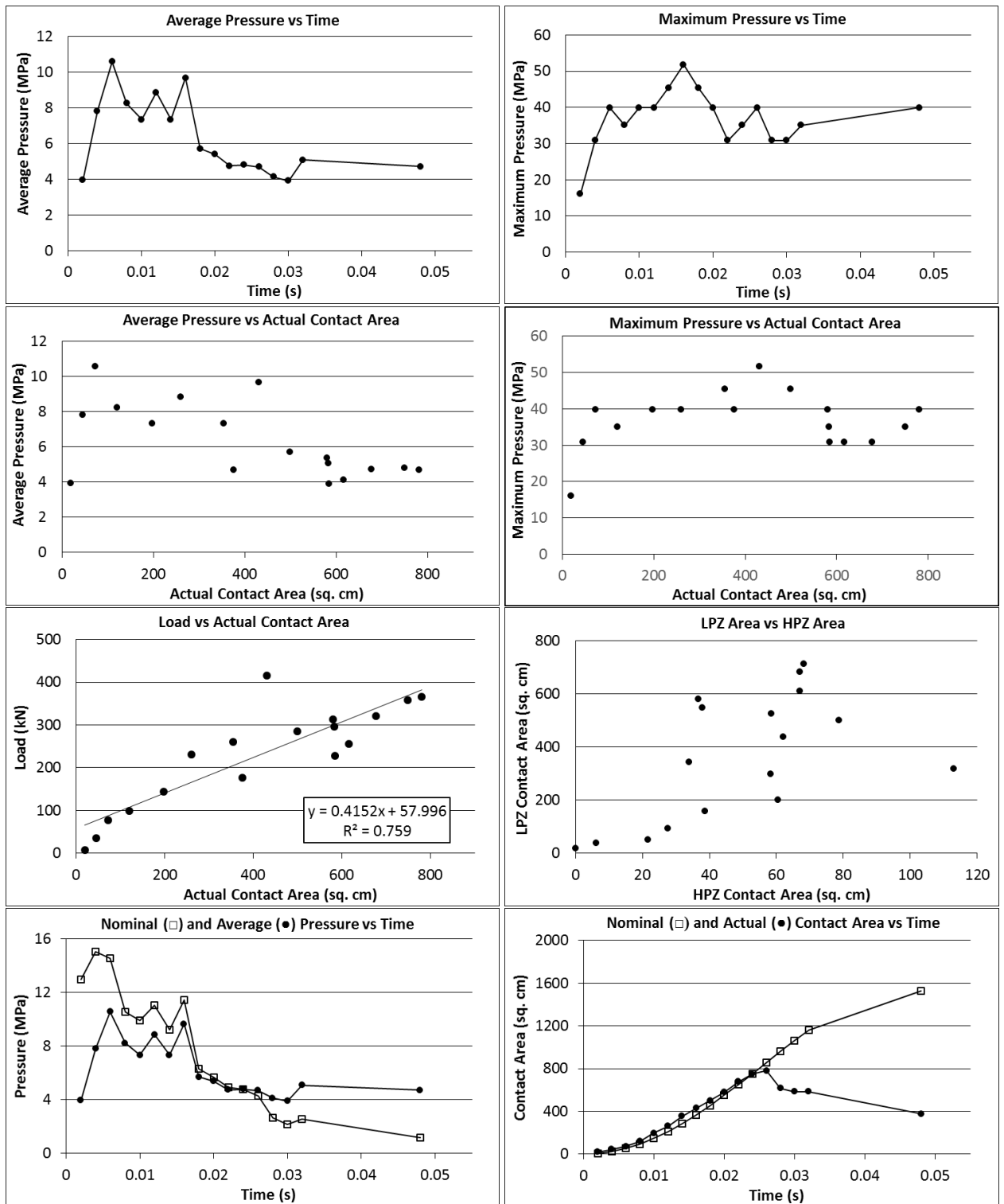
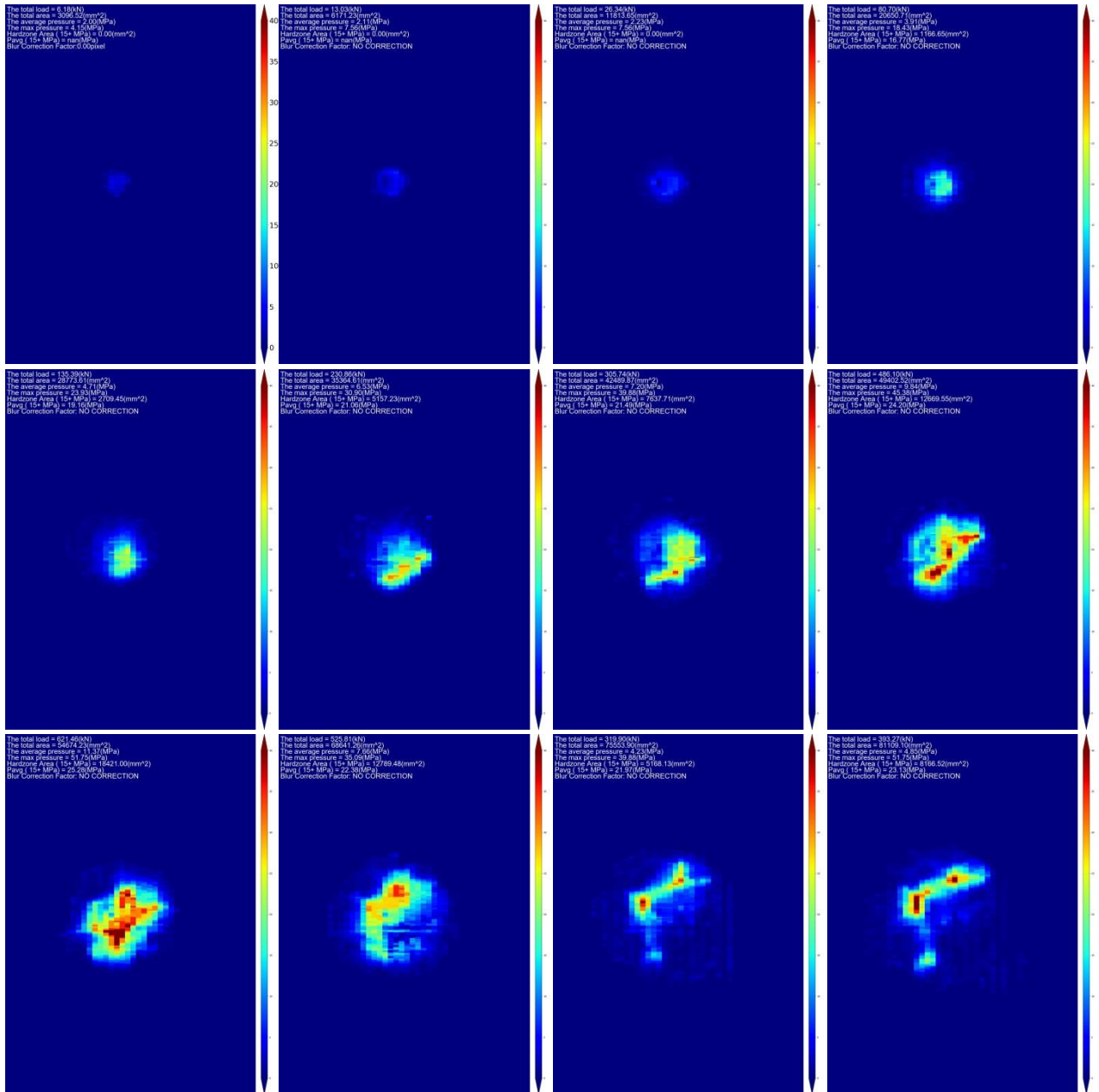


Figure 2-13. Data plots from test Jan20_2015.



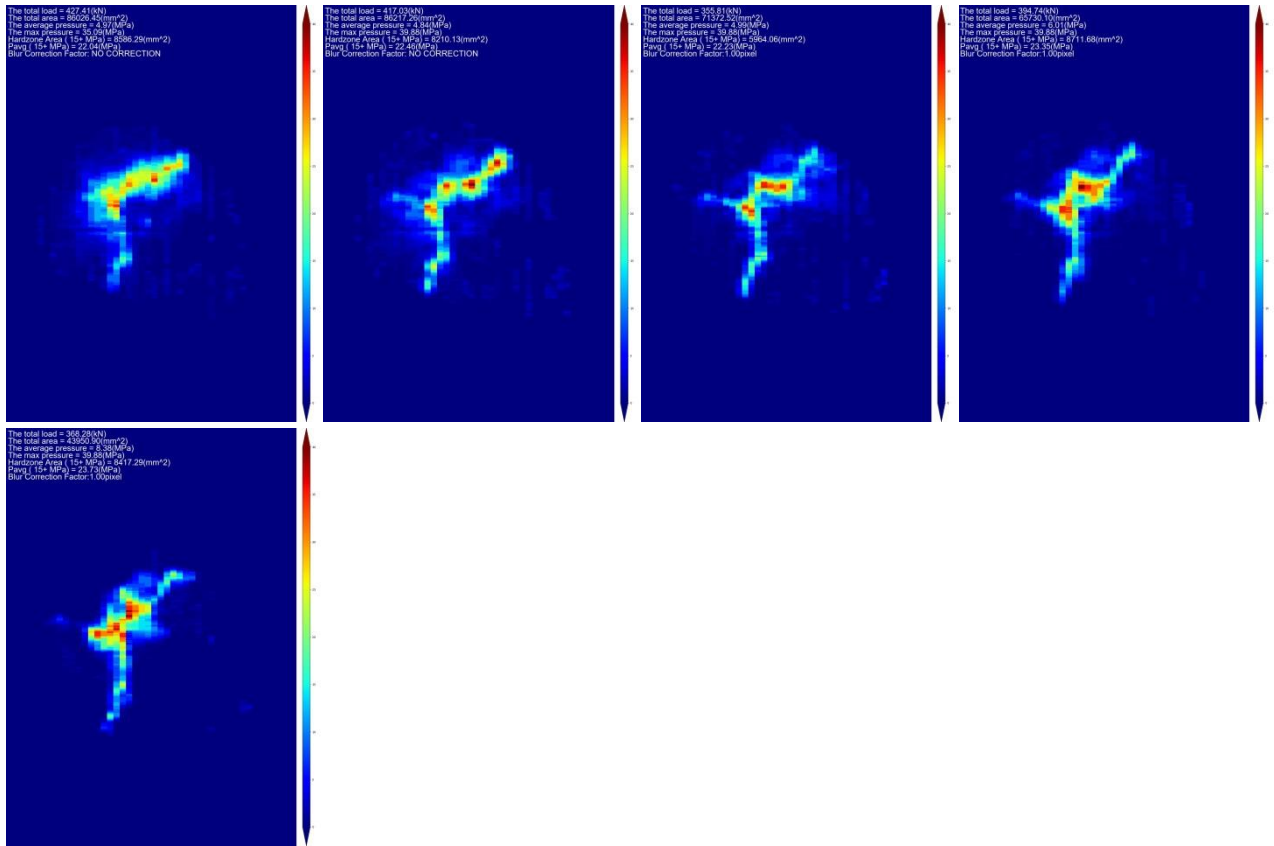
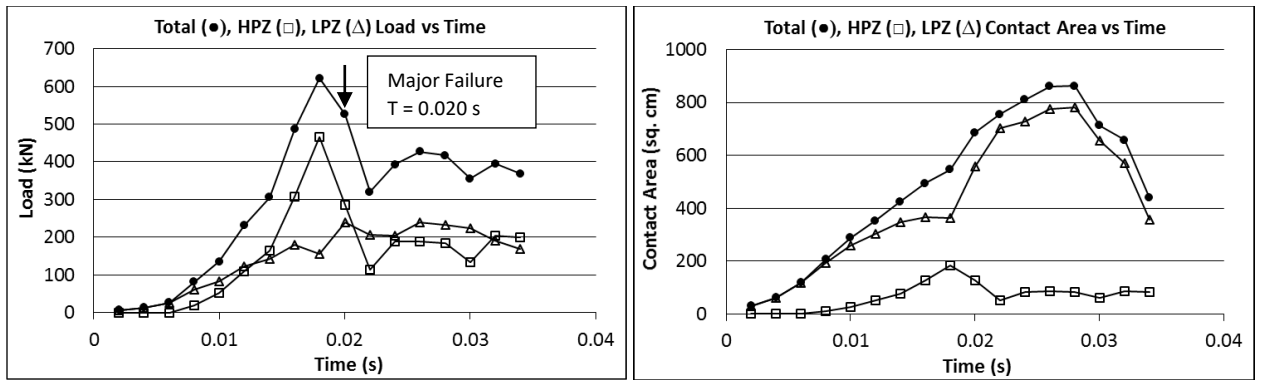


Figure 2-14. Sequence of pressure-pattern images from test Feb25_2016. The images run from left to right in each row from top to bottom. The capture rate was 500 images/s. The width of a blue box is ~ 60 cm.



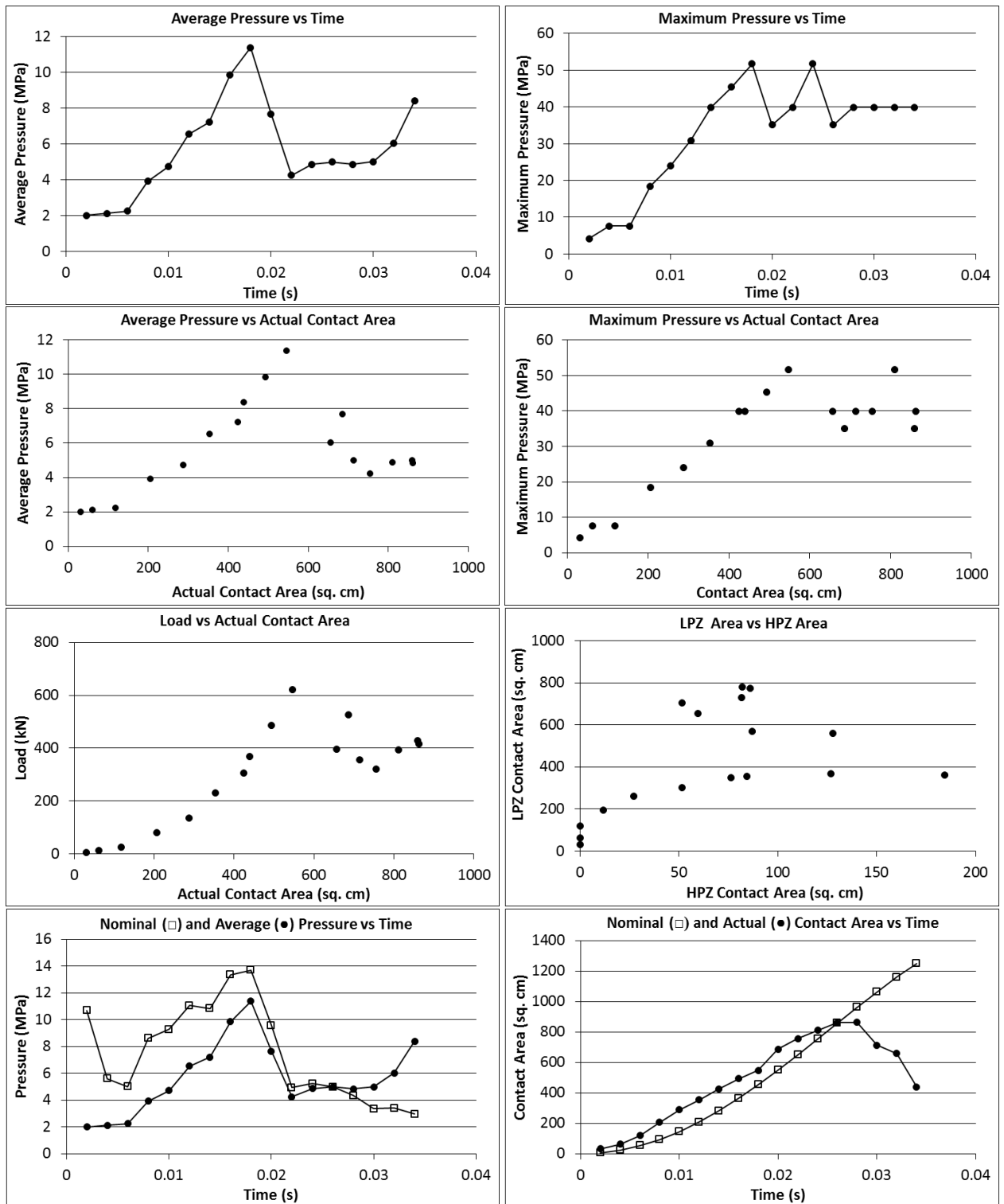


Figure 2-15. Data plots from test Feb25_2016.

Note that prior to the present technology it has not been possible to characterize details of HPZ's and LPZ's in the manner described here. Another related observation of interest is that, with the exception of test Dec10_2015, the time-averaged total load is distributed roughly equally over the HPZ and LPZ contact areas (Table 2-2).

2.12.2 Average pressures of HPZ's and LPZ's, and total-area nominal pressure and average pressure

An extraordinary aspect of the pressure data is the consistency of the HPZ average pressure both during the course of any particular test and also amongst the whole set of tests (Table 2-2). The consistency of the LPZ average pressure is also noteworthy. In like manner the hard-zone ice pressures reported from ship/bergy bit impacts (Gagnon, 2008c) were usually constant or slightly increasing with contact area. Recall that pressure is the same as 'specific energy', and it is reasonable in our tests to assign single values to HPZ's and LPZ's due to the level of consistency. We caution the reader, however, not to treat these specific energy values as though they were material properties. It is very likely that the test configuration, and test parameters, would influence the average pressure values for HPZ's and LPZ's. However, for any particular scenario the specific energy values would likely show similar consistency to that shown here and would for that reason be potentially useful quantities for engineering design. What is certain is that consistency would not be guaranteed unless one could account for how the energy is dissipated in a test, that is, how much energy is actually dissipated in the ice-crushing process and how much energy is dissipated in the apparatus. The only way to reliably achieve this accountability is through the use of a pressure-sensing technology such as we use here, since it indicates fairly precisely where

and what amount of energy is absorbed by the ice. As discussed by Kim and Gagnon (2016) the shape of the indenter/impactor can influence the amount of energy that may be absorbed in the apparatus. The issue is even more complex when the structure that the ice is impacting itself undergoes plastic deformation, such as when an iceberg impacts and damages the hull of a vessel (e.g., Gagnon and Wang, 2012; Quinton, 2019; Quinton et al., 2017a-b).

Given the consistency of HPZ and LPZ pressures, it is not surprising that the average pressure over the whole contact area during any particular test shows a roughly constant (e.g. test May8_A+B_2014) or somewhat increasing (e.g. test May22_2014) value for the Category I tests (Figure 2-16 and Figure 2-17), and also for the portions of the Category II tests before the major failure event occurs.

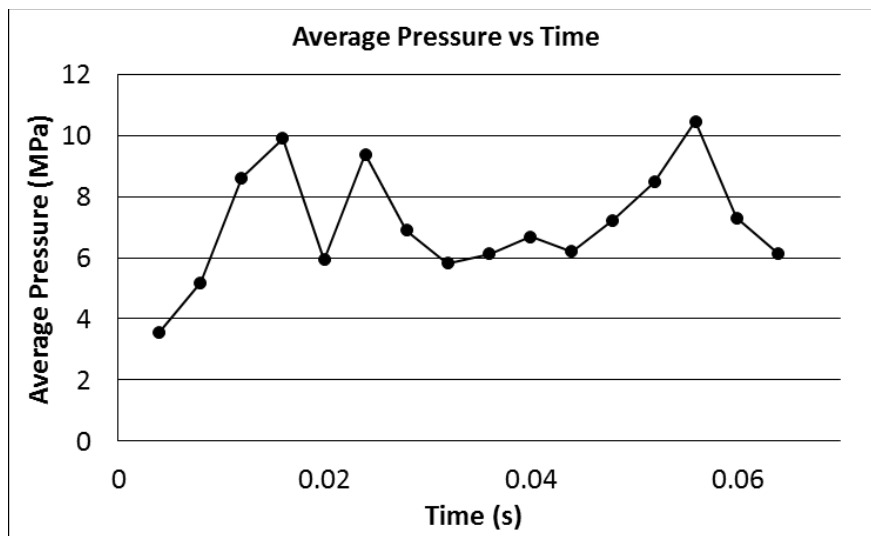


Figure 2-16. Test May8_A+B_2014. Recall that this was actually two impacts on the same ice specimen.

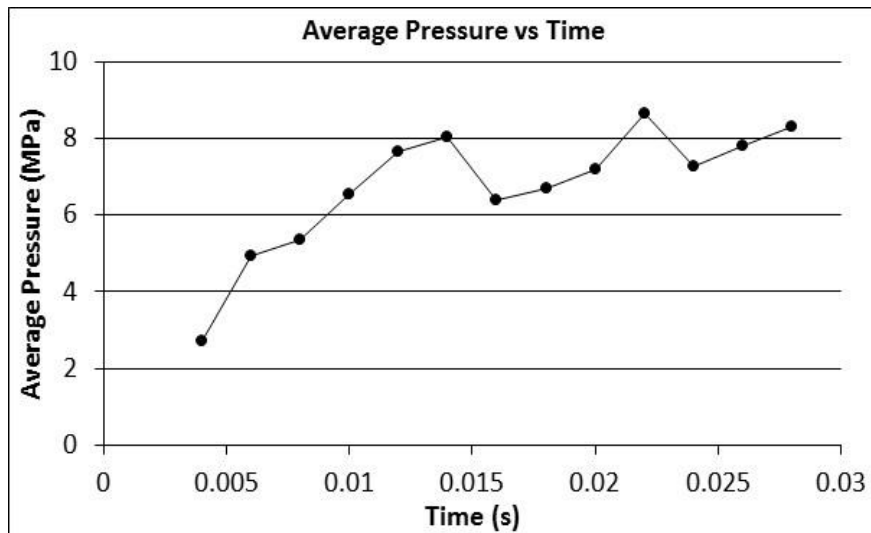


Figure 2-17. Test May22_2014.

Similarly, pressure vs area plots show the same basic trends as the time series plots since the area is generally increasing with time. Also, the time-averaged pressure is fairly consistent for Category I and II tests, i.e., 7.4 ± 1.1 MPa. The time-series average pressure will nevertheless reflect spallation events by a drop in average pressure because a spall(s) has separated from the HPZ and shattered to become LPZ material, so both the total load and average pressure will reflect a drop in magnitude. Test Dec10_2015 is a good example of this (Figure 2-18 and Figure 2-19).

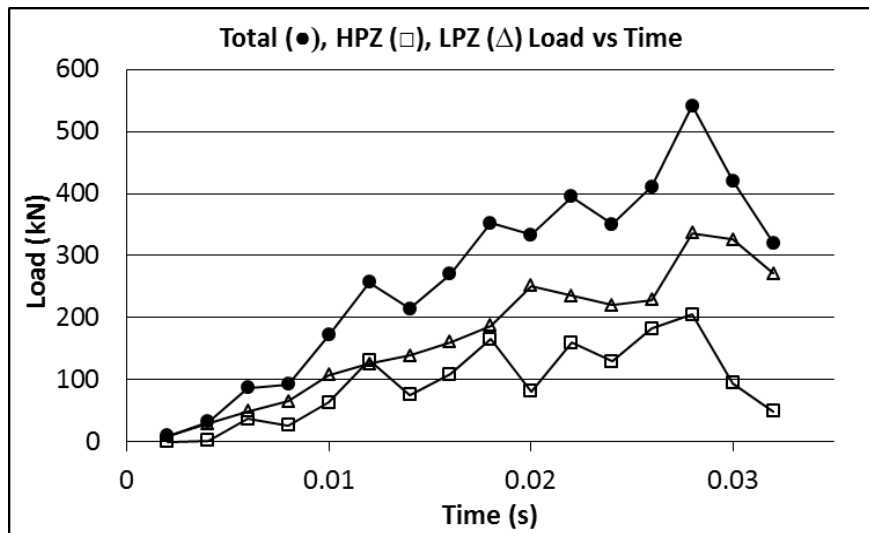


Figure 2-18. Test Dec10_2015. A series of moderate spalling events (load drops) is evident in the ‘Total’ and ‘HPZ’ load records.

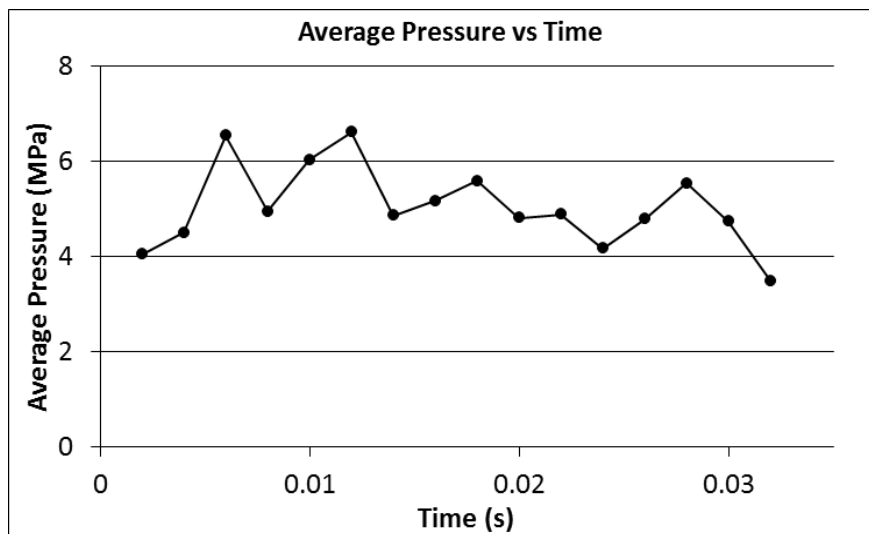


Figure 2-19. Test Dec10_2015. The spalling events evident in Figure 2-18 are also manifested in the ‘Average Pressure’ time series.

The associated pressure-area data plots show the same behavior. Similar constant average pressure behavior has been noted before for ship/sea ice impacts (Gagnon, 2014), where actual ice contact areas were used, and even for Hobson’s Choice Ice Island tests

(Frederking and Sudom, 2008) involving multi-year sea ice that was attached to the perimeter of the Ice Island, where the nominal contact area was used. In the case of nominal pressure vs area data, it is more often reported that the average pressure decreases as the nominal contact area increases, such as was exhibited in the widely known data compiled by Sanderson (1998). That type of pressure-area behavior has been the source of much consternation and debate (Daley, 2004).

This brings us to a potentially important observation in the present tests. The data-plot figures in section 2.18 Appendix C show the time-series actual ice contact areas and nominal contact areas from all the tests. Similarly, section 2.18 Appendix C includes the associated time-series records of the actual average pressure and the nominal pressure for all tests. As a convenient example, we show again the two relevant plots (Figure 2-20 and Figure 2-21) from test May22_2014.

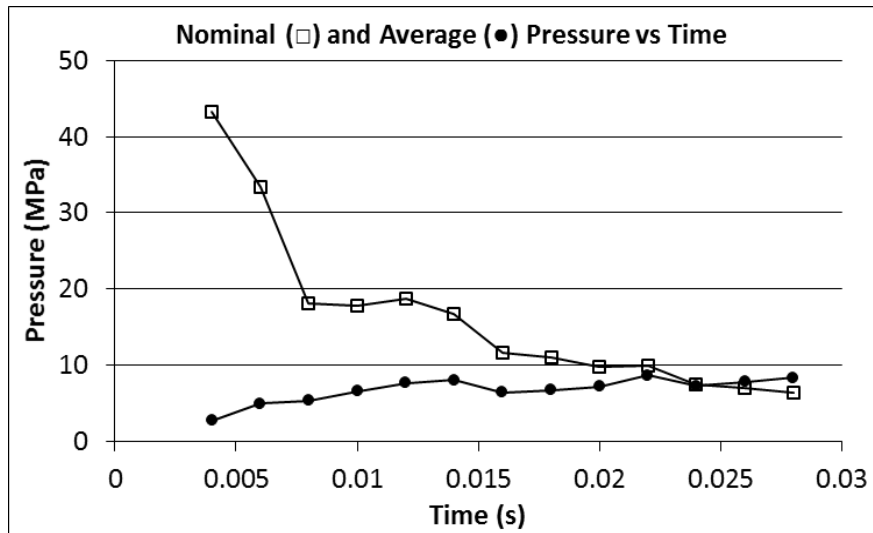


Figure 2-20. Data plot from test May22_2014. The ‘Nominal Pressure’ is decreasing while the actual ‘Average Pressure’ is relatively stable.

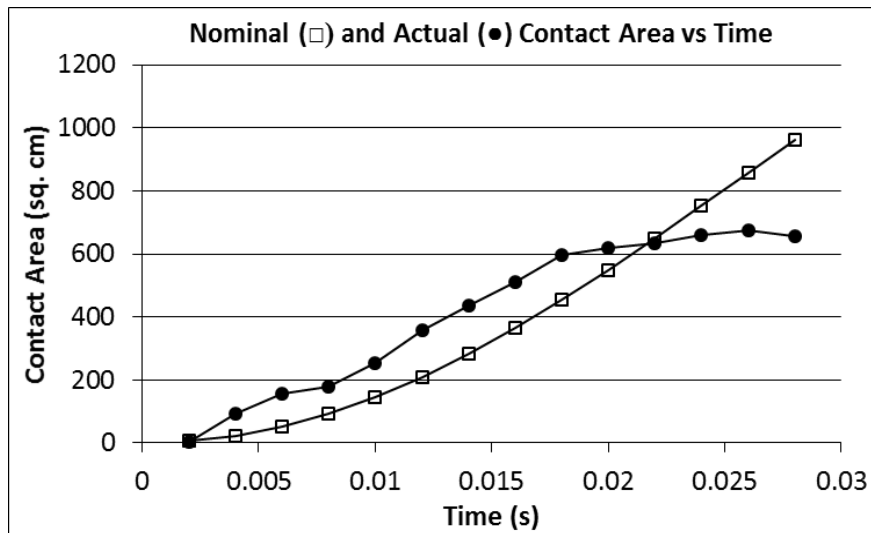


Figure 2-21. Data plot from test May22_2014. The initial ‘Actual Contact Area’ is greater than the ‘Nominal Contact Area’ and becomes less later.

Without exception all the tests show that for an initial portion of the records the actual contact area was greater than the nominal contact area, and then after the crossover point the actual contact area continued to diminish compared to the nominal contact area. Hence, while for all the tests the true average pressure was roughly constant, or slightly increasing, the nominal pressure followed a decreasing trend. The physical reason for this is that the crushed ice that accumulates around the periphery of the roughly centralized HPZ extends the contact region outside of the nominal contact region. This behavior has not been clearly observed in previous studies because the only study that has incorporated the high spatial and temporal pressure-sensing technology necessary to capture the behavior is the present one. The observation also speaks to the fact that the crushed material that is produced by spallation at the hard zones, and that flows away from the hard zones, maintains a level of strength integrity within itself so that it can extend outside the nominal contact area and exert some interfacial pressure. This is due in part to the inter-particle crushing that occurs

within the crushed ice matrix where wet slurry material (comprised of fine ice particles and about 20% liquid) serves to sinter/weld the material matrix. Some slurry is also produced and squeezed/ejected from the HPZ/ impactor interface to mix with the crushed ice. General aspects of the slurry layer have been discussed by Gagnon (2016). The production and welding behavior of slurry has been observed in the ice-on-ice crushing experiments of Gagnon (2013). Similarly, crushed ice material from the Ice Island tests was observed to bond to a steel indenter due to freezing of its small liquid component (Gagnon and Sinha, 1991). We assume that the process surface of the ice contact zone eventually becomes small relative to the nominal surface area later in the tests so that the actual contact area is less than the nominal contact area, as shown in the records (e.g., Figure 2-21). The slurry material freezes quickly, in part at least, due to two effects. One is that when the slurry is produced the pressure is high (Table 2-1 and Table 2-2) so that the liquid content of the mix is at the melting temperature corresponding to that pressure, e.g. for a pressure of 30 MPa the melt temperature is about -3 °C. A portion of the melt in the slurry therefore immediately freezes upon moving to the lower pressure regions. Additionally, the shattered spall debris that comprises the low-pressure crushed ice is at the initial temperature of the ice, i.e., some degrees below zero Celsius. Coming into contact with that cold ice would also contribute to rapid freezing of the fresh slurry.

2.12.3 Pressure and contact area comparisons with other studies and instrumentation

We now draw the reader's attention to the results of other studies that corroborate with those we present here. The measured contact area of HPZ's, obtained from video images acquired during the early stages of two ice indentation experiments (TFR2 and TFR4) at

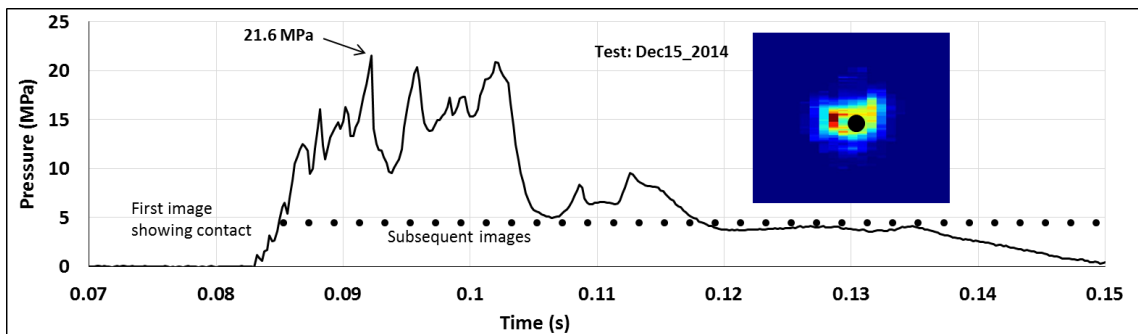
Hobson's Choice Ice Island (Gagnon, 1998), agree quite well with our results. That is, for loads in the vicinity of 350 kN, i.e., the average load associated with the Ice Island HPZ contact area data set, the average value of the HPZ contact area from all of our experiments is $\sim 74 \pm 12 \text{ cm}^2$, and the Ice Island result is $\sim 73 \text{ cm}^2$. Furthermore, at the ends of all four TFR experiments at the Ice Island, measurements of the hard-zone area (referred to as the 'Blue Zone' in that study) were taken from photographs of the ice face after the indentation apparatus was withdrawn. From the final load measurements and the measured HPZ contact areas, and assuming that about half the load is supported on the HPZ's (as we have reported here), a crude value of the HPZ pressure at the end of the tests was $23.5 \pm 8 \text{ MPa}$, whereas our average pressure for HPZ's is 21 MPa.

To continue, the impact panel data from growler impact tests that were performed in the lab (Gagnon, 2004) yielded typical pressure values of about 22 MPa, similar to our average HPZ pressure (21 MPa). The growler impact pressures must have been (for the most part) associated with HPZ contact areas, since that earlier panel could not sense pressure less than 5 MPa, and our present test data show that all of the average LPZ pressures were less than that, i.e., LPZ pressures were under-represented in the growler impact tests. In the drop-ball type impact tests conducted by Gagnon and Gammon (1997) the peak pressures measured at the center of impact, where HPZ's are most likely to be located, spanned a range of 14 – 50 MPa. If we ignore possible temperature effects, this is similar to the range (13 – 50 MPa) of maximum pressures in the present tests, where the range is the average range for all tests excluding Feb25_2016, that exhibited an anomalous slow rise in maximum pressure at the beginning of the test. The fit to the drop-ball test data, over the range of temperatures that the tests were conducted, yielded a center pressure value that

spans 25 – 30 MPa for a corresponding temperature range of 0 °C to -4 °C. Since the pressure sensor in the drop-ball tests was relatively small (a sensing area of 2.8 cm²), and since it was located in the center of the impactor where HPZ's would tend to be centered, in general it would be biased to sample the central area of HPZ's (where pressure is higher) more so than a peripheral segment of the HPZ's where the pressure is lower. This would explain, in part at least, why the maximum pressure values (25 – 30 MPa) were higher than our average pressure (from all the tests) for HPZ's (21 MPa). Furthermore, since confinement of centrally-located ice would have been greater in the drop-ball type tests, this may also have contributed to the higher-pressure measurements compared to those here. In spite of these issues we note, however, that four of the pendulum impact tests (Feb25_2016, Dec15_2014, Oct16_2014 and Jan20_2015) each had a few pressure-pattern images where the average HPZ pressure values for those images were in the range of the drop ball maximum pressures.

The Impact Module also incorporated pressure-sensing plugs, as mentioned before. The symmetric array of nine pressure-plugs is visible in section 2.16 Appendix A Figure 2-26. Data from the centrally located pressure-plug is useful, at least qualitatively, for comparison with the pressure-sensing strip data. Since the pressure-plug is usually fairly well-centered with respect to the impacted ice feature, and since its sensing area is ~ 5 cm², we may expect that there are times during a test when the pressure-plug is encompassed within a HPZ so that the measurements would be somewhere in the range of pressure associated with HPZ's. We cannot directly compare the pressure from the pressure-sensing strip technology with that from the pressure-plug because there are no measurements from the pressure-sensing strip segments situated directly over the pressure-plug, i.e., the view

is blocked by the plug. Another factor that might have some bearing on comparisons of data from the pressure-sensing strip technology with that from the pressure-plug is a bias phenomenon that some single-point pressure sensors which are imbedded into a hard surface are subject to. In those cases, the imbedded pressure sensor is generally more compliant than the bulk material that it is imbedded in. Hence, some of the load that would normally be experienced by the sensor face is taken up by the less-compliant surface that surrounds the sensor surface, with the result that the measured pressure is somewhat lower. This effect may be a factor with the cylindrical pressure-plug because its side wall is not attached to the surrounding bulk acrylic, i.e., it is free-standing. Hence, it is longitudinally more compliant than a volume of acrylic with the same shape extending into the bulk acrylic. With the above considerations in mind, we might still reasonably expect that there would be times during a test that the pressure-plug would register pressures that are typical of HPZ's. Figure 2-22 shows pressure-plug data for tests Dec15_2014 and Oct16_2014 where the respective peak measured pressures (21.6 MPa and 21.3 MPa respectively) are very close to the average HPZ pressure (21 MPa) determined from the pressure-sensing strip data. The top graph in the figure has an inset (the fourth pressure-pattern image for that test) showing the location of the pressure-plug surrounded by a pressure field with magnitudes indicative of HPZ's.



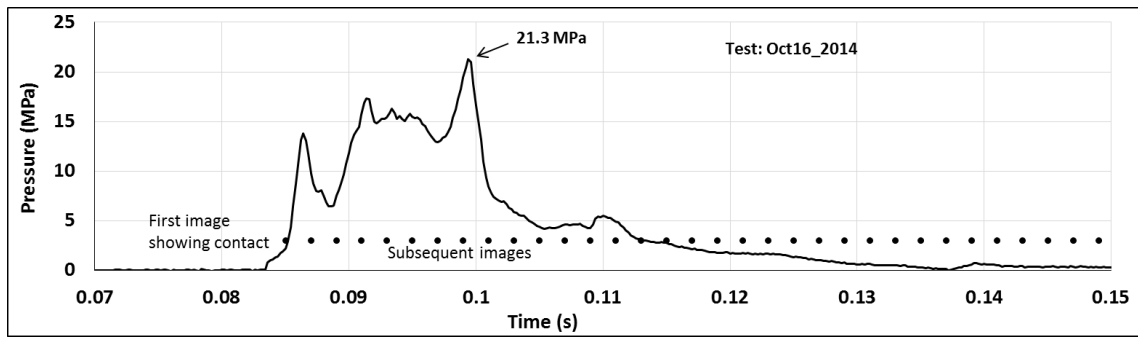


Figure 2-22. Pressure-plug data for two tests. The horizontal sequence of solid circles correspond approximately to the times when the Impact Module camera captured pressure-pattern images. The inset on the top graph corresponds to the fourth image in the sequence. It shows a HPZ that had developed and the location and sensing area (dark circle) of the central pressure-plug. Peak pressures are indicated on the graphs. The pressure-color scale is the same as for all pressure-pattern images throughout the paper.

To conclude the discussion of pressure data comparison we note that unfortunately the bergy bit impact field study pressure data are likely not suitable to use in this context. As explained by Gagnon (2008c), due to the broad shapes of the ice masses the contact areas were large whereas the loads were relatively small so that not much actual crushing was happening during the impacts. Hence, the pressures within hard zones spanned a relatively low range (8-20 MPa) compared to the range of pressures within HPZ's in our study (roughly 15 – 52 MPa). This was due to the lack of much actual penetration during the sliding-type impacts. Therefore, the bergy bit impact pressure data set is of limited use for comparisons with other lab and field tests where samples are typically shaped to concentrate load and where very substantial penetration, and development of the process surface, occurs.

We may further conclude from this discussion that the lab-grown granular freshwater ice that our samples consisted of yielded impact test results that were characteristic of glacial ice and multiyear sea ice.

2.12.4 Confining aspects of LPZ's

Earlier we explained that we designate hard-zone ice as relatively-intact ice where the interfacial pressure starts at 15 MPa at the periphery and rises to higher values when moving towards the center, where (from Table 2-2) the average is approximately 21 MPa. The LPZ ice has an average interfacial pressure of ~ 3.7 MPa. The HPZ/LPZ border interfacial pressure of 15 MPa may be understood from the confining aspects of an LPZ that helps maintain the structural integrity of an HPZ. The triaxial strength test results of Gagnon and Gammon (1995) on iceberg ice showed that a confining stress of ~ 4 MPa would enable cylindrical ice samples to support uniaxial compressive stresses of roughly 12 MPa at a strain rate of $5 \times 10^{-2} \text{ s}^{-1}$ (i.e., within the brittle regime). With this in mind, and further considering that the confining pyramidal shape of the intact-ice process surface would also contribute some strength to the HPZ, we note that this is consistent with the interfacial pressure that we identified (i.e., ~ 15 MPa) as the defining boundary pressure that distinguishes HPZ's and LPZ's.

2.12.5 HPZ load correlation with the total load

We have previously pointed out that in most cases the time-averaged loads on the HPZ's and LPZ's are roughly similar. However, it is worth noting that the details (i.e., abrupt changes) in the time evolution of the HPZ size and shape (and consequent load) are much more reflected in the total load than are the aspects of the LPZ evolution. This is due to the fact that the HPZ contact area is generally much less than the LPZ contact area. Recall that the average pressures on HPZ's and LPZ's are approximately constant (i.e., 21 MPa and 3.7 MPa respectively), so it is their contact areas that largely determine the loads they

support. Consequently, when a spallation from the HPZ occurs that involves, for example, 20% of the contact area of the HPZ shattering to become LPZ material, the relative change in area of the LPZ contact area is considerably less because the LPZ areas are generally 2-6 times the size of HPZ areas. That is, the 20% contribution from the HPZ amounts to only a 3-10% change in the LPZ contact area at the time of the event. Figure 2-23 shows close correspondence between the peak load and the maximum HPZ contact area for all tests, whereas there is no statistically significant correspondence with the maximum LPZ contact area. Since most of the contact area consists of LPZ contact, understandably there is a correlation between the maximum total contact area and the maximum LPZ contact area (Figure 2-24), whereas there is no statistically significant correspondence with the maximum HPZ contact area. It is also not surprising that the time averaged HPZ load correlates with the maximum HPZ load.

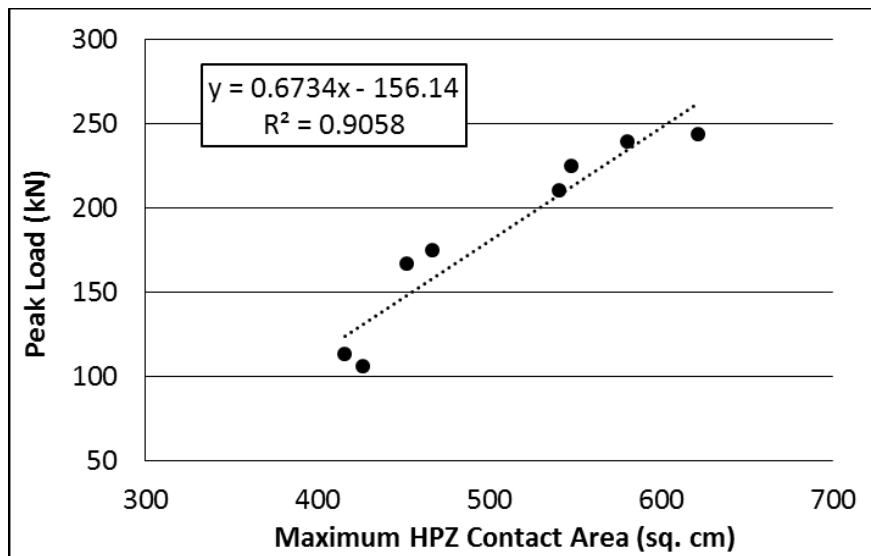


Figure 2-23. Peak Load vs Maximum HPZ Contact Area for all tests.

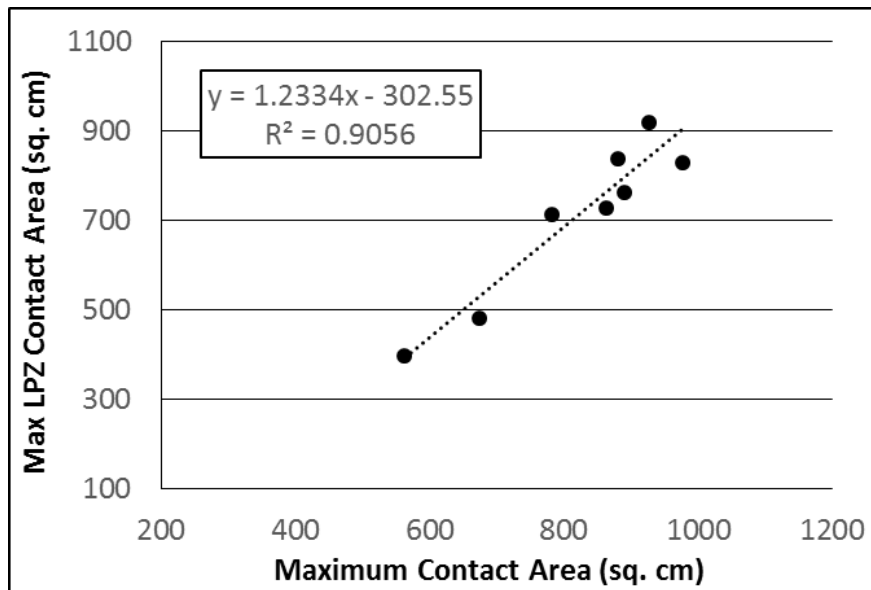


Figure 2-24. Maximum LPZ Contact Area vs Maximum Contact Area for all tests.

A final correlation of note for the set of tests is between the maximum ice contact area and the impact speed (Figure 2-25). The correlation makes physical sense, however there was no similar correlation between peak load and impact speed.

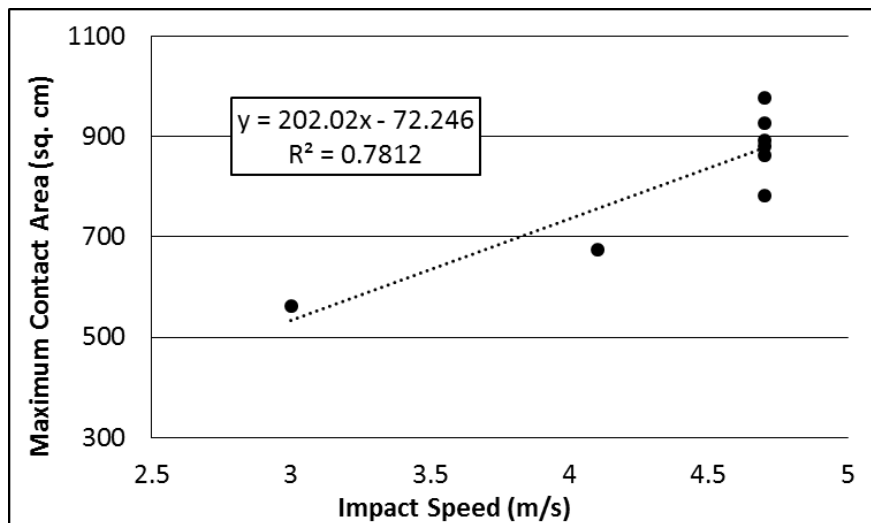


Figure 2-25. Maximum Ice Contact Area vs Impact Speed for the full set of tests.

2.12.6 Maximum pressure characteristics

Maximum pressure was found to be in the 30-55 MPa range, tending more so towards the higher end of the range. The time series of the maximum pressures for the tests generally exhibited roughly constant or an increasing trend in most cases. Test Dec15_2014 showed a somewhat decreasing trend.

2.13 Conclusions

The pressure-sensing strip technology has been shown to be robust and capable of providing accurate pressure distribution maps during small-to-medium-scale ice impact tests in the lab at high data throughput rates enabled by high-speed CCD technology. The in-situ time evolutions of HPZ's and LPZ's have been documented for the first time, revealing intriguing aspects such as: the extraordinary consistency of HPZ and LPZ average pressures; level or slightly increasing average pressure with actual contact area, and the role of HPZ's in defining details of the total load time series. Another significant observation is that in the earlier stage of tests crushed ice, generated during the impacts, can maintain strength, and extend the actual contact area beyond the nominal contact area. This suggests a possible explanation, in part at least, as to why a decreasing trend in pressure-area data has been reported in the past and debated frequently. Since loads obtained by integrating the pressure-distribution data agreed well with the actual load-cell measurements we are led to consider that the technology can function as a 'massless' load cell, that is, where the system is not impaired by resonance effects that are inherent in traditional mass-on-a-spring type load-cell configurations.

2.13.1 CCD enabled technology

As mentioned previously, the pressure-sensing technology is such that we may think of an effective unit sensor as having an area of $\sim 1.7 \text{ cm}^2$. The image acquisition rate is 500 images/s for the existing camera and the ‘active’ area of the Impact Module surface is roughly 0.8 m^2 , implying that the system is capable of acquiring ~ 2.4 million individual pressure measurements per second. Furthermore, high-speed imaging cameras can acquire full-frame images at 2000 images/s or more, so one is left to marvel at the capability that is enabled by using high-speed CCD technology to capture the data. The richness of the data we present here testifies to this.

2.14 Acknowledgements

The authors would like to acknowledge the financial support of Atlantic Canada Opportunities Agency, Research and Development Corporation, American Bureau of Shipping, BMT Fleet Technology, Husky Energy, Rolls-Royce Marine, Samsung Heavy Industries. Also, we are grateful for the invaluable participation of the National Research Council Canada in the form of providing expertise for all aspects of the apparatus development and experiments, and for the use of a unique scientific instrument.

Finally, we are grateful to the Canadian physicist Willard Boyle and his American co-inventor George Smith for their invention of the charge-coupled device (CCD) for which they were awarded the Nobel Prize in Physics in 2009.

2.15 References

Alam, M.S., Daley, C., Colbourne, B., Hermanski, G., Gagnon, B., Bruneau, S., Clarke,

- G., Quinton, B., 2012. Double pendulum dynamic impact test set-up for ice-grillage collision. In: Proceedings of ICETECH 2012. Paper No. ICETECH12-134-RF.
- Daley, C.G., 1990. Ice edge contact - an iterative failure process model. In: Report from Finnish-Canadian Joint Research Project No. 5, Ships interaction with actual ice conditions, Otanieme, 1990/M-103.
- Daley, C.G., 1991. Ice edge contact and failure. *Cold Reg. Sci. Technol.* 21, 1–23.
- Daley, C., 2004. A Study of the Process-Spatial link in Ice Pressure–Area Relationships. PERD Report. March 20.
- Evans, A.G., Palmer, A.C., Goodman, D.J., Ashby, M.F., Hutchison, J.W., Ponter, A.R.S., Williams, G.J., 1984. Indentation spalling of edge-loaded ice sheets. In: Proceedings of IAHR 1984, Hamburg, pp. 113–121.
- Frederking, R., 2004. Ice pressure variations during indentation. In: Proc IAHR Symposium on Ice, St. Petersburg, Russia, pp. 307–314.
- Frederking, R., Sudom, D., 2008. Local ice pressure distributions during 1990 Hobson’s Choice Ice Island multi-year ice indentation tests. In: Proc. 19th IAHR International Symposium on Ice. Vol. 2. pp. 815–827.
- Gagnon, R.E., 1994. Generation of melt during crushing experiments on freshwater ice. *Cold Reg. Sci. Technol.* 22 (4), 385–398.
- Gagnon, R.E., 1998. Analysis of visual data from medium scale indentation experiments at Hobson’s Choice Ice Island. *Cold Reg. Sci. Technol.* 28 (1998), 45–58.

- Gagnon, R.E., 1999. Consistent observations of ice crushing in laboratory tests and field experiments covering three orders of magnitude in scale. In: Proceedings of POAC-99. 2, pp. 858–869.
- Gagnon, R., 2004. Analysis of laboratory growler impact tests. *Cold Reg. Sci. Technol.* 39 (2004), 1–17. Gagnon, R., 2008a. A new impact panel to Study bergy bit / ship collisions. In: Proceedings of IAHR 2008. Vol. 2. Vancouver, Canada, pp. 993–1000.
- Gagnon, R., 2008b. Analysis of data from bergy bit impacts using a novel hull-mounted external impact panel. *Cold Reg. Sci. Technol.* 52 (2008), 50–66.
- Gagnon, R., 2012. An Explanation for the Molikpaq May 12, 1986 event. *Cold Reg. Sci. Technol.* 82 (2012), 75–93.
- Gagnon, R.E., 2013. High-speed imaging of ice-on-ice crushing. In: Proceedings of POAC 2013 (Paper No. 159).
- Gagnon, R., 2014. Re-analysis of load and pressure data acquired from Ice Impacts during the CCGS Louis St-Laurent 1994 Arctic voyage. In: Proceedings of the 22nd IAHR International Symposium on Ice, Singapore, August 11 to 15, 2014.
- Gagnon, R.E., 2016. New friction mechanisms revealed by ice crushing-friction tests on high-roughness surfaces. *Cold Reg. Sci. Technol.* 131 (2016), 1–9.
- Gagnon, R.E., Bugden, A., 2007. Ice crushing tests using a modified novel apparatus. In: Proceedings of POAC-07, pp. 235–244.
- Gagnon, R.E., Bugden, A., 2008. 2-dimensional edge crushing tests on thick sections of ice

- confined at the section faces. In: Proceedings of IAHR 2008. Vol. 2. Vancouver, Canada, pp. 973–981.
- Gagnon, R.E., Daley, C., 2005. Dual-axis video observations of ice crushing utilizing highspeed video for one perspective. In: 18th International Conference on Port and Ocean Engineering Under Arctic Conditions, 26-30 June 2005, Potsdam, New York, p. 271- 281. IR-2005-02.
- Gagnon, R.E., Gammon, P.H., 1995. Triaxial experiments on glacier and iceberg ice. *J. Glaciol.* 41 (139), 528–540.
- Gagnon, R.E., Gammon, P.H., 1997. In situ thermal profiles and laboratory impact experiments on iceberg ice. *J. Glaciol.* 43 No. 145.
- Gagnon, R.E., Sinha, N.K., 1991. Energy dissipation through melting in large scale indentation experiments on multi year sea ice. In: Proceedings of the 10th International Conference on Offshore Mechanics and Arctic Engineering, Stavanger, Norway, June, 1991. 1991 OMAE, VOL. IV, Arctic/Polar Technology, 157 161. NRC/IMD Report IR- 1991-07, pp. 157–161.
- Gagnon, R.E., Wang, J., 2012. Numerical simulations of a tanker collision with a bergy bit Incorporating hydrodynamics, a validated ice model and damage to the vessel. *Cold Reg. Sci. Technol.* 81 (2012), 26–35.
- Gagnon, R., Daley, C., Colbourne, B., 2015. A large double-pendulum device to study load, pressure distribution and structure damage during ice impact tests in the lab. In: Proceedings of POAC 2015, paper 143, Trondheim, Norway.

- Gudimetla, P.S.R., Colbourne, B., Daley, C., Bruneau, S.E., Gagnon, R., 2012. Strength and pressure profiles from conical ice crushing experiments. In: Proceedings of the International Conference and Exhibition on Performance of Ships and Structures in Ice (ICETECH), Banff, Alberta, Canada.
- Izumiyama, K., Wako, D., Uto, D., 1998. Ice force distribution on a flat indenter. In: Hung, T.S. (Ed.), In Proc. 14th Int. Symp. on Ice (IAHR 1998), Potsdam, USA. 2.
- Jefferies, M.G., Rogers, B., Hardy, M., Wright, B., 2011. Ice load measurement on Molikpaq: methodology and accuracy. In: Proc. 21st Int. Conf. On Port and Ocean Engineering under Arctic Conditions, Montreal, Canada, POAC 2011, paper #189.
- Kim, E., Gagnon, R., 2016. A preliminary analysis of the crushing specific energy of iceberg ice under rapid compressive loading. IAHR 2016, Ann Arbor, Michigan.
- Määttänen, M., Marjavaara, P., Saarinen, S., 2011. Ice crushing pressure distribution against a compliant stiffened panel. In: Proc. 21st Int. Conf. On Port and Ocean Engineering under Arctic Conditions, Montreal, Canada, POAC 2011, paper #038.
- Quinton, B.W.T., 2019. Lateral (sliding) motion of design ice loads on IACS polar classed structures. In: Ships and Offshore Structures, pp. 1–11. <https://doi.org/10.1080/17445302.2019.1580844>.
- Quinton, B.W.T., Daley, C.G., Gagnon, R.E., Colbourne, D.B., 2017a. Guidelines for the nonlinear finite element analysis of hull response to moving loads on ships and offshore structures. *Ships Offshore Struct.* 12, S109–S114. <https://doi.org/10.1080/17445302.2016.1261391>.

- Quinton, B.W.T., Daley, C.G., Gagnon, R.E., Colbourne, D.B., 2017b. Experimental investigation of accidental sliding loads on the response of hull plating. In: Progress in the Analysis and Design of Marine Structures: Proceedings of the 6th International Conference on Marine Structures (MARSTRUCT 2017). Portugal, Lisbon.
- Sanderson, T.J.O., 1988. Ice Mechanics: Risks to Offshore Structures. Graham and Trotman, London.
- Sodhi, D.S., Takeuchi, T., Nakazawa, N., Kawamura, S.A.M., 2001. Measurements of ice force and interfacial pressure during medium-scale indentation tests in Japan. In: Proc. 16th International Conference on Port and Ocean Engineering under Arctic Conditions, Ottawa, Ontario, Canada, pp. 617–626.
- Sopper, R., Gagnon, R., Daley, C., Colbourne, B., 2015. Measurements of spatial and temporal variations in ice impact pressure. In: Proceedings of POAC 2015, Paper 149, Trondheim, Norway.
- Spencer, P.A., Masterson, D.M., 1993. A geometrical model for pressure aspect-ratio effects in ice–structure interaction. In: Proceedings of the 12th International Conference on Offshore Mechanics and Arctic Engineering. Vol. 4. OMAE, pp. 113–117.
- Sumiya, T., Suzuki, Y., Kasahara, T., Ogata, H., 1998. Sensing stability and dynamic response of the F-Scan in-shoe sensing system: a technical note. J. Rehabil. Res. Dev. 35 (2), 192–200.

2.16 Appendix A

2.16.1 Preparation and conversion of raw images to pressure-distribution patterns

Three major corrections need to be performed before the images can yield good pressure data. First, each image might be slightly displaced in relation to the next, since the high-speed camera inside the Impact Module sits on four soft-rubber pads behind the acrylic block, which protects the camera and reduces vibrations. However, this means that the camera is not perfectly fixed. Second, image noise needs to be removed, since there are air bubbles inside the acrylic block and other features that are not of interest. Finally, the fisheye effect must be corrected, because the high-speed camera was instrumented with a fisheye lens to widen the field of view and capture almost the entirety of the Impact Module surface. The following image analysis procedure is based on an updated version of the original presented by Sopper et al. (2015).

2.16.2 Fisheye correction and first image centering

This first step uses the software PTLens 9.2™ to correct the fisheye effect and perform a coarse alignment of the images, with the central pressure plug as reference. This is illustrated in Figure 2-26.

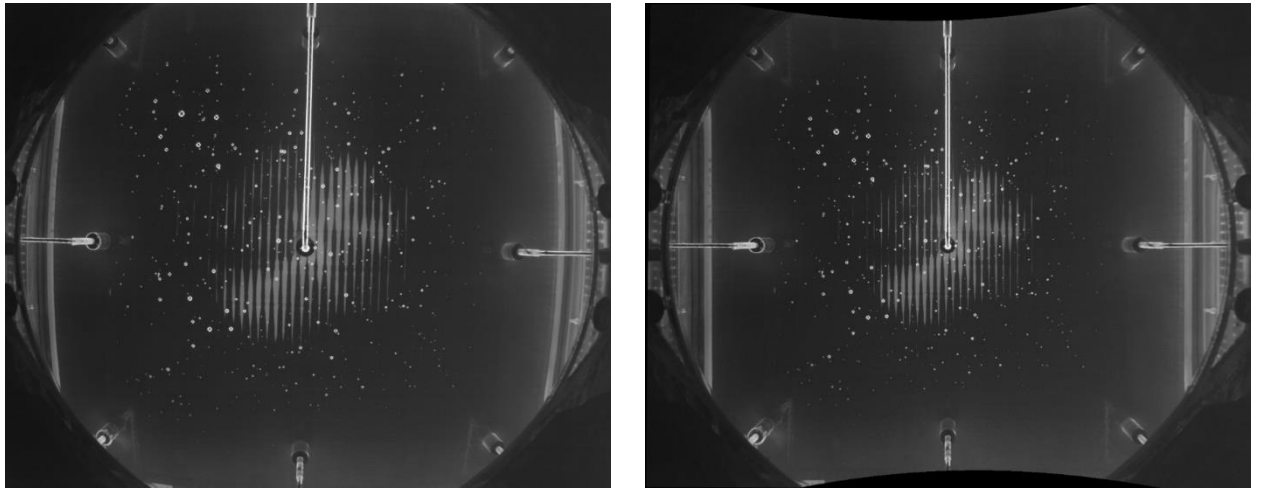


Figure 2-26. The first picture (left) is an untreated sample of an image recorded by the high-speed camera. The second picture (right) is the same image with fisheye effect correction applied. Note that the symmetric array of nine pressure-sensing plugs is visible in the image.

2.16.3 Isolation of the pressure information and edge detection

This next step involves using the software Paintshop®Pro 2019 to separate the pressure-sensing strips from all the noise – in this case noise is defined as features unrelated to pressure information (e.g., the camera casing, cables, air bubbles, pressure-sensing plugs, and Impact Module walls). For each image in a set, a new image is created with the pressure information manually removed (i.e., blacked out). This “negative” image is then subtracted from the original one to primarily obtain the pressure-sensing strip information. A small amount of residual noise is still present that is easily removed. The final result is a clean image with only the pressure-sensing strip information. The steps described above are illustrated in the first three images of Figure 2-27. Then an edge-detection routine is necessary in order to enable a Python™ routine to determine the width of contact of the pressure-sensing strips.

The accuracy of the Python routine is dependent on good definition of the pressure-sensing strip contact edges. This is achieved in two steps using the GNU Image Manipulation Program 2.10.6™ (GIMP). In the first step a noise reduction is performed, followed by the edge detection. Then in the second step, also using GIMP, the resulting image is resized from 1280x1024 pixels to 2560x2048 pixels and aligned in accordance with the requirements of the Python™ routine. The result is the last image of Figure 2-27.

2.16.4 Pressure-data determination and presentation

The Python™ routine measures the distance in pixels (with sub-pixel accuracy since the original images were resized) between the edges of the contact width for each pressure-sensor strip along its length and translates this information into pressure data. The information is displayed as a color-coded pressure distribution pattern, where the color-pressure scale appears at the right of the image.

This study updated the original Python™ routine used by Sopper et al. (2015) to analyze the impact test performed on the 16th of October, 2014. The modified code performs a simple linear interpolation in the regions obstructed by the cable and a bilinear-interpolation in the region obscured by the pressure-sensing plug. This correction provides reasonable estimates for information obscured by the cables and plugs. Additionally, a blur correction factor was introduced to improve the fidelity of a few select images.

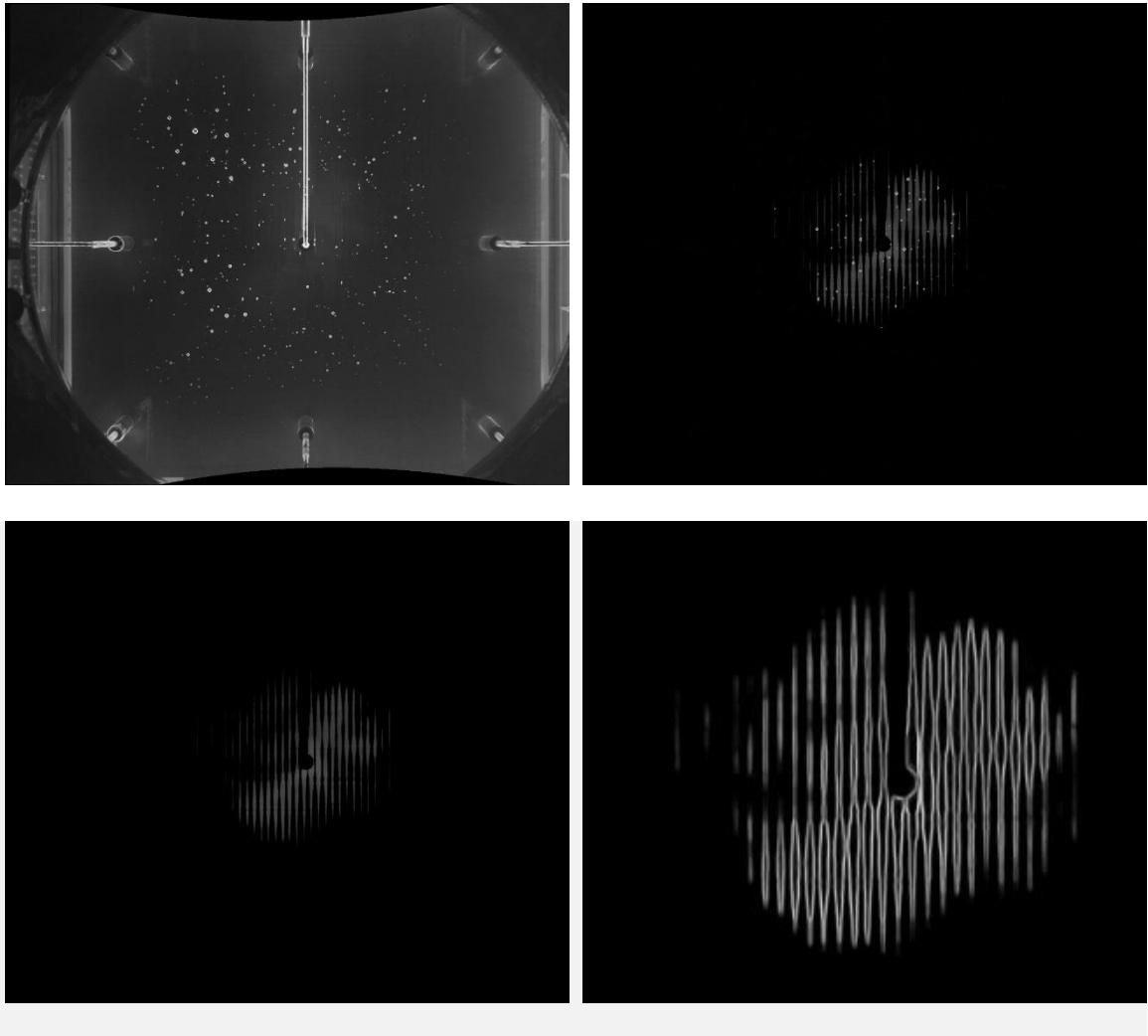


Figure 2-27. Image preparation required before using the Python™ routine to obtain the width of contact that it then uses to calculate pressure from a calibration curve of pressure vs contact-width. The first image (top-left) shows the negative image obtained by cleaning the pressure information. The second image (top-right) is the result of subtracting the original (second image of Figure 2-26) from the negative image. The third image (bottom-left) is totally cleaned. The fourth image (bottom-right) is the result of the edge detection step.

Figure 2-28 compares the load that was recorded by the load cells in the Impact Module with the load determined by integrating the pressure distribution data.

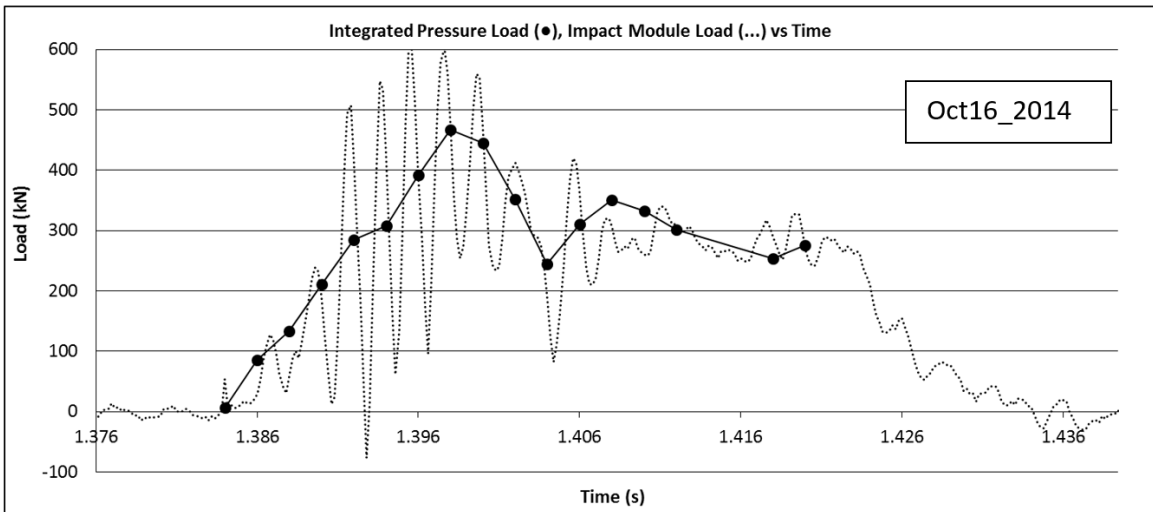


Figure 2-28. Comparison between the integrated-pressure load (solid black circles) and the load from the load cells in the Impact Module. The broad-scale agreement demonstrates the quality of the integrated-pressure data, and the robustness of the techniques used for analysis of the associated raw images. The oscillations in the load-cell data are due to typical resonance of the load-cell system. Note that the integrated-pressure measurements are free from the inherent resonance of the load-cell system.

As mentioned above, at the end of the impact (just prior to the elastic-rebound phase) a blur effect is present in a small number of images. A correction procedure was developed to improve the information obtained from those images. The last 4 data points of Figure 2-28 were obtained using the method. The average blur intensity is measured by analysing some distinct features at different time instants of an impact (e.g., large bubbles and plug-cable width). By comparing images that are not blurred and images that are blurred, the blur effect can be quantified as an approximate number of pixels that can be subtracted from a moderately blurred contact width of a pressure-sensor strip to get an estimate of the actual contact width. Note that this procedure was only used when the blur effect was somewhat minimal and did not obscure too severely the edges of any adjacent strips (due to the overlap effect). Hence, there were sometimes a few missing pressure-data points near the end in the sequence for some tests that were subject to more blur.

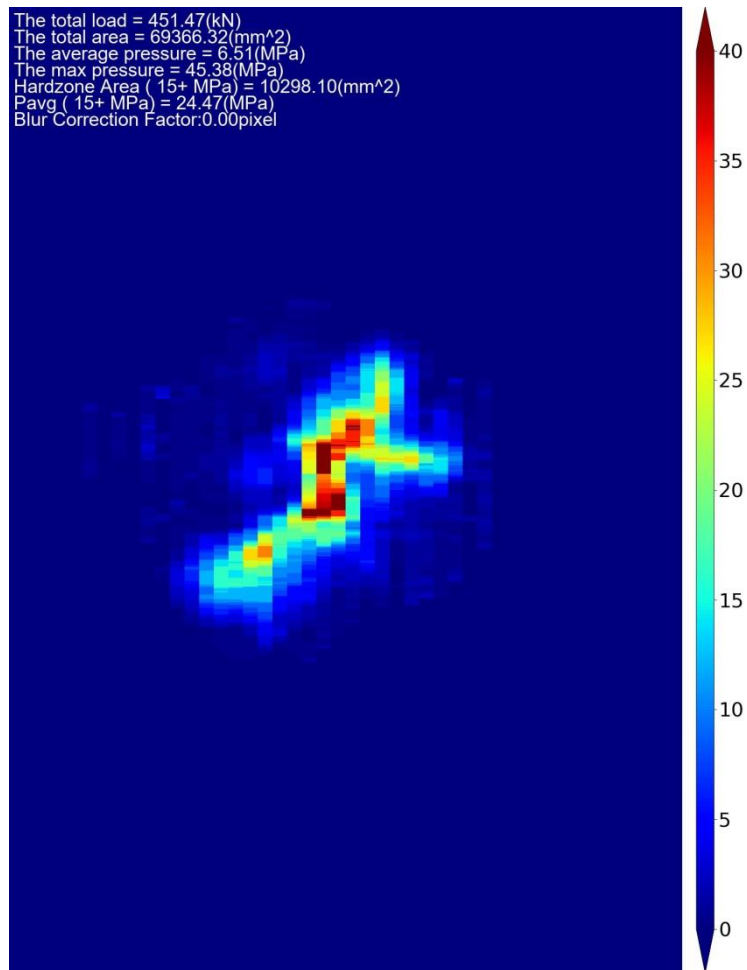


Figure 2-29. The output of the procedure is the color-coded version of the pressure distribution measured by the Impact Module.

In addition to the pressure distribution, the code outputs total load, total contact area, average pressure, maximum pressure, and the HPZ average pressure and contact area. The final image is shown in Figure 2-29.

2.16.5 Pressure-sensing technology calibration and accuracy

The pressure-sensing technology was calibrated in an MTS testing frame in a cold room where the ambient air temperature was -2 °C. Five sensor strips, each 8 cm in length, were placed touching side-by-side on a thick acrylic slab (50 mm thick). A thin sheet of the

opaque white plastic film (Monokote™, same as in the Impact Module) was loosely situated between the acrylic strips and the acrylic slab to highlight the contact width during loading. A thin stainless-steel sheet (same type as in the Impact Module) covered the strips. An aluminum block, with bottom face dimensions 6 cm x 6 cm, was situated on top of the steel sheet. A 40-layer stack of paper-towel sheets was located between the block and the sheet to enable some degree of surface compliance during loading that ensured a reasonably uniform pressure patch, corresponding to the load divided by the block area. Because acrylic exhibits some recoverable creep during slow loading (on the scale of minutes) we applied the calibration load (155 kN) quickly in a linear ramp spanning 5 seconds. Figure 2-30 shows two images from the calibration, one at the left exhibiting the contact widths of the vertically-oriented strips at a certain load value, and the image at the right shows the contact widths when the load was substantially higher. The mid-height contact widths of the three central pressure-sensor strips, where the indicated pressure was very uniform, were determined at time intervals of ~ 0.24 s in the load/pressure record.

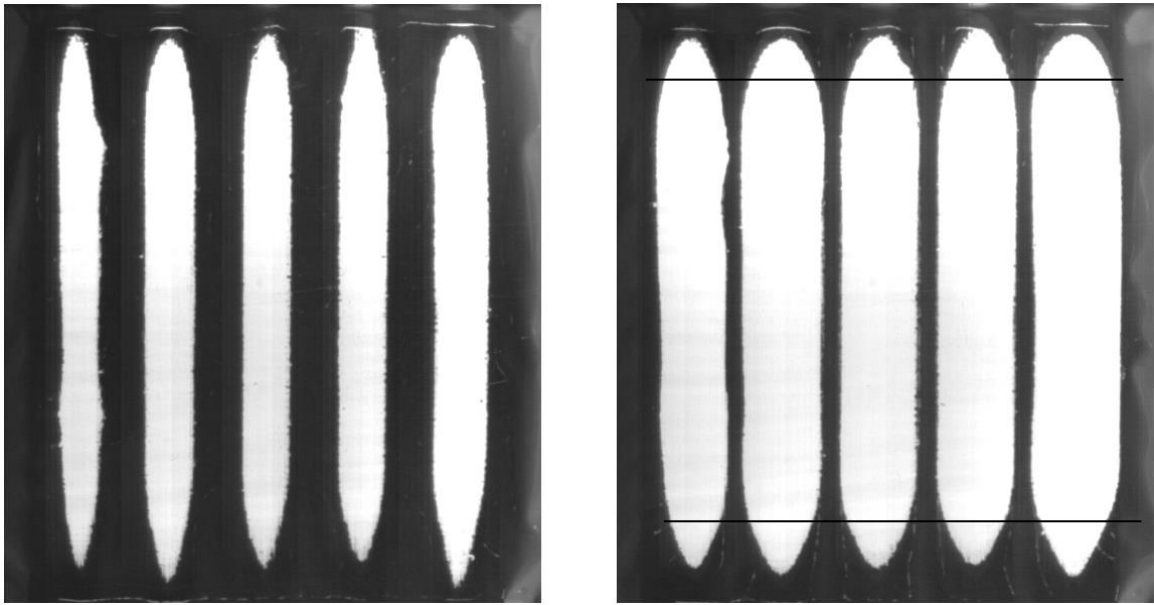


Figure 2-30. Two images from a calibration test conducted for the pressure-sensing technology. The image at the left shows the contact patches (white) created by five vertically-oriented pressure-sensor strips at a certain time during the 5 second ramp when an increasing uniform pressure was applied to the strips. The image at the right shows the same situation at a later time during the ramp when the pressure was significantly higher. The horizontal lines at the top and bottom of the strips indicate opposing edges of the square pressure patch that was applied to the strips.

Figure 2-31 shows the calibration data and the fit to the data (ratio of polynomials). The calibration shows a hysteresis effect of about 12%, where the ascending portion corresponds to the solid line and solid circles, and the descending portion is the dashed curve.

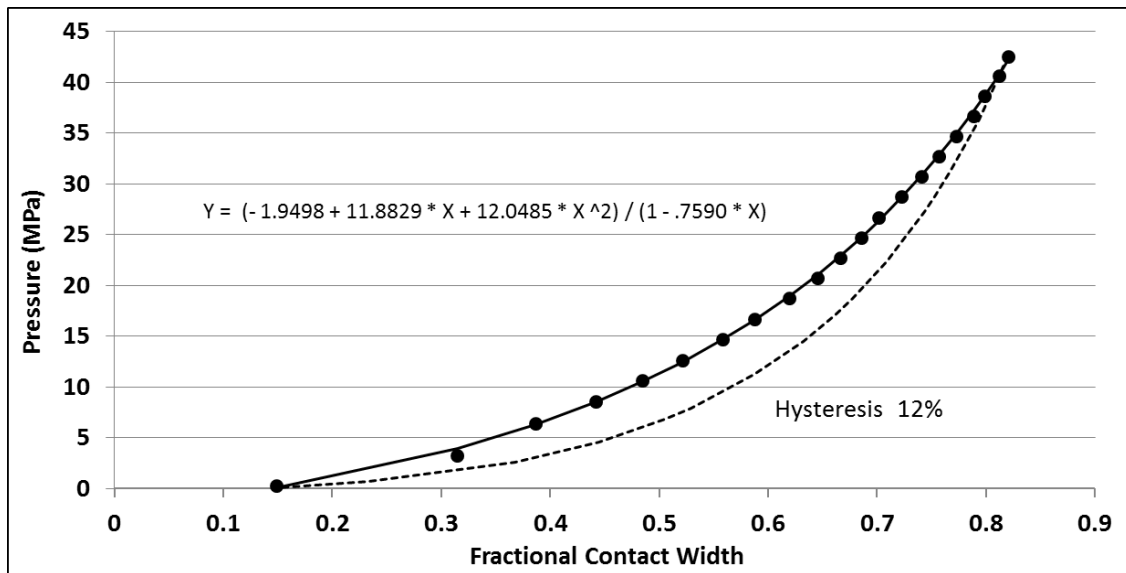


Figure 2-31. Calibration data (solid circles) and fit curve (solid line) for the pressure-sensing technology. The data were acquired during the ascending linear portion of the loading ramp that was applied during the calibration. The dashed curve corresponds to the output from the pressure-sensor strips during the descending linear unloading ramp.

An earlier calibration, at a much lower loading rate conducted over several minutes, also showed hysteresis of about 12%. We have used the data from the ascending portion of the calibration data set to obtain the fit curve shown on the plot for three reasons. The first reason is that while the earlier and present calibration data show the same hysteresis, we cannot be sure that there is the same (or indeed any) hysteresis at loading rates associated with the actual ice impact tests, that are three orders of magnitude faster. Note that there is no feasible way to conduct a calibration at such rates. Secondly, since most of the ice crushing in these impact tests occurs during the generally-increasing-load portion of the tests, it makes sense to use that portion of the calibration data set for the fit that is used to generate the pressure data. Thirdly, as we see in other sections of this paper, we cannot discern any attributes in the pressure data that would suggest error associated with our

decision to use the ascending-load calibration data, or hysteresis. That is, the integrated-pressure load records we obtained match the load-cell records reasonably well, even in the instances where there is a sharp rise in load immediately followed by a sharp drop in load, such as at the peak loads in the records for tests Dec10_2015, June27_2014 and Dec15_2014. In a similar vein, the agreement of the present HPZ average pressure and contact area values with other field and lab tests, and with the pressure data from the central pressure-sensing plug of the Impact Module, further attests to the accuracy of the calibration equation.

The reader will note that at the top and bottom ends of the pressure-sensor strip contact patches we see a rounded portion of contact that actually extends beyond the 6 cm edge length of the aluminum block by about 6.5 mm. We have drawn two horizontal lines on the right image to indicate the edges of the block. These small extensions of the contact area are due to the flexural strength of the pressure sensor strips and, to a lesser extent, the flexural strength of the stainless-steel sheet that tends to spread the applied load slightly. The net result is an averaging effect in the pressure measurement at any point along the length of the strip due to the mutual influence of adjacent strip material up to 6.5 mm on either side of that point. Hence, at any point along the strip the pressure reading represents the average of the actual pressure over a patch area that is the width of the strip (13 mm) times twice the influence length ($2 \times 6.5 \text{ mm} = 13 \text{ mm}$). Therefore, we may consider the spatial resolution of the technology in this configuration to be $1.3 \text{ cm} \times 1.3 \text{ cm} \approx 1.7 \text{ cm}^2$. The automated data analysis technique (above) obtains pressure measurements at 0.42 mm increments along each pressure-sensor strip, that is, at each pixel in the resized image, amounting to many thousands of measurements for the whole sensing surface.

The pressure measurement range for the technology is approximately 0 – 60 MPa. The smallest pressure that can be measured is about 0.31 MPa. The absolute accuracy of pressure measurements is dependent on the magnitude of pressure, according to the non-linear calibration curve Figure 2-31. The cause of the variable absolute accuracy of pressure data is the fixed pixel dimensions of the resized images when applying the non-linear calibration curve. This causes measurements to occur in a stepwise fashion associated with changes of the contact width that occurs in pixel-by-pixel increments in the resized images. For example, if measurements span a range of 50 MPa to 5 MPa, the size of the steps correspondingly ranges from 6 MPa down to 1 MPa. The net effect is that the pressure measurements, in this range, have an average relative accuracy of $\pm 7\%$. Hence, one may notice ~ 6 MPa steps in the plots of maximum pressure at the high values around 50 MPa, whereas for lower pressures the steps are correspondingly smaller in height and not as noticeable. Higher resolution images would reduce the dimensions of the pixels and reduce the associated step heights. These step effects apply to single point measurements (i.e., as in the plots of maximum pressure), where the area per measurement is 13 mm x 0.42 mm (i.e. 31 pixels x 1 pixel), and are much less noticeable for average pressures over either HPZ or LPZ areas that encompass many single point measurement areas with various step magnitudes.

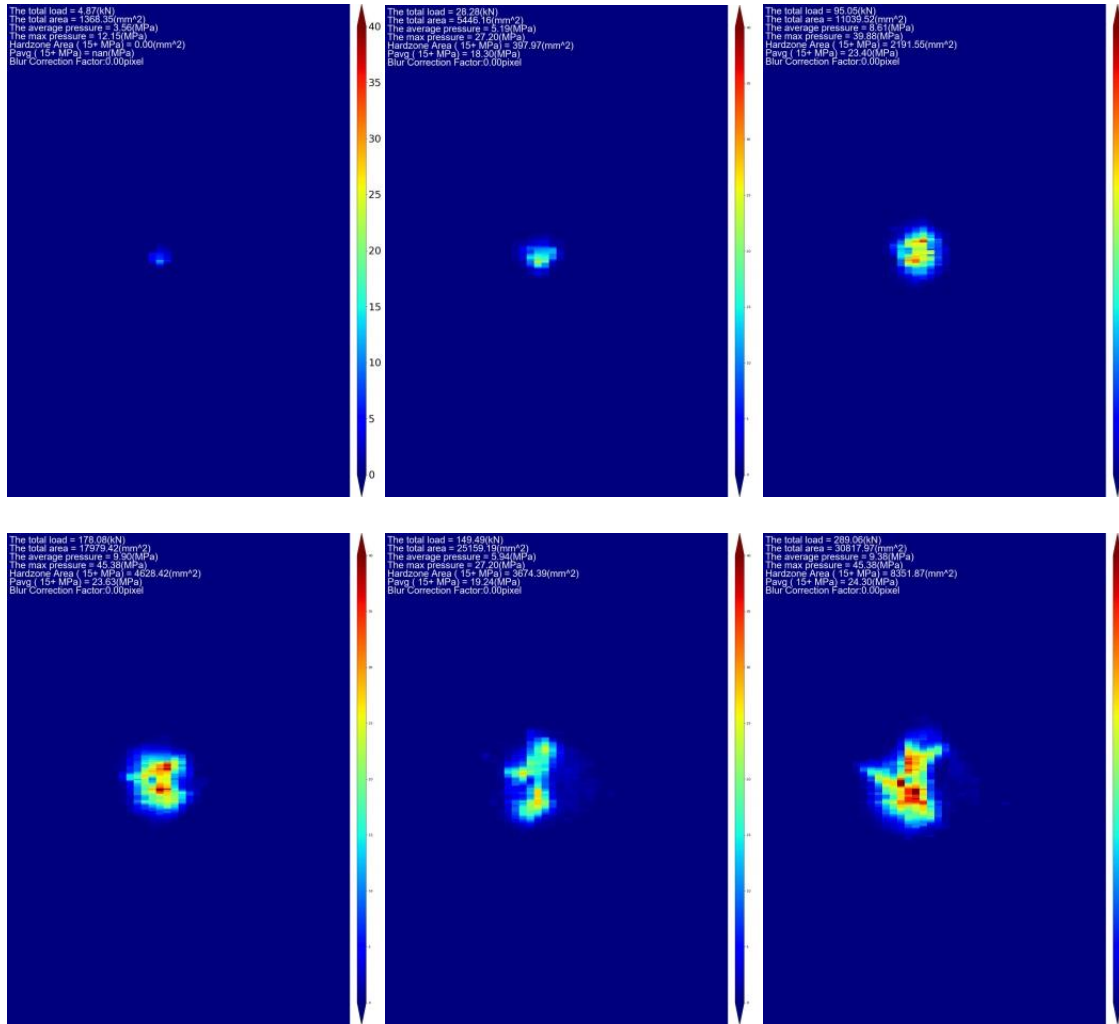
There are many instances in the pressure data records where substantial pressure (up to ~ 10 MPa) registered at a location along a pressure-sensor strip and where an adjacent strip does not register any pressure. One might expect that the thin steel sheet would exert some force on the adjacent pressure-sensor strip due to its flexural strength, however this does

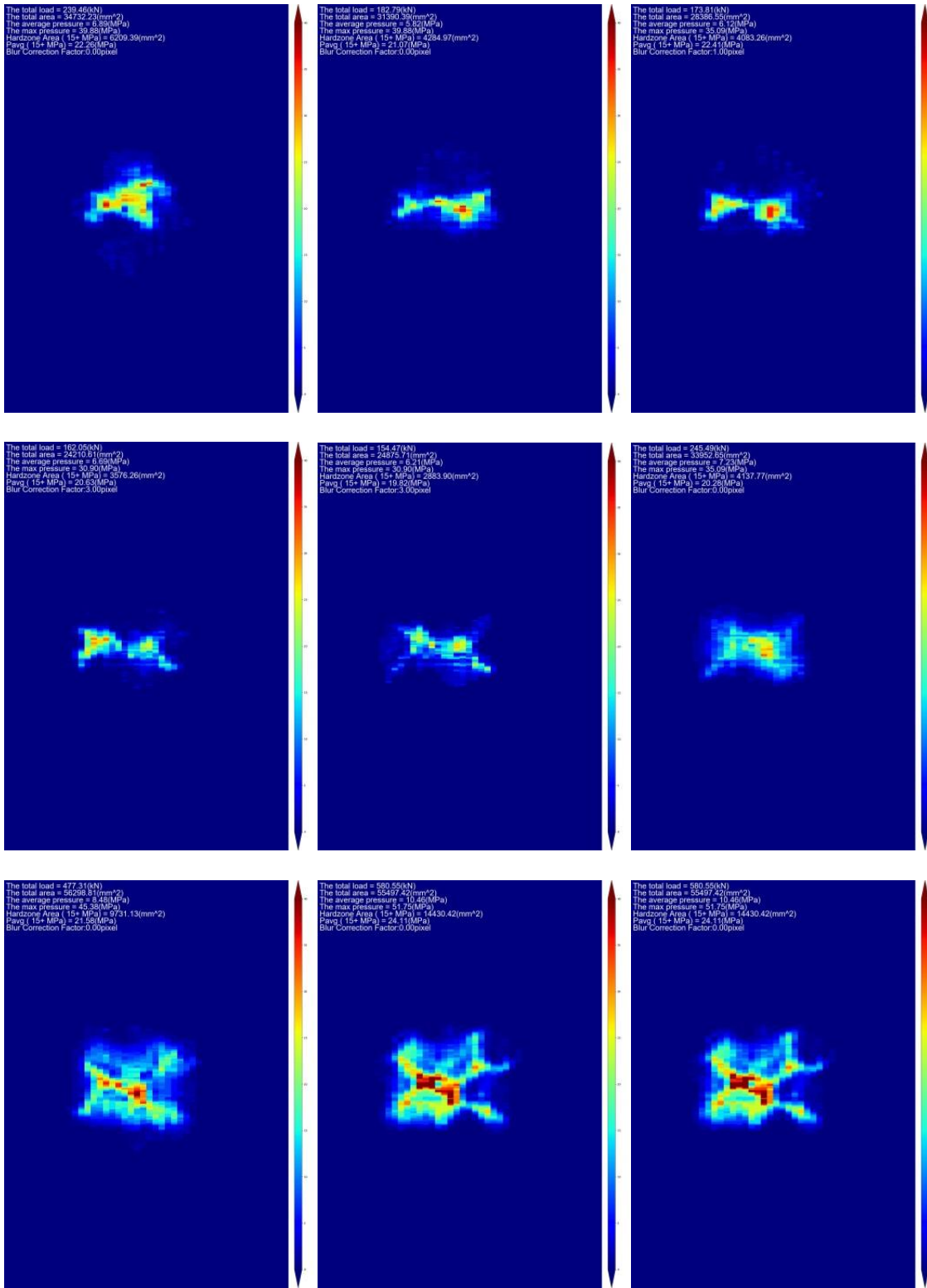
not happen because the construction of the Impact Module is such that the sheet is very slightly raised above the pressure-sensor strips (by about 0.2 mm) when no load is applied. The sheet is also pinned at its edges with many small bolts to the large acrylic block (Figure 2-4). That is why no pressure is indicated anywhere on the panel prior to ice contact. If pressure is applied to one strip the slightly raised aspect of the sheet above the strips, and the effect of its pinned edges, apparently is enough to prevent the sheet from applying load to the adjacent pressure-sensor strip. We have reproduced a similar effect in a desktop demonstration where a series of eight 7 cm pressure-sensor strip portions were placed side-by-side under the same type of steel sheet and load applied to a 25 mm long x 7 mm wide patch at the mid-width of one strip. The square steel sheet was raised at two opposing edges of the array of strips by about 0.3 mm by two layers of adhesive tape. Pressure (~ 12 MPa) was indicated only by the strip that was primarily loaded, and no pressure signal was indicated by the two adjacent pressure-sensor strips. However, removal of the elevating tape layers at the edges of the sheet led to a slight but noticeable signal showing up on the adjacent pressure-sensor strips. From these considerations we conclude that crosstalk between adjacent pressure-sensor strips was not an issue during the ice impact experiments.

2.17 Appendix B

2.17.1 (Test: May8_A+B_2014) –

Note: Full-resolution images are available on request for all tests.





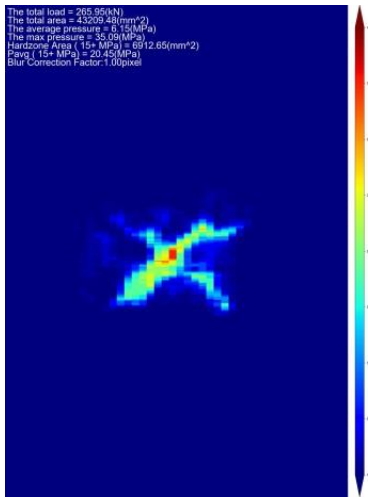
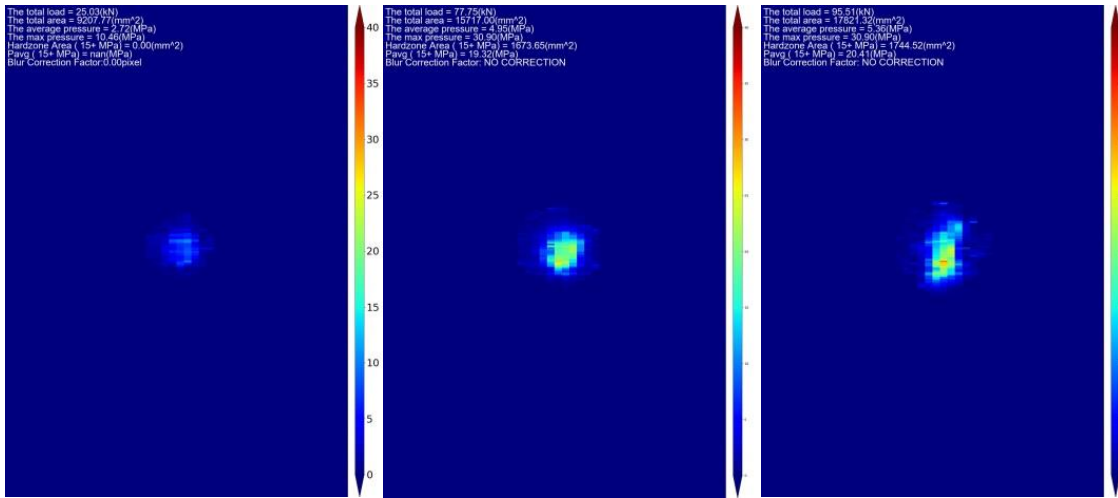
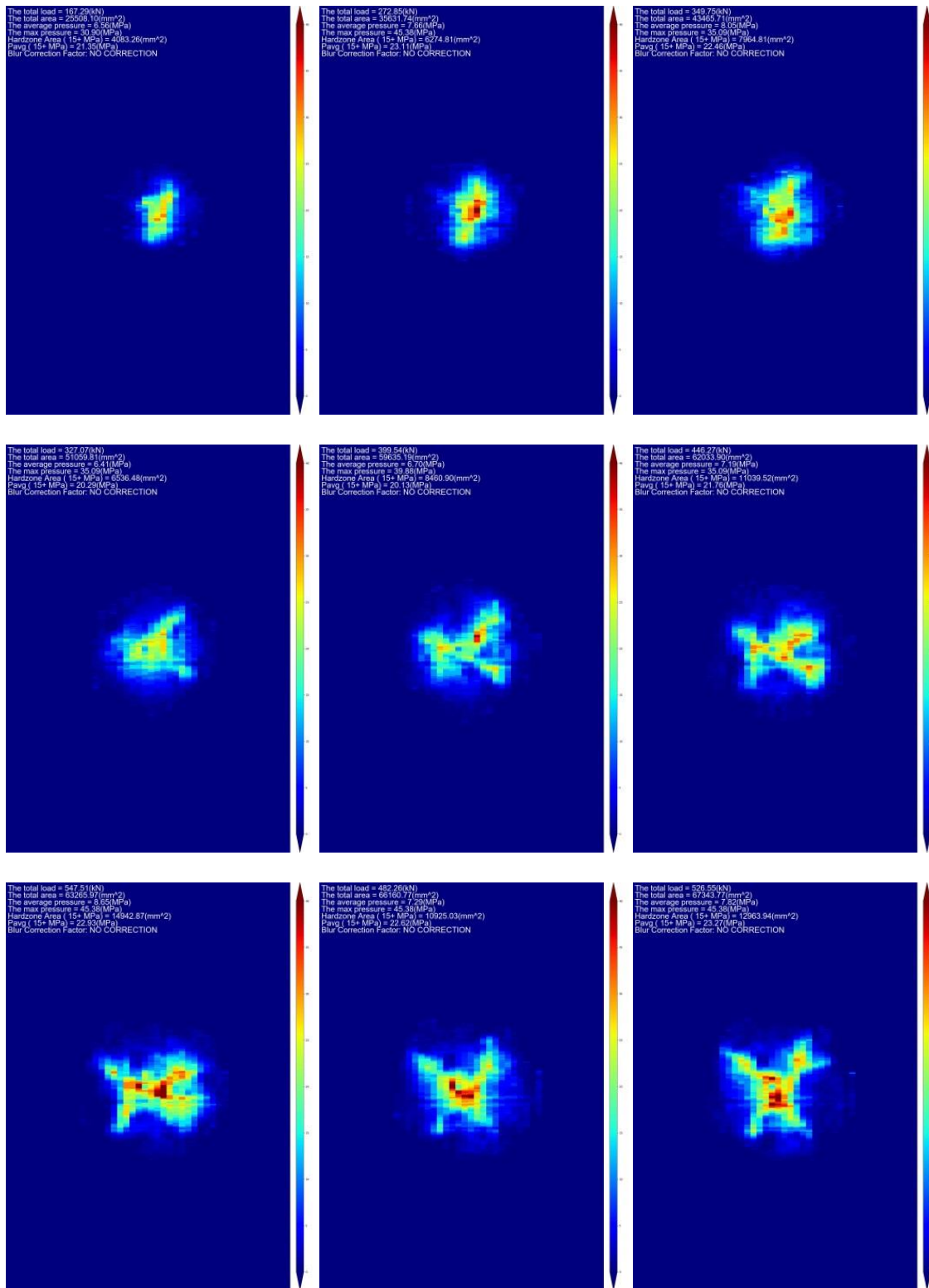


Figure 2-32. Sequence of pressure-pattern images from test May8_A+B_2014. The images run from left to right in each row from top to bottom. The capture rate was 250 images/s. The width of a blue box is ~ 60 cm.

2.17.2 (Test: May22_2014)





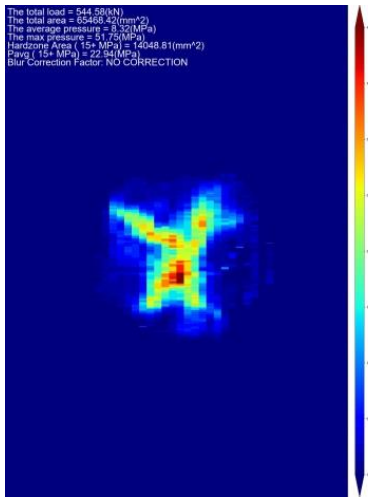
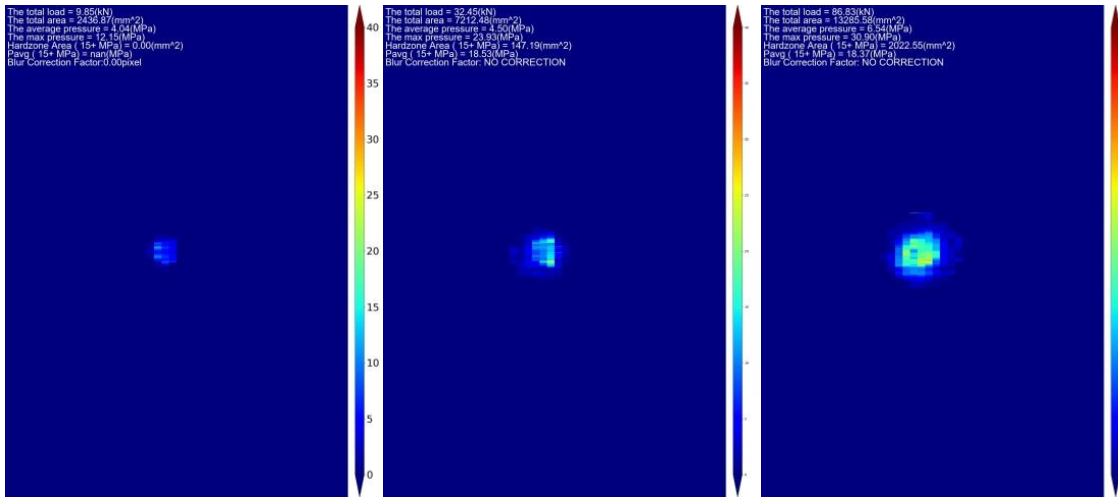
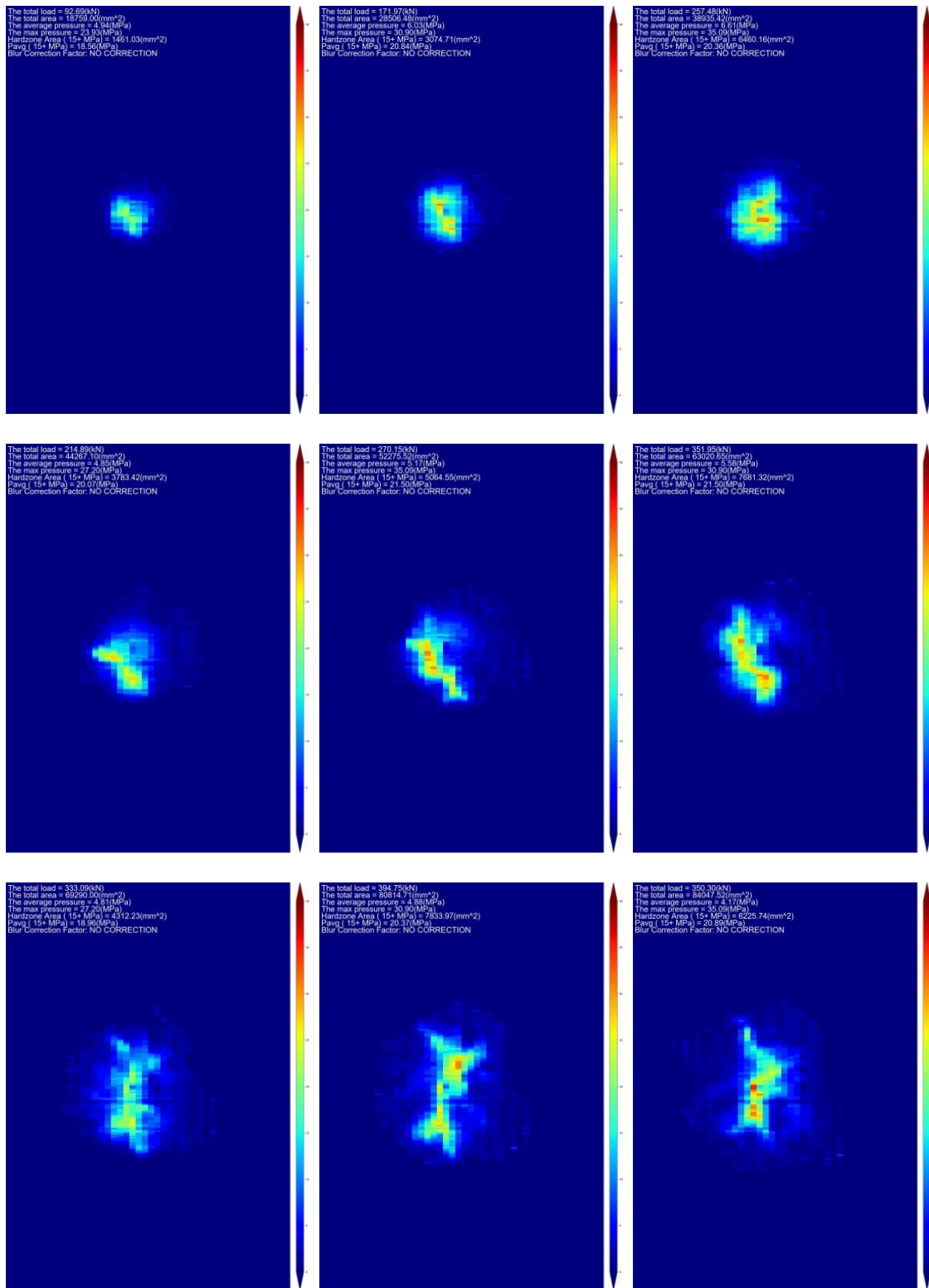


Figure 2-33. Sequence of pressure-pattern images from test May22_2014. The images run from left to right in each row from top to bottom. The capture rate was 500 images/s. The width of a blue box is ~ 60 cm.

2.17.3 (Test: Dec10_2015)





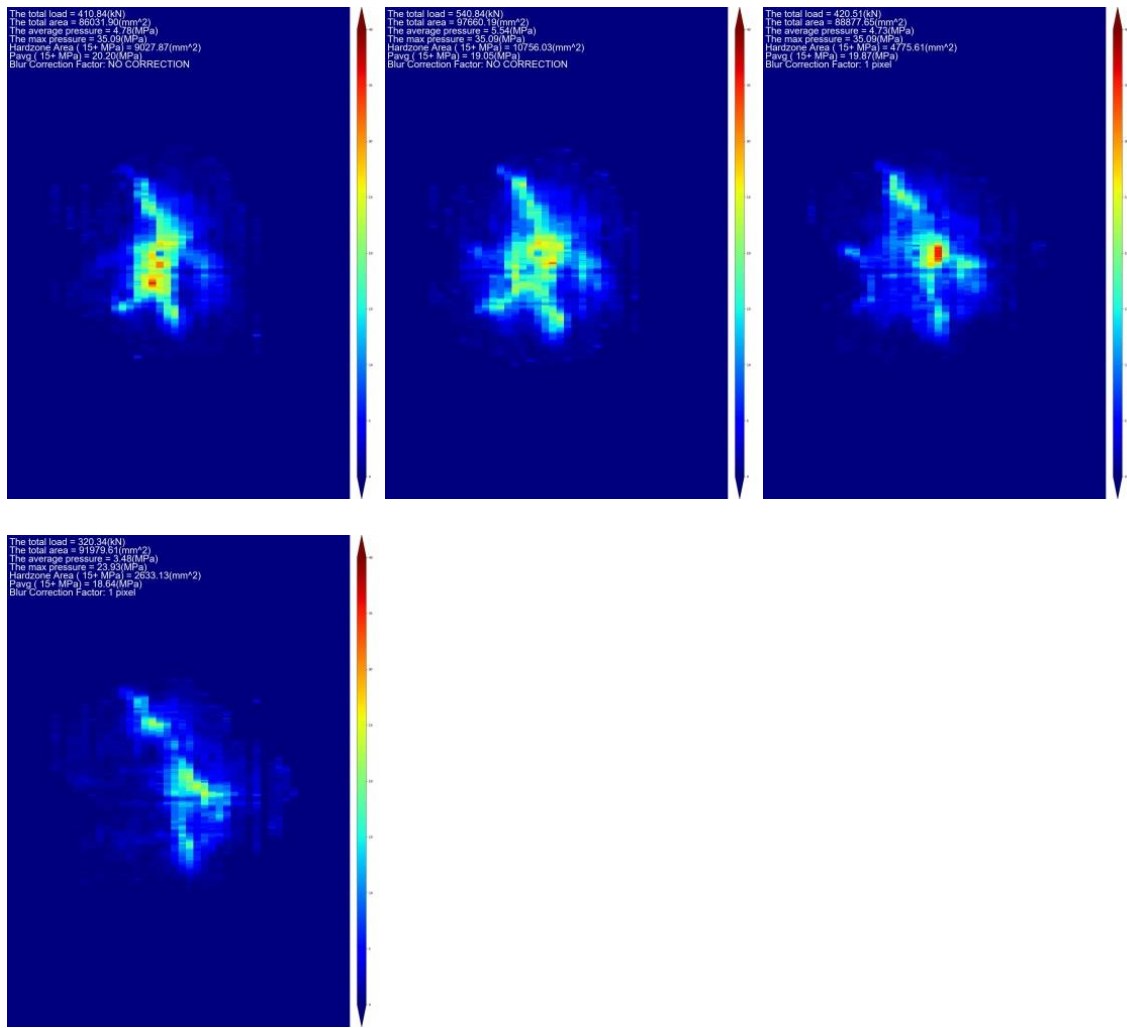
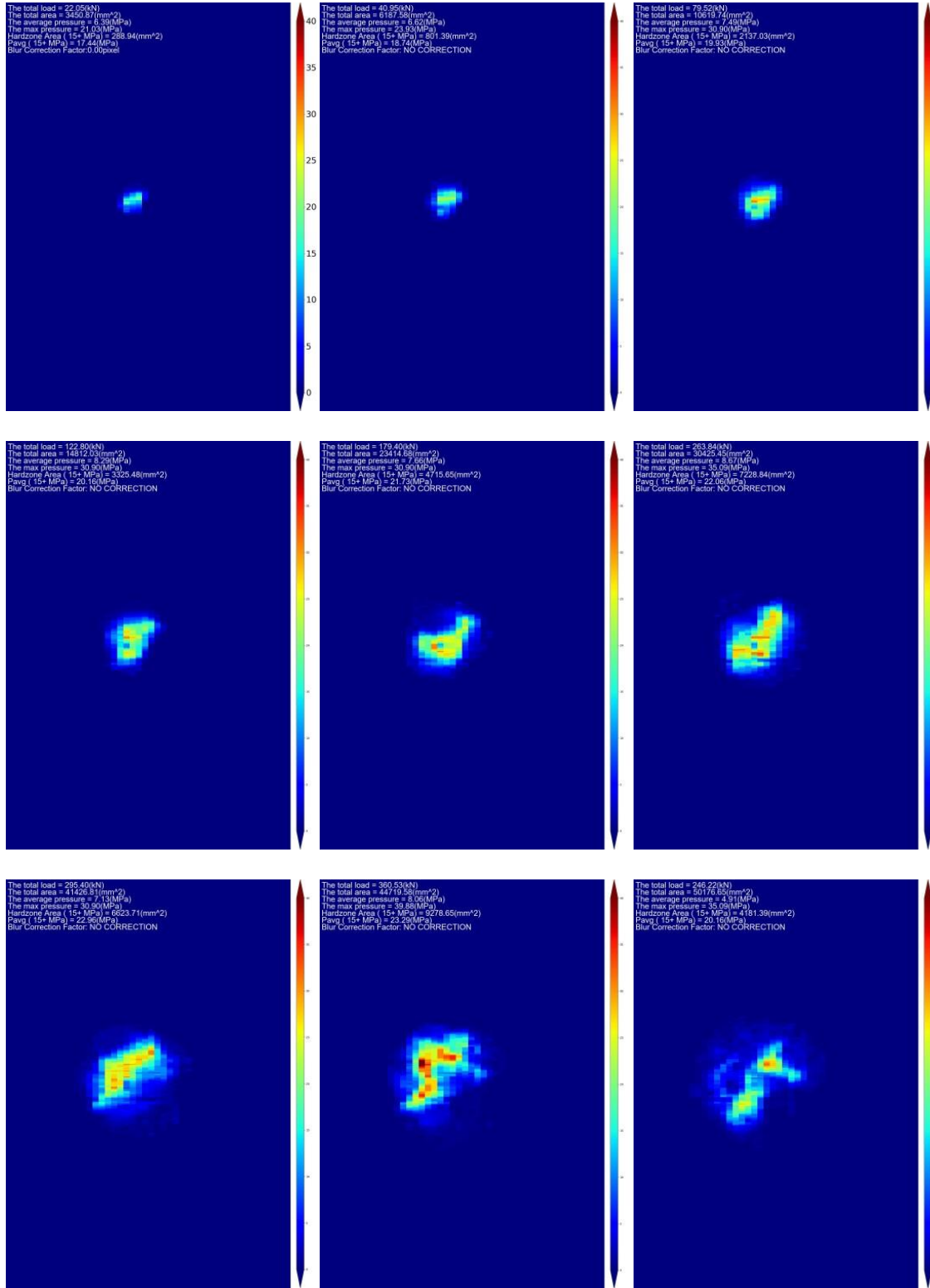


Figure 2-34. Sequence of pressure-pattern images from test Dec10_2015. The images run from left to right in each row from top to bottom. The capture rate was 500 images/s. The width of a blue box is ~ 60 cm.

2.17.4 (Test: June27_2014)



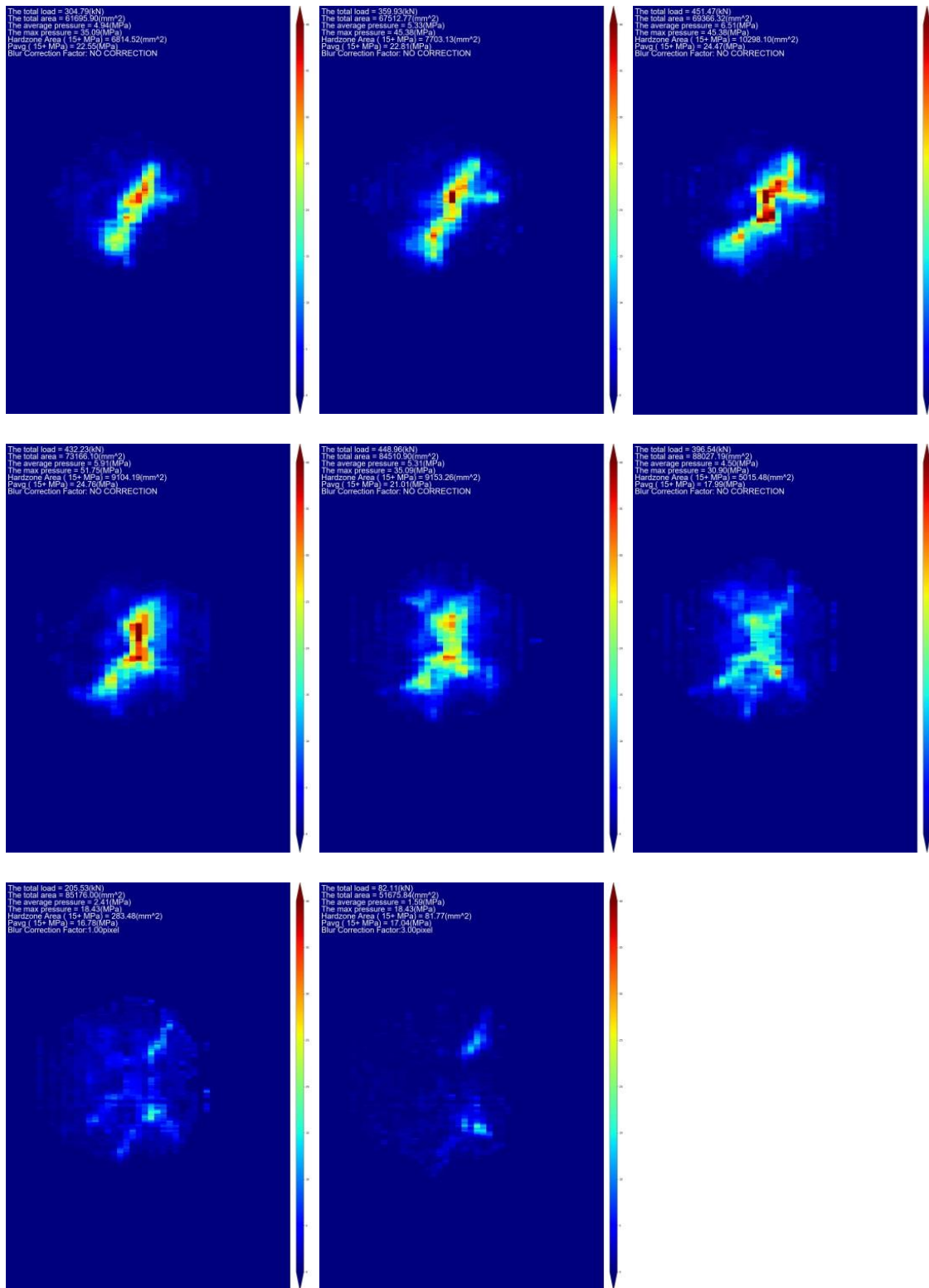
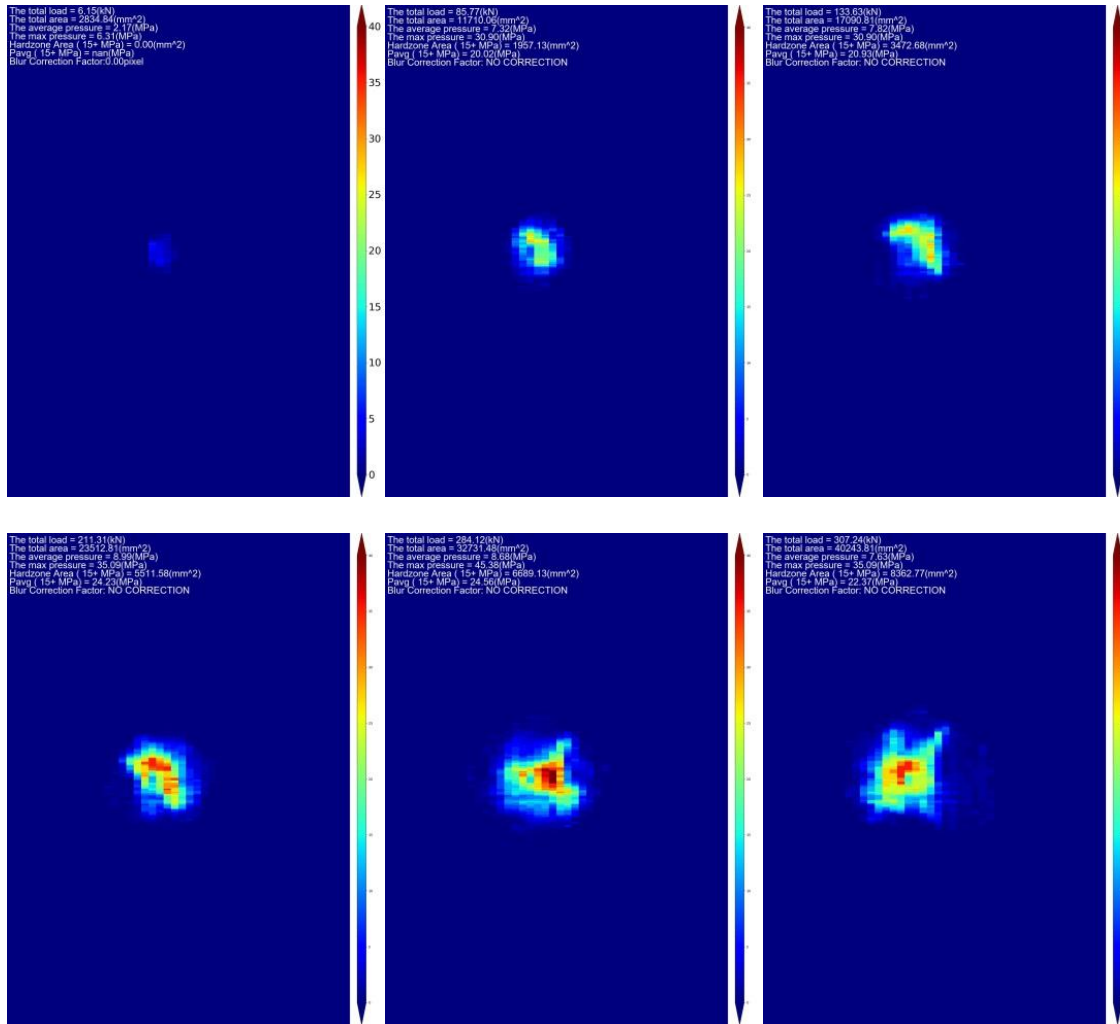
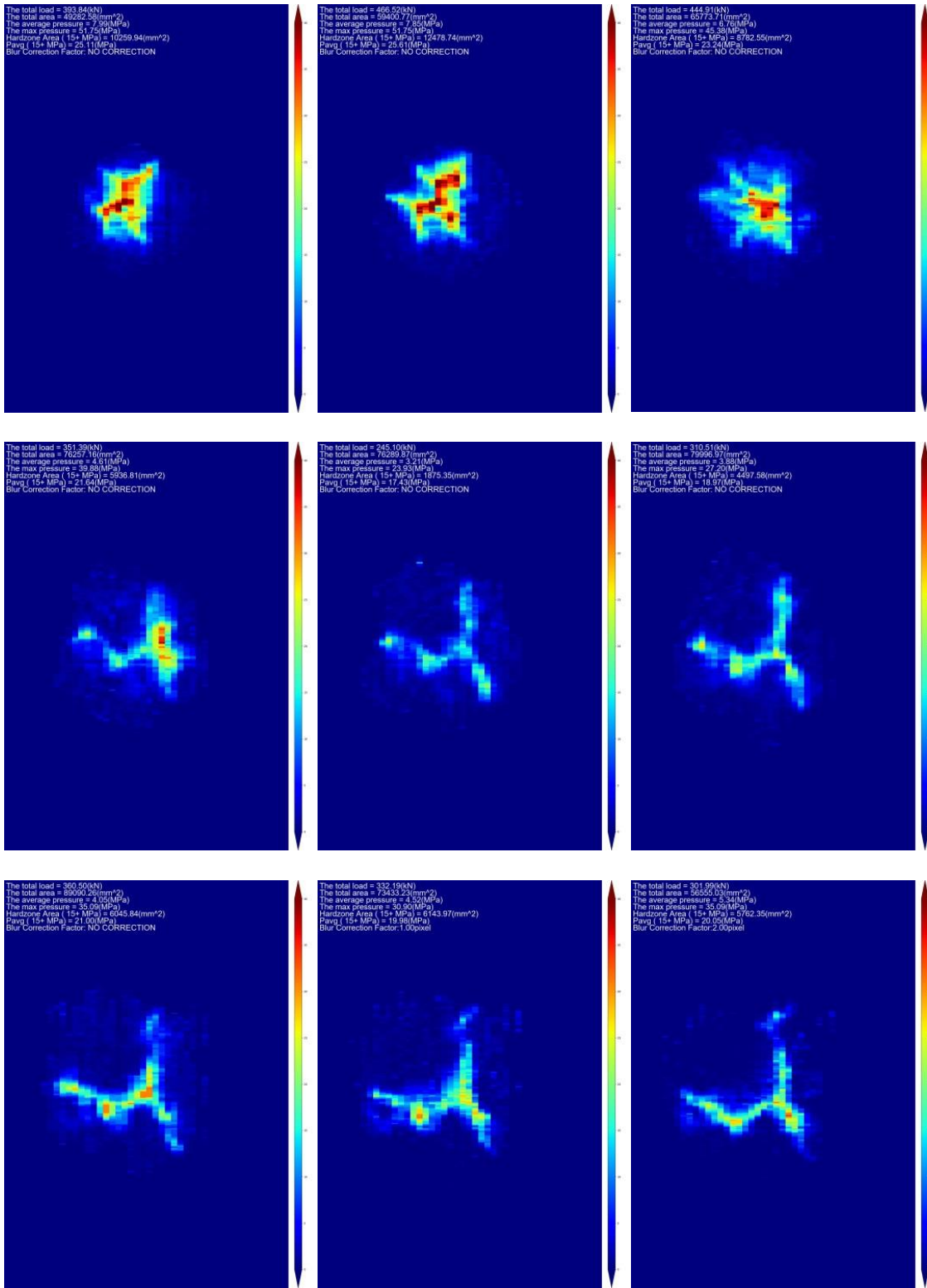


Figure 2-35. Sequence of 17 pressure-pattern images from test June27_2014. The images run from left to right in each row from top to bottom. The capture rate was 500 images/s.

The width of a blue box is ~ 60 cm. There were 19 raw images, but the 17th and 18th were too blurred to process.

2.17.5 (Test: Oct16_2014)





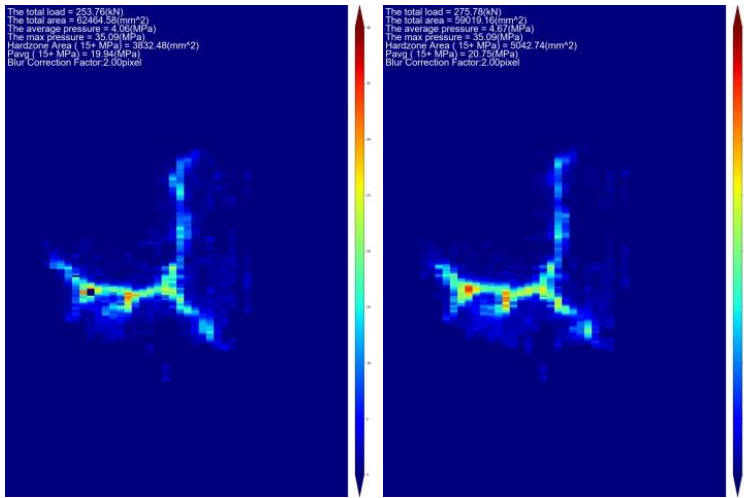
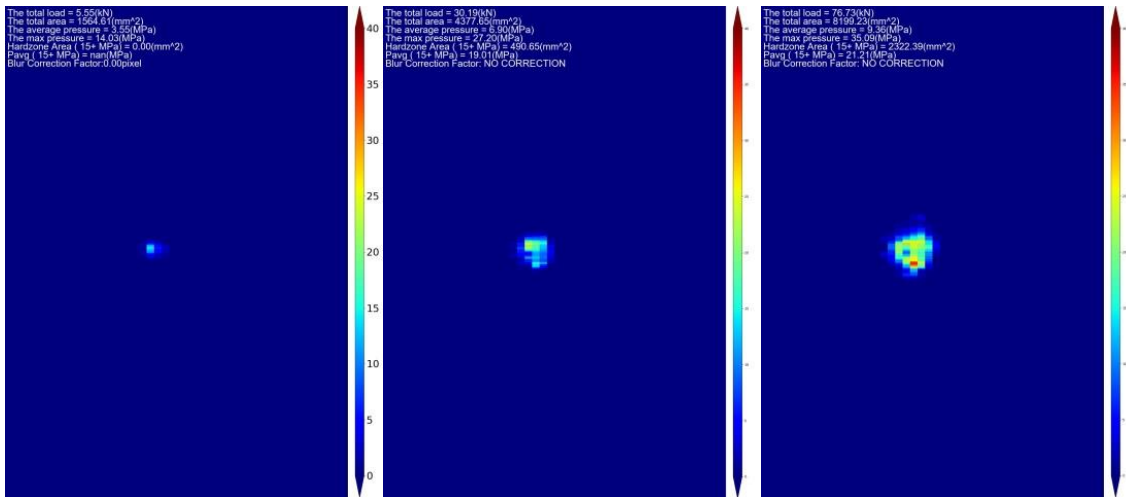
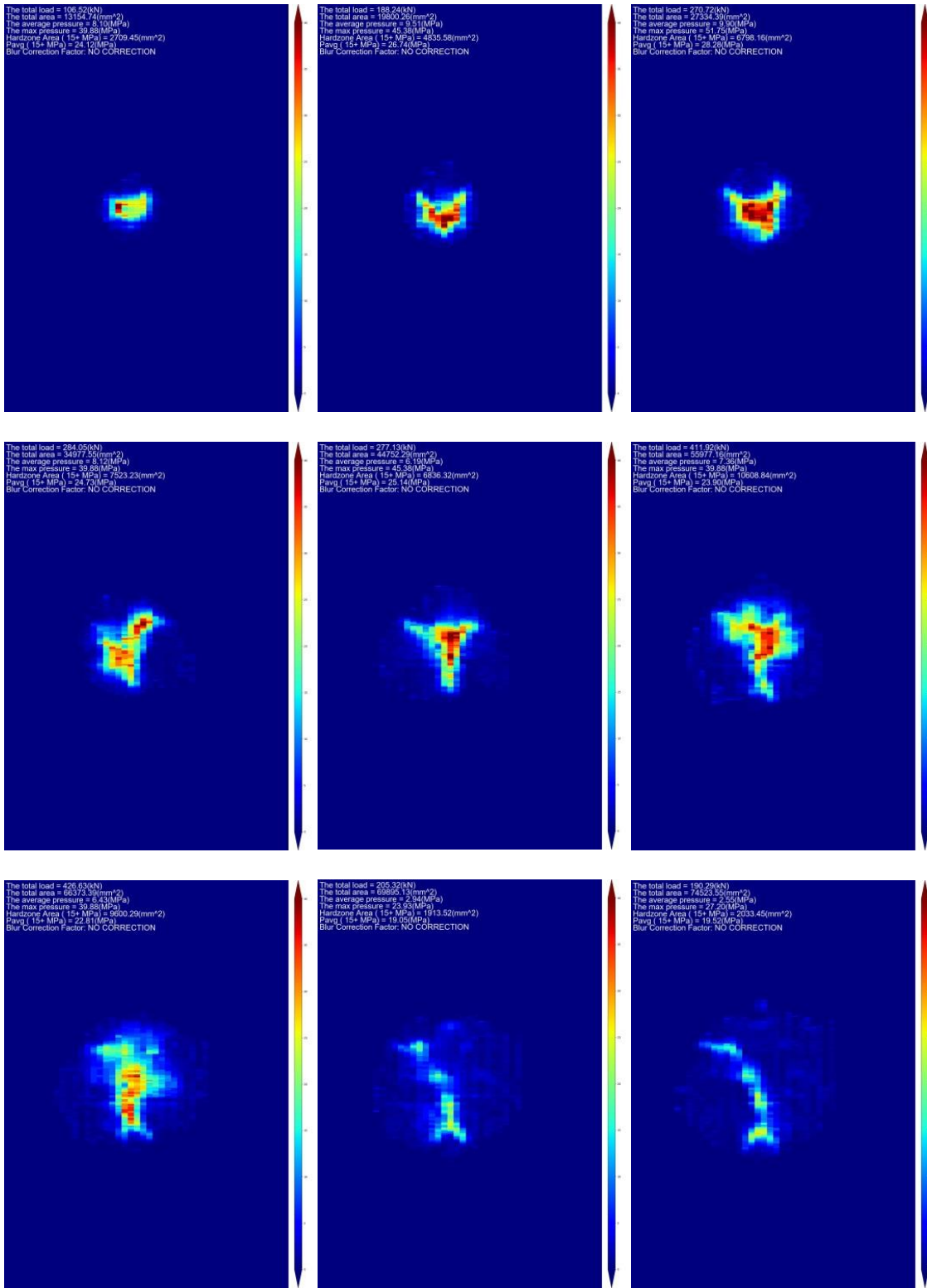


Figure 2-36. Sequence of 17 pressure-pattern images from test Oct16_2014. The images run from left to right in each row from top to bottom. The capture rate was 500 images/s. The width of a blue box is ~ 60 cm. There were 19 row images, but the 16th and 17th were too blurred to process.

2.17.6 (Test: Dec15_2014)





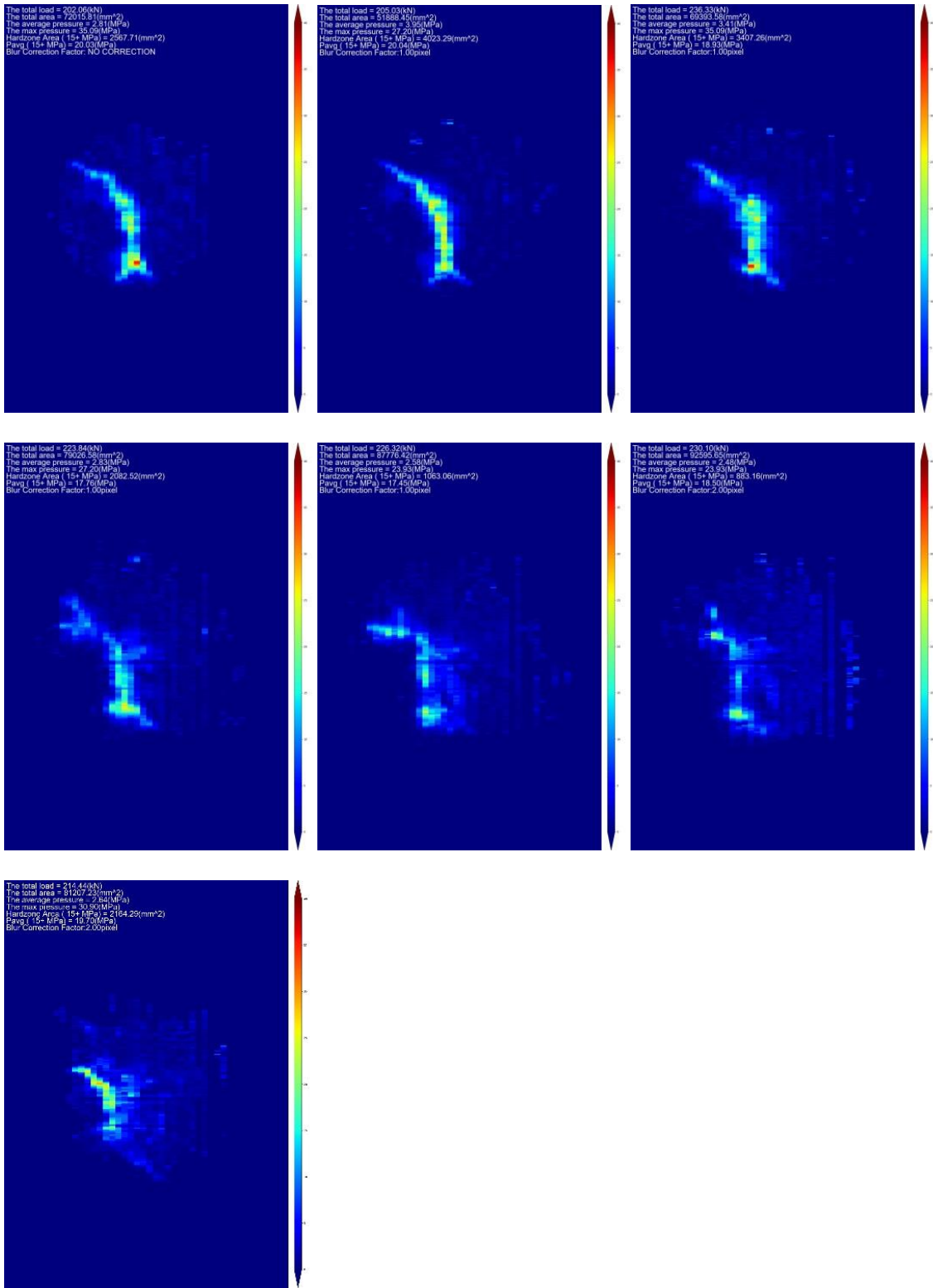
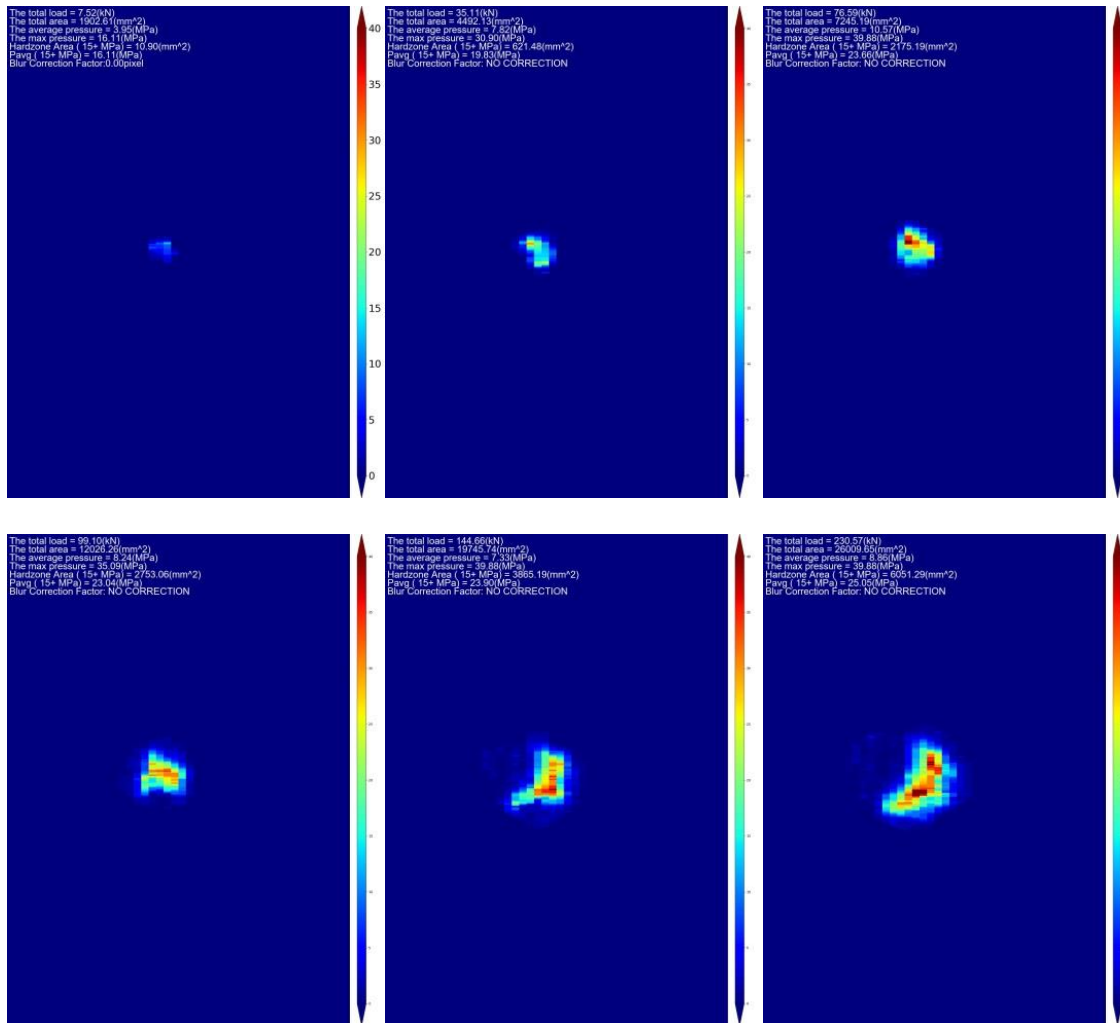
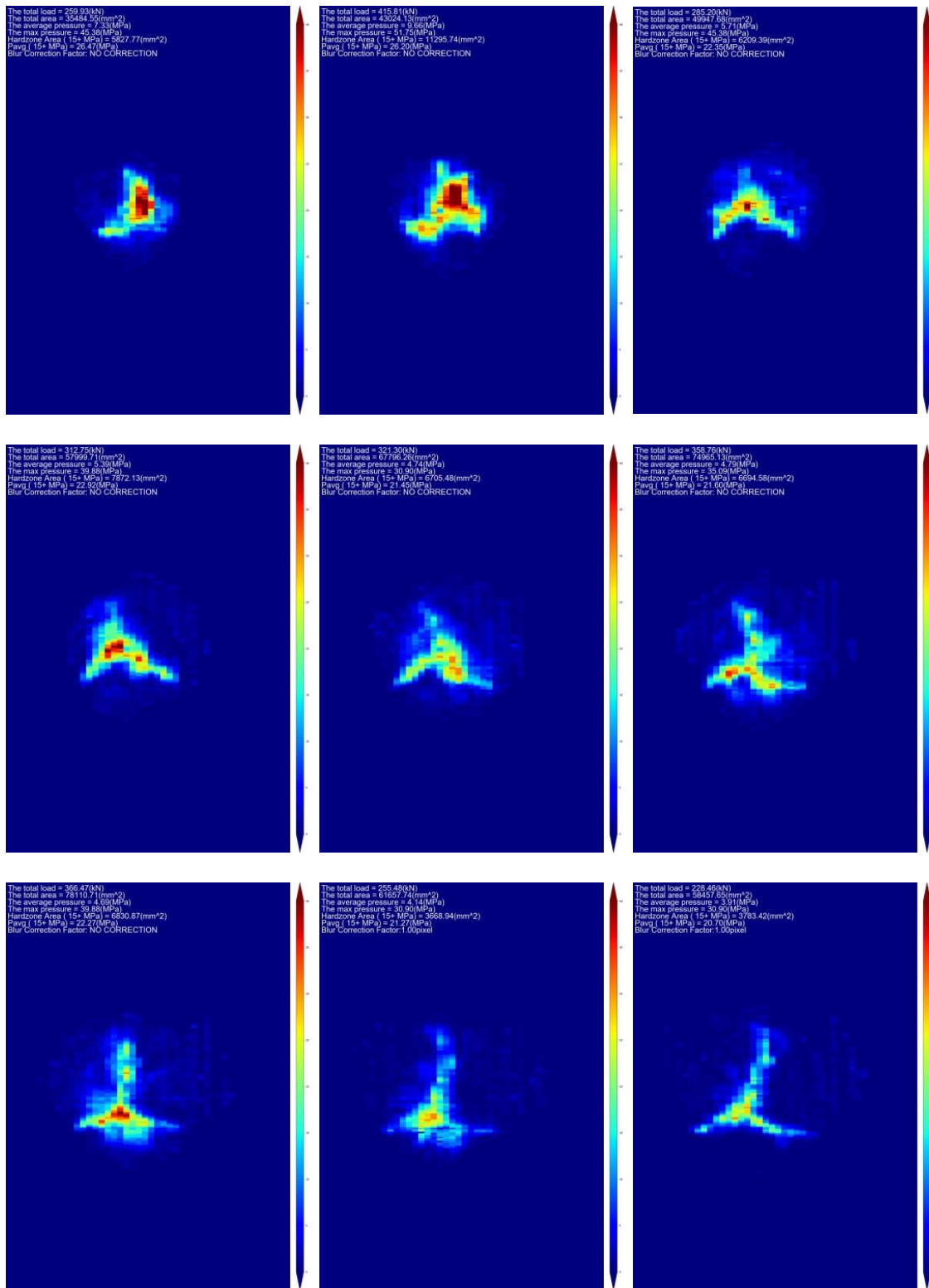


Figure 2-37. Sequence of 19 pressure-pattern images from test Dec15_2014. The images run from left to right in each row from top to bottom. The capture rate was 500 images/s. The width of a blue box is ~ 60 cm. There were 25 raw images but the 19th - 24th were too blurred to process.

2.17.7 (Test: Jan20_2015)





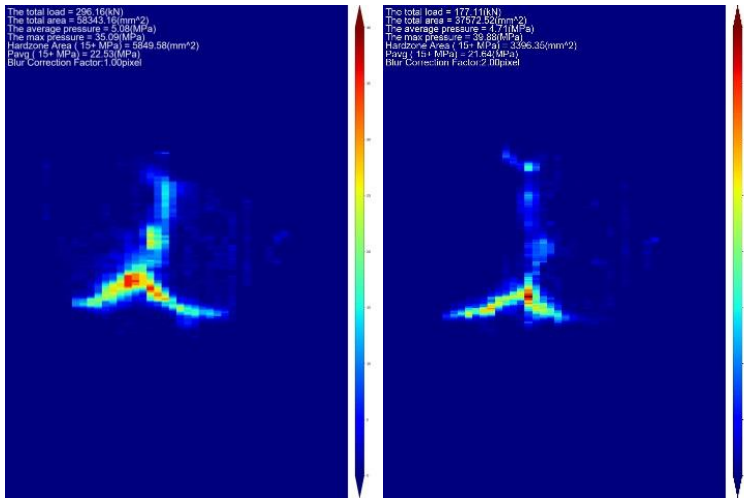
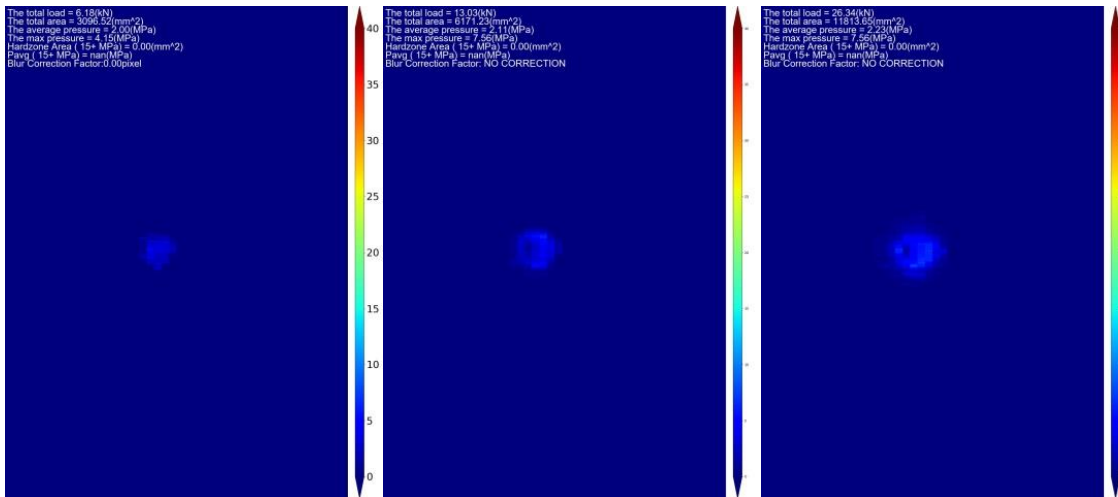
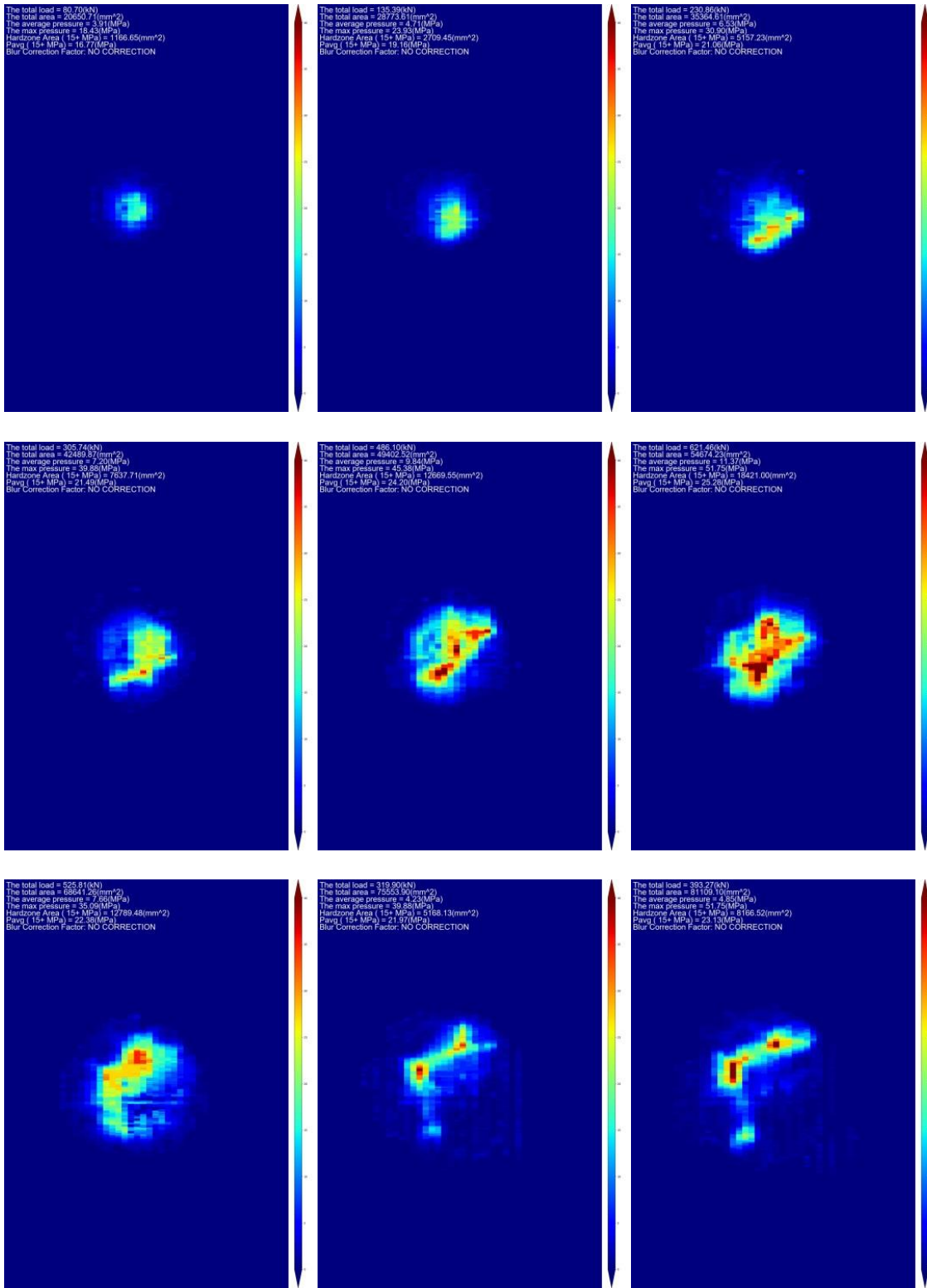


Figure 2-38. Sequence of 17 pressure-pattern images from test Jan20_2015. The images run from left to right in each row from top to bottom. The capture rate was 500 images/s. The width of a blue box is ~ 60 cm. There were 24 raw images but the 17th – 23rd were too blurred to process.

2.17.8 (Test: Feb25_2016)





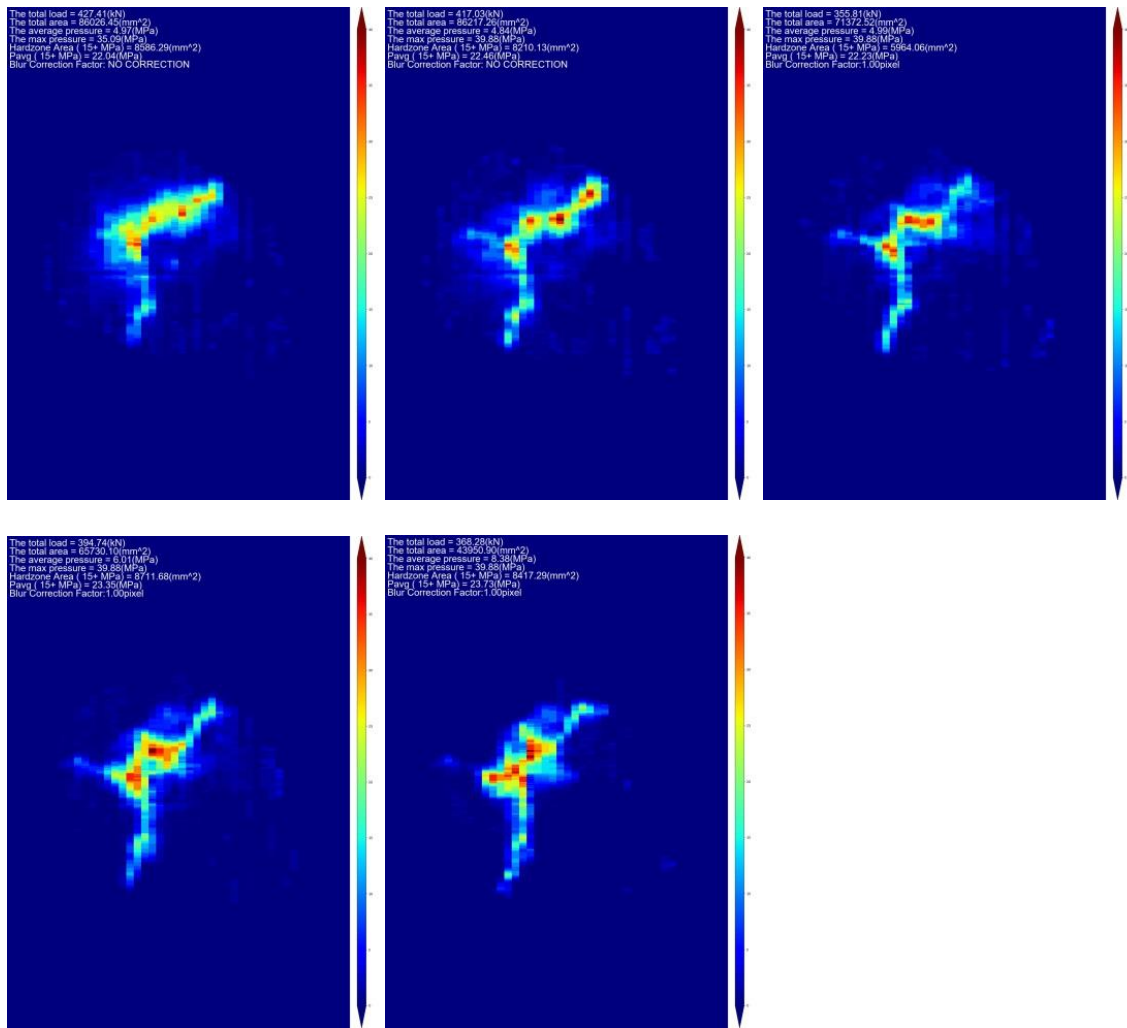
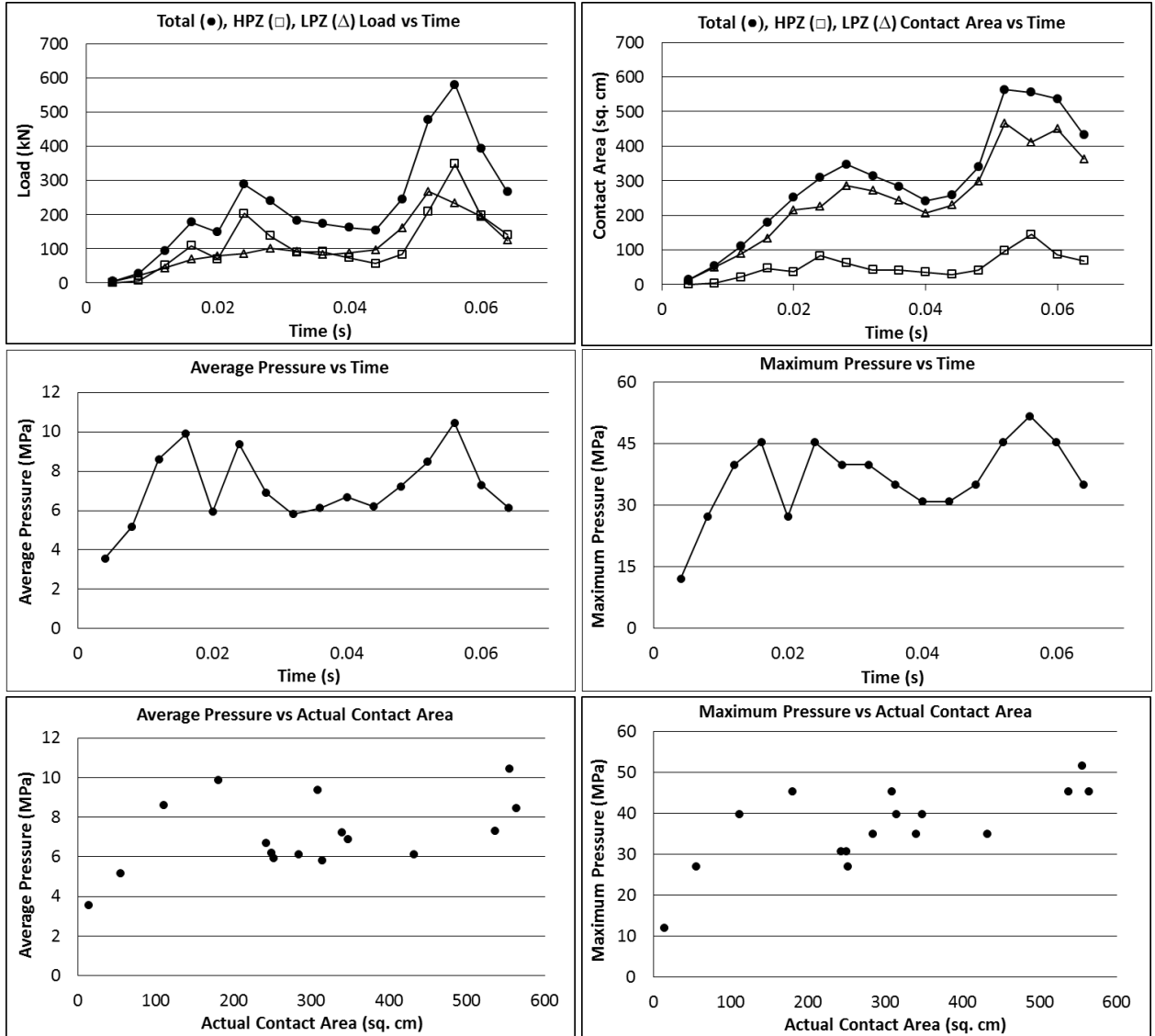
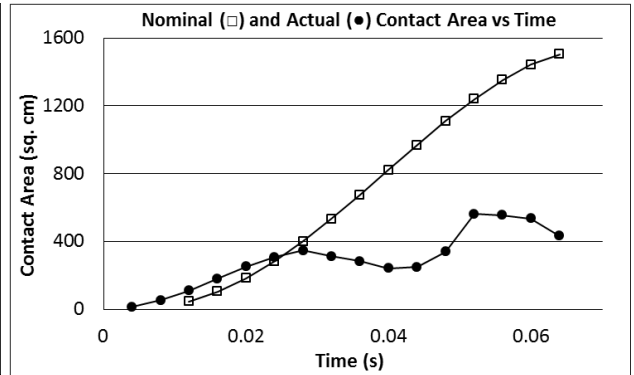
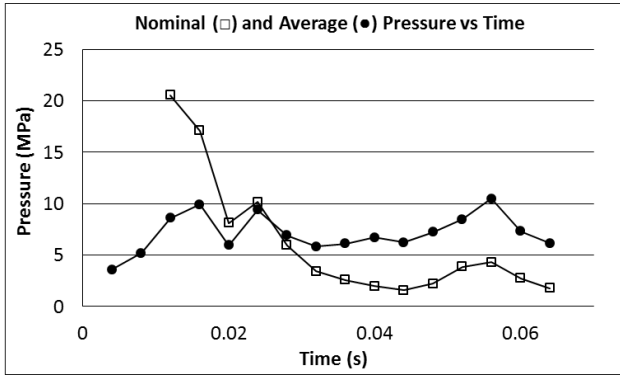
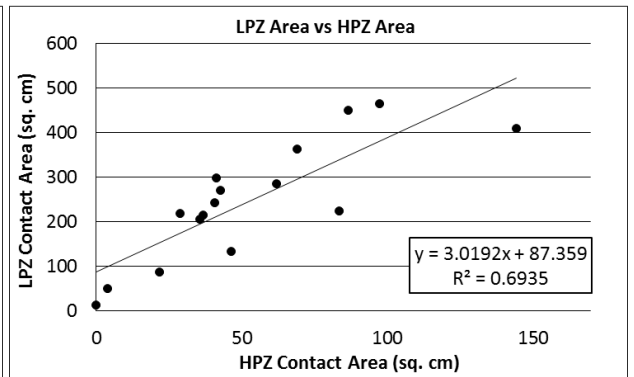
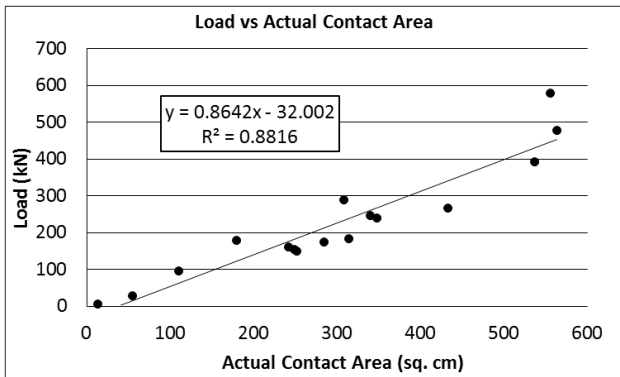


Figure 2-39. Sequence of 17 pressure-pattern images from test Feb25_2016. The images run from left to right in each row from top to bottom. The capture rate was 500 images/s. The width of a blue box is ~ 60 cm. There were 19 raw images, but the 17th and 18th were too blurred to process.

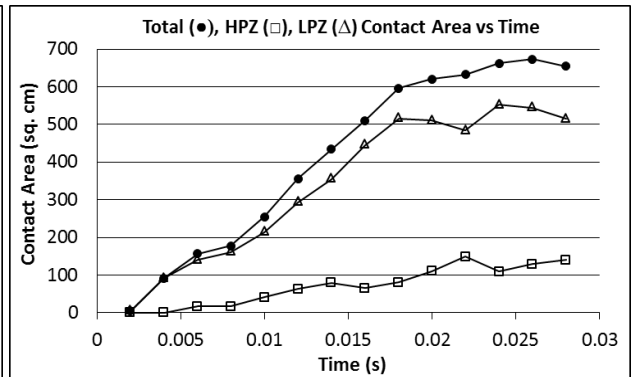
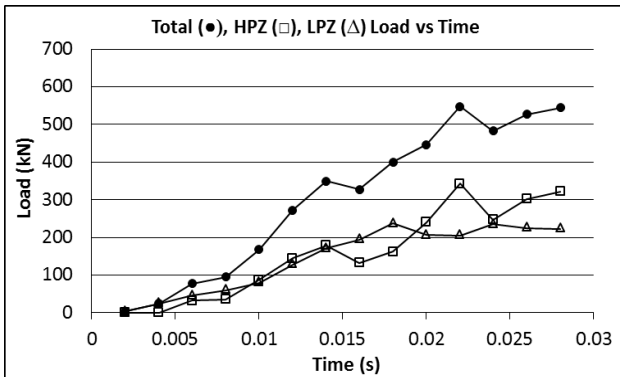
2.18 Appendix C

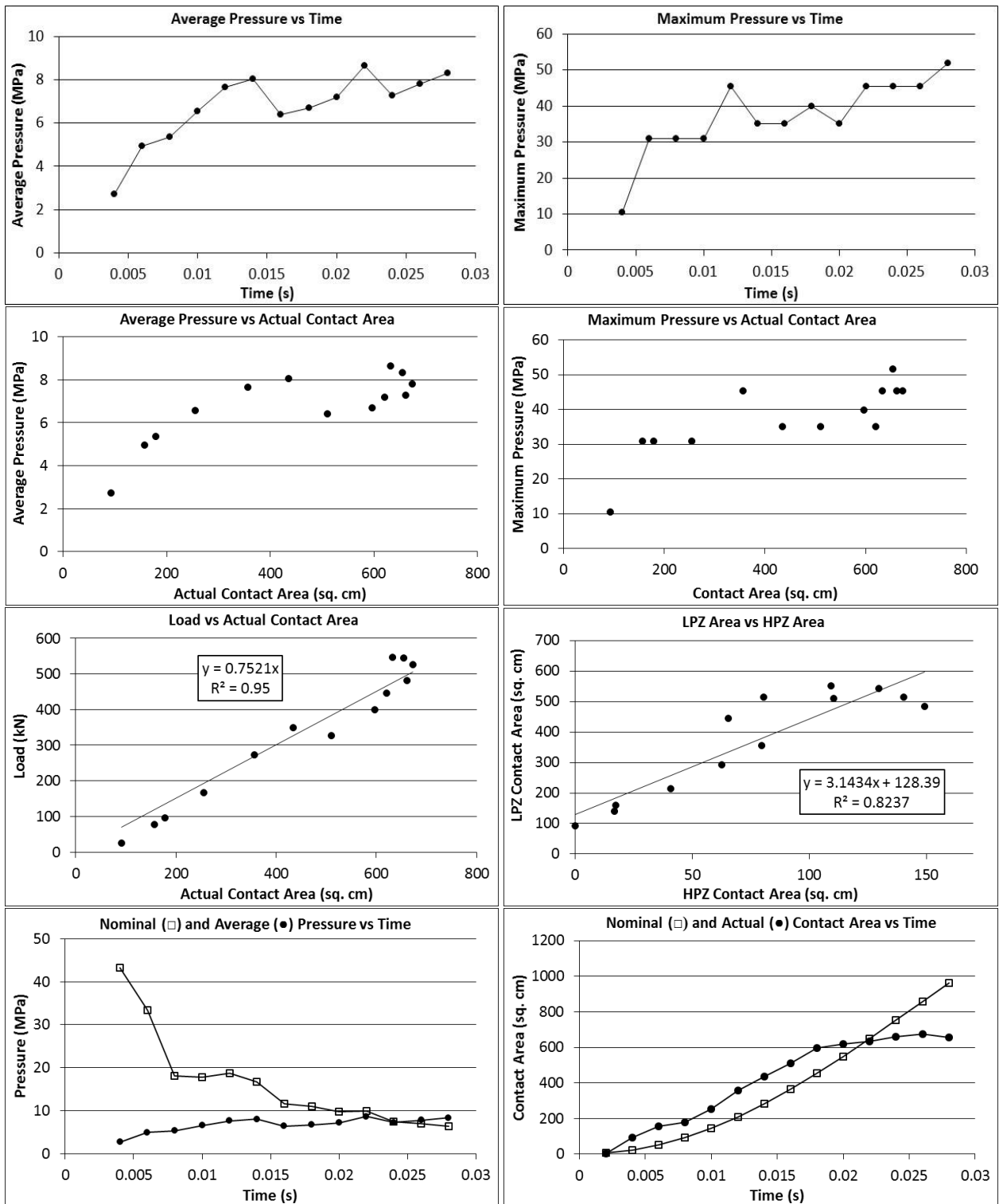
2.18.1 (Test: May8_A+B_2014)



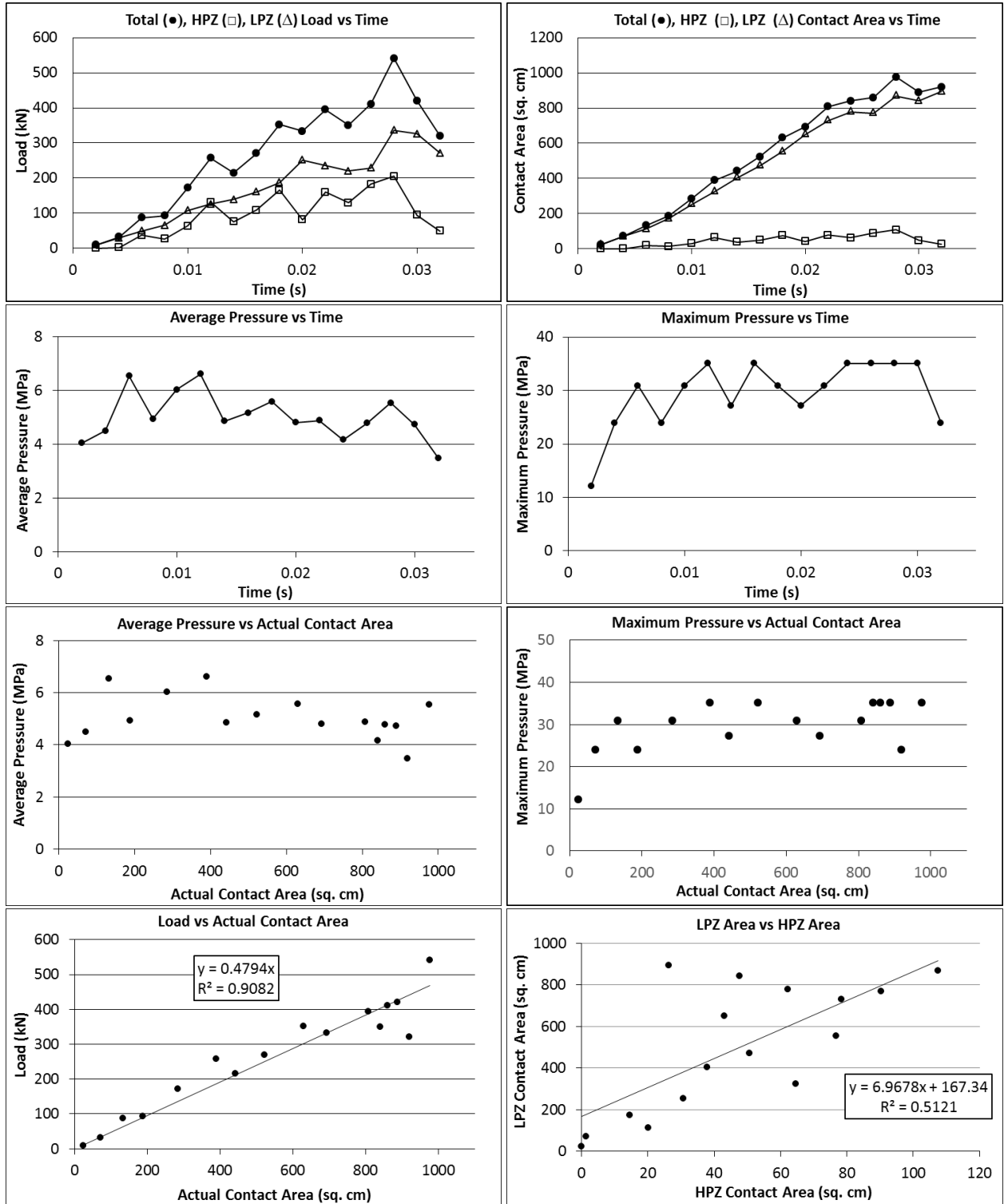


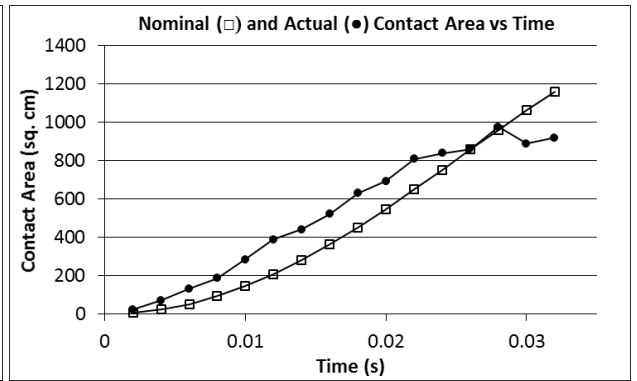
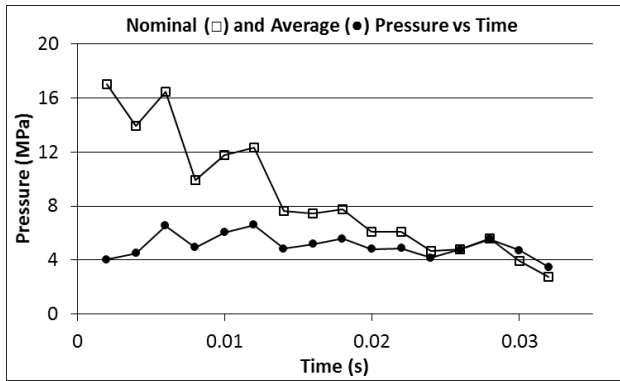
2.18.2 (Test: May22_2014)



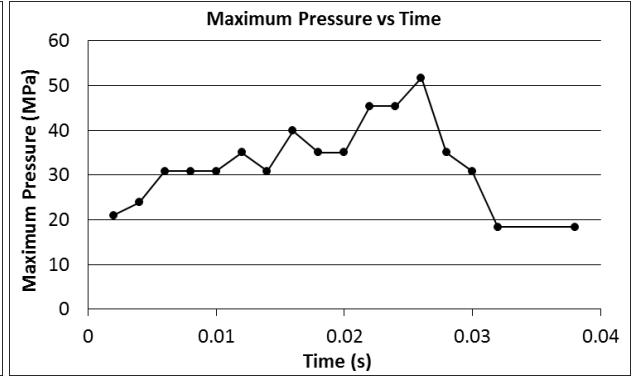
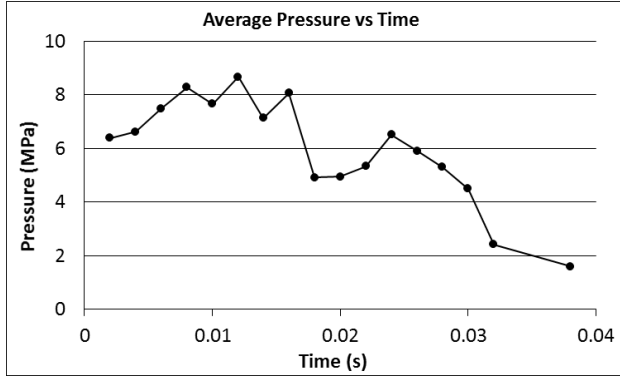
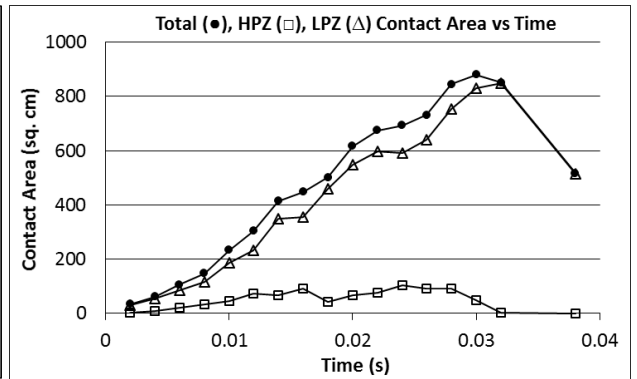
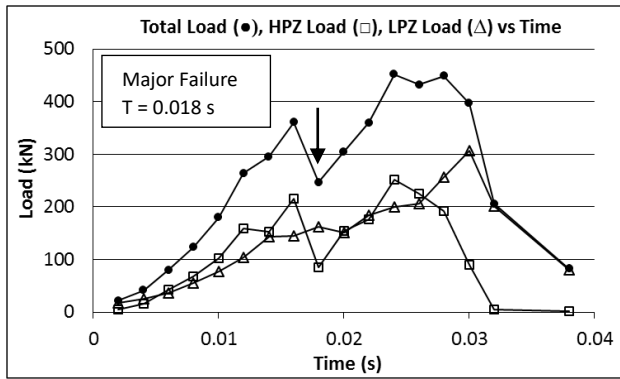


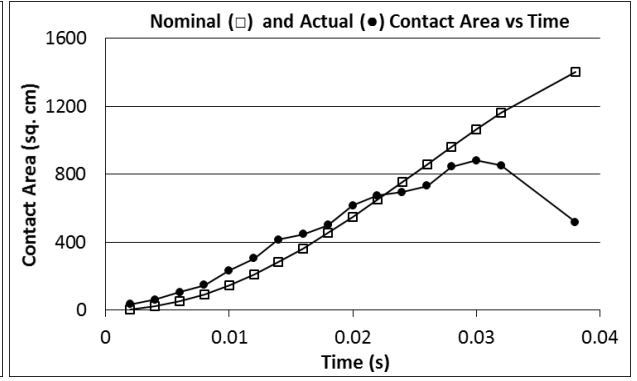
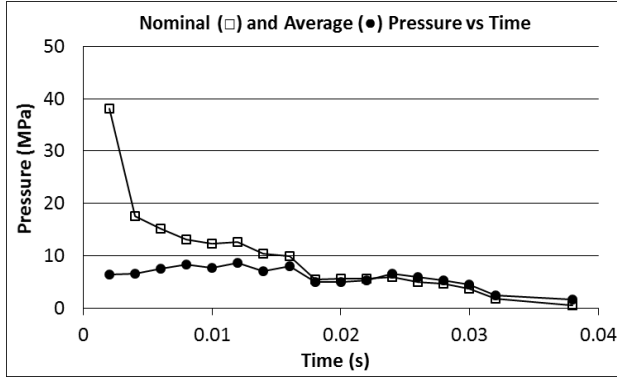
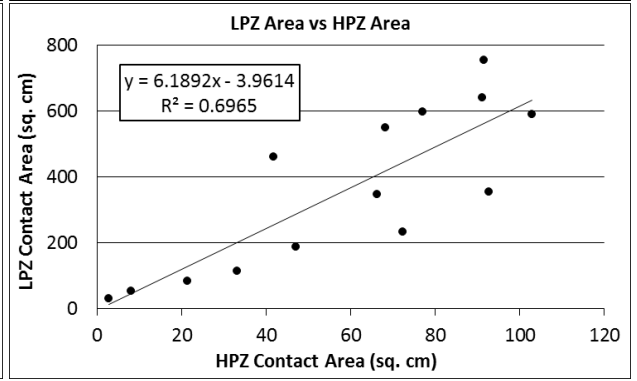
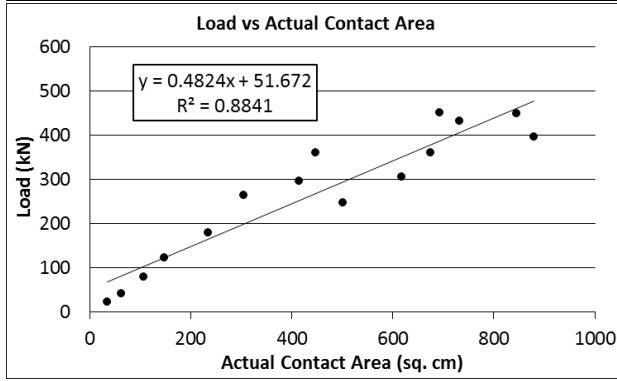
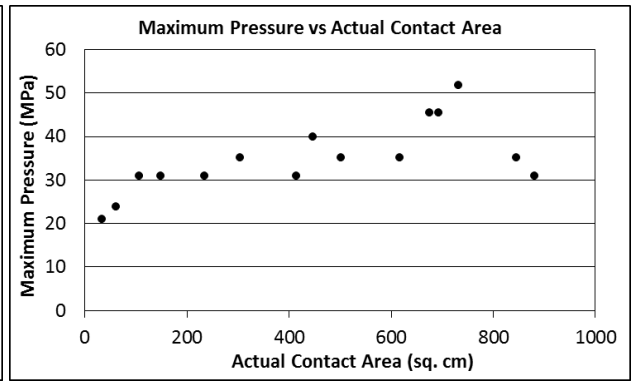
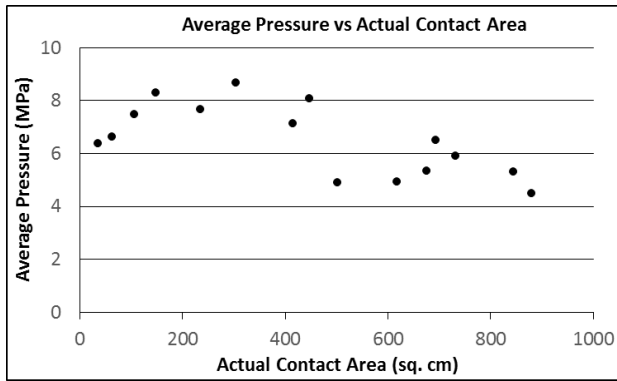
2.18.3 (Test: Dec10_2015)



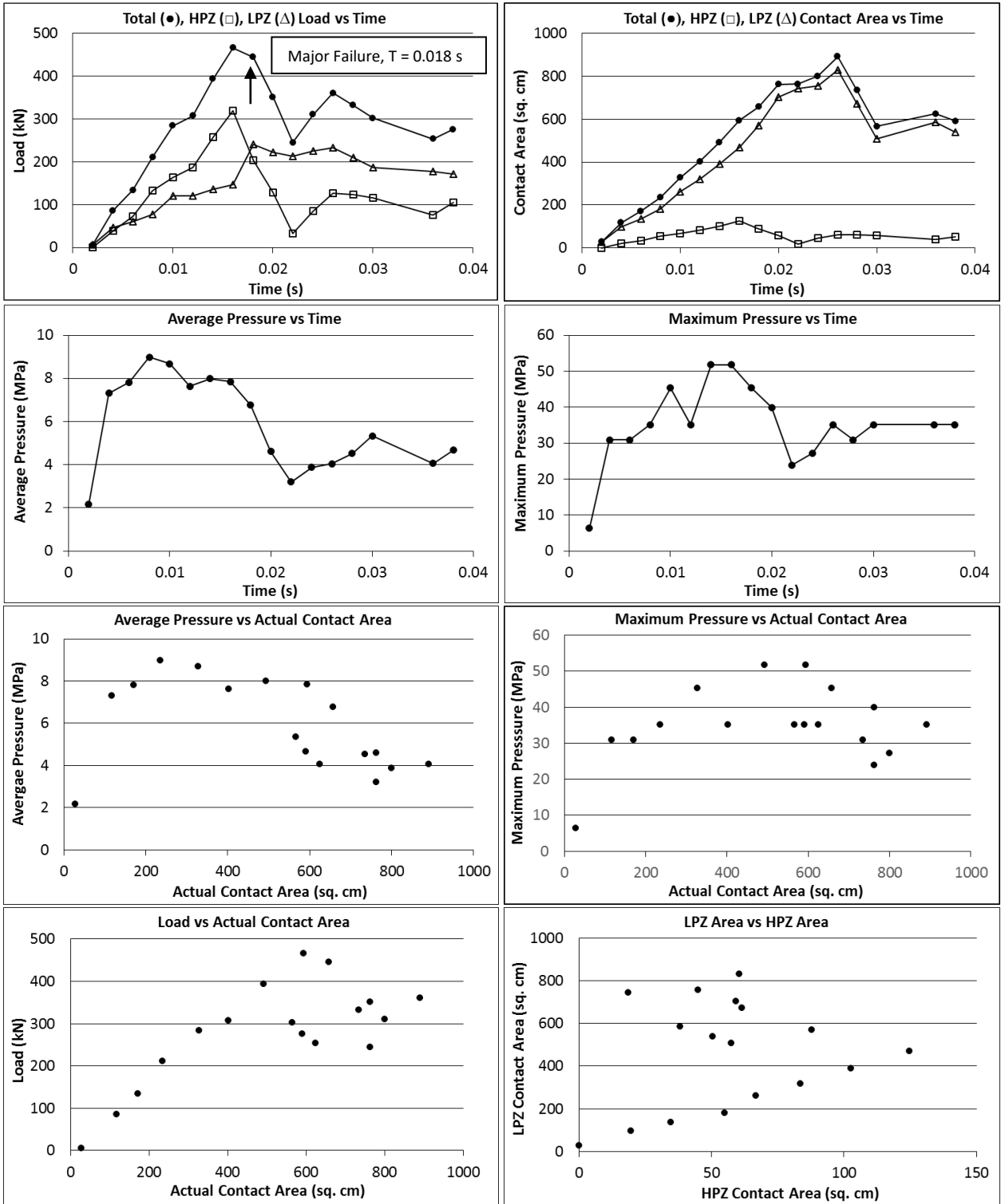


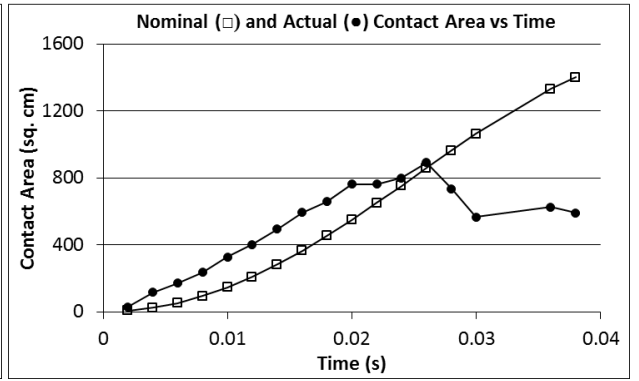
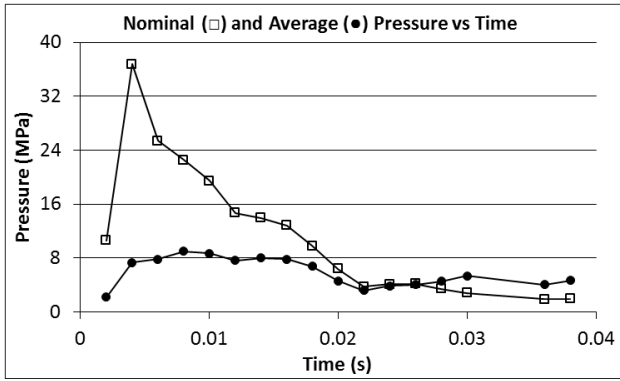
2.18.4 (Test: June27_2014)



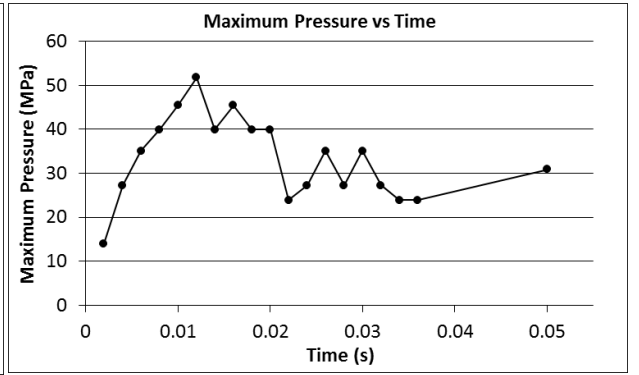
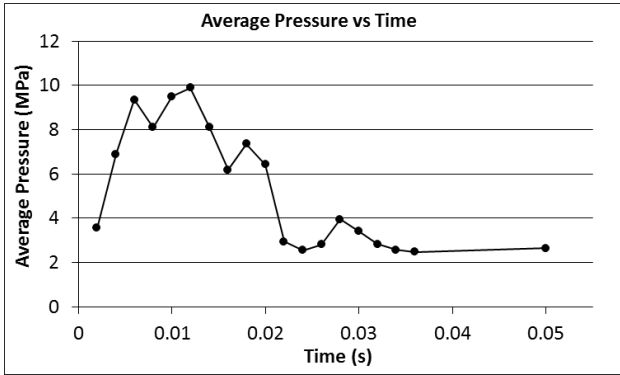
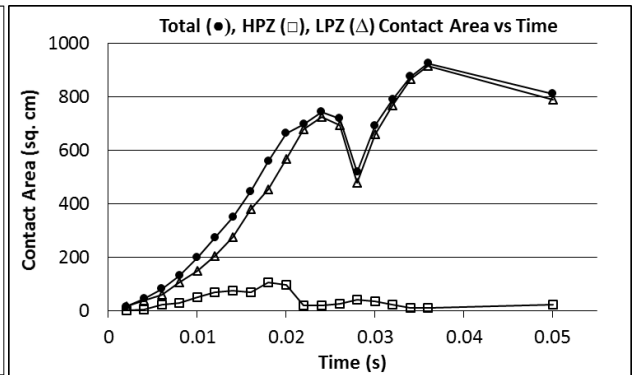
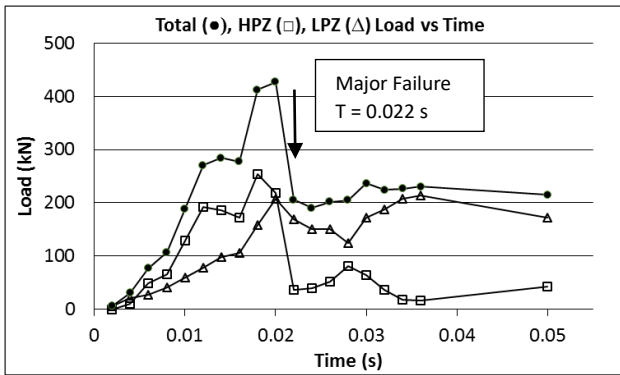


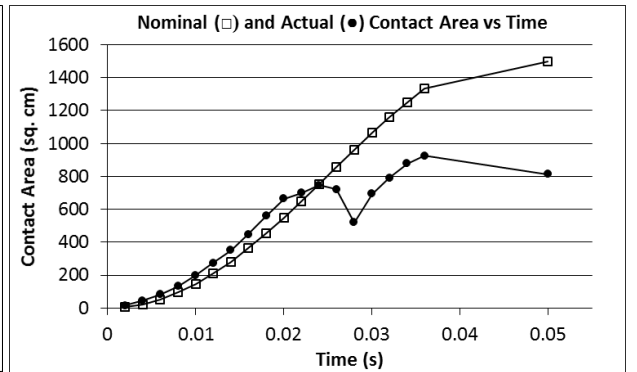
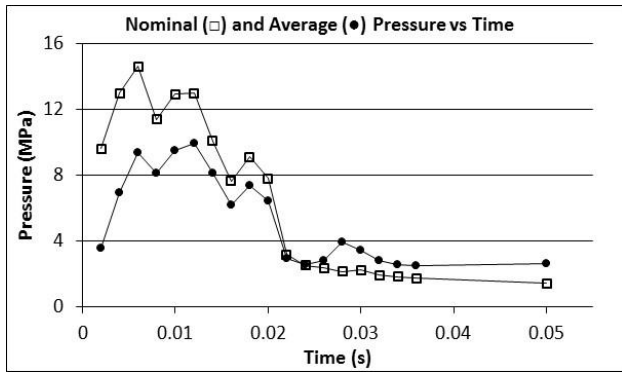
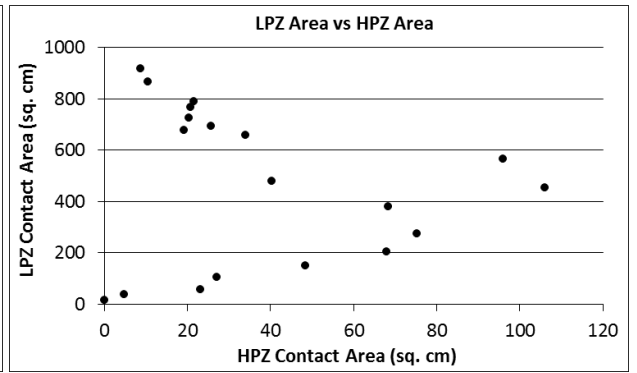
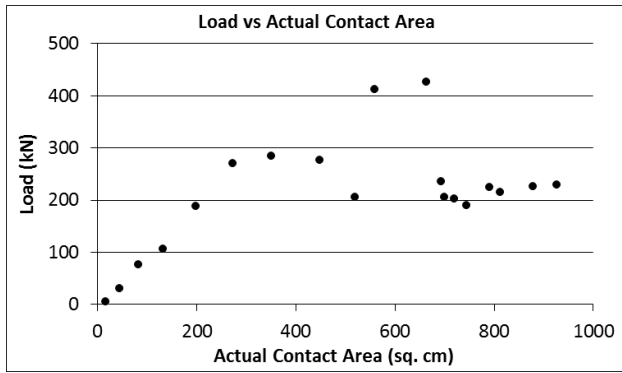
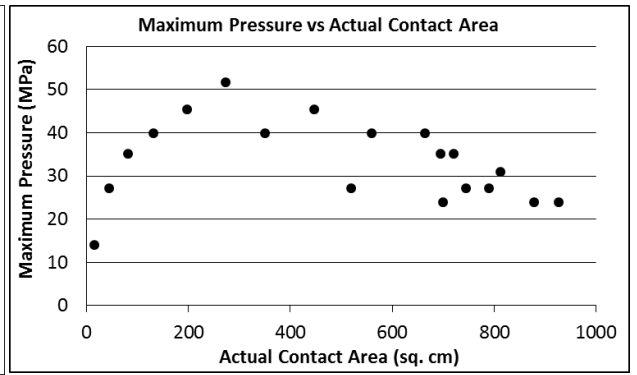
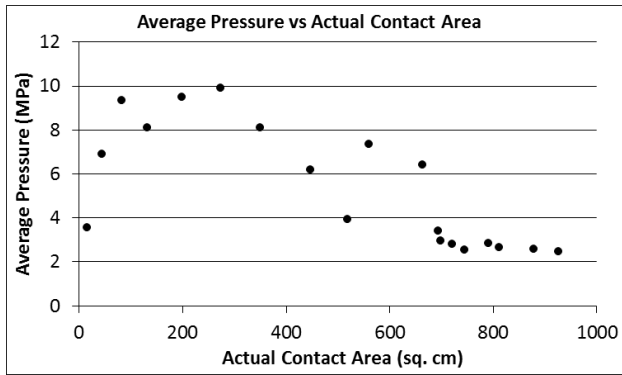
2.18.5 (Test: Oct16_2014)



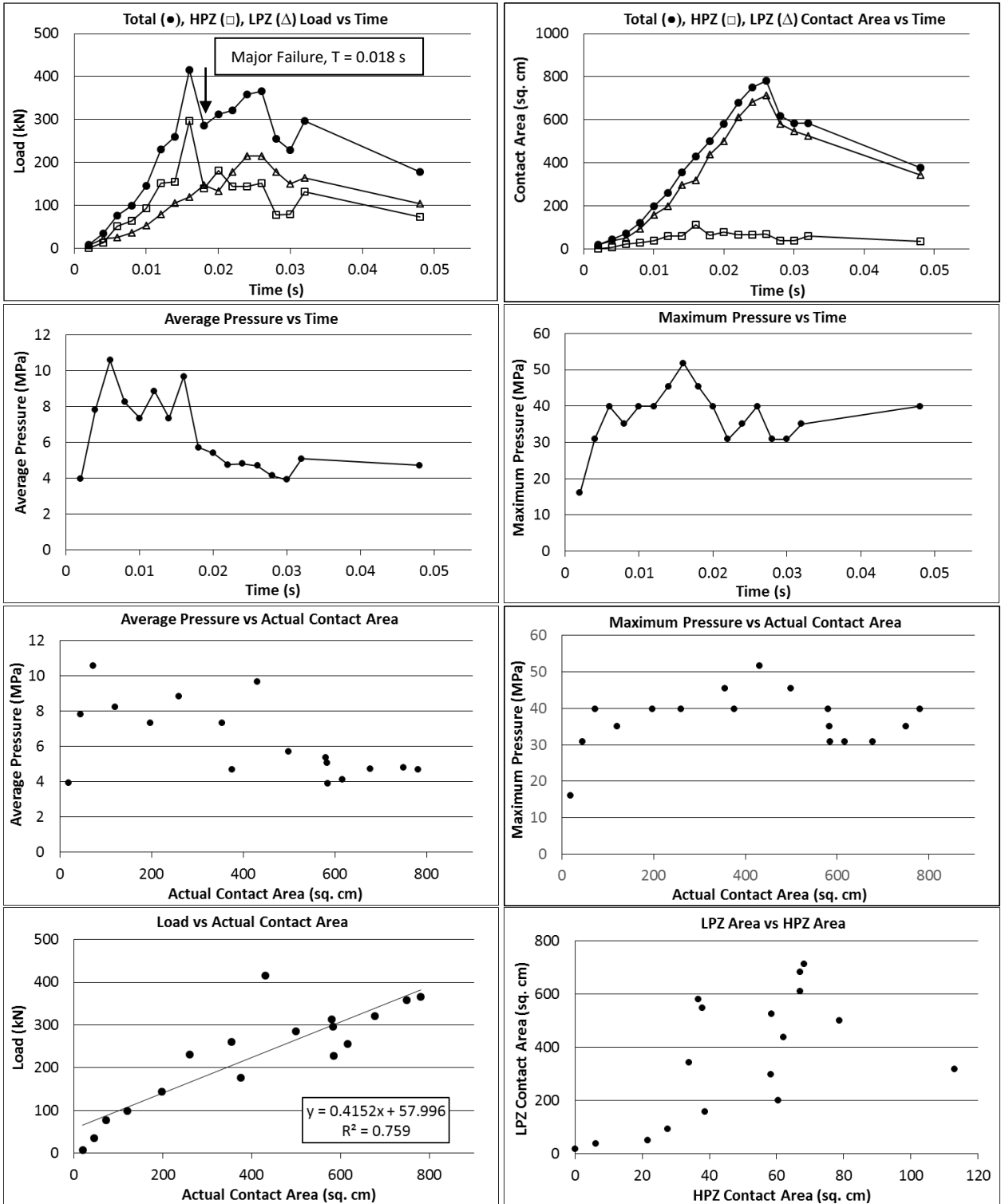


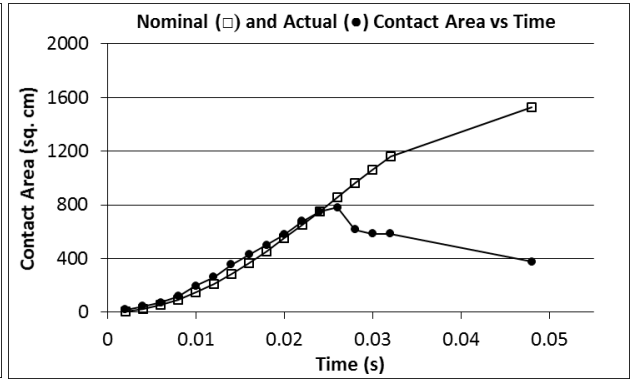
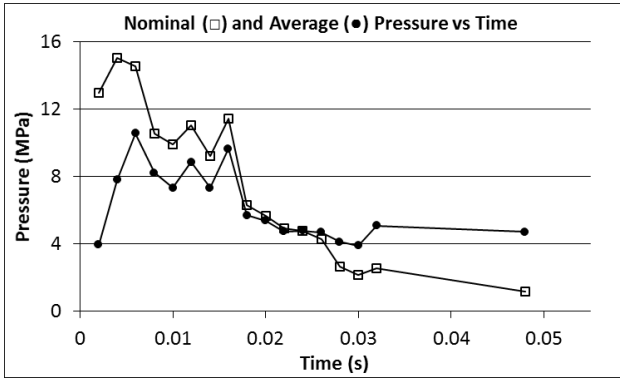
2.18.6 (Test: Dec15_2014)



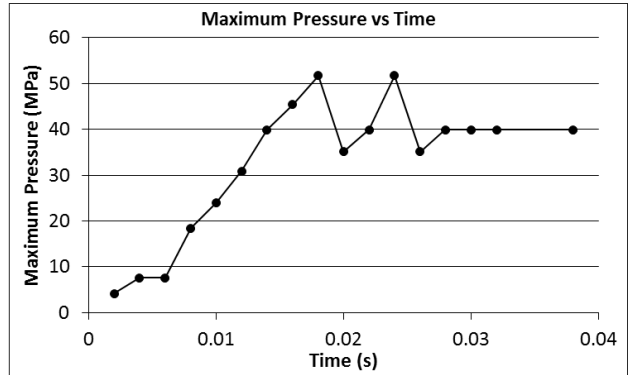
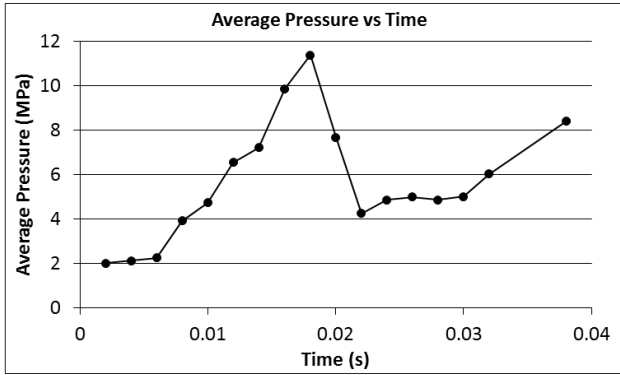
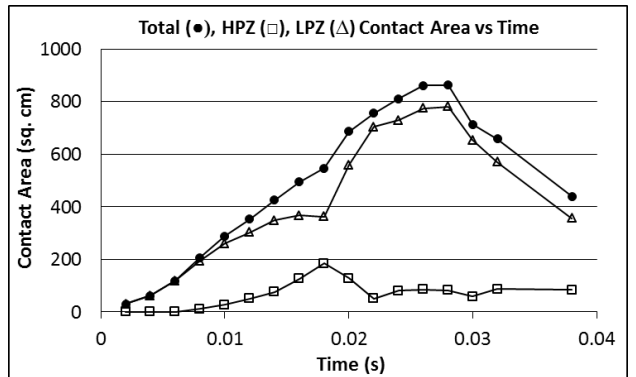
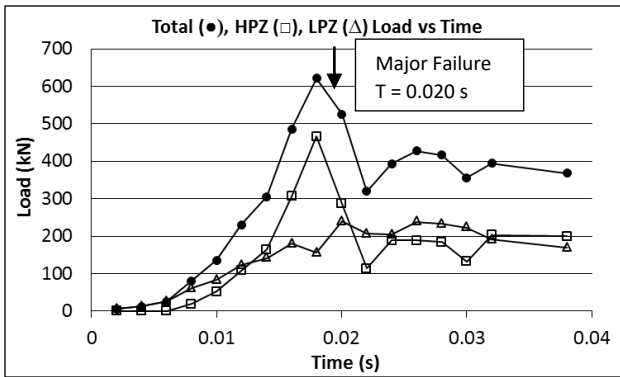


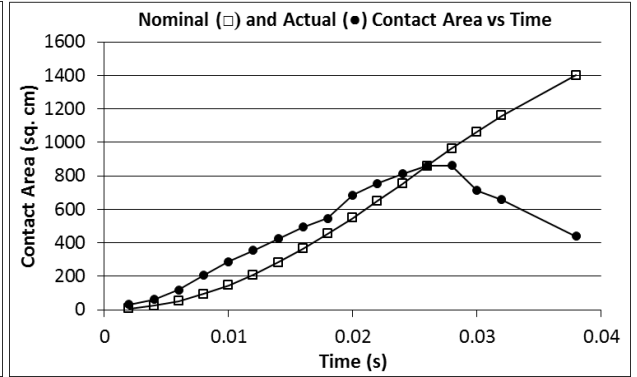
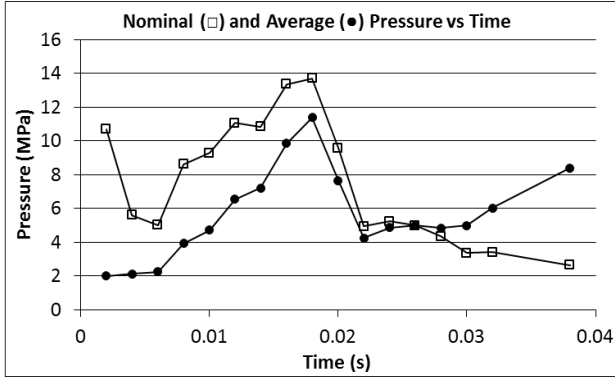
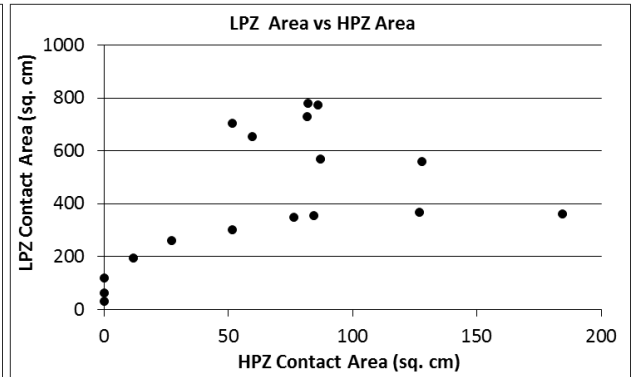
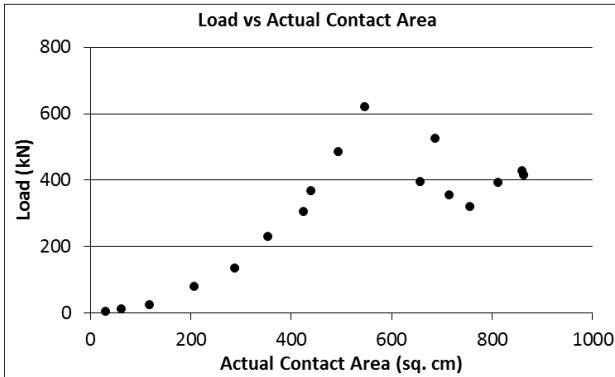
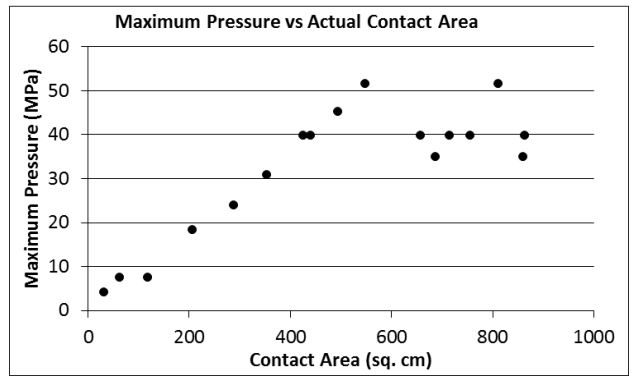
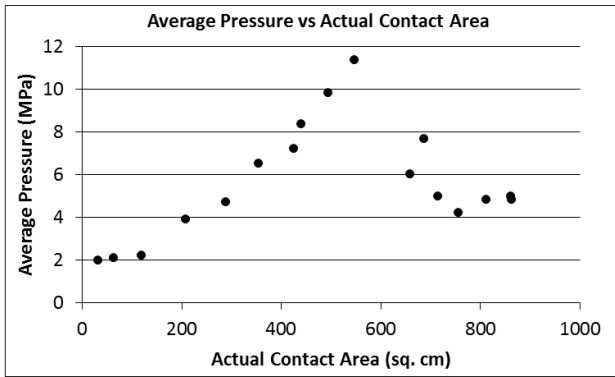
2.18.7 (Test: Jan20_2015)





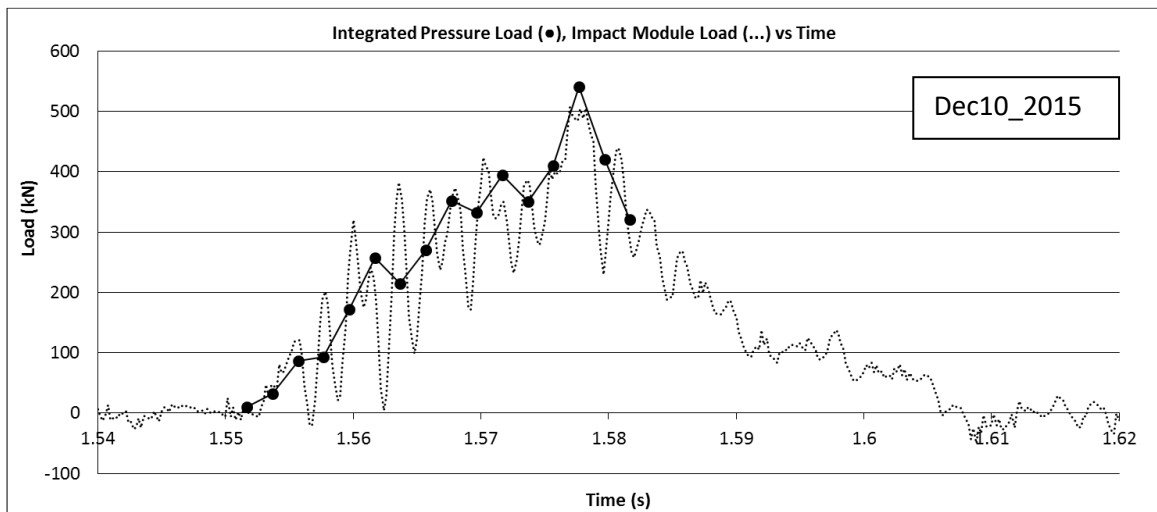
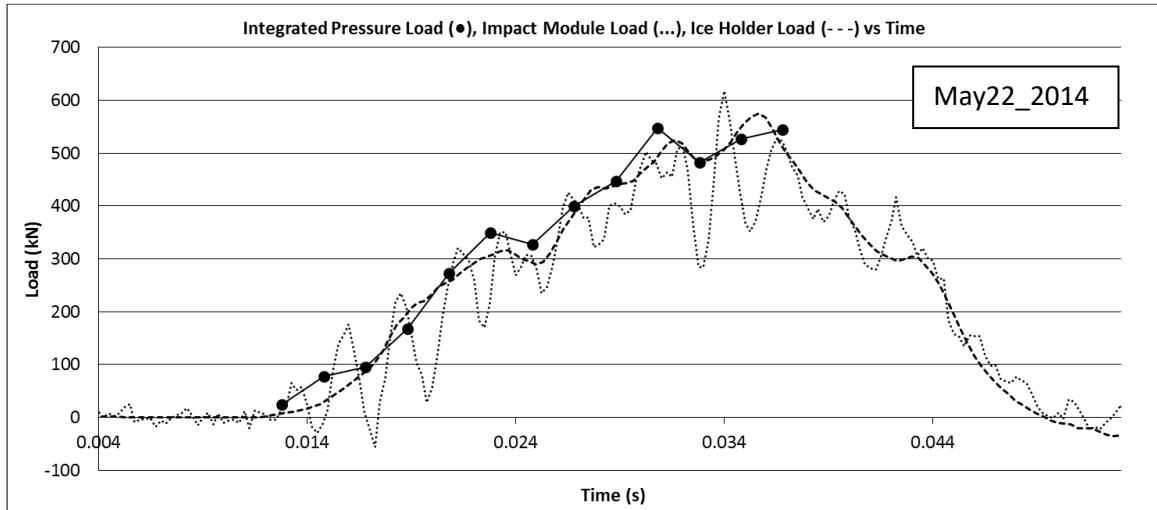
2.18.8 (Test: Feb25_2016)

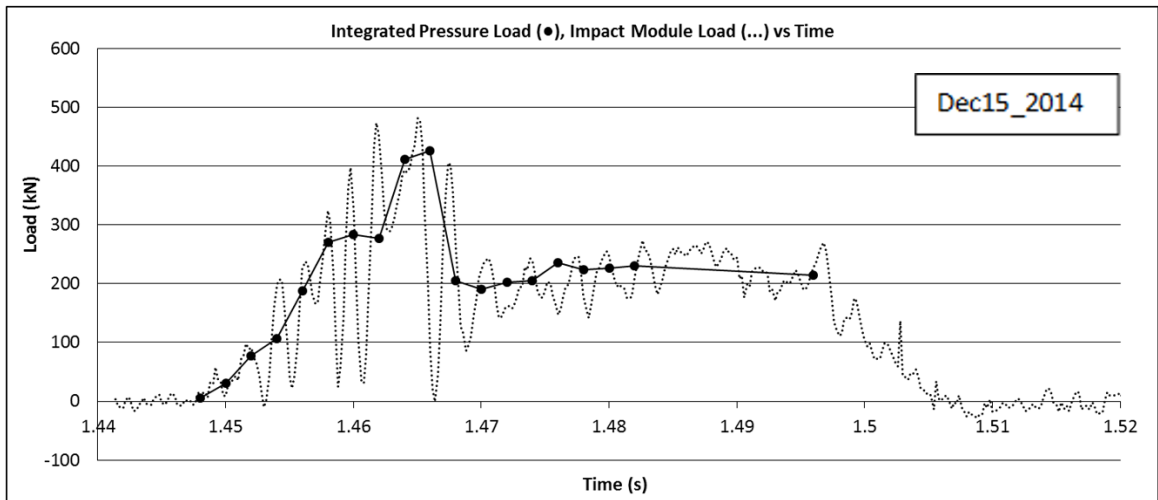
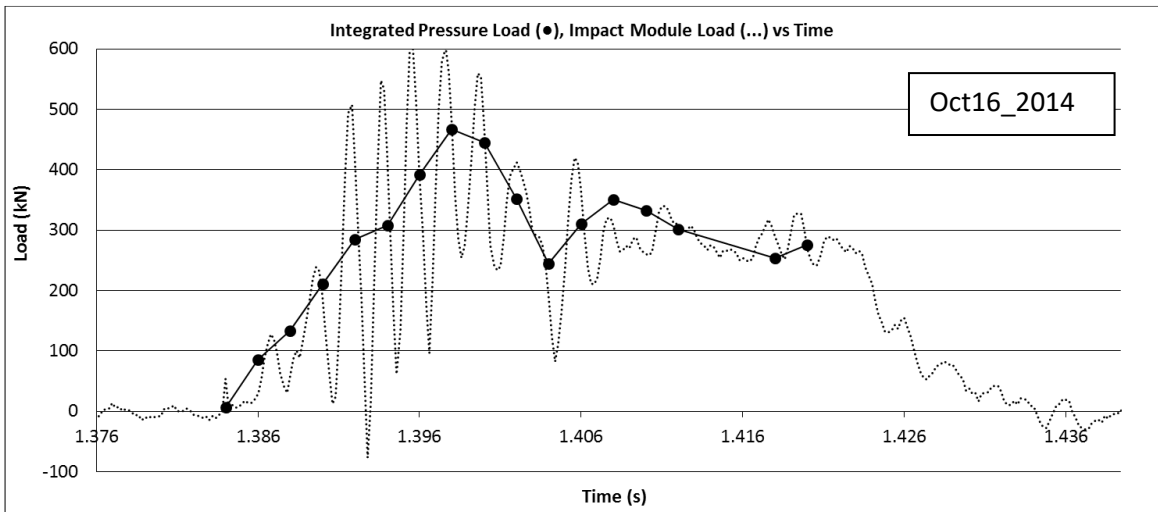
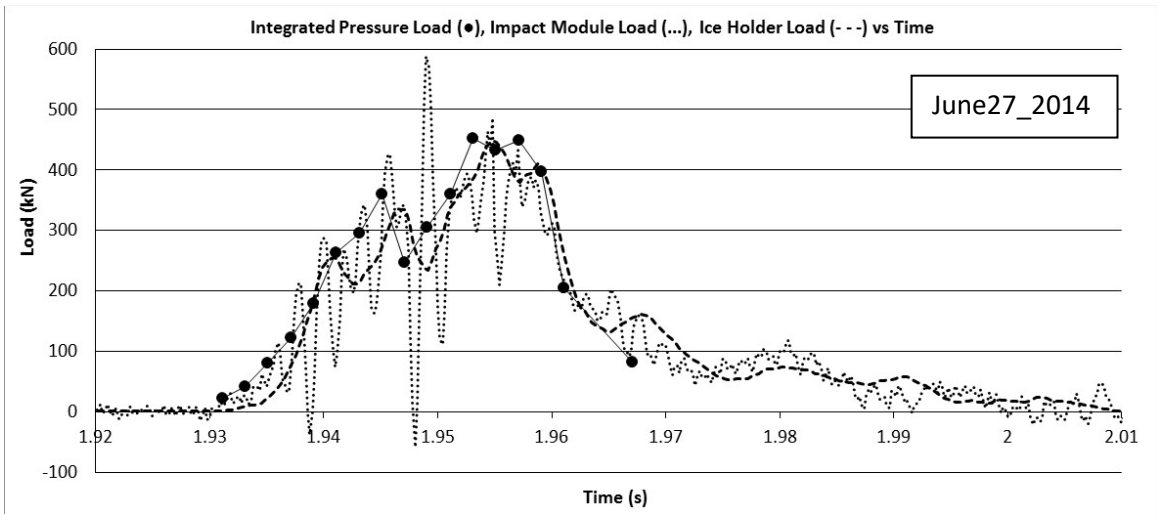


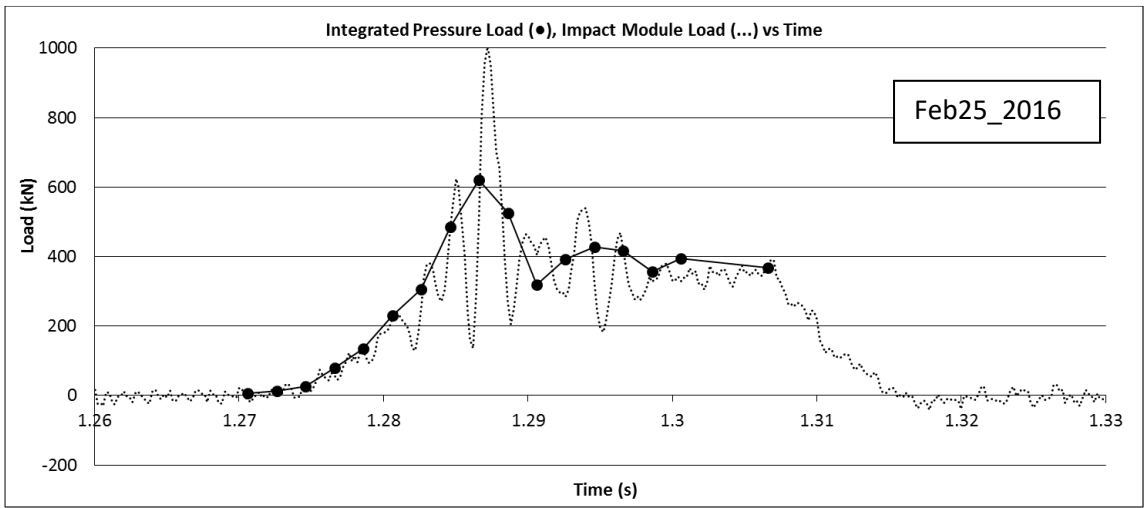


2.19 Appendix D

(Notes: The Impact Module load-cell data for the May 8, 2014 tests were contaminated with ambient electrical noise and the Ice Holder load cells had malfunctioned. The Ice Holder load cells functioned reliably for only two tests: May22_2014 and June27_2014.)







Chapter 3 Numerical study of large pendulum ice impact loads

3.1 Co-authorship statement

This chapter has been presented at the 39th International Conference on Ocean, Offshore & Arctic Engineering which took place in Fort Lauderdale, FL, as an online only conference. The work was published as a peer-reviewed conference paper: Andrade, S.L., Quinton, B.W.T., Daley, C.G., Gagnon, R.E., 2020. Numerical Study of Large Pendulum Ice Impact Loads, in: Volume 7: Polar and Arctic Sciences and Technology. American Society of Mechanical Engineers, Virtual, Online, pp. 1–10. <https://doi.org/10.1115/OMAE2020-19068>.

S. L. Andrade proposed and performed the numerical structural simulations. S. L. Andrade performed the data analysis. S. L. Andrade wrote the manuscript. S. L. Andrade, B. Quinton, C. Daley, and R. Gagnon were responsible for the paper editing and revisions. The current version was edited to expand the background literature.

3.2 Abstract

The large pendulum ice impact experiments performed at the Memorial University of Newfoundland recorded pressure distributions using a novel high-fidelity measurement device, the Impact Module, which is capable of fine spatial and temporal resolutions - effectively 2 cm² at 500 Hz. These experiments achieved impact energies approaching 29 kJ, velocities of 4.7 m/s, and loads reaching 620 kN. The data obtained by the device are unique, as the Impact Module is capable of recording ice pressure data with both high spatial and high temporal resolution over a large contact area. Until recently, there was no

ice load measurement technique capable of excelling in all these aspects. This work aims to study the simulation of a numerical test panel model under the action of the loads measured during the ice impact experiments. This is done by using a non-linear numerical model with explicit time integration capable of simulating the dynamic transient ice loads and comparing their effects to a quasi-static approach.

Keywords: Ice loads; numerical structural analysis; large pendulum impacts.

3.3 Introduction

The continuous reduction of ice coverage in the Arctic is leading to an increase in ship traffic in the region (Aksenov et al., 2017). However, even during the summer, when ice cover retracts and many routes become virtually ice free, multi-year ice presence is still of concern to vessels navigating the polar waters, as it might cause accidental impacts and damage the ship's structure. Despite the efforts to map ice loads on a ship structure and predict the extent of damage, ice load development and distribution in the contact zone are not entirely understood. This is due in part to the chaotic nature of the ice failure process and in another part due to technological limitations related spatial resolution and recording speed. Until recently, most pressure sensing technologies were limited by spatial definition or refresh rate. This study simulates the effects of a highly detailed ice load distribution on a numerical model based on a non-ice class ship. The ice load map originates from a novel pressure sensing technology capable of high spatial and temporal resolution over a large contact area.

The objective of this paper is the study of dynamic ice load application in numerical structural simulations of ship structures. The effects of dynamic ice loads are compared with those of a quasi-static load application approach. The load data originates from ice impacts with limited kinetic energy. In the original impact most of the kinetic energy available was absorbed by the ice crushing process. The numerical simulations in this work cause significant energy loss by structural deformation and this effect is studied.

3.4 Background

The desire for commercial development of the arctic led to a great research effort in understanding the complexity behind the ice crushing process. Temperature, crystalline structure, presence of impurities, and strain-rate are important factors in determining the failure regime and ice strength (Timco and Weeks, 2010). Strain-rate seems to have a direct effect on the pressure distribution over the ice-structure contact area due to the type of failure regime. At strain-rates lower than $2 \times 10^{-4} \text{s}^{-1}$, ice fails under a ductile regime while, after a transition period, at strain rates higher than $2 \times 10^{-3} \text{s}^{-1}$ it changes to a brittle failure regime (Timco and Weeks, 2010). Riska's (2018) review of full, medium and laboratory scale ice crushing experiments describe that in brittle regime the actual contact area between ice and the indenter is smaller than when it is in the ductile regime (Sodhi et al., 1998). In addition to that, the brittle regime has lower average pressure but higher concentrated magnitudes than the ductile regime. This is relevant as ice-ship interaction is mostly within the brittle range for normal operations.

Full scale measurement campaigns were organized in the Arctic with vessels instrumented to measure local ice loads on the ship hull, like the ones of the Polar Sea trials (St. John et

al., 1984) and the Louis St. Laurent (Ritch et al., 1994). These trials showed that during the icebreaking process, pressure spikes occur in localized regions within the contact area. The same behavior was observed in the Baltic Sea during full scale measurements campaigns, like with the ship Agulhas II (Suominen et al., 2013). The Arctic and the Baltic have different ice conditions, most noticeably, the Baltic has exclusively first year ice, while the Arctic has multi-year ice, which is considerably stronger (Sanderson, 1988) to failure. However, in both regions, localized pressured spikes were observed in the instrumented hulls. Even though the full-scale measurement campaigns were capable of mapping ice pressures in a large contact area on the ship hull, they had low spatial resolution.

Medium scale field experiments performed in different locations in the Arctic shed new light over the development of the contact region, like the ice indentation tests at Hobson's Choice (Frederking et al., 1990), which observed that the contact zone is defined by a combination of intact ice, normally at the center of the contact zone, surrounded by crushed ice. Experiments with multi-axial stress states (Timco and Weeks, 2010) showed that ice compressive strength increases when it is confined, with ice that has a higher density of cracks benefitting the most from a confining pressure (Gagnon and Gammon, 1995). It is conjectured that the crushed ice confines the intact ice, increasing its compressive strength, which in turn creates zones of low and high pressure in the contact region. Laboratory scale tests show that the flow of crushed ice from the contact zone has a large influence on the ice edge indentation process (Riska, 2018; Tuhkuri, 1994).

Ice pressure-area measurements were compiled and described by Sanderson in the form of a Pressure-Area curve (P-A curve) model (Sanderson, 1988). This approach can be used to

characterize the pressure distribution development in space, called spatial P-A curve, and in time, called process P-A curve. The Unified Requirement (UR) for Polar Class ships, compiled by International Association of Classification Societies (IACS), uses the process P-A curve model to predict loads and pressures in a multi-year ice collision scenario (International Association of Classification Societies, 2011). The UR recognizes the importance of accounting for localized high-pressure zones, but this is done indirectly through a correction factor in the structural scantling formulation of the smaller structural elements, as the prescribed load patch itself has a constant pressure value. Another organization that provides a code for structural design of ships navigating in polar waters is the Russian Maritime Register of Shipping (RMRS), but it uses instead the Kurdymov Khesin ice extrusion model (Kim and Amdahl, 2016) to predict ice collision loads.

More recently, the spatial pressure distribution was studied in higher detail during field measurements using Tekscan® pressure sensing technology (Frederking, 2004; Kamio et al., 2000) (the JOIA tests in Hokkaido), which showed a clear presence of high and low pressure zones in the ice crushing contact area. Erceg et al. (2014) demonstrated numerically that the type pressure distribution over the contact area has a clear effect on structural deformation of an ice strengthened ship structure, which includes permanent damage when load concentration is considered (Erceg et al., 2014). The study compared the effects of two load patterns on a ship local structure: a rule prescribed ice load (Finnish-Swedish Ice Class Rules) with constant pressure distribution and a variation of the same total load but with a distribution that followed the high- and low-pressure patterns observed

in the Hokkaido measurements. The second load scenario caused significantly more plastic damage to the structure in comparison to the rule prescribed load.

It is important to remark that Tekscan® technology is capable of fine spatial resolution, however it is limited in terms of response speed. The manufacturer states that the product is not calibrated to measure dynamic loads with rise-time faster than 0.1 - 0.3 seconds, as this is the time required for the sensor to settle (Tekscan, 2022). Experimental measurements of ice impacts have faster load rise-time than 0.1 s (Sopper et al., 2015).

The large pendulum ice impact experiments performed at the Memorial University of Newfoundland recorded pressure distributions using a novel high-fidelity measurement device, the Impact Module (Gagnon et al., 2015). Recently the full data pertaining these experiments were analyzed (Gagnon et al., 2020) and are used in the current work to study the effects of dynamic ice loads on the numerical model of a ship grillage. The next section offers a more detailed explanation pertaining the impact module and the recorded pressure distributions.

3.5 Ice impact experiments

Conducted between 2014 and 2016, the double pendulum large ice impacts were a series of 9 experiments, where ice cones and the impact module, a pressure sensing apparatus, are attached to opposing pendulums, suspended, and released. The freshwater cones were 1m in base diameter and had 30 degrees base angle. The ice specimen production follows the procedure given in Gudimetla et al. (Gudimetla et al., 2012). Commercial freshwater ice is

crushed to pieces of 12mm in diameter, then it is covered with tap water and left to freeze for 3 to 4 days at -10 °C. This forms a granular ice cylinder that is shaped into a cone.

The impact module is a structure consisting of a series of thin acrylic strips, 13 mm wide, placed side-by-side on top of a large acrylic block (1 m x 1 m x 0.46 m), which rests on top of 4 flat jack load cells and is encased in and firmly bolted to a steel case (Gagnon et al., 2015). The thickness of the acrylic block is such that it gives the apparatus the flexural strength required to resist the impact loads, while being supported from all sides by the steel case. This results in very small elastic deformations of the load sensing apparatus, which can be considered negligible (Gagnon et al., 2015). Figure 3-1 illustrates this scheme.

The base of the strips has a gentle curvature and leaves no visual mark while resting. When the acrylic strips are pressed against the acrylic block, they flatten, and their reflectivity change in the flat contact region. This allows a camera to record their deformation (this reflectivity is enhanced by a thin white plastic film loosely placed between the strips and the acrylic block, Monokote™). The instantaneous strip deformation is visually recorded by a high-speed camera. The localized contact width can be used to extrapolate the pressure required to cause the recorded deformation (Gagnon et al., 2020). When the load is released/reduced, the acrylic strip springs back to its original shape.

Each individual frame from the recording is later translated into a pressure map. This means that the impact module is capable of fine spatial and temporal resolutions, limited only by strip width, acrylic elastic properties, and the recording speed. For the impact experiments, the spatial resolution was 2 cm² recorded at 500 Hz.

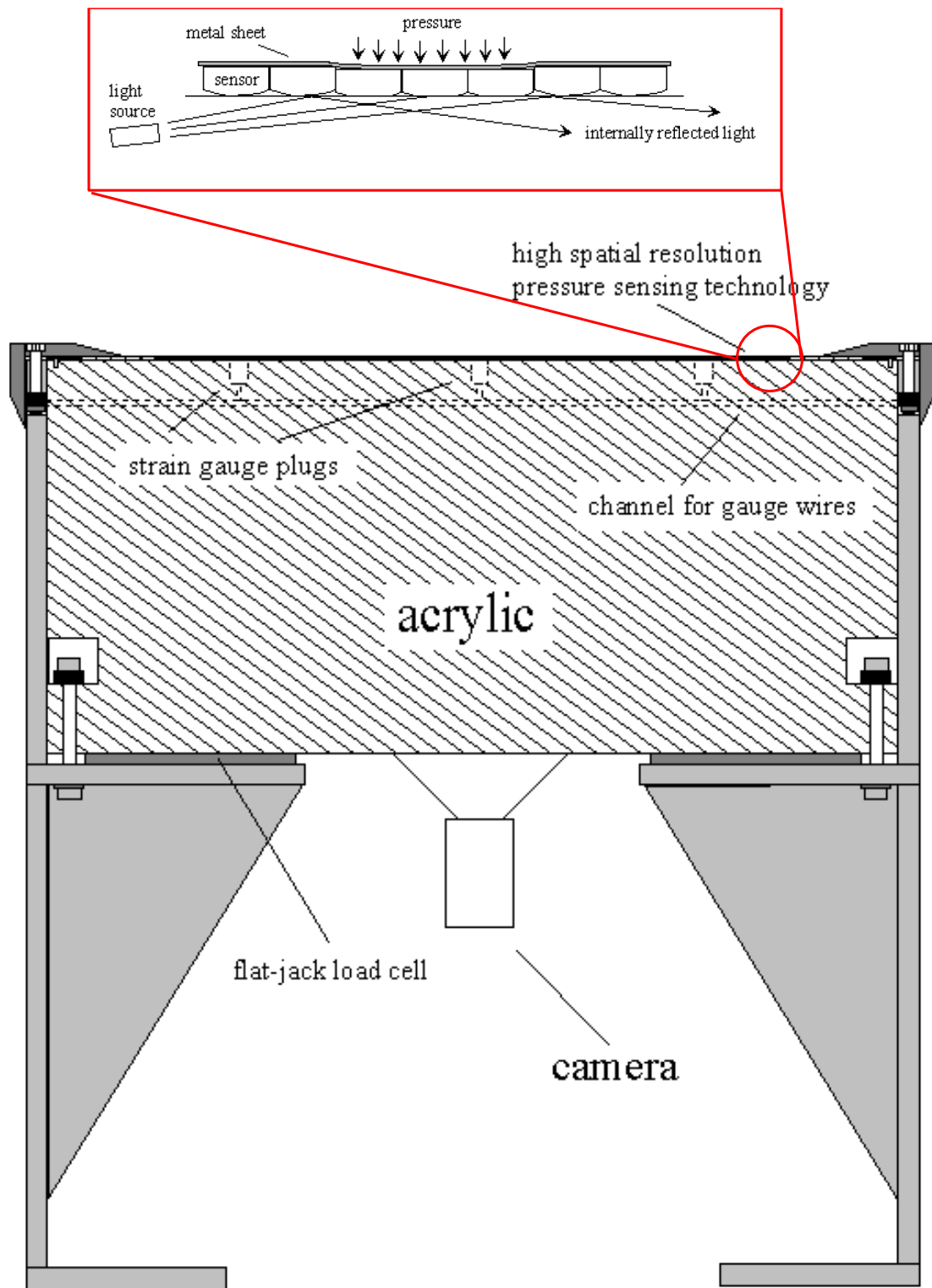


Figure 3-1. Pressure - sensing technology. Figure modified from Gagnon et al. (2020).

The high-speed camera recorded between 16 and 20 usable images per impact experiment. For a full description, refer to (Gagnon et al., 2015) and (Gagnon et al., 2020). Figure 3-2 shows a raw sample image. The deformation of the acrylic strips is visually recorded by the high-speed camera in the form of gray vertical lines. Other features in the image are considered noise (air bubbles trapped in the acrylic, cables, and the housing) and cleaned from the image.

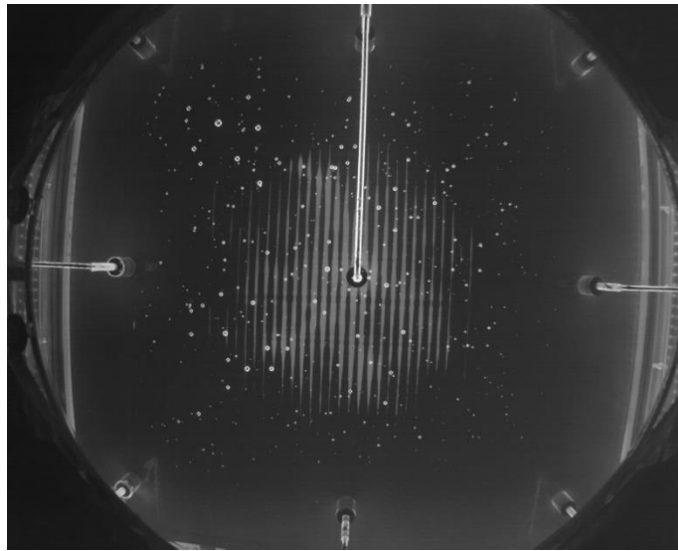


Figure 3-2. Untreated sample image from the high-speed camera. (Gagnon et al. 2020)

Each frame contains a series of pressure lines. They are translated into pressure information using a computer routine that measures the contact width, pixel by pixel. The result is a map of the pressure distribution on the panel at different instants of the impact (Sopper et al., 2015). Figure 3-3 shows a color-coded pressure map of the pressure distribution over the contact area. Figure 3-3 was obtained from Figure 3-2.

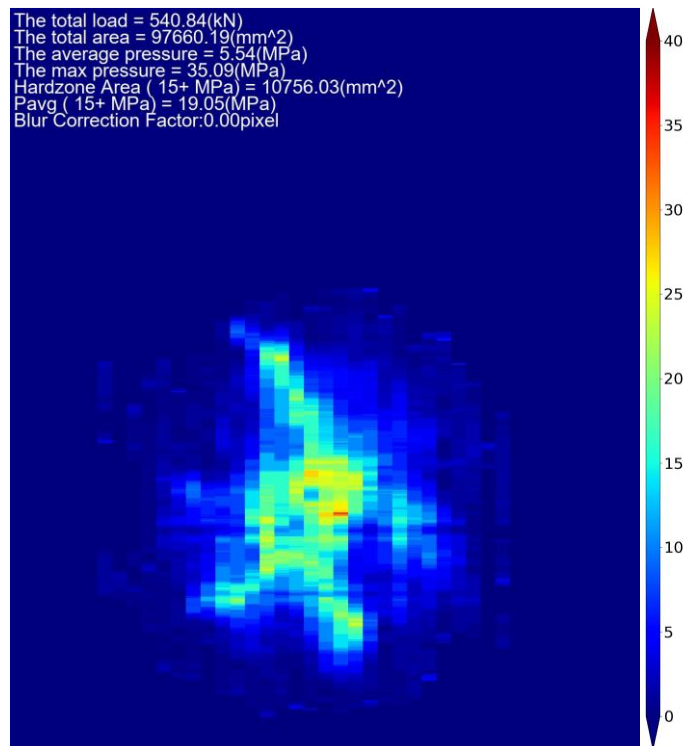


Figure 3-3. The output of the procedure is a color-coded pressure distribution image. (Gagnon et al. 2020)

The images were analyzed for the duration of the crushing event, the elastic rebound phase was not included. Some images recorded at the end of the impact event showed blur effect, which usually could be corrected, but some images were simply too blurred to obtain meaningful data, thus some experiments will show an information gap close to the end of the impact event.

Integrating the pressure information over the contact area results in the total impact force at each timestep. Since the force values were recorded by more than one measurement device, it was possible to benchmark the quality of the image analysis. The force values observed in Figure 3-4 are from the Dec10_2015 impact. They show a nice agreement between the measurements of the impact model load cells and the integrated pressure load

values obtained from the pressure distribution images. The oscillation of the Impact Module Load curve observed in Figure 3-4 is caused by a resonant response of the load cell itself to the vibrations experienced during the impact. The Integrated Pressure Load curve, however, does not suffer from this problem.

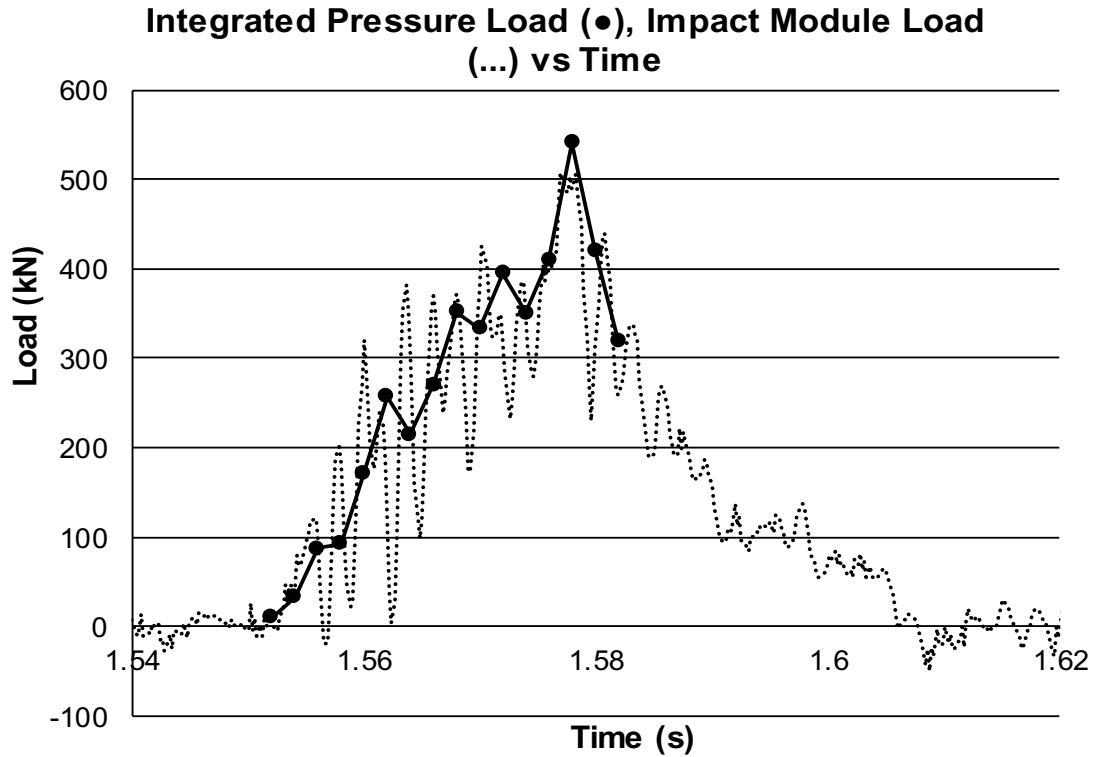


Figure 3-4. Load comparison for the dec 10 2015 experiment. The integrated pressure pattern only shows data for duration of the penetration. (Gagnon et al., 2020)

Besides pressure data, contact area, and integrated force, information regarding relative impact speeds and ice penetration is available for these experiments. In the current work only 6 of the 9 experiments are considered, as 6 out of 9 tests were performed at the same drop angle of 35 degrees. The theoretical maximum speed differs from the measured speed at the point of contact. High speed camera analysis determines that 4.7m/s is the speed at

the instant of contact for these 6 experiments. The kinetic energy available at the instant of impact was of 28.86 kJ. The impact module is very rigid and suffers minimal deformation during the impact, this means that the kinetic energy is absorbed almost exclusively by the ice crushing process, in a relatively inelastic process. The fact that minimal bounce back effect was observed during the impacts supports this affirmation. This is also shown by the impulse analysis, Table 3-1.

Table 3-1. Integrated impulse and maximum penetration for each experiment.

Experiment	Ice Penetration*	Crushing Impulse	Total Impulse	Total / Crushing
	[cm]	[kNs]	[kNs]	[%]
June 27, 2014	12.2	7.94	9.98	80%
Oct 16, 2014	12.2	9.08	11.23	81%
Dec 15, 2014	11.9	8.69	10.66	82%
Jan 20, 2015	11.1	8.33	10.01	83%
Dec 10, 2015	11.1	8.89	10.75	83%
Feb 25, 2016	11.5	9.32	11.76	79%

* The ice penetration at the time of the last pressure pattern. The penetration was estimated using video recordings of the impact (NTSC and high-speed) and photos of the damaged ice cone.

The total impact impulse is calculated by integrating the force information recorded by the load cells contained in the impact module. By analyzing the high-speed images, it is possible to divide the impulse data into 2 phases, the crushing phase and the elastic rebound phase. Table 3-1 shows the crushing component of the impulse compared to the total impulse of the impact.

This is a good confirmation that most of the kinetic energy in these impacts is consistently being absorbed by the ice crushing process and not much is left for the elastic restitution.

3.6 Methodology

This study will apply the ice loads measured during the tests to a numerical structural model. For simplicity, the impact will be considered inelastic. The 4DPM (4-Dimensional Pressure Method) methodology developed by Quinton (Quinton et al., 2012) is used in these simulations to apply the ice loads to the model. It is ideal to solve numerical problems that require the application of pressure loads changing in space and time. The 4DPM routine maps the elements contained within a zone that represents each subpanel, then apply the pressure load to the elements contained inside the zone, changing the magnitude appropriately at each timestep. Ideally, the element size must be equal to or an integer of the subpanel size, otherwise the total load applied over the entire model would not correspond to the measured load.

In addition to the simulation over the actual duration of the impact, a quasi-static numerical analysis is performed for each experiment. This is achieved by simply applying the same loads over a longer time.

For all quasi-static simulations performed, the average largest divergence between the applied load and the load calculated at the boundary conditions of the model is 2.4%, which is relatively small considering the large deformations to which the model is subjected and negligible when compared to the difference in response in the dynamic simulations (disclosed in results section 3.8). An even greater agreement would be possible with smaller elements but using the current approach would require halving the element size, and this would increase solution time considerably. The solution would be very computationally

expensive. A better approach for future iterations of this work is to develop a new routine that applies nodal forces to the model instead of pressure load.

A limitation of this contactless approach is that load and structural deformation are decoupled. However, this is no different of any other contactless approach used for design purposes. Still, for this study the effect of local structural deformation on load distribution and magnitude is not considered, but future work will attempt to couple the effect.

Another concern is that the ice loads were measured by a rigid apparatus within the elastic regime. This work studies the effects of ice loads on a structure that is expected to suffer local plastic deformation. The plastic deformation causes the structure to become a considerable energy sink in this impact scenario with limited energy, thus the contribution of both ice crushing and structural deformation process in the overall energy absorption should be accounted for.

The current work is but a small component of a larger project interested in studying operational capabilities of low and non-ice class vessels navigating in ice infested waters. For this purpose, test panels similar to the IROQUOIS class vessel grillage were produced at Memorial University of Newfoundland. The fabricated panels were adapted to be used in impact experiments in the large pendulum. The structural model of these test panels is used in the numerical simulations presented in this work. Experimental impacts between the test panels and ice cones are planned for the near future. Those will allow benchmarking the simulations when available.

3.7 Numerical model

Since transient loads, material plasticity and large geometric deformations are present in the simulations, explicit time integration approach is used for this study. The FEA software chosen for this task is LS-DYNA™. The grillage model, Figure 3-5, has the following dimensions:

- Width: 2.032 m
- Height: 1.36 m
- Frame spacing: 0.61m
- Frame dimensions (T-bar):
 - Web: 0.178m x 7.9mm
 - Flange: 0.102m x 7.9mm
- Thickness of plate and stiffeners: 7.9 mm (5/16 inches)

The mesh is composed of reduced integration shell elements with an average edge length of 13 mm. Special attention was taken towards aligning elements and the pressure distribution information. The load application zone is shown in yellow in Figure 3-5.

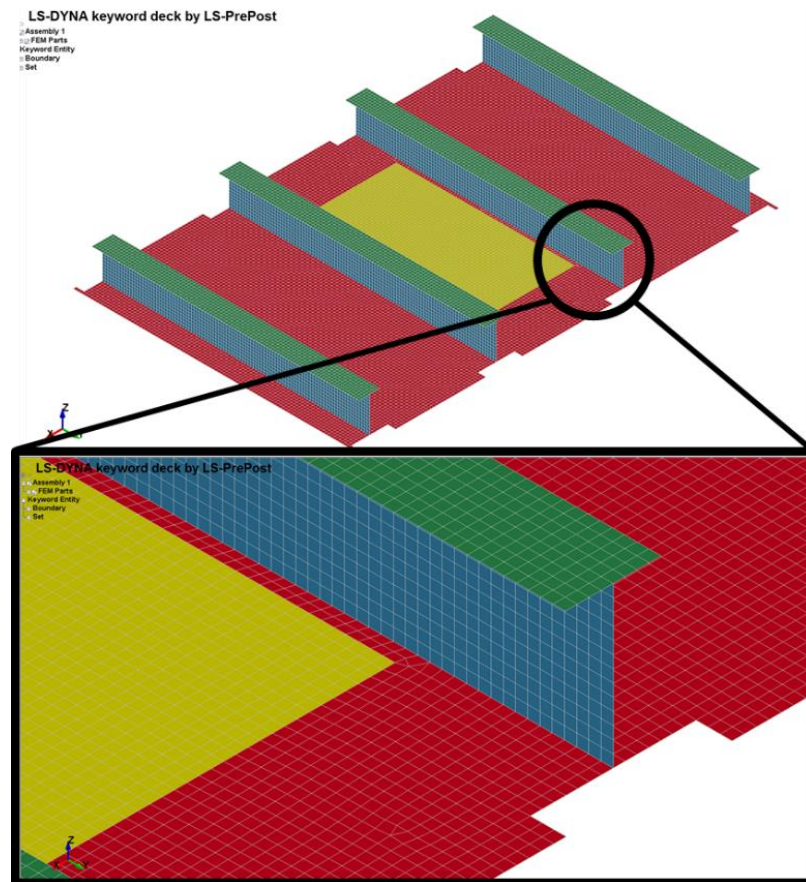


Figure 3-5. Meshed model with close-up.

The material properties are based on stress-strain test data from the steel used to build the test panels. This allows a multilinear plastic kinematic material model to be used (no strain hardening effects were applied).

- Yield strength, $\sigma_{yield} = 420MPa$
- Elastic Modulus, $E = 207GPa$
- Density, $\rho = 7850 kg/m^3$
- Poisson's ratio, $\nu = 0.3$
- Ultimate stress, $\sigma_{ult} = 580MPa$

- Strain at ultimate strength: $\varepsilon_{ult} = 19\%$

The model has a fixed boundary condition around its perimeter. This reflects the way the test panel is integrated into the pendulum carriage. The carriage was designed in such a way as to mimic an ideal fixed boundary condition as closely as possible, this is also the reasoning for the cuts at the base of the stiffeners, where a fixing plate is installed to make that region as rigid as possible. As commented in the previous section, the load applied comes from the large pendulum ice impacts pressure data.

It is important to remark that the simulations were done under the assumption that pressure distribution and magnitude are decoupled from structural deformation in time. This assumption is not accurate, as the structural deformation affects the local pressure in two major ways: One involves the creation of confinement zones, which would increase the ice resistance to failure and consequently apply larger loads on the structure (Kim, 2014). The other is related to the fact that ice penetration-rates locally would change as the structure is deforming at that location.

However, the assumption that load and structural deformation are decoupled is necessary at this stage. The results in this paper are intended to be the first step in developing a coupled model for ice load simulations using dynamic pressure data.

3.8 Results

Two sets of simulations were performed using pressure data from the ice impact experiments: dynamic-transient and quasi-static. In the dynamic simulations, the pressure loads are applied at the same rate at which they are recorded during the experiments and

the simulations have the same duration of the crushing phase of the actual impact. In the quasi-static simulations, the pressure loads are applied for a time period 100 times longer than the actual impact duration, thus minimizing inertial response of the structure.

In general, all experiments for both set of simulations caused large plastic deformation directly at the contact region, small plastic deformation close to the stiffeners, and no plastic deformation in the stiffeners themselves. This is exemplified in Figure 3-6.

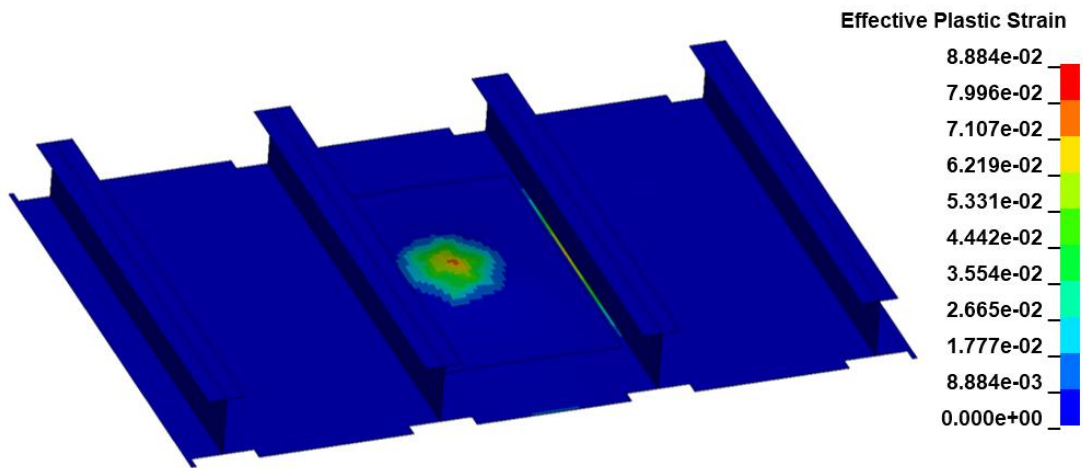


Figure 3-6. Effective plastic strain color plot relative to the dynamic simulation using pressure data from the dec 10 2015 experiment.

Table 3-2 shows maximum plastic strain, maximum indentation, permanent indentation, and maximum Von-Mises Equivalent stress (V-M stress) for all dynamic simulations.

Table 3-2. Structural response parameters for the dynamic simulation scenario.

Experiment	Max. Plastic Strain	Max. Indentation	Perm. Indentation	Max. V-M Stress
	-	mm	mm	MPa
June 27 2014	8.7%	48.6	39.2	537
Oct 16 2014	10.2%	51.2	41.9	541
Dec 15 2014	9.0%	48.4	37.2	523
Jan 20 2015	10.7%	48.4	40.6	535
Dec 10 2015	8.9%	49.4	39.2	526
Feb 25 2016	12.7%	61.7	51.6	538

In these simulations the maximum indentation always occurred at the instant when the load reached its maximum value. Also, the maximum stress values suggest the panel would not reach its ultimate stress or strain under such loads.

The force experienced at the boundary condition was studied and compared to applied experimental loads. Figure 3-7 shows a good agreement between applied load, solid (-) curve, and the load calculated at the boundary conditions, dashed (- -) curve, for the quasi-static case. For all quasi-static simulations performed, the average largest divergence between the applied load and the load calculated at the boundary conditions of the model is 2.4%. This is related to element deformation and the use of a pressure load in the simulations. As the load is applied the elements deforms, its area increases, and consequently the total force applied to the model diverges slightly from the experimentally

measured force. For these experiments this was not a concern, as the divergence is very small.

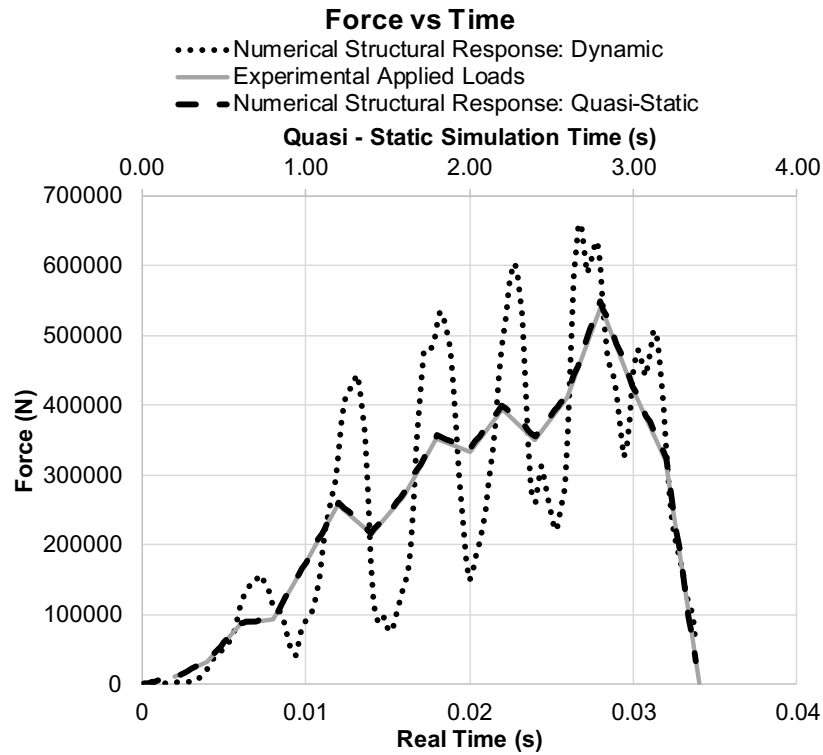


Figure 3-7. Force curves, for the simulation using the loads measured during the dec 10 2015 impact test.

The dynamic transient load curve in Figure 3-7 shows significant oscillation. This is a result of the plate vibrating in response to the applied dynamic loads. Because of this, the force response of the structure in the dynamic case (measured at the boundary conditions (BC)) is on average 21% larger than the quasi static approach. Table 3-3 shows this comparison for all dynamic simulations.

Table 3-3. Comparison of the structural force response between the dynamic and quasi-static simulations

Experiment	Response @ BC: Dynamic Case	Response @ BC: Quasi-Static Case	$\frac{\text{Difference}}{\text{Dyn. Force}}$
	kN	kN	%
June 27 2014	591	460	22%
Oct 16 2014	628	478	24%
Dec 15 2014	552	435	21%
Jan 20 2015	642	426	34%
Dec 10 2015	660	549	17%
Feb 25 2016	705	645	9%

The effects of the dramatic increase in maximum load, however, is not reflected in the following parameters: maximum plastic strain, maximum indentation, permanent indentation, and maximum stress, shown in Table 3-4.

Table 3-4. Structural response comparison between quasi-static (QS) and dynamic transient (DT) simulations.

Exp.	Max. Plastic Strain		Max. Indentation		Perm. Indentation		Max. V-M Stress	
	-		mm		mm		MPa	
	QS	DT	QS	DT	QS	DT	QS	DT
June 27 2014	9%	8%	48.6	48.6	39.2	39.2	525	537
Oct 16 2014	10%	10%	51.2	51.2	41.9	41.9	534	541
Dec 15 2014	9%	9%	48.4	48.4	37.2	37.2	525	523
Jan 20 2015	11%	11%	48.4	48.4	40.6	40.6	539	535
Dec 10 2015	8%	9%	49.4	49.4	39.2	39.2	517	526
Feb 25 2016	13%	13%	61.7	61.7	51.6	51.6	553	538

It is possible to observe in the parameters from Table 3-4 do not show appreciable difference between the two load application scenarios.

The energy study tells a different story. Figure 3-8 shows the total amount of work done by load on the structure for the Dec 10 2015 test. It shows a significant difference between the dynamic and quasi-static simulations.

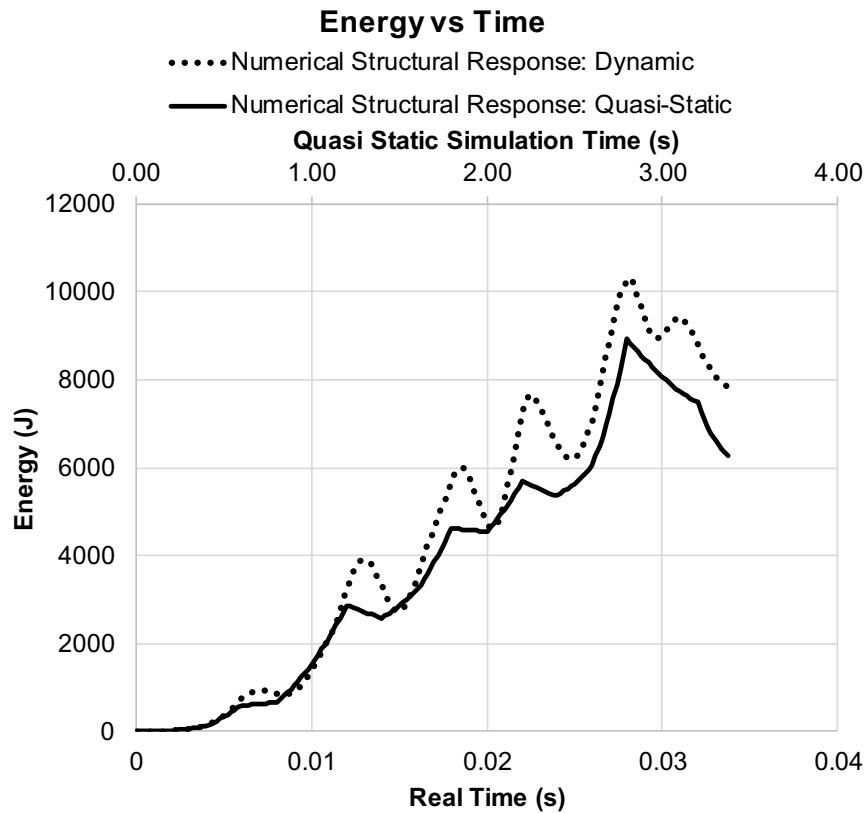


Figure 3-8. Curves for structural deformation energy (Dec 10 2015 experiment).

This behavior difference is present in all tests. Table 3-5 shows the maximum energy absorbed by the structure for all experiments.

Table 3-5. Comparison between maximum energy absorbed by the structure in the dynamic and quasi-static simulation scenarios.

Experiment	Max. Dynamic Energy	Max. Quasi-Static Energy	<u>Difference</u>
	J	J	Dyn. Energy %
June 27 2014	9096.6	8341.5	-8.3%
Oct 16 2014	10001.3	8930.3	-10.7%
Dec 15 2014	8550.4	7192.6	-15.9%
Jan 20 2015	9676.7	7786.9	-19.5%
Dec 10 2015	10308.1	8922.4	-13.4%
Feb 25 2016	15666.9	14618.4	-6.7%

3.9 Energy study of the dynamic simulations

As commented previously, it is possible to assume that during the impact experiments all the kinetic energy is transformed into crushing energy, as the other components of the double pendulum are much more rigid and suffer negligible deformation. The numerical simulations are different, as the panel model suffers significant plastic deformation. In this case the kinetic energy available is absorbed by both the ice crushing process and the structural deformation of the plate. The crushing energy is estimated by integrating the force over penetration, and the plate deformation energy is the work done by the load on the structure. The energy study focuses on the dynamic simulations. Figure 3-9 shows two curves for the Dec 10 2015 experiment:

- The Ice Crushing Energy.
- Difference: (Initial Kinetic Energy) - (Structural Deformation Energy).

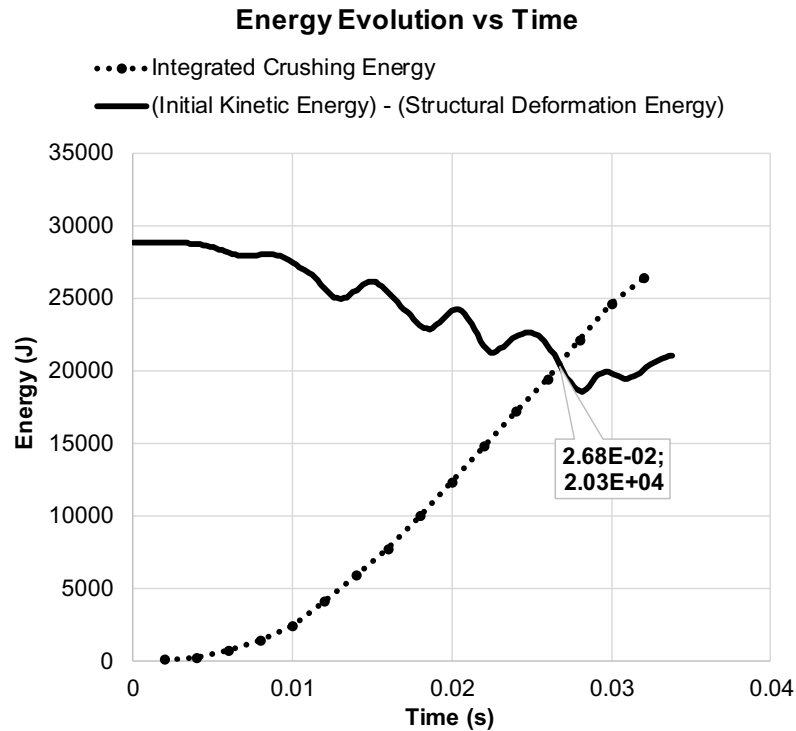


Figure 3-9. Curves showing the energy evolution in time and the point of total kinetic energy depletion (Dec 10 2015).

The crossing point between the two curves is the theoretical instant when all kinetic energy available would be absorbed by the system and it occurs before the end of the simulation, under the assumption that structural deformation and load are decoupled. At that instant, there would be no kinetic energy left to cause further ice crushing or plate deformation. For simplicity, this will be referred as the instant of energy depletion.

For the experiment shown in Figure 3-9 the total simulation time was of 0.032s and the energy depletion occurred approximately at 0.0268s of simulation time. Figure 3-10 shows the force curves, same as Figure 3-7, but includes the instant of energy depletion. Note that the energy is depleted right after the instant of maximum dynamic response.

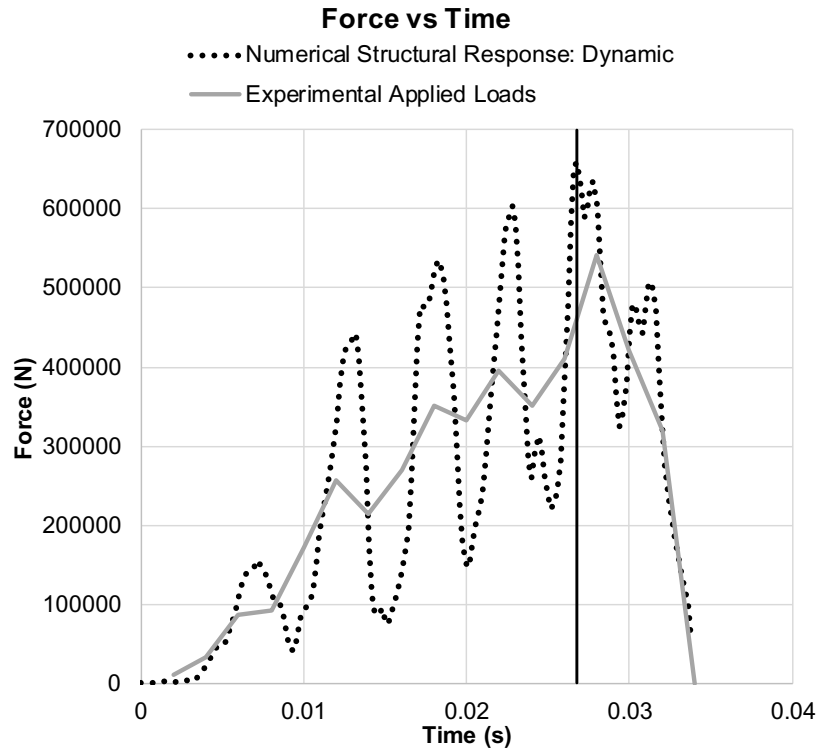


Figure 3-10. Force curves plot (Dec 10 2015) showing the instant of energy depletion (vertical line).

For all the experiments the maximum dynamic force occurs before or very close to the instant of kinetic energy depletion. This is shown in Table 3-6.

Table 3-6. Force comparison between the full impact analysis and the depleted kinetic energy scenario.

Experiments	Complete Impact: Max Force	Depleted Impact: Max Force	Difference
	kN	kN	Complete I. Force %
June 27 2014	591.00	575.36	-2.6%
Oct 16 2014	628.48	628.48	0.0%
Dec 15 2014	552.13	552.13	0.0%
Jan 20 2015	642.31	642.31	0.0%
Dec 10 2015	659.99	659.99	0.0%
Feb 25 2016	705.27	705.27	0.0%

Table 3-7 shows the maximum energy absorbed by the structure during the complete simulation duration and the energy absorbed before the moment of kinetic energy depletion.

Table 3-7. Energy comparison between the full impact analysis and the depleted kinetic energy scenario.

Experiments	Complete Impact: Max Energy	Depleted Impact: Max Energy	$\frac{\text{Difference}}{\text{Complete I. Energy}}$
	J	J	%
June 27 2014	9096.63	9044.14	-0.6%
Oct 16 2014	10001.28	10001.28	0.0%
Dec 15 2014	8550.37	8550.37	0.0%
Jan 20 2015	9676.69	9676.69	0.0%
Dec 10 2015	10308.08	10139.98	-1.6%
Feb 25 2016	15666.90	15662.17	0.0%

The results shown in Table 3-6 and Table 3-7 suggest that the experiments reach their peak dynamic load and maximum permanent deformation, before or at the instant of energy depletion.

Again, this conclusion is only valid under the assumption that the structural deformation will not affect the load applied to the structure. This of course, is not strictly true for large structural deformation, but it is a valid initial approach to simulate the structural deformation of a panel under dynamic ice loads.

3.10 Conclusion

This paper studies the effects of high spatial and temporal resolution ice pressure loads applied to a numerical model of a test panel made similar to the IROQUOIS class vessel grillage. Dynamic-transient and quasi-static analyses were performed. The numerical

design showed large local plastic deformation, and a significant difference in structural response between the dynamic and quasi-static scenarios. Additionally, an energy balance study was performed under the assumption that the ice crushing energy and energy absorbed by the deforming structure should balance with the total available kinetic energy. The following conclusions were drawn:

1. The comparison between quasi-static and dynamic simulations shows a clear response difference in the structure. The dynamic load application approach caused a significantly larger reaction force measured at the boundary condition of the model. Consequently, the structure absorbed a larger amount of energy. This caused a more extensive permanent plastic deformation. In scenarios where energy is limited, like the ice pendulum impacts, this information becomes more relevant.
2. The study of energy balance indicates that the critical stages for structural deformation would happen before or right at the instant of total kinetic energy depletion. This affirmation is solely based on the data from controlled impact events and the assumption that ice pressure development and structural deformation are decoupled from one another.

3.11 Future Work

There are a series of new analyses that the authors are working on:

- Study the evolution of actual contact area and its relation to load and energy.
- Include strain hardening effect in the material model.

- The difference of applying load patches of uniform pressure at each timestep of the simulation.
- Study the individual effects of low- and high-pressure regions.
- Introduction of lateral movement to the structure while the load is applied.
- Applying the loads on top of a stiffened region instead of the center of the plate.
- Develop a model to couple ice load and structural deformation.
- Perform experimental impacts to benchmark the simulations.

3.12 Acknowledgements

The authors gratefully acknowledge the financial support of the Natural Sciences and Engineering Research Council of Canada (NSERC) DND/CRD program; the NL Innovation Council's CRD Supplement program; NSERC's Discovery Grant program; the NL Innovation Council's IgniteR&D program; and the financial contributions of Defence Research and Development Canada (DRDC), Vard Marine Inc., and ABS

3.13 References

- Aksenov, Y., Popova, E.E., Yool, A., Nurser, A.J.G., Williams, T.D., Bertino, L., Bergh, J., 2017. On the future navigability of Arctic sea routes: High-resolution projections of the Arctic Ocean and sea ice. *Mar. Policy*.
<https://doi.org/10.1016/j.marpol.2015.12.027>
- Erceg, B., Taylor, R., Ehlers, S., Leira, B.J., 2014. A response comparison of a stiffened panel subjected to rule-based and measured ice loads, in: *Proceedings of the International Conference on Offshore Mechanics and Arctic Engineering - OMAE*.

pp. 1–6. <https://doi.org/10.1115/OMAE2014-23874>

Frederking, R., 2004. Ice pressure variations during indentation, in: International Association of Hydraulic Engineering and Research Proceedings IAHR'04, Vol.2. Saint Petersburg, Russia, Russia, pp. 307–314.

Frederking, R.M.W., Jordaan, I.J., McCallum, J.S., 1990. Field Tests of Ice Indentation at Medium Scale Hobson's Choice Ice Island, 1989, in: IAHR. Espoo, Finland, pp. 931–944.

Gagnon, R., Andrade, S.L., Quinton, B.W., Daley, C., Colbourne, B., 2020. Pressure distribution data from large double-pendulum ice impact tests. *Cold Reg. Sci. Technol.* 175, 103033. <https://doi.org/10.1016/j.coldregions.2020.103033>

Gagnon, R., Daley, C.G., Colbourne, B., 2015. A large double-pendulum device to study load, pressure distribution and structure damage during ice impact tests in the lab, in: Proceedings of the 23rd International Conference on Port and Ocean Engineering under Arctic Conditions, POAC. Trondheim, Norway, pp. 1–10.

Gagnon, R.E., Gammon, P.H., 1995. Triaxial experiments on iceberg and glacier ice. *J. Glaciol.* 41, 528–540. <https://doi.org/10.1017/S0022143000034869>

Gudimetla, P.S.R., Colbourne, B.D., Daley, C.G., Bruneau, S.E., Gagnon, R., 2012. Strength and pressure profiles from conical ice crushing experiments, in: International Conference and Exhibition on Performance of Ships and Structures in Ice 2012, ICETECH 2012. Banff, Canada, pp. 167–174.

International Association of Classification Societies, 2011. Requirements concerning Polar

Class. IACS Int. Assoc. Class. Soc.

Kamio, Z., Takawaki, T., Matsushita, H., Takeuchi, T., Sakai, M., Terashima, T., Akagawa, S., Nakazawa, N., Saeki, H., 2000. Medium scale field indentation tests: physical characteristics of first-year sea ice at Notoro Lagoon, Hokkaido. Proc. Int. Offshore Polar Eng. Conf. 1, 562–568.

Kim, E., Amdahl, J., 2016. Discussion of assumptions behind rule-based ice loads due to crushing. Ocean Eng. 119, 249–261. <https://doi.org/10.1016/j.oceaneng.2015.09.034>

Kim, H., 2014. Ice Crushing Pressure on Non-Planar Surface. Doctoral thesis. Memorial University of Newfoundland.

Quinton, B.W.T., Daley, C.G., Gagnon, R.E., 2012. Realistic moving ice loads and ship structural response, in: Proceedings of the Twenty-Second International Offshore and Polar Engineering Conference. pp. 17–22.

Riska, K., 2018. Ice edge failure process and modelling ice pressure. Philos. Trans. R. Soc. A Math. Phys. Eng. Sci. 376. <https://doi.org/10.1098/rsta.2017.0340>

Ritch, A., St. John, J.W., Browne, R., 1994. Ice Load Impact Measurements on the CCGS Louis S. St-Laurent during the 1994 Arctic Ocean Crossing - Analysis and Conclusions. Canada.

Sanderson, T.J.O., 1988. Ice mechanics: Risks to offshore structures, First. ed. Graham & Trotman, London, UK.

Sodhi, D.S., Takeuchi, T., Nakazawa, N., Akagawa, S., Saeki, H., 1998. Medium-scale

- indentation tests on sea ice at various speeds. *Cold Reg. Sci. Technol.* 28, 161–182.
[https://doi.org/10.1016/S0165-232X\(98\)00017-2](https://doi.org/10.1016/S0165-232X(98)00017-2)
- Sopper, R., Gagnon, R., Daley, C., Colbourne, B., 2015. Measurements of spatial and temporal variations in ice impact pressures, in: *Proceedings of the International Conference on Port and Ocean Engineering under Arctic Conditions, POAC*. Trondheim, Norway.
- St. John, J., Daley, C.G., Blount, H., 1984. *Ice Loads and Ship Response to Ice*. Washington, DC.
- Suominen, M., Karhunen, J., Bekker, A., Kujala, P., Elo, M., Von Bock Und Polach, R., Enlund, H., Saarinen, S., 2013. Full-scale measurements on board PSRV S.A. Agulhas II in the Baltic Sea. *Proc. Int. Conf. Port Ocean Eng. under Arct. Cond. POAC*.
- Tekscan, n.d. Can I use FlexiForce sensors to measure dynamic loads? [WWW Document]. URL <https://www.tekscan.com/support/faqs/can-i-use-flexiforce-sensors-measure-dynamic-loads> (accessed 1.10.20).
- Timco, G.W., Weeks, W.F., 2010. A review of the engineering properties of sea ice. *Cold Reg. Sci. Technol.* 60, 107–129. <https://doi.org/10.1016/j.coldregions.2009.10.003>
- Tuhkuri, J., 1995. Experimental observations of the brittle failure process of ice and ice-structure contact. *Cold Reg. Sci. Technol.* 23, 265–278. [https://doi.org/10.1016/0165-232X\(94\)00018-S](https://doi.org/10.1016/0165-232X(94)00018-S)

Chapter 4 Full-scale ship-structure ice impact laboratory experiments: experimental apparatus and initial results

4.1 Co-authorship statement

This chapter has been published as a peer-reviewed journal article: Lande Andrade, S., Elruby, A.Y., Hipditch, E., Daley, C.G., Quinton, B.W.T., 2022. Full-scale ship-structure ice impact laboratory experiments: experimental apparatus and initial results. *Ships Offshore Struct.* 1–15. <https://doi.org/10.1080/17445302.2022.2032993>.

B. Quinton designed and managed the tests program of ice impacts in non-polar class structures using the Large Pendulum Apparatus. S. L. Andrade proposed the publication of the initial results. S. L. Andrade, A. Elruby, E. Hipditch, and B. Quinton performed the experiments and data collection. S. L. Andrade performed the data analysis of the load cells and accelerometers and wrote most sections of the paper. A. Elruby performed the digital image correlation (DIC) and wrote the section regarding the DIC results. E. Hipditch measured the panel deformation. S. L. Andrade, A. Elruby, E. Hipditch, C. Daley, and B. Quinton were responsible for proposing changes to the experimental procedure to improve quality of the results. S. L. Andrade, A. Elruby, E. Hipditch, C. Daley, and B. Quinton were responsible for the paper editing and revisions.

The current version was edited to include discussion on the sampling rate and filtering of future experiments data.

4.2 Abstract

This paper presents the experimental apparatus design for, and the initial results of a series of planned laboratory full-scale dynamic ice impact experiments. The experiments aim to simulate a scenario in which an approximately 5 tonne ice feature impacts a full-scale ship stiffened hull structure at up to medium ship speed (~ 12 knots). The experiments are at full scale in the sense that the ice and structure have full scale material properties and dimensions, but the impact energy levels are in the medium-scale range. These experiments are carried out using a large double-pendulum apparatus in which one pendulum constrains and supports an ice feature, and the other constrains and supports a ship hull grillage structure. Impact speed is defined by the starting angle from which the pendulums are released. This double-pendulum apparatus is modified from an earlier configuration that was used to conduct ice cone impacts against a novel ice pressure sensor panel. Experiments involving the ice pressure sensor panel and ice cone indenters were conducted between 2014 and 2016; and achieved a maximum impact energy of 29 kJ (dropped from a 30° starting angle). Experiments involving full-scale ship hull grillage structures impacted by ice cones and other shaped steel indenters began in 2019 and are presently ongoing. In particular, a new pendulum carriage was designed and constructed to accommodate and properly constrain the ship hull grillages. This carriage provides ideally clamped boundary conditions at the perimeter of the grillage plating, as well as to the grillage stiffeners. These constraints were chosen to facilitate the benchmarking of corresponding numerical simulations. This article discusses the upgraded experimental apparatus, sensors, and experimental conditions and presents the results of three ice impacts against a stiffened

panel cut from the recently decommissioned ex-HMCS IROQUOIS (Royal Canadian Navy Iroquois class destroyer). The ex-HMCS IROQUOIS was not ice-strengthened. These impacts utilized a 1 m diameter ice cone as the impacting ice feature. All three impacts were performed at approximately a 40° starting angle which resulted in each carriage attaining a speed at impact of 3 m/s (i.e., 6 m/s relative speed). The total impact energy was approximately 46 kJ. The first ice impact had data integrity and ice cone geometry issues, and so is treated as a commissioning test. During the second impact the impact force peaked at 553.9 kN, the total impact duration was 0.055 s and the hull plating acceleration at the centre of the impacted location was a maximum of 10877 m/s². The third impact exhibited a peak force of 773.6 kN, 9691 m/s² of acceleration, and had an impact duration of 0.039s.

Keywords: Ship Ice Impact; Low Ice Class; Non-ice Class; Large Double Pendulum; Dynamic Ice Impact; ex-HMCS IROQUOIS

4.3 Introduction

The decrease in ice coverage in the Arctic Ocean will open new routes to commercial ship traffic, possibly attracting the operation of low- and non-ice class vessels; for example, the *Crystal Serenity* transited the Northwest Passage in the summer of 2016 and again in 2017 carrying more than 1500 passengers and crew. Further, low- and non-ice-class ships may be called upon in rare emergency scenarios to operate in ice-infested waters to provide search and rescue, respond to oil spills, protect sovereignty, and conduct other essential operations. In the Arctic, multi-year ice floes are still an operational risk in the summer. Such ship-ice interactions are categorized as accidental impacts, and thus it is of interest to understand ship structural strength limits under this type of scenario. Multi-year ice is sea

ice that has survived multiple summer seasons and thus has little to no brine content. This means it is much stronger than 1st year sea ice and, for the purposes of ship structural analysis, is comparable with glacial ice in terms of material properties. The compressive strength differences between 1st year ice and multi-year in the brittle range is summarized in Timco & Weeks, (2010). In general, at comparable strain- rates, 1st year ice strength is lower than multi-year ice, however as ice temperature decreases this difference also decreases. Still, ice strength can vary widely. In Jones (1997)), compressive tests at high strain rates show 1st year ice strength ranging from 8 to 12 MPa.. The same is observed in Johnston et al. (2003) borehole tests, where multi-year ice bi-axial compressive strength ranged from 3 to 40 MPa at various temperatures.

An effective way of studying the structural behaviour of ship structures under accidental loads is with explicit time-integration finite element simulations (Gagnon and Wang, 2012; Quinton et al., 2017). The experiments presented in this paper contribute to a continuous effort to study and properly benchmark ice impacts on ship structures in controlled laboratory conditions using the Large Double Pendulum apparatus built and housed at Memorial University. This equipment, originally described in Alam et al. (2012) and Gagnon et al. (2015), is currently in its second experimental program. The first program was a series of ice impact experiments that occurred between 2014 and 2016 and aimed at studying the complex interaction between an ice specimen and a rigid structure. The impact energies approached 29 kJ, relative impact velocities of 4.7 m/s, and loads reaching 620 kN (Gagnon et al., 2020). In its current design, the Large Double Pendulum can support stiffened panels from real ship structures with clamped boundary conditions, and it is

capable attaining much higher energy levels than in the previous experiments. The experiments are at full scale in the sense that the ice and structure have full scale material properties and dimensions, but the impact energy levels are in the medium scale range, as shown in Table 4-1.

This article describes upgrades to the apparatus that provide new capabilities to the pendulum and presents results from an initial set of experiments involving ice impacts against a section of real non-ice strengthened ship structure recovered from a Canadian warship, the ex-HMCS IROQUOIS (the first of the IROQUOIS-class destroyers), prior to her decommissioning in 2015.

The experiments presented in this work are the first in a series of planned ice-ship structure impacts with the objectives of benchmarking numerical ice impact simulations and studying the effect of aged steel on the strength of ship structures subjected to impact loads.

4.4 The Large Double Pendulum Apparatus

The Large Double Pendulum apparatus (see Figure 4-1) consists of two suspended pendulum carriages. One carriage holds an indenter, the other holds a stiffened structural panel (which may be referred to simply as the panel or grillage throughout this document). To generate an impact, these two carriages are initially pulled away from each other and set at a fixed starting angle. They are then released simultaneously and allowed to accelerate under the action of gravity until they strike each other at the bottom of their swings. At this point, the total potential energy of each carriage has been completely converted into available kinetic energy.

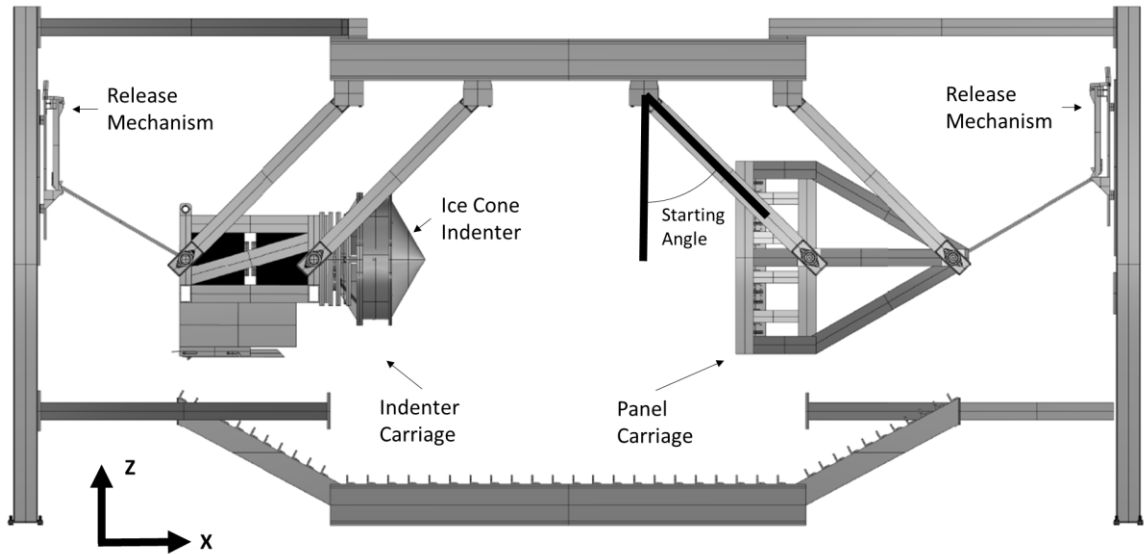


Figure 4-1. Large Pendulum schematic with some structure removed to show the carriages.

In its initial configuration (Gagnon et al., 2015), the maximum energy available from the large pendulum apparatus was limited by the maximum weight able to be supported by the electromagnetic release mechanisms. For this study these release mechanisms were upgraded and are now equipped with three electromagnets per side (originally only one per side). This has increased the maximum starting angle to 50°, measured from the vertical axis. Table 4-1 lists the theoretical range of impact speeds for the available starting angles.

Table 4-1. Theoretical carriage speed and impact energy versus starting pendulum angle.

Pendulum Angle	Pendulum Speed	Kinetic Energy Indenter Carriage ¹	Kinetic Energy Panel Carriage ²
Degree	m/s	kJ	kJ
5	0.386	0.396	0.350
40	3.030	24.351	21.528
50 (max)	3.744	37.180	32.870

¹When loaded with an ice indenter the total Indenter Carriage (IC) mass is 5305 kg.

²When loaded with a structural panel the total Panel Carriage (PC) mass is 4690 kg.

During impact, a very small amount of kinetic energy may be lost to gravitational potential energy if the impact is slightly off centre and/or there is significant interpenetration of the ice and the structure during the impact, since, as the pendulum passes the point of maximum kinetic energy, each side will gain elevation again. These losses are however much smaller when compared to the energy absorbed due to panel deformation and/or ice crushing.

4.5 Ice impact experimental setup

The three experiments presented here were performed with two different ice cone indenters. The impacts were performed against the same ex-HMCS IROQUOIS panel, however, each experiment was slightly different as described below. The first impact experiment had a few procedural problems that resulted in test results much different than originally intended. This included damage done to the ice sample during installation in the pendulum and a failure in the data acquisition process that resulted in the loss of the impact force data. We are including discussion of this test because some damage to the panel was evident, and therefore influenced the response of subsequent two panel impact experiments. The second impact experiment proceeded as planned with a well-formed ice cone and good quality of recorded data. The third experiment was conducted by resetting the pendulum and re-using the damaged ice cone from the second experiment. This was done because it was known from previous laboratory ice structure interaction experiments that damaged ice cones can induce higher impact loads due to the flat impact surface, as reported in Gagnon et al. (2020).

4.5.1 Ice cone indenters

The ice cones were prepared in accordance to the method described in Gudimetla et al. (2012). They have a base diameter of 1 m, base angle of 30°, and are prepared and stored at -15°C. Gudimetla et al. (2012) reports that the ice cone nominal pressure at maximum indentation force was 14MPa for a conical specimen. Similar cones were used in impact experiments by Gagnon et al. (Gagnon et al., 2020) and, although not a true compressive test, maximum average pressures ranged from 6.6 to 11.4 MPa. These values are within the upper range of ice compressive strength (including iceberg, 1st year ice, and old ice) as reported in different works (e.g. Timco & Frederking 1983; Jones 1997; Jones et al. 2003; Jones 2007; Timco & Weeks 2010). For example, Sinha (1985) performed confined compressive strength in second year ice and recorded values ranging from 7 to 15 MPa, and Jones (1997) reports 1st year ice compressive strength ranging from 8 to 12 MPa.

Timco and Weeks (2010) discuss that the main difference between old ice and 1st year ice compressive strength is mainly its consistency for different temperatures. While 1st year ice strength can vary widely depending on temperature (as temperature affects brine pockets size), multi-year ice is generally consistently comparable to laboratory freshwater ice in terms of compressive strength. The ice cones used in the experiments reported in this work are produced as to obtain consistent properties. During their manufacturing, trapped internal stresses are reduced by favouring oriented heat transfer, freshwater ice is used (brine is not present), crystal size is controlled, and *c*-axis are randomly oriented by seeding the specimen.

The ice cone used in Impact 1 was damaged prior to the experiment. Its tip was blunted to a flat surface during the installation in the indenter carriage (IC). As discussed below, this blunting resulted in a “truncated cone” geometry instead of a “sharp-tipped” cone geometry. This completely changed the ice failure process compared with the sharp-tipped cone failure process that we desired for these experiments. The ice cone used in Impact 2 was undamaged and well-shaped, and as discussed above, Impact 3 re-used the ice cone utilized in Impact 2. These geometric differences are illustrated in Figure 4-2 and in section 4.11 Appendix A.

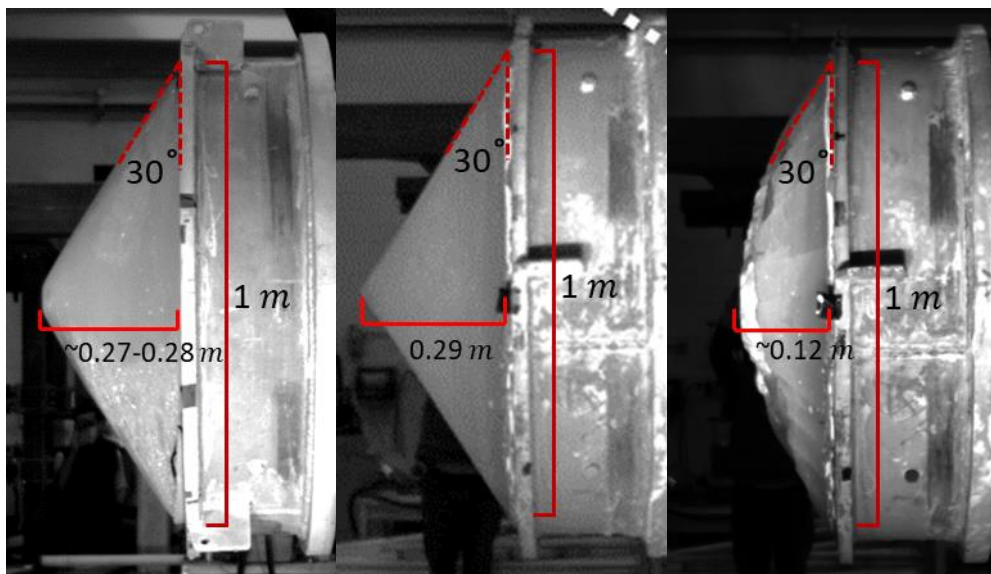


Figure 4-2. Impact 1 pre-damaged “truncated” cone (left), Impact 2 sharp-tipped cone (centre), and Impact 3 re-used cone (right).

4.5.2 Panel carriage design

For these initial experiments, and further upcoming experiments, a “panel carriage” (PC) was designed (Quinton, 2017), fabricated and installed. It is shown in Figure 4-3.



Figure 4-3. Panel Carriage.

The panel carriage provides clamped boundary conditions at the perimeter of the panel's plate and to the ends of the panel's transversal frames. The carriage can accommodate plates stiffened with three or four frames oriented vertically or horizontally. The panel can also accommodate unstiffened plates. A 2.54 cm (1 inch) x 7.62 cm (3 inches) perimeter bar is welded to the plate perimeter (shown in Figure 4-4). The bar fits into a recess of the ringframe (Figure 4-5). The ends of the stiffeners have 2.54 cm (1 inch) thick plates welded to them (shown in Figure 4-4). The perimeter bar is bolted to the ringframe using 156 Grade 8 bolts torqued to 108.4 Nm (80 lbf-ft). Each stiffener end is bolted to frame with 12 Grade 8 bolts. A 1.26 cm (1/2 inch) removable steel spacer is fitted between the stiffener end plate and ringframe to facilitate release of the panel after the impact. The fitted panel is illustrated in Figure 4-6.

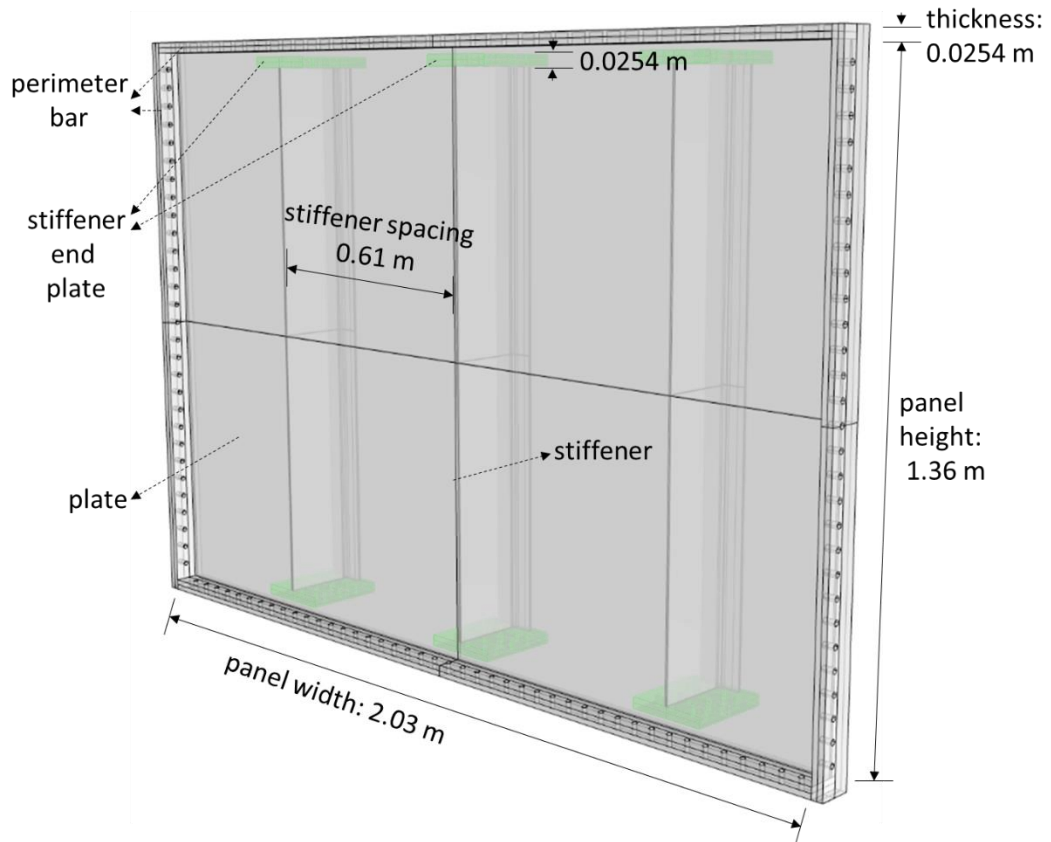


Figure 4-4. ex-HMCS IROQUOIS panel illustration. Perimeter bar is seen represented in the drawing (grey bar with bolt holes around the plate perimeter). The stiffener end plates are also shown (green).

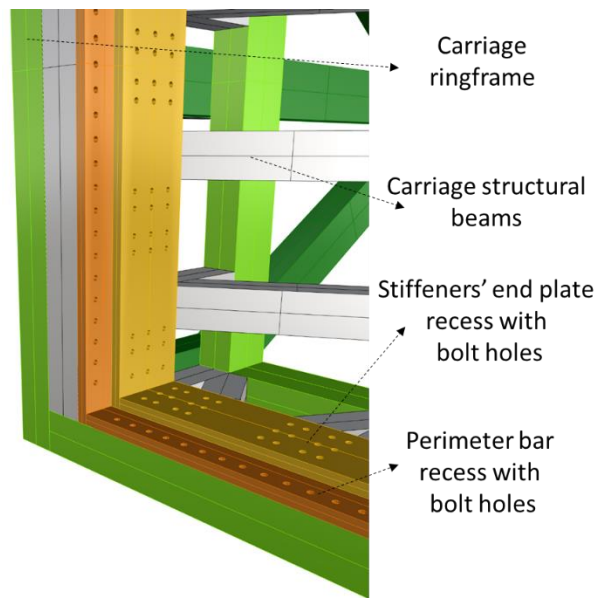


Figure 4-5. Corner of the ringframe showing the recess locations where perimeter bar is clamped with bolts (orange) and, similarly, where the stiffener plates are clamped (yellow).

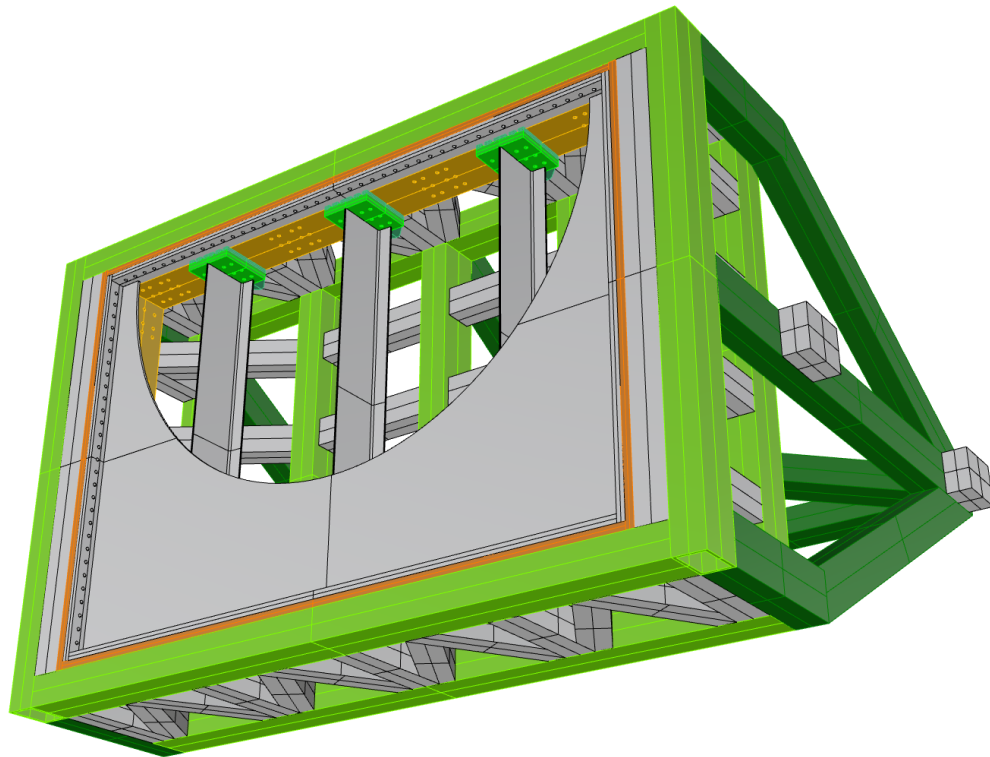


Figure 4-6. Cutaway view showing the fitted panel. Note how stiffener end plates and the perimeter bar align with the bolt holes in the ringframe of the carriage.

All physical experiments described here were specifically designed to provide data for numerical model benchmarking. While the panels tested are, in fact, full-scale sections of ship structures, it is realized that the clamped boundary conditions provided to the Panel plating and frames by the panel carriage are much stiffer than the real boundary conditions provided to a similar panel forming part of the structure of a much larger ship. Rather than try to predict and emulate the boundary conditions that a panel would experience as part of a larger ship structure, it was decided to apply “ideal” boundary conditions to the perimeter of the Panel plating and the ends of the panel frames. Clamped boundary conditions were chosen. This design choice facilitates the preparation and comparison of numerical models of the experiments with the experimental data. Once validated against experimental data, the numerical models can then extrapolate the structural behaviours of larger ship structures.

4.5.3 Test panel details

The HMCS IROQUOIS was decommissioned in 2015. In early 2018, Memorial University of Newfoundland received 6 sections of the side shell cut from approximately the midships location. The uncut panels consist of hull plating, stiffeners, and frames. To fit them into the Panel Carriage, the uncut IROQUOIS panels were trimmed to the required size and outfitted with stiffener end plates and plate perimeter bars. The web frame spacing is slightly larger than the carriage ringframe dimensions, thus the web frames are not included. The experiments reported in the current work relate to the panel originally located at approximately amidships; specifically, between frames 28-29 and longitudinals 20-22 of the ex-HMCS IROQUOIS.

The panel as modified to fit into the panel carriage had plate dimensions 2.032 m in the horizontal direction by 1.36 m in the vertical direction with three 7"x4"x8.60lbT stiffeners running vertically and spaced 610 mm (2 ft) apart from each other. The middle stiffener was located at the centre of the plate (as illustrated in Figure 4-7). The horizontal distance from the edge of the plate to the outside stiffeners was 406 mm. The plate final dimensions are illustrated in Figure 4-7. The plate thickness is 8 mm (5/16th inch) and is made of CSA G40.21 260WT Cat 5 steel, while the stiffeners are made of CSA G40.21 260WT Cat 3 steel. The panel is shown fitted in the carriage in Figure 4-8. The impact occurred at the centre of the panel and coincided with the location of the middle frame.

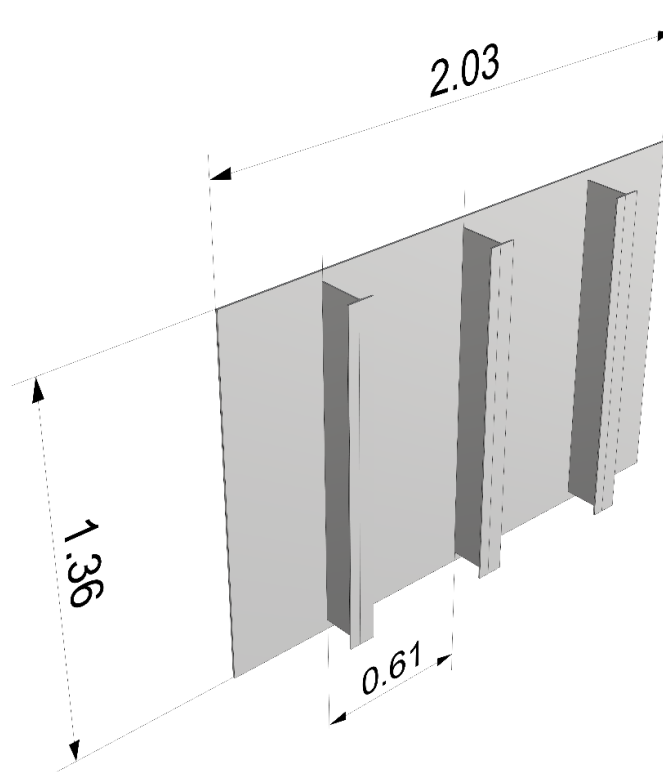


Figure 4-7. CAD drawing of the ex-HMCS IROQUOIS panel (shown in metres). Perimeter bars and stiffener end plates are not shown.

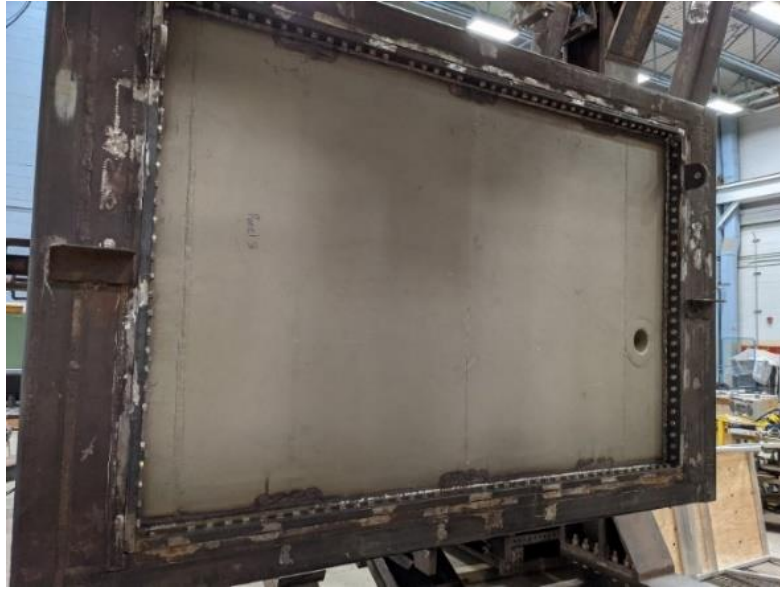


Figure 4-8. The ex-HMCS IROQUOIS panel in the test carriage (right).

For archiving purposes, the ex-HMCS IROQUOIS panel after being cut and fitted into the Test Carriage was named as IROQ1.

4.5.4 Sensor array

Figure 4-9 illustrates the locations of the sensors installed in the carriage. The impact force was collected by an array of three 1.2 MN Kistler 9091B piezoelectric load washers located behind the Indenter (i.e., between the indenter carriage and the indenter mounting plate). Panel impact acceleration in the X-direction was measured by placing a Kistler 5000g accelerometer on the stiffener side of the panel plate at the centre of the impacted plate area next to the central stiffener. A 500g accelerometer was installed at the back of the indenter carriage to measure carriage rigid body acceleration.

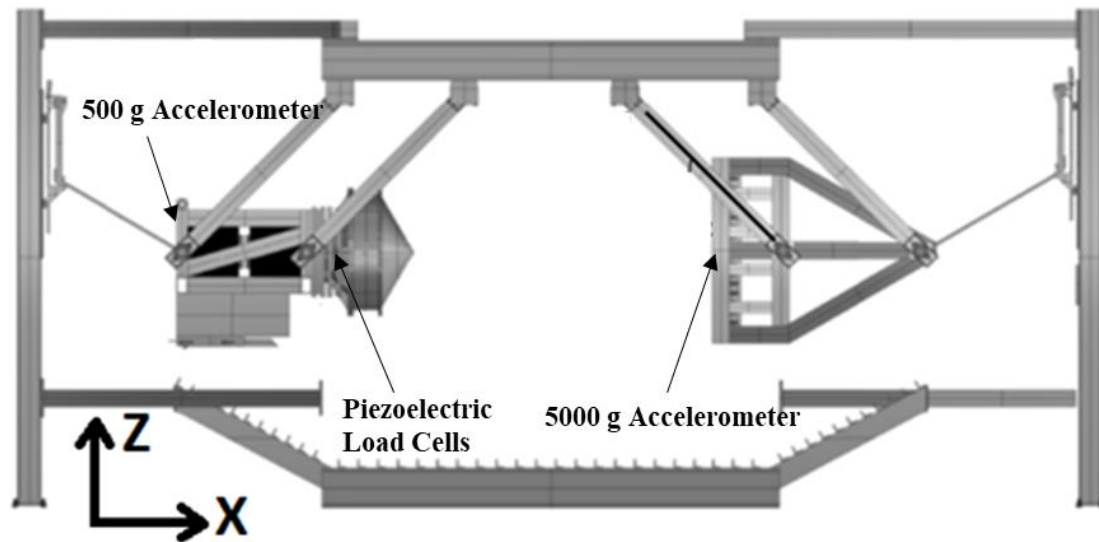


Figure 4-9. Location of the accelerometers and load cells in relation to the pendulum components

Load Cells and accelerometers are connected to the same data acquisition system (DAQ) recording at 5000 samples per second, so the reference time for all data streams is the same. The High-Speed Cameras (HSC) are controlled by another computer system however, with different computer clock times. Both systems' recording is manually started with different triggers. Data from these two systems are thus required to be manually synchronized.

4.5.5 High speed imaging

The image/video capture of the three impact tests was conducted utilizing two individual high speed (HS) cameras combined with digital image correlation (DIC) for measurements. Mega Speed industrial cameras were used namely, the MS 130K models. An individual camera was used to record the movement of each pendulum. The cameras were positioned perpendicular to the plane of carriage motion with their principal focal axis aligned to each

carriage at impact. This was necessary to provide best accuracy of measurements for each pendulum. The high-speed cameras are shown in Figure 4-10.

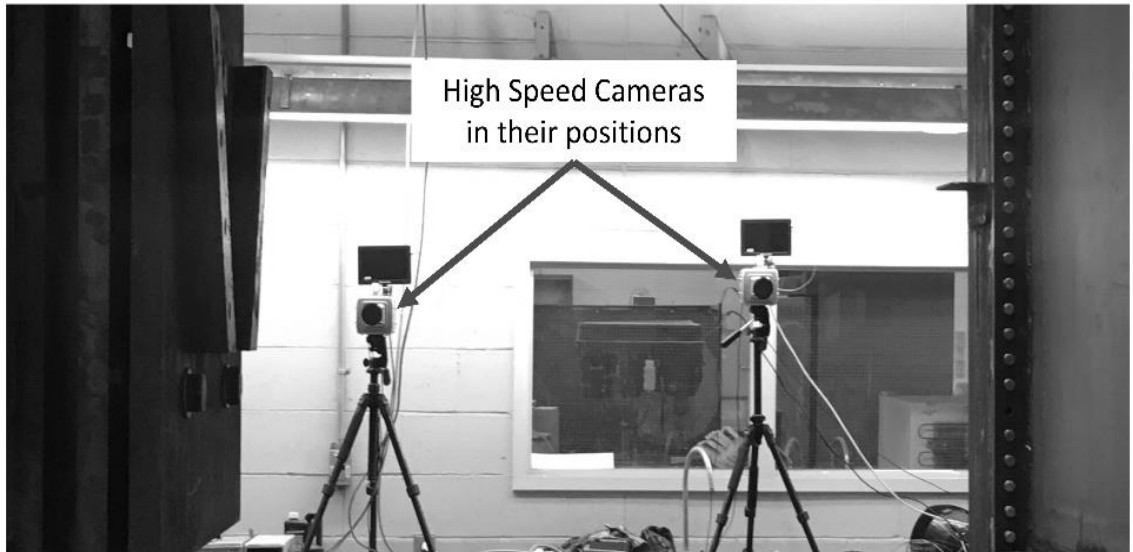


Figure 4-10. High speed cameras positioned perpendicular on each pendulum side for capturing the test.

The HS cameras were set to record at 1,000 frames per second (fps). Laser cut circular reference (points) markers were placed on each carriage to facilitate measuring the displacements, and calculation of the velocities and accelerations of the carriages at different positions using digital image correlation (DIC), as shown in Figure 4-11. The software GOM Correlate Professional 2017 was used for DIC measurements to analyse the impacts.

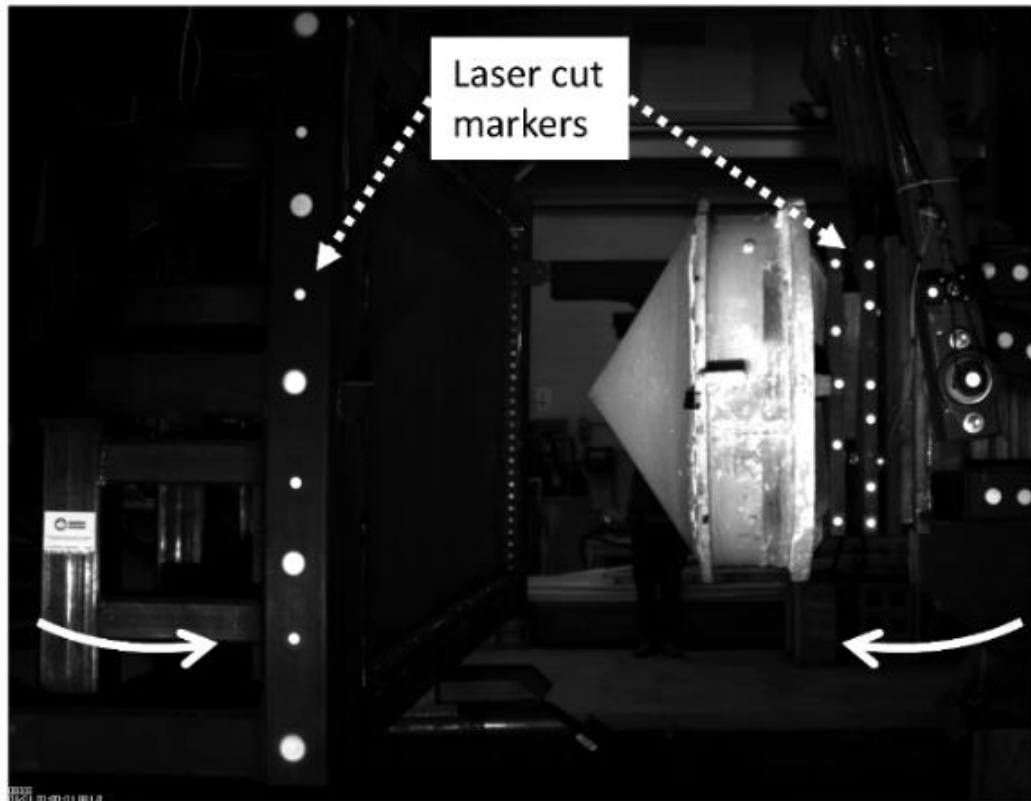


Figure 4-11. Image showing the movement direction and the laser cut markers for DIC measurements.

4.5.6 Experimental setup summary

Table 4-2 contains a description summary of the three ice impacts experiments performed against the IROQ1 panel.

Table 4-2. Experimental setup summary.

Experiment	Date	Panel type	Indenter type	Sampling rate DAQ ³ /HSC ³	Drop Angle PC ⁴ /IC ⁴	Weight PC/IC	Potential Energy
				Hz	degree	kJ	kJ
Impact 1	12/09/20	IROQ1	Ice cone ¹	5k / 1k	38.6 / 38.6	4690 / 5305	42.84
Impact 2	02/05/21	IROQ1	Ice cone	5k / 1k	40.5 / 40.6	4690 / 5305	47.1
Impact 3 2 nd strike	02/05/21	IROQ1	Ice cone ²	5k / 1k	40.3 / 40.6	4690 / 5305 ⁵	46.82

1. The ice indenter had its tip truncated during handling.
2. Impact 3 is a repeated impact. The ice indenter is the damaged cone from Impact 2.
3. DAQ, data acquisition system, refers to sensors in the pendulum (accelerometers, rotary encoders, load cells). HSC refers to high speed cameras.
4. PC (Panel Carriage) refers to pendulum carriage with the test panel. IC (Indenter Carriage) refers to pendulum carriage with the indenter.
5. Approximate ice carriage weight, as some ice was lost in the previous impact. This weight loss was estimated to be less than 2% of the total carriage weight, as the total mass of the ice cone is approximately 70 kg.

4.6 Load cell, accelerometer and DIC data

As described in the previously, three impact experiments were performed, Impact 1 and 2 were performed with a fresh cone, and Impact 3 is a 2nd strike using the damaged indenter from Impact 2.

The experiments can be divided into three phases: Swing phase, Impact Phase, and post-Impact Phase. The swing phase starts from the moment the electromagnetic release mechanisms are activated and ends at the moment of initial contact between indenter and the ex-HMCS IROQUOIS panel. The impact phase starts at the instant of initial contact and ends with the end of this contact. The post-impact phase starts at the end of the contact

and ends after the pendulums have ceased to move and are locked by their braking mechanisms. Figure 4-12 illustrates the experimental phases in relation to data curves from two accelerometers and the combined load cell curves. Note: as impact force is measured from an array of three piezoelectric load cells (as discussed above), the total impact force is the sum of the individual forces from each load cell.

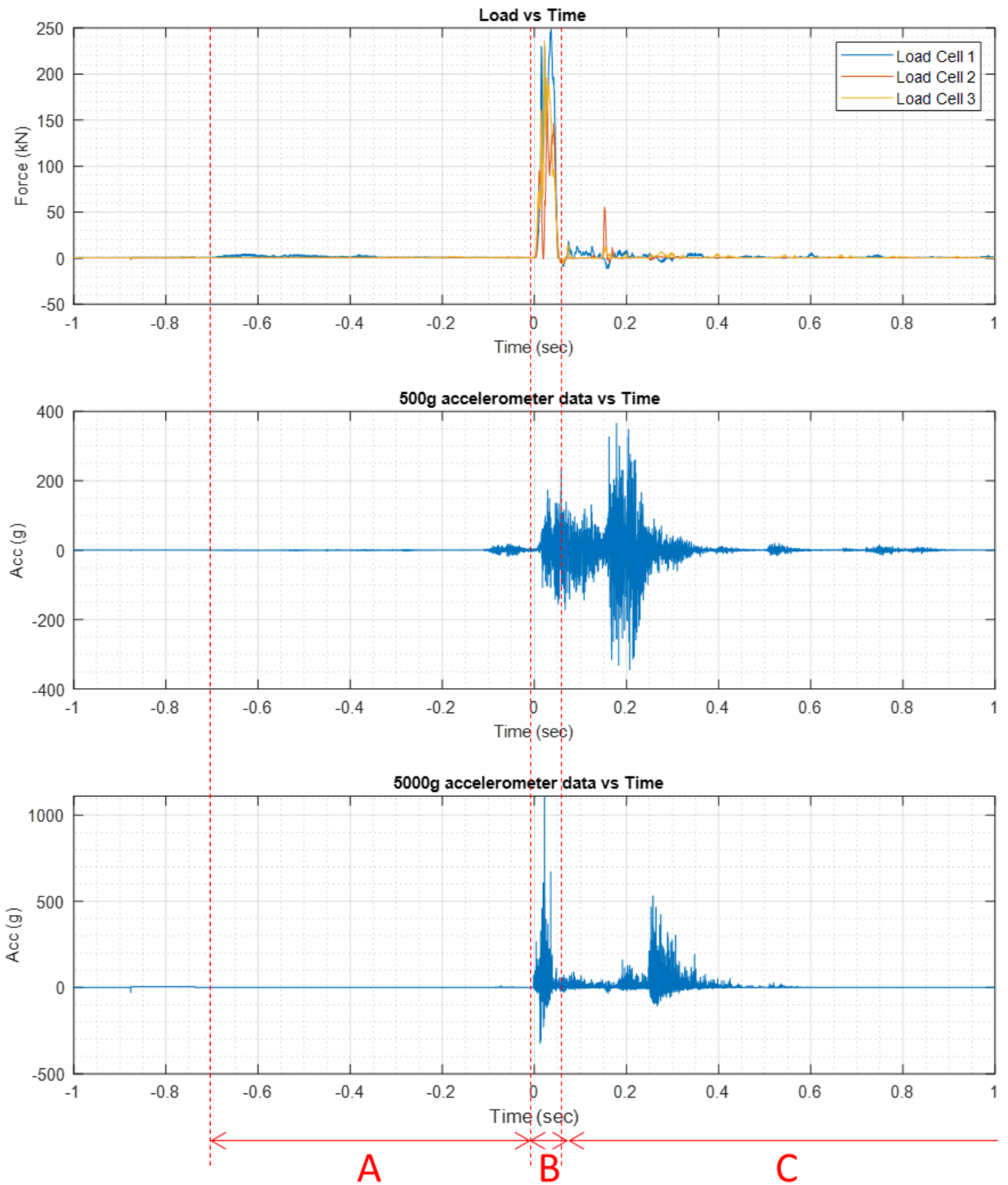


Figure 4-12. Experiment phases. A is the swing phase; B is the impact phase; C is the post-impact phase (Impact 2 shown here).

When dropped from a 40° starting angle, the pendulum's period (T) should theoretically be 2.964 s. The duration of the swing phase should then be 0.73 s (or $T / 4$). The DIC analysis confirms this. The 5000g accelerometer located behind the panel is the closest sensor to the initial point of impact, thus it is used to determine the instant at which contact occurs. Figure 4-13 shows the instant when the first spike is observed in that accelerometer.

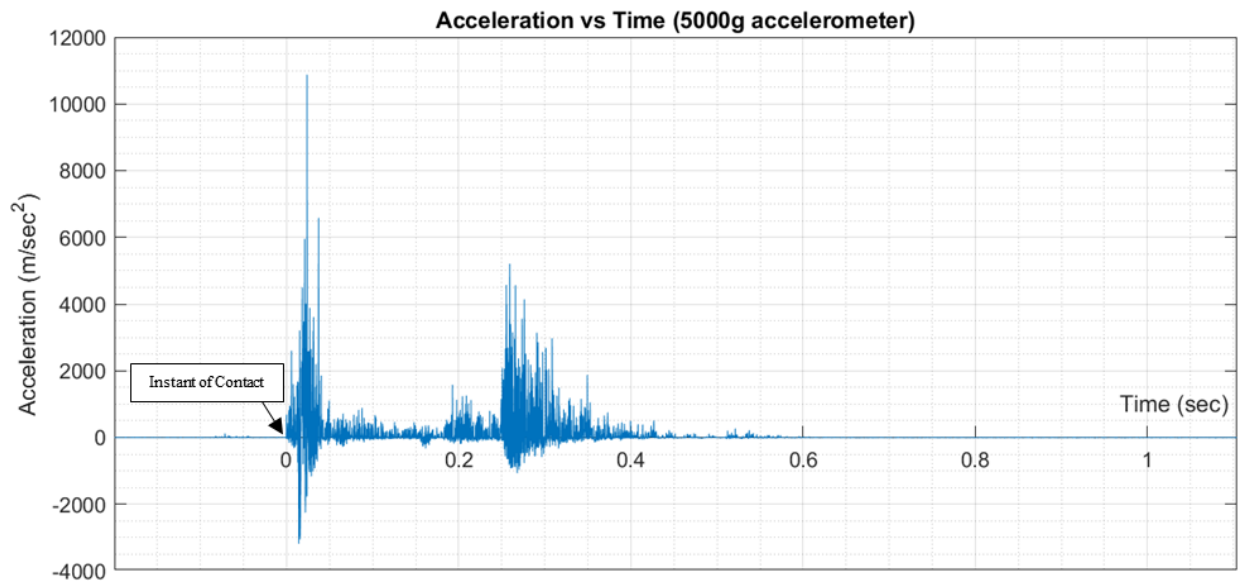


Figure 4-13. The 5000g accelerometer data for Impact 2. The instant of contact is also noted.

The denoted instant of contact marks the beginning of the impact phase and defines a standard time origin for all data in the experiment. The piezoelectric load cells are used to determine the end of the impact phase, since they have an extremely low response time and are not naturally excited by the vibrations arising from the impact (they have very low hysteresis and very high natural frequency, as stated previously). In Impact 2 the contact ends at approximately 0.0554 s, as shown in Figure 4-14.

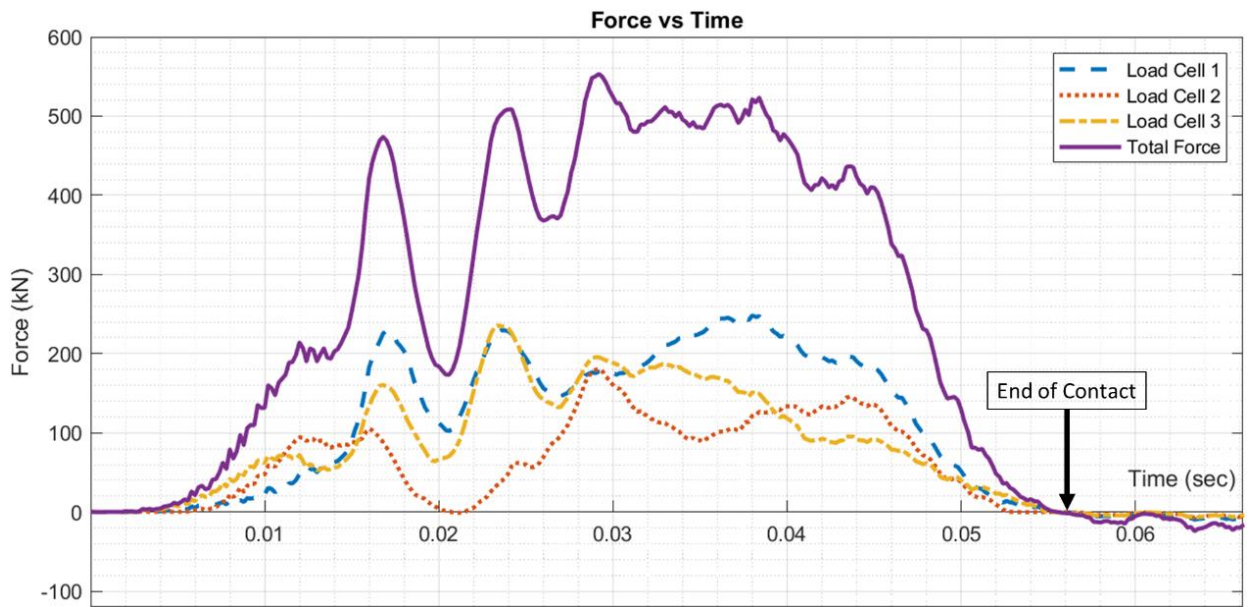


Figure 4-14. Impact force data for Impact 2.

There is a small but noticeable delay between the times when each of the three sensors show their initial response to the impact. By studying the data from impact 2 it was observed that the piezoelectric load cells measurements start to change from their baseline values roughly 1.8 ms after the 5000 g accelerometer reacts to the impact. The delay for the 500g accelerometer is even larger than that of the load cells (which is the sensor that is located furthest from the point of impact and is located on the trailing side of the ice indenter carriage), but it is harder to pinpoint exactly due to noise. This delay can be seen in Figure 4-15.

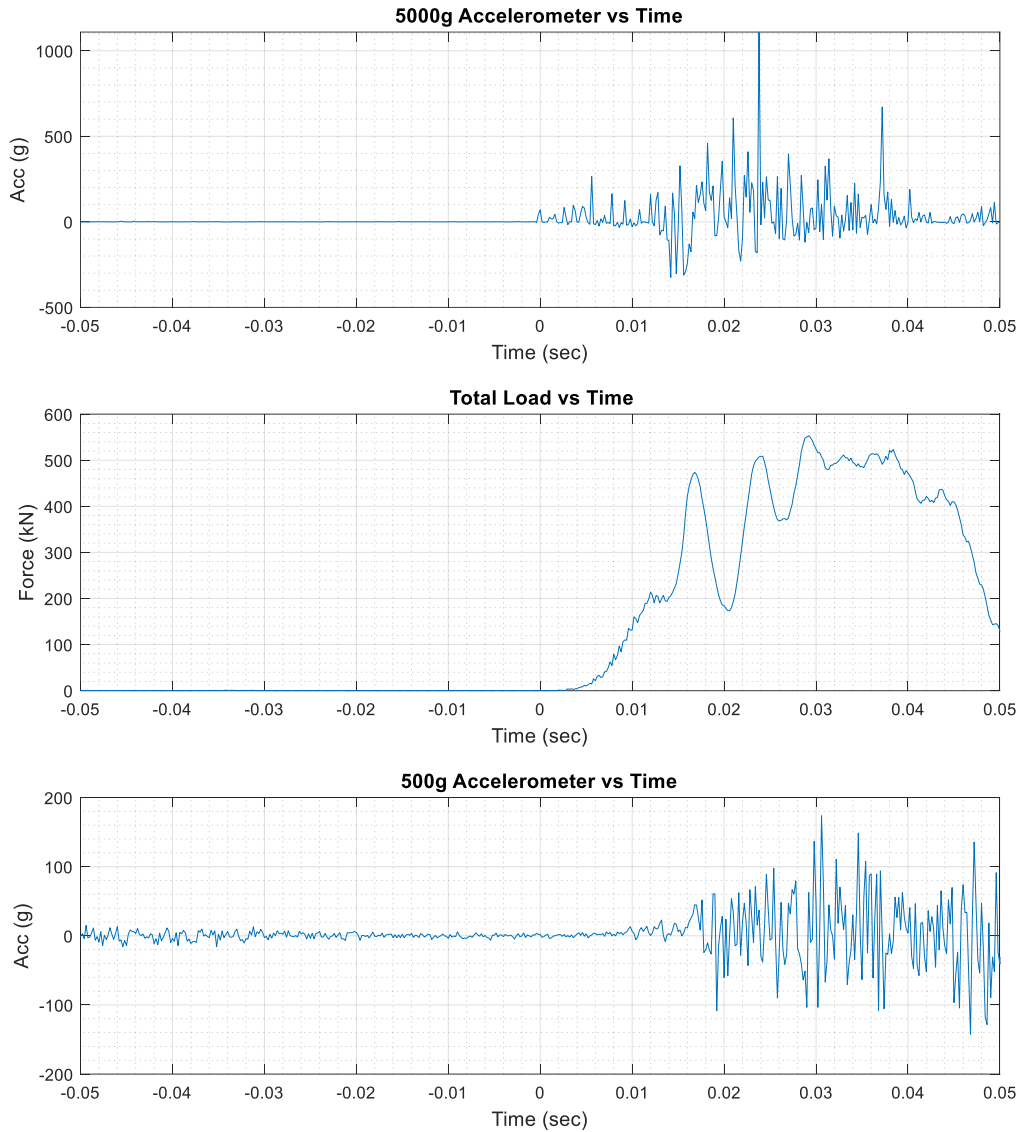


Figure 4-15. Delay difference between the sensors (Impact 2).

4.6.1 Peak load and accelerations

The load cell and accelerometer data curves for Impact 1, 2, and 3 are presented in section 4.12 Appendix B. Table 4-3 summarizes peak load and accelerations observed in each impact.

Table 4-3. Peak Load and Peak acceleration for the 3 experiments.

Experiment	Impact duration	Peak / Average ¹	Peak / Average ¹ acceleration	
			(500g acc.)	(5000g acc.)
	ms	kN	m/s ²	m/s ²
Impact 1	~ 60.0 ²	N/A ¹	2008 / 8	45987 / 107
Impact 2	55.4	553 / 282	3585 / 41	10877 / 375
Impact 3	39.2	773 / 348	4899 / 45	9691 / 348

1. for the duration of the impact.
2. Load Cell data was unavailable for Impact 1.
3. Value estimated based on HS camera results and accelerometer data.

As previously described, Impact 1 ice cone was truncated, which caused its behaviour to significantly change. In the case of Impact 2 there was enough ice cone left to afterwards perform a 2nd subsequent impact, but Impact's 1 ice cone was completely destroyed after a single experiment and could not be used for a second strike (this difference can be seen in section 4.11 Appendix A). Variability in ice properties is not enough to explain this behaviour, thus the authors believe that this can be partially attributed to the Impact 1 cone's flattened tip. The flattening of the ice cone tip was caused by accidental contact melting that occurred during its installation in the carriage. After the ice cone was installed, the carriage was slowly lowered to its resting position, and it contacted the panel surface. This basically turned the originally tipped ice cone into a truncated ice with flat surface composed solely of intact ice. Furthermore, the authors have observed similar behaviour during previous test programs conducted using cones that were truncated (i.e., flattened) by design (e.g., Habib et al, 2014). Impact 1 also caused the 5000g accelerometer on the panel to reach its saturation limit. However, it caused significantly less damage to the plate

when compared to the others experiments as presented in Figure 4-18. Unfortunately, load data for Impact 1 is not available (as discussed above).

The accelerometer data requires some discussion. The 5000g accelerometer was installed on the plating at the location where indenter and plate first make contact and does not represent the rigid body acceleration of the indenter carriage. Instead, it measures the acceleration of the panel's plating at the point of impact. The 5000g accelerometer shows an extremely high peak value (as 45987 m/s^2 for the truncated cone impact (i.e., Impact 1)). This acceleration dissipates quickly (0.4 ms) as shown in the 5000g accelerometer data for Impact 1 in section 4.12 Appendix B. The same behaviour can be observed in the other impacts, but the peak values are not as high.

The 500g accelerometer measures the rigid body motion of the indenter carriage. In this case, one would expect that the peak and average measured accelerations would compare well with the peak and average measured impact forces. The measured peak 500g acceleration for, e.g., Impact 2, of 3585 m/s^2 suggests a peak force of approximately 19 MN. This is clearly incorrect as the measured peak force for Impact 2 is 553 kN. The average accelerations observed by the 500g accelerometer yield more agreeable results when compared to the average load, e.g., for impact 2, the average acceleration of 40.9 m/s^2 translates into an average force of 217 kN for that carriage, while the average measured force is 282 kN.

The authors are presently investigating the cause of this discrepancy, and the magnitudes of the measured accelerations presented here should be regarded with scepticism. Possible causes of this discrepancy include: the accelerometer mounting might not be as rigid as

intended changing the natural frequency of the sensor; the ballast weights might be imparting shock as they shifted during the impact (this has since be fixed); external noise might be influencing the peak values recorded by the sensors; the accelerometer may require recalibration; finally, a sampling rate of 5 kHz was later determined to be insufficient to properly capture the acceleration data. It should be noted here that significant upgrades to the measurement of accelerations in the large pendulum apparatus were instituted (as described below in the Future work, section 4.9) after these experiments were completed.

4.6.2 High-speed camera and DIC results.

The results from the digital image correlation (DIC) for impact 2 are presented here. The results are not synchronized with the previously established timeline, but instead are synchronized with the first image recorded by the HS cameras. The rigid body carriage motion results from the analysis of Impact 2 are presented in Figure 4-16 (a) and (b), respectively. The horizontal axes represent the time in seconds while the left vertical axis is used for both displacements and resultant velocities which are measured in mm and mm/s, respectively. Finally, the second vertical axis is employed for resultant acceleration measurements in mm/s^2 .

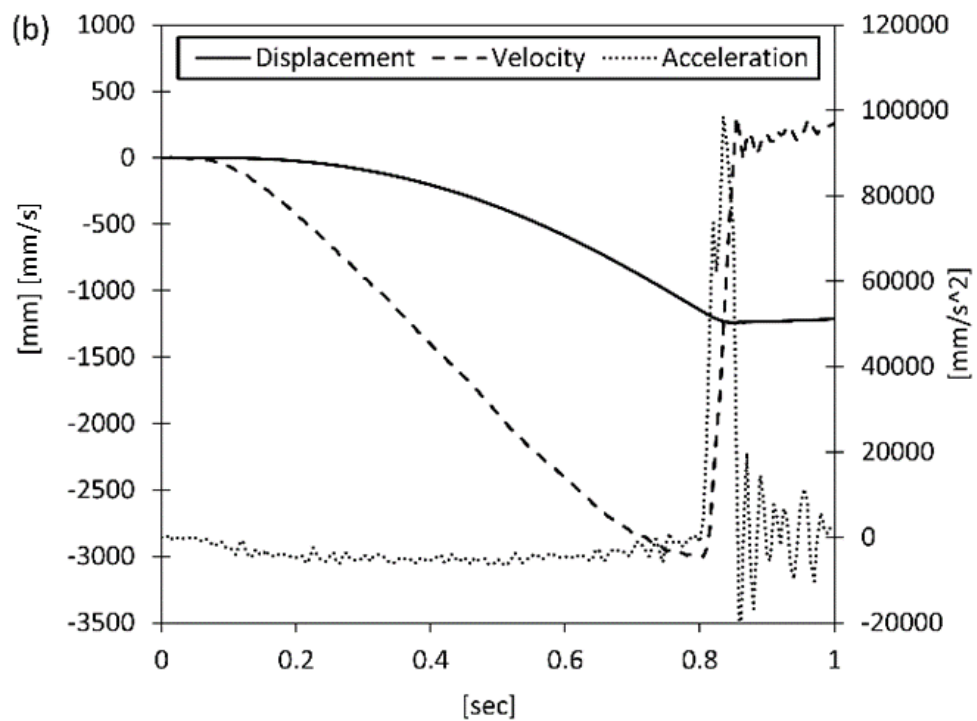
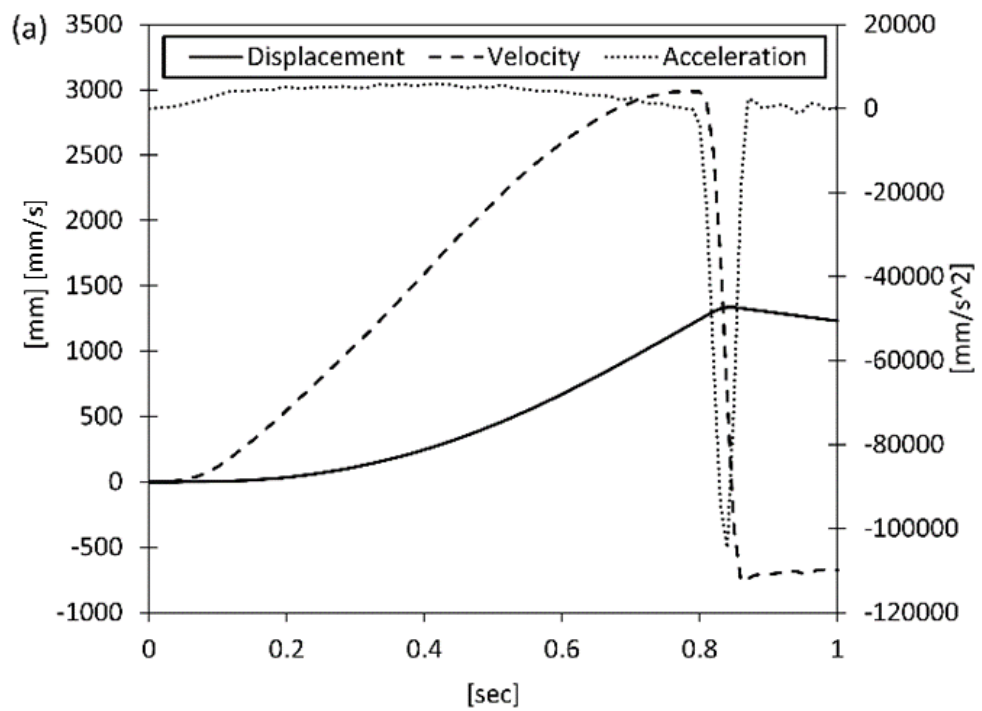


Figure 4-16. DIC measurements (Impact 2): (a) Panel carriage (b) Ice cone carriage.

Due to the chosen coordinate system the IROQ1 panel side (Figure 4-16 (a)) and the ice cone side (Figure 4-16 (b)) show positive and negative values, respectively, as they are moving in opposite directions. The resultant speed of each side reaches a maximum of 3 m/s at the instant of impact. Therefore, the relative impact speed between the carriages is approximately 6 m/s.

4.6.3 Ex-HMCS IROQUOIS panel deformation

In this section the progressive damage done to the same test panel during these three impacts is evaluated. The residual indentation depth measurements were obtained using a for-purpose jig placed on the two small “shelves” shown on the front of the ring frame in Figure 4-17. The jig provides a consistent basis for residual dent depth measurements taken using a metric tape measure.

A horizontal reference axis was used for measuring the indentation depths of subsequent impacts, Figure 4-17. The reference axis was centred horizontally on the panel and consisted of 11 measurements taken along this axis 200 mm apart, with the point of impact being the centre point (point 6) Figure 4-18 is a graphical representation showing the progressive indentation on the panel.

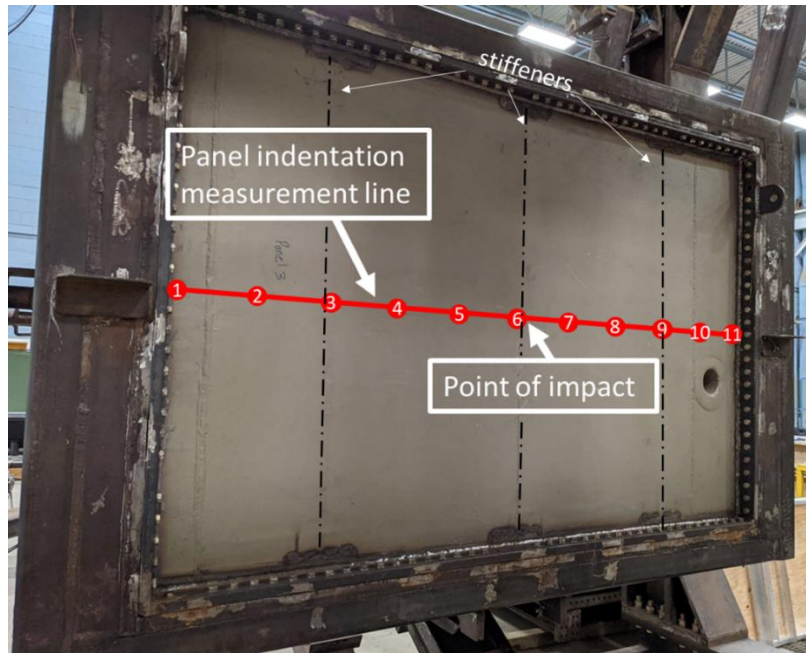


Figure 4-17. Representation of panel indentation measurement axis and location. Jig “shelves” shown on the left and right faces of the ringframe.

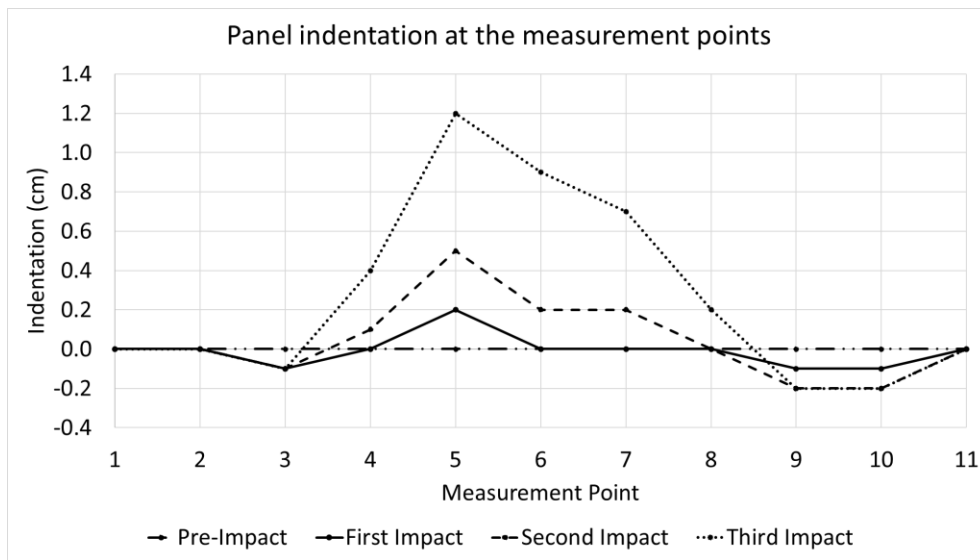


Figure 4-18. Representation of the test panel IROQ1 progressive indentation through the impact experiments. The X-axis shows the points where indentation depth measurements were taken on the panel, as illustrated in Figure 4-17. The Y-axis shows the measured displacement of those of points. The different lines illustrate the panel deformation after each impact.

When impacted with a new ice cone (Impact 1 and 2), the damage was small compared to the damage done by the second-strike cone (Impact 3). For all ice cone impacts, larger indentation depths occurred in the plating (point 5) to the left of the central frame (point 6). This was expected as impacts were centred on a frame (point 6) which has greater resistance to deformation than the adjacent plating. The fact that the left side was preferred was a function of the ice failure process and the panel geometry in this case.

Generally, the panel deformation was not significant for any of the impacts, as permanent deformation was observed mostly in the plating (point 5) adjacent to the central stiffener; and even then, with generally small depth. The section 4.13 Appendix C shows a compilation of photographs taken from the panel before and after impact. Regarding the stiffener, no damage to welds or out of plane deformation was observed in any of the sequential impacts. Regarding the boundary conditions, subsequent impact experiments using rigid indenters resulting in much higher forces have been modelled using finite element analysis (in publication). Those results clearly demonstrate that the boundary conditions behave very well as approximations of ideal clamped boundary conditions.

4.6.4 Ice behaviour, carriage displacement, and energy analysis

Ice load values are within expected range. Impact 2 and Impact 3 had peak loads of 553 and 773 kN respectively. Gagnon et al. (Gagnon et al., 2020) reports peak loads ranging between 415 to 621.5 kN for their impact experiments for ice against a rigid indenter.

Ice cone crushing behaviour was according to expectations, but not consistent. As discussed in section 4.6.1 and shown in section 4.11 Appendix A, the truncated cone from Impact 1 was nearly obliterated. This is different from Impact 2, which had sufficient residual ice to

be reused for a second experiment. While using a truncated cone was not originally intended for Impact 1, once it was noticed that the cone was indeed truncated prior to impact, the ice behaviour observed in Impact 1 was indeed expected, as similar behaviour has been observed previously using purposefully truncated cones in controlled compression tests as well as and pendulum experiments using a small-scale pendulum similar to the one described above.

A useful aspect of the DIC analysis is that it allows the relative separation between the carriages can be determined from the high-speed video. This is exemplified in Figure 4-19.

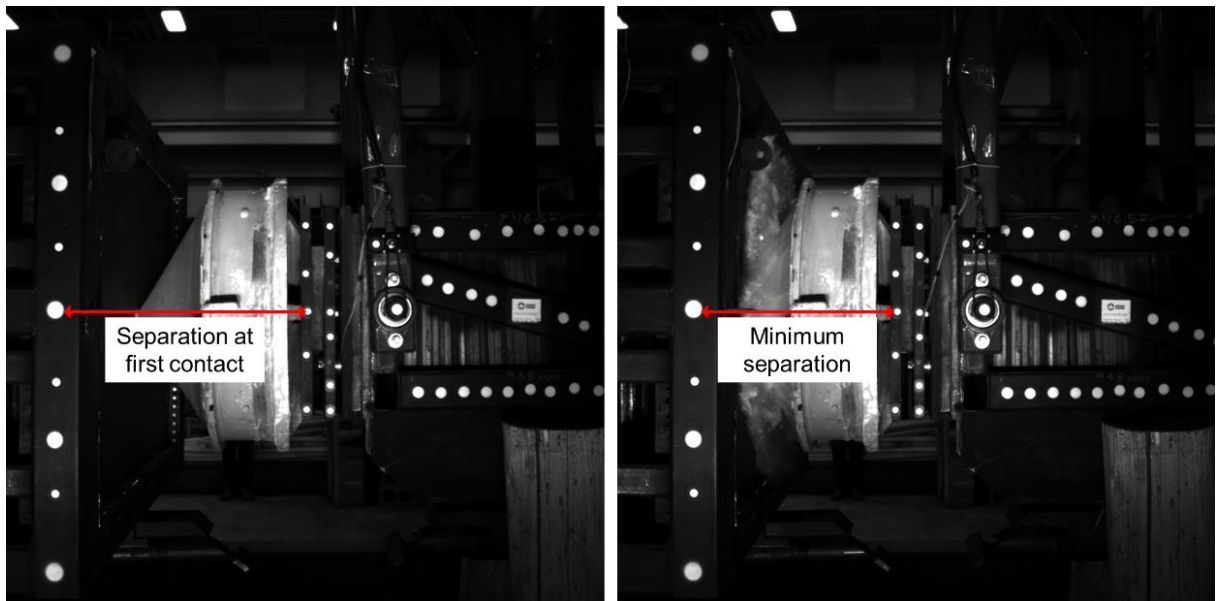


Figure 4-19. Carriages separation during impact (Impact 2).

For Impact 2, from initial contact between ice and panel to the instant of minimum separation, the total relative displacement between the two carriages is 17 cm, as indicated in Figure 4-20. After the relative carriage displacement is determined, it is also interpolated

so that it matches the sampling rate of the load cell data 1:1 (from 1000 samples per second to 5000).

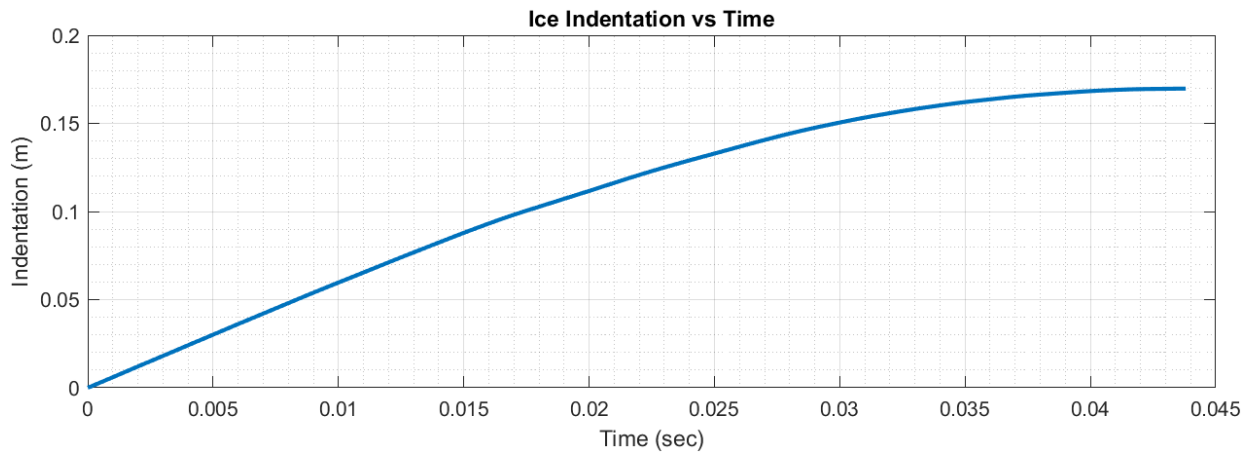


Figure 4-20. Ice indentation progression of Impact 2.

Force and relative carriage displacement can be used to estimate the work done by the impact forces. This has been done in Andrade et al. (2020) to estimate the impact energy using load and displacement data reported in Gagnon et al. (2020). There, the work done was used to estimate ice crushing energy, but the losses were not compared with theoretical kinetic energies.

In the current study, the theoretical impact kinetic energy is 47.1 kJ (Table 4-2) for Impact 2. Figure 4-21 indicates that the ice crushing and panel deformation mechanisms absorb 45.4 kJ of the total available kinetic energy. The difference between theoretical and measured kinetic energies is 4.7%.

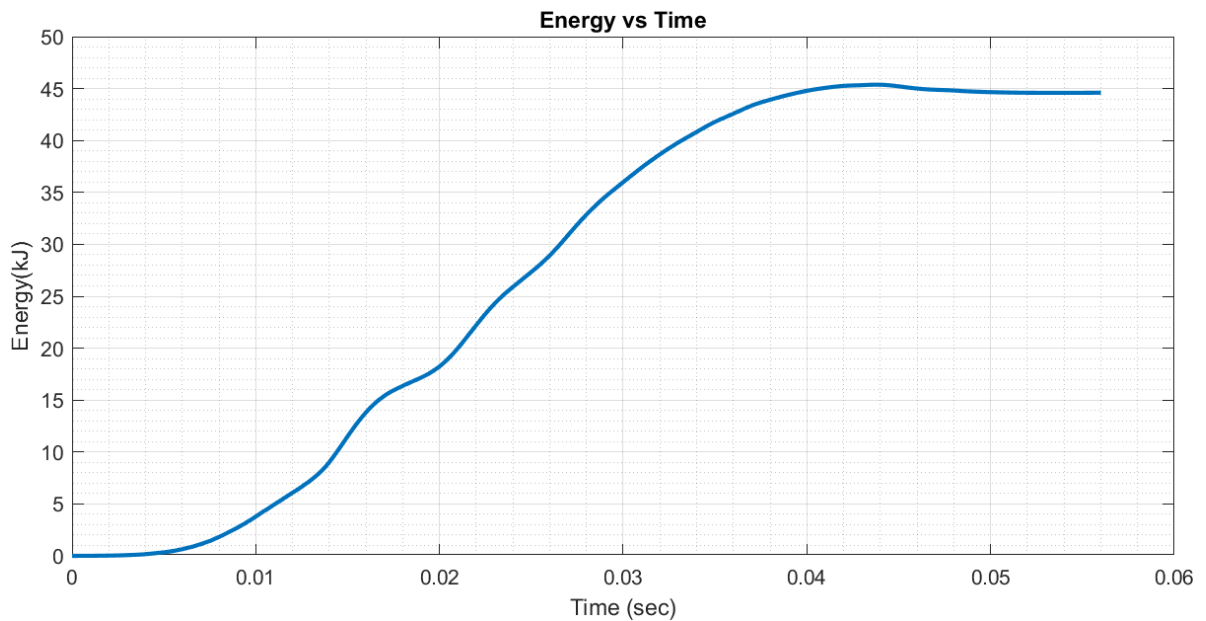


Figure 4-21. Energy balance for Impact 2.

4.7 Lessons learned

An important aspect of this work relates to the lessons learned and resulting procedural changes necessary for future experiments. The mass of the ice holder pendulum is controlled using multiple 90 kg (200 pounds) steel plates. In the experiments reported in the current work they were sequentially placed with their normal axes oriented towards in the pendulum movement direction (shown in Figure 4-22). During these experiments, some shifting of the steel plates used as ballast weight for the indenter carriage (IC) was noticed. This shifting was practically eliminated in future experiments by changing the orientation of the steel plates, which are now laid flat and stacked vertically in the IC. Further, the weight discrepancy between the panel and indenter carriages (i.e., 4690kg vs. 5305 kg, respectfully) has been equalized to 4650 kg each. Weighing of each pendulum carriage is an involved process that requires disassembling the pendulum apparatus and weighing each

carriage using an overhead crane mounted scale. During pendulum modifications immediately subsequent to these experiments, the pendulum weights were re-measured, and the mass difference between both pendulum carriages was observed and corrected.

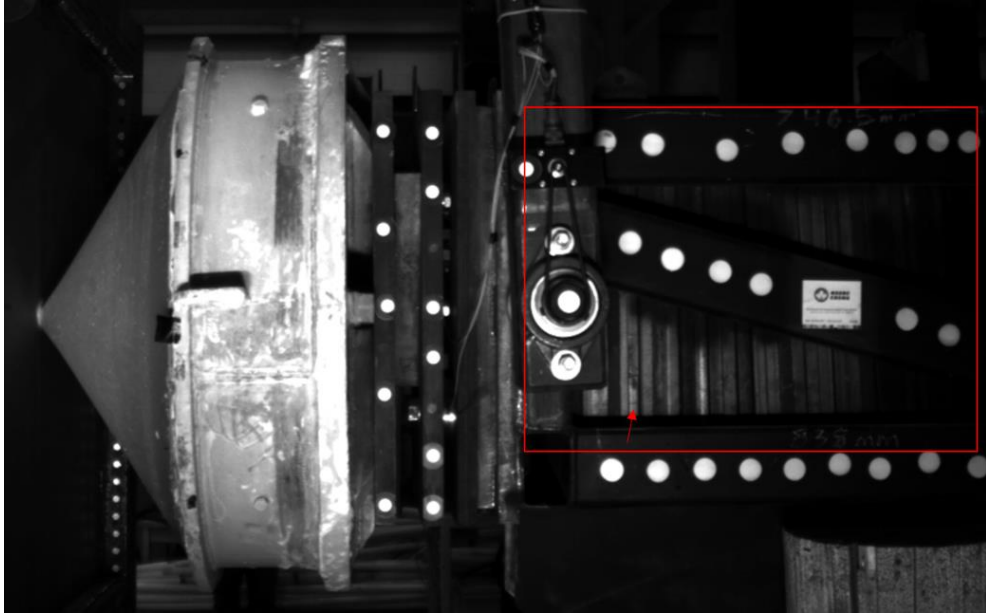


Figure 4-22. Original ballast plate arrangement. A single plate is indicated by the red arrow.

In regard to the data recorded by the accelerometers, the sampling rate used in the current experiments (5000 samples per second) was not sufficient to fully describe the impact accelerations. The sampling rate has since been increased to 100 kHz and a low-pass filter with a cut-off frequency of 10 kHz is utilized. The signal conditioner (Kistler type 5134b) for the piezoelectric accelerometers has 4 settings for the low pass filter cut-off frequencies (0.1, 1, 10, and 30 kHz). The authors were concerned that the 30 kHz cut-off frequency would allow for the presence of excessive noise in the signal, while 1 kHz would certainly cut-off desired signal frequencies. Thus the 10 kHz cut-off frequency was selected. The

project related to this work is primarily interested in properly characterizing the signal in the time domain, in which case the Nyquist frequency for the desired maximum frequency would potentially not be enough to describe the highly transient signal amplitude of the impacts. The analog – digital converter was capable of sampling up to 10 times the desired cut-off frequency, thus this led to the sampling rate of 100 kHz.

Further, it was desired to investigate the spatial distribution of impact acceleration measure in the panel's plating, so the existing 5000g accelerometer at the centre of the stiffened panel was augmented with 5 more 5000g accelerometer at varying alternate locations.

4.8 Conclusion

The large double-pendulum is an apparatus designed to perform medium energy ship-ice impact experiments in controlled laboratory conditions with full scale ice and full-scale ship structure. The results of three ice impacts against a framed section of the recently decommissioned ex-HMCS IROQUOIS are presented. The first impact does not have load cell data, the test panel accelerometer almost saturated, and the indentation of the test panel was minimal. For the second impact, the force peaked at 553.9 kN, the total impact duration was of 0.054 s and up to 10877 m/s² of acceleration was measured on the grillage. The third impact caused a peak force of 773.6 kN, 9691 m/s² of acceleration measured on the grillage, and had an impact duration of 0.039 s. The grillage's total maximum measured permanent indentation after each successive impact was of 0.2 cm, 0.5 cm, and 1.2 cm. The high-speed image quality and resulting digital image correlation (DIC) analysis was good. The DIC was able to describe both pendulum displacements, velocities, and accelerations with good accuracy, even for the impact duration. This allowed the energy balance to be verified,

which showed a good agreement between the work done by ice crushing and panel deformation (45.4 kJ) and available kinetic energy (47.1 kJ).

4.9 Future work

In general, the initial trials with the upgraded pendulum apparatus showed good results and more impact experiments are underway. The lessons learned in this initial set of experiments will be applied to the coming experiments. Future tests include further ice-structure interaction tests on ex-HMCS panels and clones of these panels built from new steel, as well as impacts with rigid indenters of varying shape.

4.10 Acknowledgements

The authors graciously acknowledge the financial support from the NSERC DND/CRD “Operational Capabilities of Low- and Non-ice-class Structures in Ice” grant, and the following contributing project partners: Defence Research and Development Canada (Atlantic), Vard Marine Inc., the American Bureau of Shipping (ABS), and the Newfoundland & Labrador Provincial Government.

4.11 References

- Alam MS, Daley C, Colbourne B, Hermanski G, Gagnon B, Bruneau S, Clarke G, Quinton B. 2012. Double pendulum dynamic impact test set-up for ice-grillage collision. In: Int Conf Exhib Perform Ships Struct Ice 2012, Banff, Canada; p. 294–297.
- Andrade SL, Quinton BWT, Daley CG, Gagnon RE. 2020. Numerical Study of Large Pendulum Ice Impact Loads. In: Vol 7 Polar Arct Sci Technol [Internet]. Virtual, Online: American Society of Mechanical Engineers; p. 1–10.

<https://asmedigitalcollection.asme.org/OMAE/proceedings/OMAE2020/84393/Virtual, Online/1092917>

Gagnon R, Andrade SL, Quinton BW, Daley C, Colbourne B. 2020. Pressure distribution data from large double-pendulum ice impact tests. *Cold Reg Sci Technol* [Internet]. 175:103033. <https://doi.org/10.1016/j.coldregions.2020.103033>

Gagnon R, Daley CG, Colbourne B. 2015. A large double-pendulum device to study load, pressure distribution and structure damage during ice impact tests in the lab. In: *Proc 23rd Int Conf Port Ocean Eng under Arct Cond POAC*. Trondheim, Norway; p. 1–10.

Gagnon RE, Wang J. 2012. Numerical simulations of a tanker collision with a bergy bit incorporating hydrodynamics, a validated ice model and damage to the vessel. *Cold Reg Sci Technol*. 81:26–35. <http://dx.doi.org/10.1016/j.coldregions.2012.04.006>

Gudimetla PSR, Colbourne BD, Daley CG, Bruneau SE, Gagnon R. 2012. Strength and pressure profiles from conical ice crushing experiments. In: *Int Conf Exhib Perform Ships Struct Ice 2012, ICETECH 2012*. Banff, Canada; p. 167–174.

Habib, KB, Taylor, RS, Bruneau, S, Jordaan, IJ, 2015. Experimental Study of Dynamics During Crushing of Freshwater Truncated Conical Ice Specimens. *Proceedings of the ASME 2015 34th International Conference on Ocean, Offshore and Arctic Engineering*. Volume 8: Ian Jordaan Honoring Symposium on Ice Engineering. St. John's, Newfoundland, Canada. May 31–June 5.

Johnston M, Timco GW, Frederking R. 2003. In Situ Borehole Strength Measurements on Multi-year Sea Ice. In: *Proc Int Offshore Polar Eng Conf*. Honolulu, Hawaii, USA; p.

445–452.

Jones SJ. 1997. High strain-rate compression tests on ice. *J Phys Chem B*. 101(32):6099–6101.

Jones SJ. 2007. A review of the strength of iceberg and other freshwater ice and the effect of temperature. *Cold Reg Sci Technol*. 47(3):256–262.

Jones SJ, Gagnon RE, Derradji A, Bugden A. 2003. Compressive strength of iceberg ice. *Can J Phys*. 81(1–2):191–200.

Quinton BWT. 2017. Experimental Planning for Large Non-Ice Class Grillage Tests Report. St. John's, Canada.

Quinton BWT, Daley CG, Gagnon RE, Colbourne BD. 2017. Guidelines for the nonlinear finite element analysis of hull response to moving loads on ships and offshore structures. *Ships Offshore Struct* [Internet]. 12(January):S109–S114. <http://dx.doi.org/10.1080/17445302.2016.1261391>




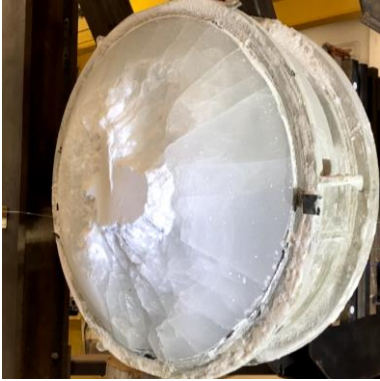


Sinha NK. 1985. Confined strength and deformation of second-year columnar-grained sea ice in Mould Bay. In: *Proc Int Conf Ocean Offshore Mech Arct Eng - OMAE*. Dallas, TX, USA; p. 209–291.

Timco GW, Frederking RMW. 1983. Confined compressive strength of sea ice. In: *Seventh Int Conf Port Ocean Eng under Arct Cond*. [place unknown]; p. 243–253.

Timco GW, Weeks WF. 2010. A review of the engineering properties of sea ice. *Cold Reg Sci Technol*. 60(2):107–129. <http://dx.doi.org/10.1016/j.coldregions.2009.10.003>

4.12 Appendix A – Ice cone

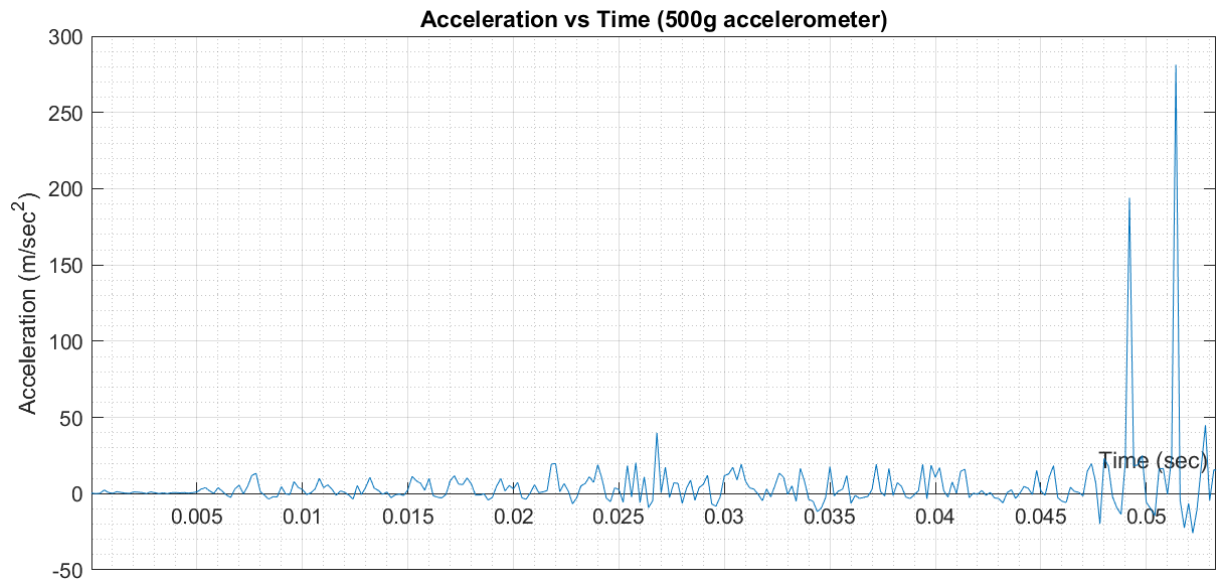
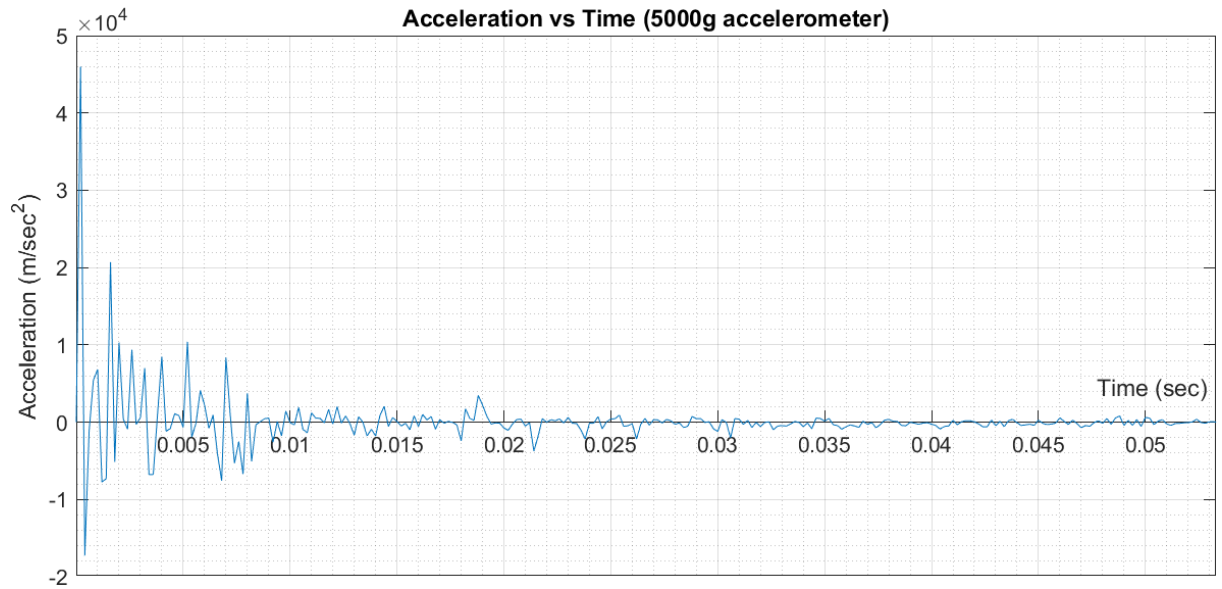
Table 4-4. Ice cones pre- and post-impact.

Experiment	Ice Cone Before Impact	Ice Cone Post-Impact
Impact 1	 A photograph of a large, white, conical ice structure mounted on a metal frame. The ice is smooth and has a uniform, cone-like shape.	 A photograph of the same ice cone after impact. The surface is highly irregular, with many cracks and a jagged, fragmented appearance.
Impact 2	 A photograph of the ice cone before the second impact. It appears mostly intact but shows some surface wear and minor cracking.	 A photograph of the ice cone after the second impact. The surface is significantly more damaged, with large areas of cracking and some material loss.
Impact 3	 A photograph of the ice cone before the third impact. The surface is heavily cracked and shows signs of significant structural damage.	 A photograph of the ice cone after the third impact. The structure is severely damaged, with large sections of ice missing and the remaining parts heavily fractured.

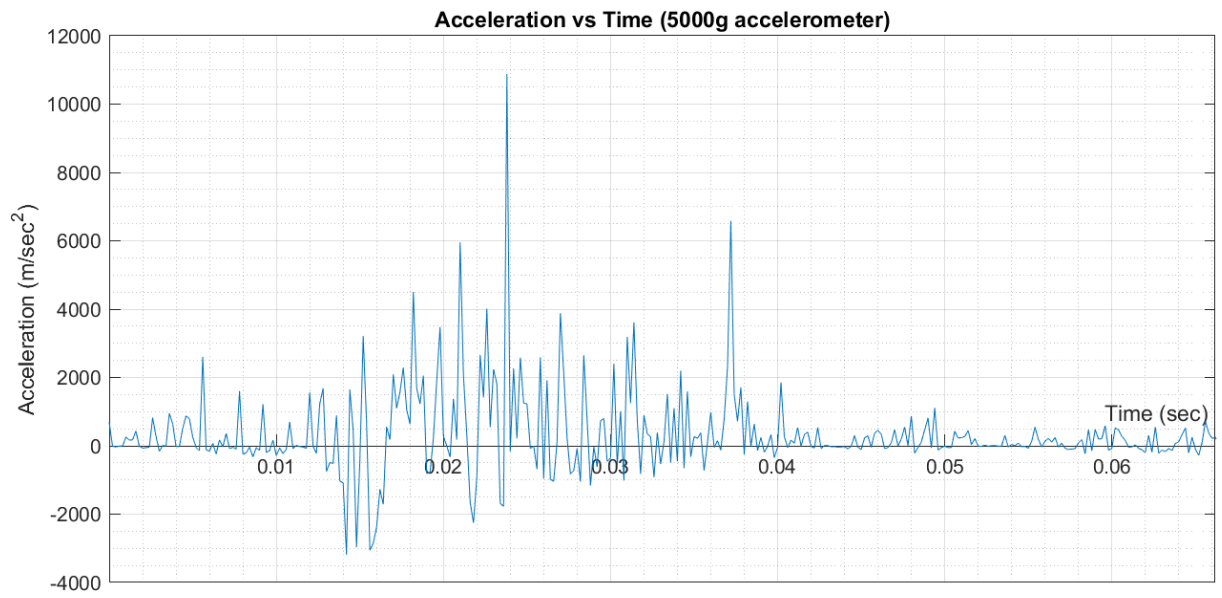
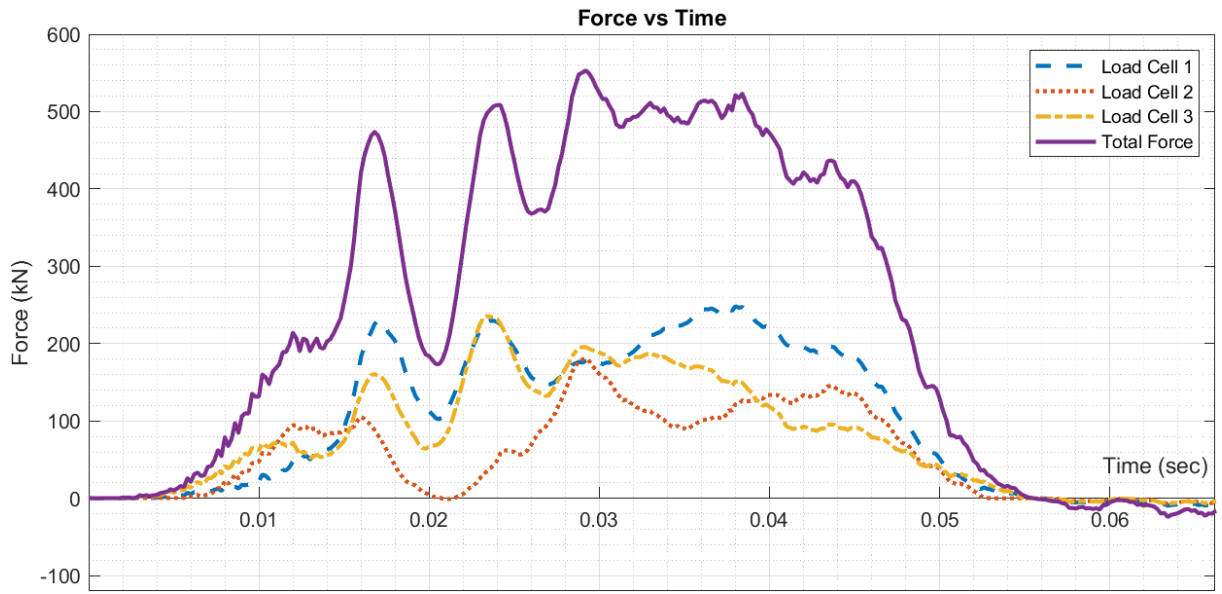
4.13 Appendix B – Load curves and accelerometer curves

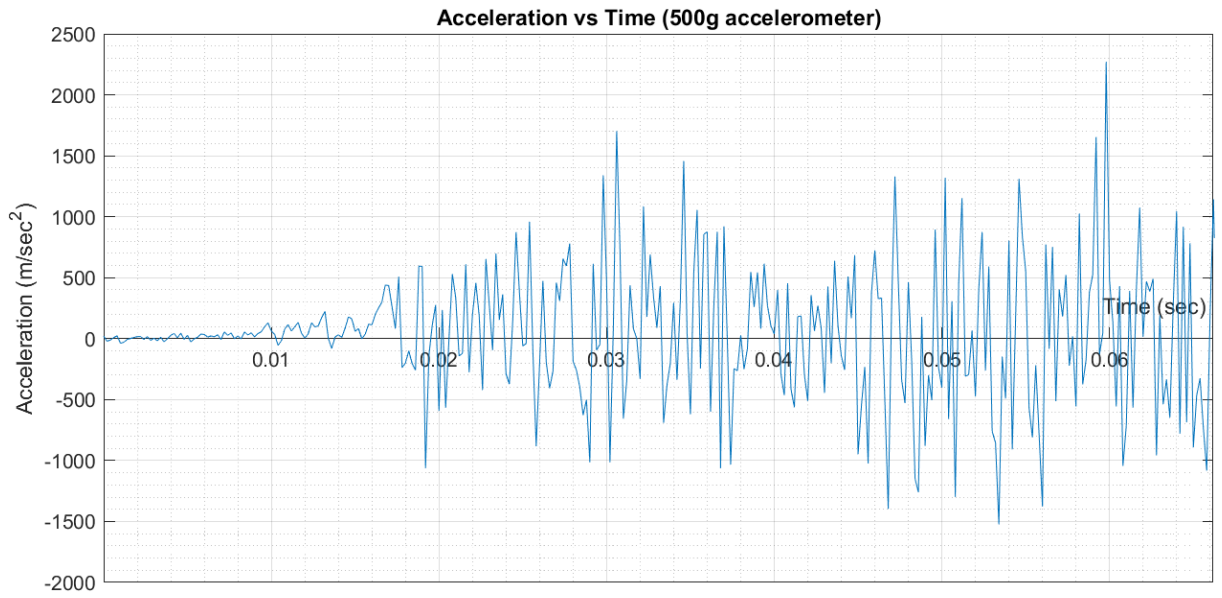
Impact 1

[Load Data is not available for Impact 1]

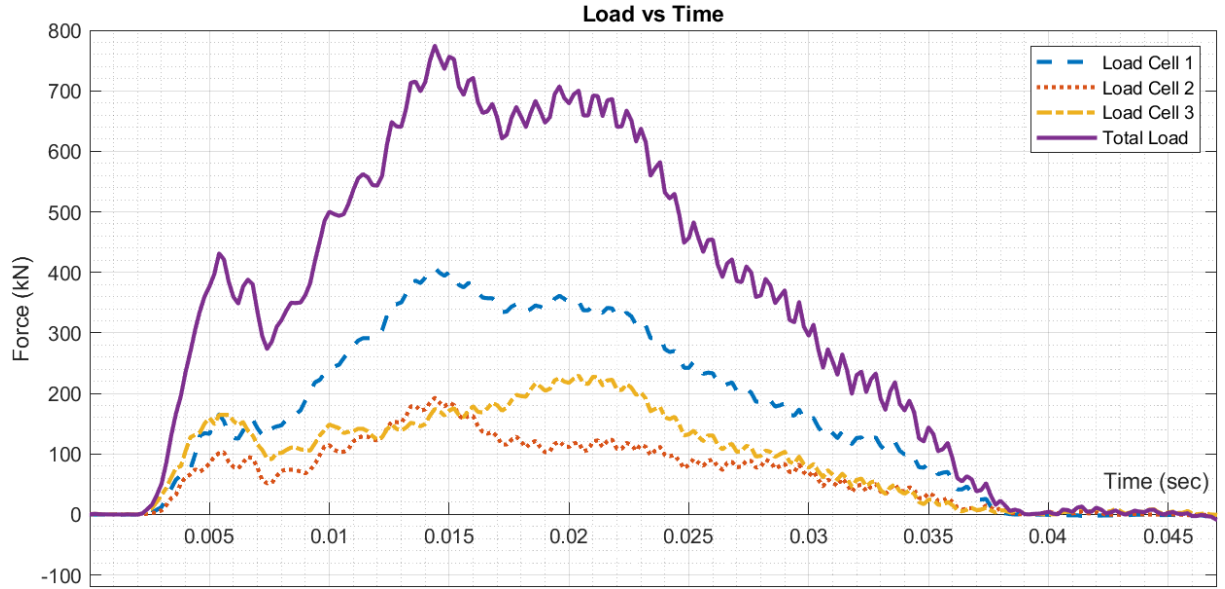


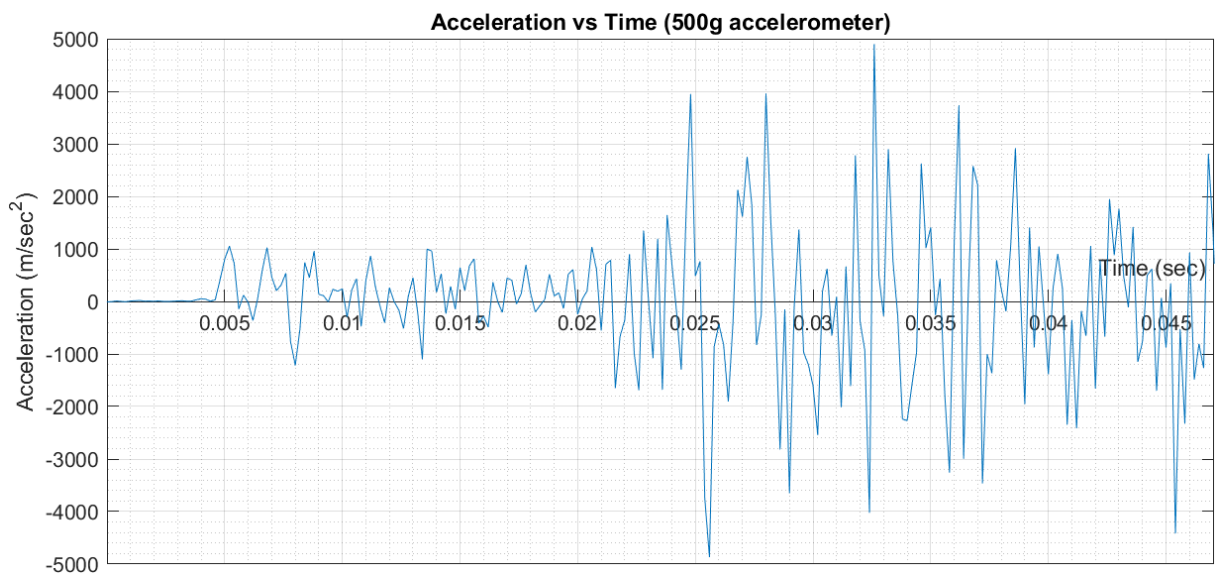
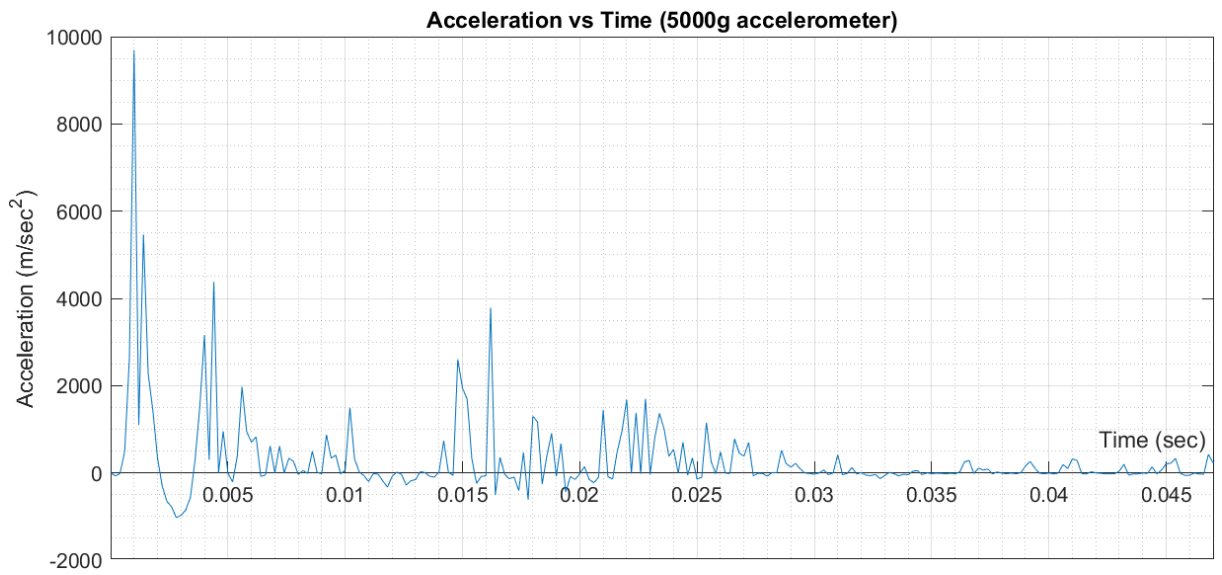
Impact 2





Impact 3





4.14 Appendix C – ex-HCMS IROQUOIS panel

Before Impact 1



After Impact 1



After Impact 2



Before Impact 3



After Impact 3



Chapter 5 Ice pressure distribution model: A geometry-based solution for high-pressure zone representation

5.1 Co-authorship statement

This chapter has been submitted to the journal *Cold Regions Science and Technology*. It has been revised once and it is currently in the second round of reviews. The paper was authored by S. L. Andrade, R. Gagnon, B. Colbourne., and B. Quinton.

S. L. Andrade proposed and developed the geometric model for HPZ/LPZ representation. R. Gagnon collaborated by providing guidance and material that allowed the model to be validated. S. L. Andrade wrote the manuscript. S. L. Andrade, R. Gagnon, B. Colbourne., and B. Quinton were responsible for the paper editing and revisions.

This Chapter was edited to include an additional reference.

5.2 Abstract

Studies have shown that the interface between ice and an indenter is a complex system that gives rise to two ice types, relatively-intact ice and crushed ice. Each type accordingly imparts different pressure magnitudes on the indenting structure, where intact ice is associated with high pressures zones (HPZs) and crushed ice with low pressures (LPZs). HPZ average pressures are almost an order of magnitude larger than LPZ pressures. This means that their relative distribution over the contact area significantly affects the structural response. This work develops a methodology for modelling ice pressure zone distributions based on the topological skeleton and distance field information of the ice-indenter contact

area. Results compare favourably with experimentally determined HPZ distributions from varying ice indentation experiments of small, medium and large scale.

Keywords: high-pressure zones, ice crushing, pressure distribution model, topological skeleton.

5.3 Introduction

In recent years the Arctic has seen an increase in ship traffic, spearheaded by new shipping routes, but with significant contribution from mineral exploration, increases in tourism, and sovereignty assertion. A vessel that transits polar waters must be prepared to sustain unanticipated ice loads without loss of function. The Arctic is a fragile ecosystem, and any kind of ship accident in the region could mean irreparable damage, both from the human and environmental points of view. In case of oil spillage, it would be difficult to mount an effective and timely response, and rescue operations would be hampered by geographical remoteness. Thus, it is important that ships navigating in polar waters can do so safely, even in cases of accidental ice loads.

The ice load characterization process is still a significant challenge. Ice compressive strength depends, at a minimum, on strain-rate, temperature, the presence of impurities, and crystalline structure. There is a good general knowledge of how each individual parameter influences ice strength, in trend if not in absolute values, however ice compressive strength shows large variation in measured values, even in laboratory settings (Timco and Weeks, 2010).

Recently, significant progress has been made in the field of dynamic ice crushing pressure measurements. Gagnon et al. (2020) presents an analysis of high fidelity data from impact experiments with a large pendulum apparatus (Gagnon et al., 2015). Based on observations from these recent experiments (Gagnon et al., 2020) and Hobson's Choice indentation experiments (Frederking et al., 1990), here we present an ice pressure model capable of describing the spatial pressure distribution patterns observed during ice structure interaction in the brittle regime. The proposed model captures the dynamically generated pressure distribution patterns for contact areas with complex shapes.

5.4 The ice feature failure process

The ice feature failure process occurs during interaction between ice and a structure, e.g., a ship. The loads and pressure distributions arising from this process are a function of the complex geometry of the contact and the presence of a non-uniform interface (Joensuu and Riska, 1989).

The contact geometry is a function of the ship's structure shape and the ice geometry but for prediction purposes it is reasonable to assume that the bulk ice feature has a known initial geometric shape, such as the edge of an ice sheet, or the corner of a growler. Complexity arises from the fact that both ship local structure and bulk ice geometries can change during this interaction. The first is related to the structural elastic and plastic deformations of the hull. For the ice, catastrophic spalling events can occur, which fundamentally change the local ice geometry, and consequently, the shape of the contact area at the ship-ice interface (Daley, 1994).

The second level of interaction occurs directly at the ice-ship contact region. At the interface two different types of ice interact with the structure (Daley, 1994; Gagnon, 1998), crushed ice and intact ice. The crushed ice that is extruded from the contact region, is represented in Figure 5-1 by a grey colour and also in Figure 5-2 (Gagnon, 1998) as ice of white milky colour located at the top left and right regions. The other ice type is the original hard ice, which remains intact and is in direct contact with the structure, is shown in blue in Figure 5-1. In Figure 5-2 hard ice appears as a translucent grey and it covers most of the bulk ice region. It can be seen where it was in direct contact with the indenter during the experiment, at the top centre.

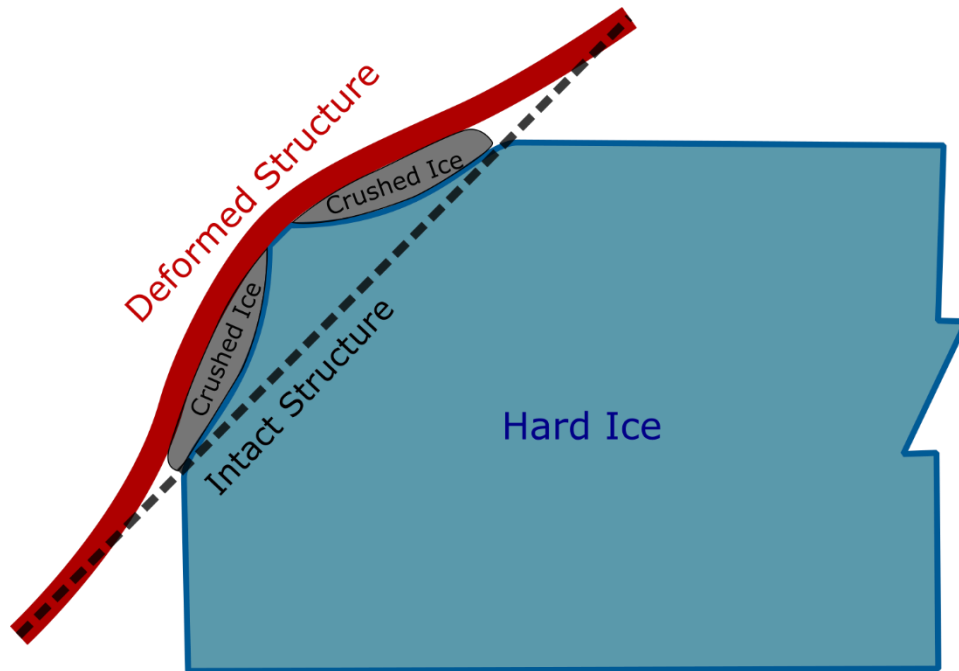


Figure 5-1 – Illustration of the ice-ship structure interaction process during crushing. The deformed ship structure is represented in red. The black dashed line represents the original intact structure. Grey and blue colours represent the crushed and intact ice regions, respectively.

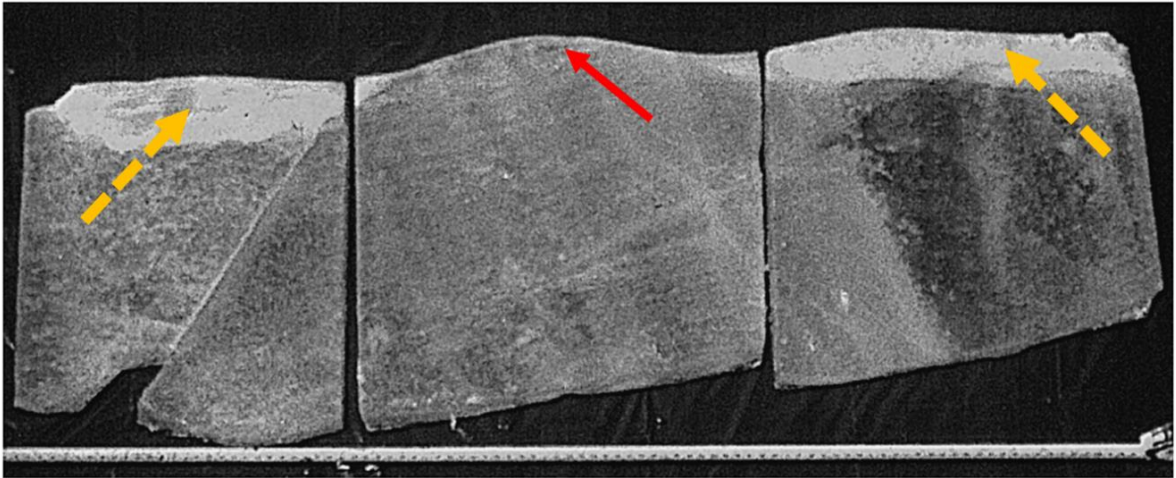


Figure 5-2 – A thick horizontal slice from the top of an indented specimen (Hobson’s Choice Ice Island experiments). The indenter was acting on the top of the ice, and the base was connected to the multiyear ice wall. Darker coloured regions (grey regions indicated by full red arrows) are intact ice, and milky white regions are crushed ice (regions indicated by dashed yellow arrows). The crushed ice starts at the edges of the intact region and tends to grow in thickness moving away from the intact region. The crushed ice region is not uniform. Larger chunks are visible within it. (Gagnon, 1998)

Crushed and intact ice regions transmit loads in different ways and at different magnitudes. The intact ice region is associated with regions where high interface pressure is applied to the structure and are designated as high-pressure zones (HPZs), or hard zones. For example, measurements from CCGS Louis S. St. Laurent using membrane transducers showed very high localized pressure readings (24-36 MPa) in small regions (membrane diameter of 8 mm) of the ice / structure contact region (Glen et al., 1981; Glen and Blount, 1984). Conversely, crushed ice is associated with low-pressure zones (LPZs). The presence of HPZs and LPZs has also been reported in other laboratory experiments (Gagnon et al., 2020; Gagnon and Daley, 2005) and field experiments (Frederking et al., 1990; Gagnon, 1998; Kamio et al., 2000; St. John et al., 1984). The HPZs in high aspect ratio contact areas have been observed to develop in “line-like” shapes, as observed in previous studies, first

by Joensu and Riska (1989), and then other works such as Riska et al. (1990), Daley (1992), and Frederking (2004).

HPZs have higher relative interface pressure than LPZs, and there is a significant pressure gradient at the boundary between an LPZ and an HPZ. The actual threshold pressure values are only strictly valid within the parameters of each experiment (i.e., temperature, ice type, strain-rate, etc.). For example, (Frederking, 2004) reports the highest measured pressure in HPZ regions was 2.55 MPa during the JOIA (Japan Ocean Industries Association) ice crushing experiments, which is different from HPZ pressures as high as 51.8 MPa from the large pendulum experiments reported by Gagnon et al. (2020). The ice type studied may explain the difference in high-pressure magnitudes between the JOIA tests and the large pendulum experiments. For the JOIA tests, the ice was relatively thin first-year ice formed in a saltwater lagoon. Conversely, the Gagnon et al. (2020) experiments were made with lab-grown granular freshwater ice. In Figure 5-3 it is possible to observe how relatively intact ice (dark region in the contact zone) correlates with the corresponding pressure map for that contact area. It is also notable that the HPZs are surrounded by crushed ice (white material), and that there is an abrupt change in the ‘pressure-color’ map at the HPZ/LPZ boundary, which indicates a sharp pressure gradient separating LPZs from HPZs.

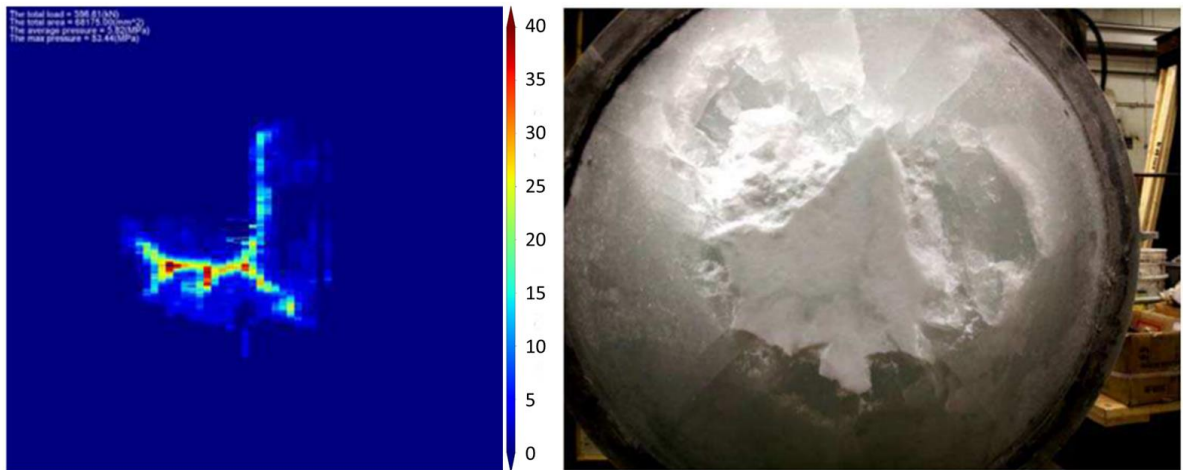


Figure 5-3 – Pressure distribution map (left) and the equivalent ice damage (right) (Sopper et al., 2015). The warmer colours from the color-pressure scale (MPa) on the left image represent high-pressure zones (HPZs). These HPZs correlate with the observed relatively intact ice (dark dendritic feature in the contact zone) observed on the image on the right.

In summary, the pressure distribution in an ice-ship hull interaction arises from a process that is dependent on the geometry of the indenting ice feature and indented structure, and it is characterized by the presence of high- and low- pressure zones (HPZs and LPZs).

5.5 Confinement and high-pressure zone formation

Non-uniform stress is an important factor in determining ice crushing strength and the development of HPZs. When ice is under uniaxial compression, a tensile stress field develops along the secondary and tertiary major axes. This tensile stress field is responsible for propagating cracks, which can arise from pre-existent flaws or from cracks initiated by shear stress (Sanderson, 1988). The introduction of confining stress makes it more difficult for crack nucleation and propagation to occur. Thus, the presence of confinement stress increases the effective ice compressive strength. Iliescu and Schulson (2004) observed this

effect for bi-axial stress states, where a relatively low-confinement state significantly increased an ice specimen's strength, from approximately 5 MPa when unconfined to over 20 MPa when confined. Gagnon and Gammon (1995) reached a similar conclusion for tri-axial compression of glacial ice, with confining pressure significantly increasing the glacial ice compressive strength.

These previous studies describe the effect of confinement on the strength of a whole ice sample, but a similar effect can be observed at the ice-indenter interface during ice crushing in the brittle regime. The local confinement at the ice-structure interface is due to both the shape of the bulk intact-ice feature (i.e., the “process surface”) and the crushed ice extrusion process. In this context, “process surface” refers to the topology of the intact bulk-ice feature when it undergoes shape changes over time due to spalling of ice from its sloped sides as penetration and crushing progresses. The hard zone is the portion of the “process surface” in direct contact with the structure, while the sloping sides of the process surface provide a supporting surface for crushed ice that typically occurs as a wedge-shape accumulation between the structure and underlying intact ice around the perimeter of the hard zone. During the extrusion process, the crushed ice applies a confining back pressure that, together with the bulk-ice confinement, leads to the development of relatively-intact hard zones (HPZs) in the approximate central regions of the contact interface (Daley, 1994), even under very high local compressive pressures (Gagnon, 1998; Tuhkuri, 1995). Tuhkuri (1995) also associated higher confinement arising from crushed ice flow obstruction with larger ice-crushing loads.

The proper characterization of HPZs is relevant because they bear a significant proportion of the total crushing load. From the results shown in Gagnon et al. (2020) it can be determined that HPZs occupy, on average, roughly 13% of the total contact area. Similarly, Frederking (2004) reports that HPZs are responsible for 90% of the total load measured in the JOIA indentation experiments, while occupying 10% of the contact area. The criteria for distinguishing LPZ from HPZ plays an important role in their relative area ratios. In Gagnon et al. (2020) this was done by choosing the pressure that is within a region of highest pressure gradient, which would indicate the transition from crushed to intact ice. The threshold value for that case was 15 MPa.

Gagnon et al. (2020) show that total load and HPZ area have similar time-varying trends in all experiments, yet the same is not true for LPZ area, as stated in that paper: "... it is worth noting that the details (i.e., abrupt changes) in the time evolution of the HPZ size and shape (and consequent load) are much more reflected in the total load than are the aspects of the LPZ evolution. This is because the HPZ contact area is generally much less than the LPZ contact area. Recall that the average pressures on HPZ's and LPZ's are approximately constant (i.e., 21 MPa and 3.7 MPa respectively), so it is their contact areas that largely determine the loads they support. Consequently, when a spallation from the HPZ occurs that involves, for example, 20% of the contact area of the HPZ shattering to become LPZ material, the relative change in area of the LPZ contact area is considerably less because the LPZ areas are generally 2–6 times the size of HPZ areas. That is, the 20% contribution from the HPZ amounts to only a 3–10% change in the LPZ contact area at the time of the event."

5.6 The importance of the contact area shape for HPZ development.

During ice crushing in the brittle regime, two different types of spalling events can occur. The first type refers to a range of small to medium size spallation events that routinely occur during impact/indentation. The shattered debris from these spallation events makes up the regions of crushed ice that typically surround HPZs at the ice/structure interface. The second type of spalling event refers to much larger, catastrophic, spalling events that lead to significant changes in the overall shape of the bulk-ice feature. This catastrophic spalling, which distinguishes the first and second spall types, causes dramatic changes in the shapes and sizes of the HPZs and LPZs at the contact interface. That is, a HPZ/LPZ distribution pattern that had been evolving over many spalling events of the first type, can suddenly change dramatically due to a single catastrophic spall event of the second type.(Daley, 1992; Taylor and Jordaan, 2015).

The effect of a catastrophic spalling event on the development of the contact area can be observed when comparing the TRF 02, 03 & 05 experiments from Hobson's Choice Ice Island (Muhonen, 1991), shown in Figure 5-4. All the ice faces for these experiments were sculpted into positive pyramidal shapes with square bases, with the TFR 05 base rotated 45 degrees in relation to TRF 02 & 03. The indentation direction is normal to the base of the pyramid in all cases. The TRF 02 & 03 experiments do not show evidence of catastrophic spallation events in the post-test images, thus their bulk-ice geometries did not change significantly. Their actual and nominal contact areas maintained a relatively similar shape (square). In both experiments, the observed HPZs developed into an X-like pattern over the contact area. On the other hand, TFR 05 shows a major change in bulk-ice geometry due

to a catastrophic spallation event in the bottom-left region. This event caused the TRF 05 HPZ pattern to differ significantly from those of TRF 02 & 03. The former square contact area developed into a sickle-shaped contact area, and, likewise, the HPZ pattern changed drastically.

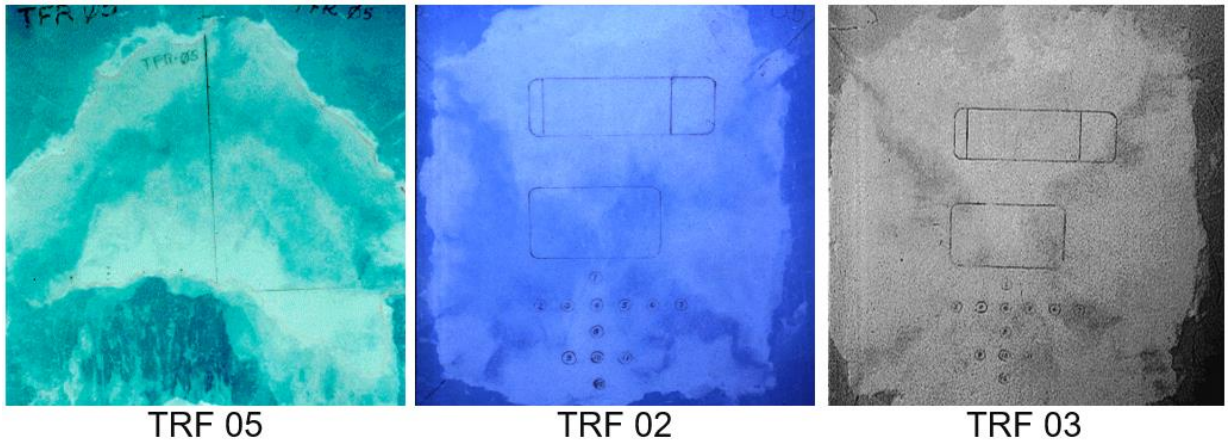


Figure 5-4 – Test face images from three Hobson’s Choice experiments. All these ice features had originally the shape of a square pyramid. TRF 02 and TRF 03 show no signs of catastrophic spallation events and developed X-shaped HPZs (hard zones). TRF 05 shows a significant change in the bulk-ice geometry and a very different HPZ pattern (sickle-shaped hard zone). (Gagnon, 1998; Muhonen, 1991)

Figure 5-5 from the Feb25_2016 experiment (Gagnon et al., 2020) shows the HPZ pattern changes that were captured at a rate of 500 images per second. Note that the HPZ (at pressures larger than 15 MPa) re-arranges from a roughly circular shape into a “sickle-like” shape after a catastrophic spall occurred (the event is indicated by the red line and arrow). The change in HPZ shape occurs quite quickly, going from circular to sickle shape in roughly 3 frames, or 0.006s. A significant load drop, shown in Figure 5-6, accompanies this event.

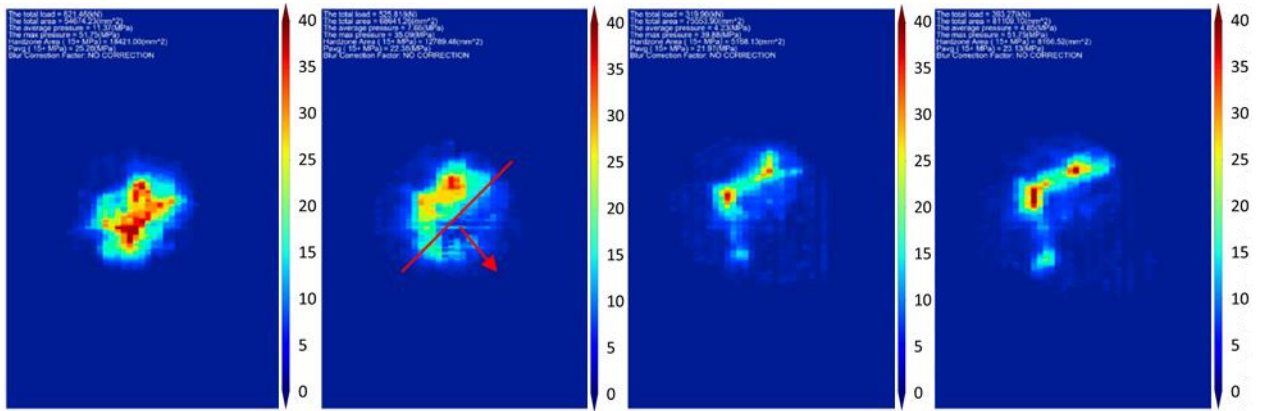


Figure 5-5 – From left to right, pressures maps #9, #10, #11, and #12 from the Feb25_2016 experiment (Gagnon et al., 2020), the colour temperature correlates to contact pressure intensity (color-bar in MPa). The maps show the sequential progression and HPZ development during the impact experiment, when spallation occurs in #10, indicated by the arrow. The images were recorded at 500 Hz.

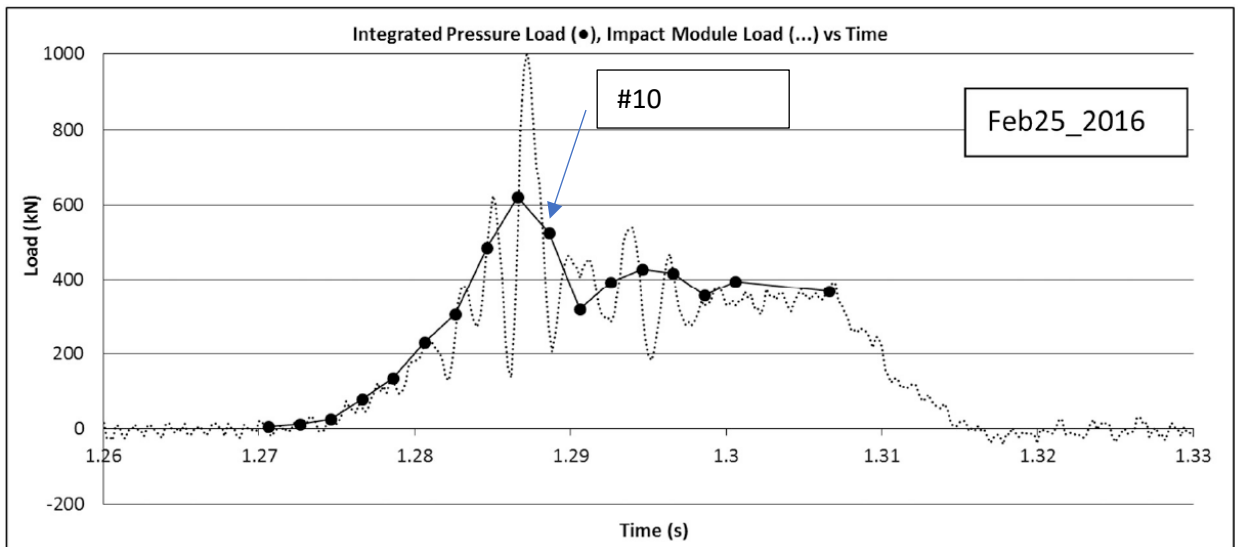


Figure 5-6 – Load curve data for the Feb25_2016 experiment. Marked is the instant a catastrophic spall was observed in the pressure maps indicated in Figure 5-5, pressure map #10.

To summarize, these observations, and those from other studies, indicate that HPZ shape and size is determined by the evolving process surface of the ice (on one scale), that in turn

is influenced (on a larger scale) by the bulk ice geometry. If the overall contact zone size and shape (i.e., comprised of HPZ and LPZ) is known, then it is reasonable that the HPZ shape and size can be related to the overall contact zone geometry at that instant, bearing in mind that HPZs evolve rapidly during the ice crushing process. This discussion illustrates the importance of the overall contact zone shape and size for the development of HPZs.

5.7 Geometrical models for HPZ representation

As discussed above, in some of the Hobson's Choice ice experiments the ice wall was sculpted into a convex pyramidal shape, which was crushed with a flat indenter surface. Spencer and Masterson (1993) observed that HPZs developed in specific patterns for square and rectangular contact areas. Figure 5-7 shows one of these pyramidal shapes post-indentation. The dendritic shapes defined by regions of translucent relatively-intact ice (darker areas) generally emanate from the centre and spread along the diagonals of the square contact area. As with the large pendulum experiments, Figure 5-3, these regions correlate to observed higher local contact pressure.

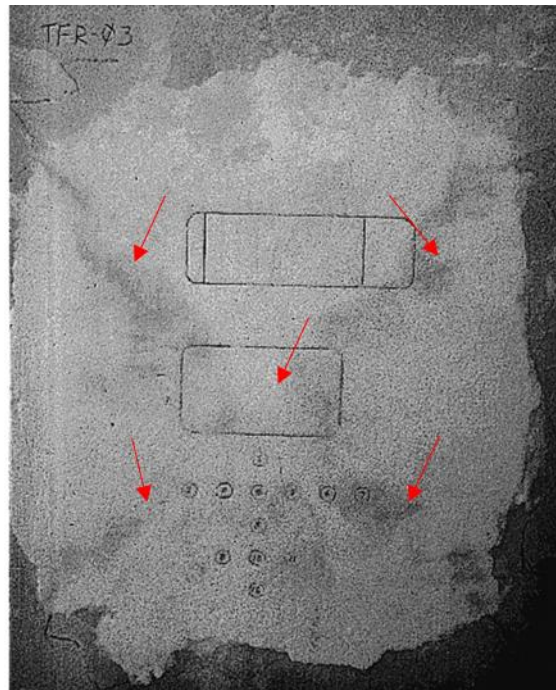


Figure 5-7 – Test face from one of the Hobson’s choice experiments (Gagnon 1998). The dark area that forms an “X” shape shows where relatively-intact ice is observed.

Based on visual observations from these ice crushing experiments, Spencer and Masterson (1993) proposed a geometric model for the pressure distribution where HPZs developed along the diagonals of a square contact area and mostly along the long geometric axis for rectangular contact areas with 45° wings towards the corners at the ends, as illustrated in Figure 5-8.

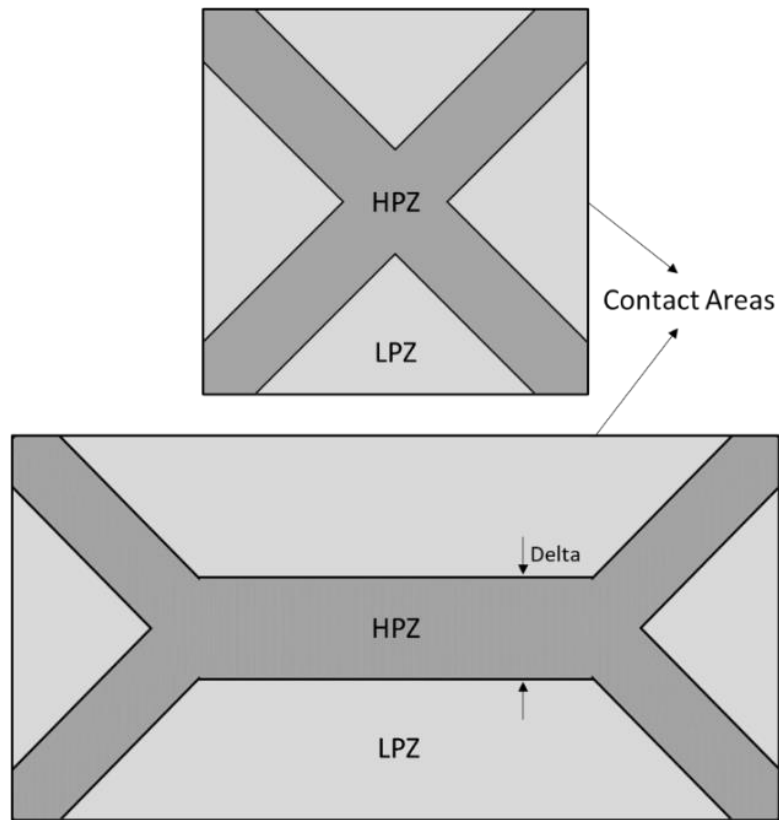


Figure 5-8 – Spencer and Masterson’s idealized HPZs model (re-drawn from Spencer and Masterson (1993))

Croasdale (2001) discusses a different geometric model for HPZ distribution. He proposes that a contact area can be discretized into two regions: a LPZ that represents the crushed ice, and HPZ that represents intact ice. The model assumes that the distance from the outer edges of the LPZ width remains constant during indentation, as exemplified in Figure 5-9.

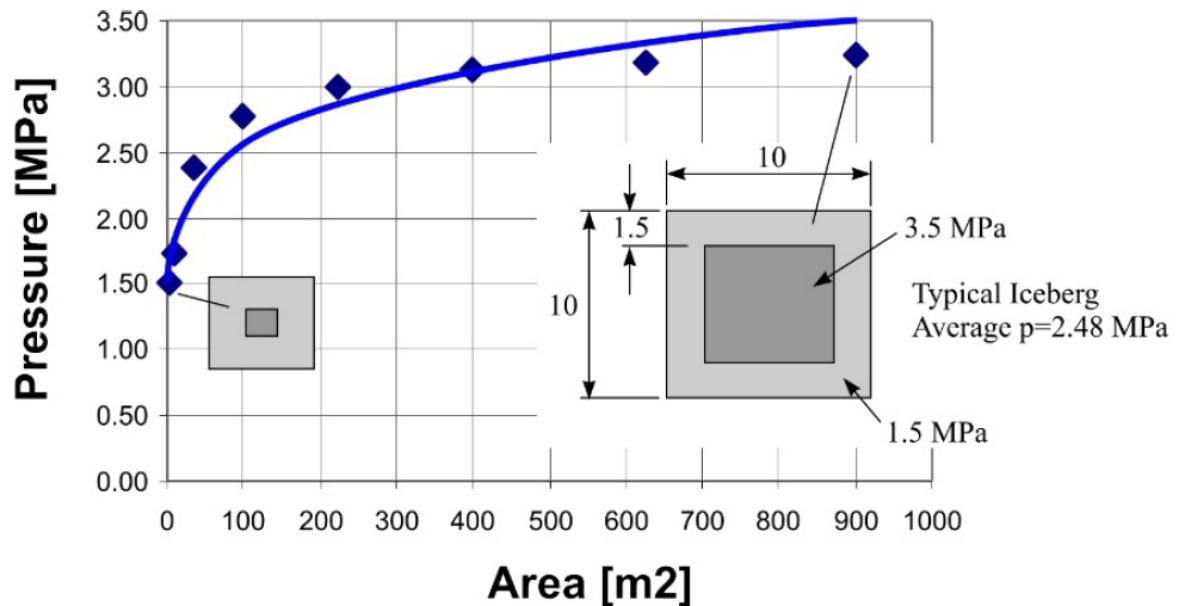


Figure 5-9 – Visual exemplification of the HPZ distribution model from Croasdale (2001). Original in (Croasdale, 2001), adapted in (Daley, 2020).

Both models try to incorporate relevant aspects of the HPZ's formation and distribution observed in experiments, but they have limitations. Spencer and Masterson's (1993) model is capable of incorporating the HPZ dendritic shapes that have been experimentally observed. Their model, however, was developed exclusively for rectangular contact areas, and as noted before, contact area geometry can be highly variable. Spencer and Masterson imply that the crushed ice fills in all space in the nominal contact area that is not occupied by the HPZ, but there is no formula for the variable width of the HPZ.

Croasdale's (2001) model would theoretically work for any contact area shape. That model appears to appreciate confinement from the bulk ice shape, but there is no intrinsic relationship, i.e., the width of the crushed ice is always the same no matter what the full contact area is. Thus, it is not capable of replicating the observed dendritic shapes, as shown

in Figure 5-7. Additionally, the model implementation allows the HPZ to occupy the majority of the contact area as indentation progresses, and this is inconsistent with experimental observations (e.g. R. Frederking, 2004; R. Gagnon et al., 2020).

5.8 A geometric descriptor for HPZ representation: The topological skeleton

Observations of HPZ development patterns indicate that they generally follow the contact area's topological skeleton. The topological skeleton is a discrete representation of the set of medial axes of an object. A medial axis is a geometric descriptor that contains all points of the object that have more than one closest point belonging to its perimeter (Blum, 1973). In a 2D object, a topological skeleton can be described as the set of all points that are also the centres of fully enclosed circles that are tangent to at least two different points of the 2D object's perimeter. An example of this is shown in Figure 5-10.

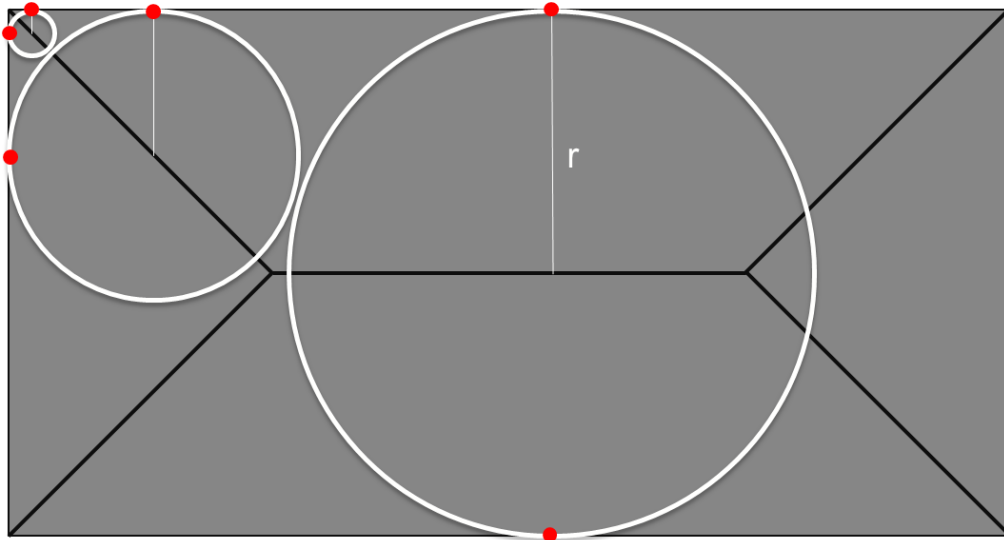


Figure 5-10 – Examples of the medial axes of a rectangle (black lines). The picture also illustrates circumferences that are enclosed in the 2D shape, whose centres belong to a point in the medial axis, and that are tangent (red dots) to at least two points belonging to the object's perimeter.

This work hypothesizes that the topological skeleton of the true contact area perimeter can be used to map the regions where ice is most likely to be uniformly confined by the bulk ice and crushed ice with respect to the two or more closest edges. In these regions ice remains mostly intact and in direct contact with the structure, as illustrated in Figure 5-2, while in regions where confinement is less and/or not uniform, spalls are more likely to occur and transform into crushed ice. Crack initiation and propagation (spalling) tends to either start within the HPZ contact area and propagate to the edge of the process surface or possibly occur in the opposite manner, i.e., initiating and propagating from the edge of the process surface to the HPZ. There is uncertainty as to whether the former or the latter is the case, or even that both are possible. Evidence from high-speed imaging data (R. E. Gagnon, 2008b) suggests that small-crack flaws left in the HPZ from prior spalling events during the crushing process serve as either nucleation points or end points for the larger fractures that result in spallation. Whatever the case may be, the result is that the spalling fracture moves in a direction that facilitates the separation of a spall (small or large) from the larger intact bulk-ice feature.

The topological skeleton set of points can only form lines. Thus, the topological skeleton by itself it is not able to fully describe an HPZ area. For this purpose, another geometrical descriptor is required.

5.9 Distance transform to determine confinement levels

The results reported in Iliescu and Schulson (2004) show that confinement magnitude, is an important factor in determining effective ice strength, even when confinement is not uniform over the secondary and tertiary major axis. Thus, it is necessary to have a measure

of the relative confinement, as a function of geometric location to guide the estimation of the HPZ size. The current work suggests that the distance transform is capable of qualitatively describing confinement magnitude over the interface region between the ice and structure.

Distance transform algorithms are commonly used to calculate the distance field of 2D (and also 3D) shapes with respect to the perimeter (Frisken et al., 2000; Strutz, 2021). For a discretized shape, the result is a distance matrix, where each mesh element of the shape will have a numerical value that represents the element's shortest distance, i.e., the least number of elements', to the perimeter. This is exemplified in Figure 5-11 for a square shape.

1	1	1	1	1
1	2	2	2	1
1	2	3	2	1
1	2	2	2	1
1	1	1	1	1

Figure 5-11 – Example of a discretized distance field of a square shape. Numbers describe how many elements there are between it and the perimeter (indicated by the bold line).

In Figure 5-11, elements scalar values represent the least number of elements between an element itself and the perimeter (the element at the point of calculation is included in this value). For a binary image (where ones represent the shape and zeros the background, or

vice-versa), the algorithm calculates the distance field of the foreground in respect to the background. Figure 5-12 illustrates a distance field for a generic square shape. Warmer colours (where ‘cold’ is at the blue end of the visible spectrum and ‘hot’ is at the red end) represent elements that are farther away from the perimeter, and cooler colours are closer to the perimeter. The warmer the colour, the more confined is the region.

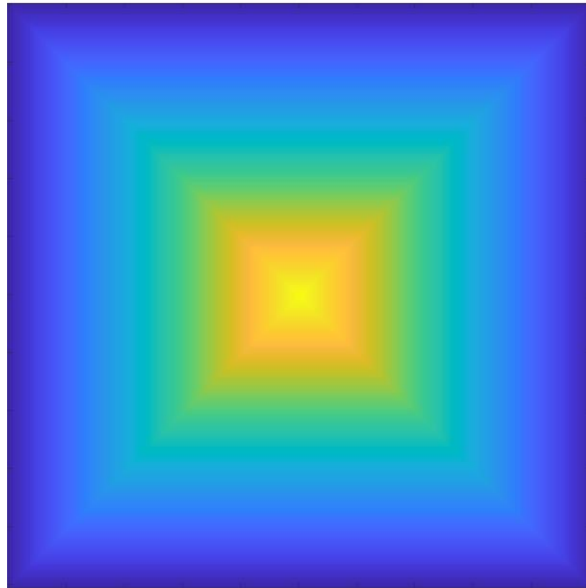


Figure 5-12 – Example of a high-resolution distance field map of a square shape. The colour warmth relates to the distance value to the perimeter, warmer colours correlate to farther regions, i.e., more confined regions.

If Figure 5-12 would represent an ice-indenter interface contact area, then the distance field map would represent the confinement magnitude generated by the bulk ice shape that enhances the ability of the intact ice at the interface to support load. Now that confinement can be quantified in a relative manner, and the paths of HPZ development (i.e., the medial lines) can be traced, the final step is to combine both measures to determine the HPZ shape.

5.10 Methodology for the ice pressure distribution and implementation

For 2D objects, the topological skeleton can be described as a set of 1D representations that can be used to recreate the original object it represents. For this, each point of the topological skeleton matrix must be assigned information regarding its distance to the perimeter of the object. This distance is the radius of a disc centred at that point, that if drawn for all points of the skeleton, is capable of recreating the original shape, (Blum, 1967; Siddiqi et al., 2002), as illustrated in Figure 5-10. In fact, distance transforms can be used to calculate the topological skeleton itself, as initially proposed by Blum (1967), but this combination of the two functions is not explored in this study. The functions that determine the topological skeleton that are available in the MATLAB library do not store the distance field information natively, so calculating the distance transform and topological skeleton separately, and then performing a scalar multiplication is the simplest computational solution found. This process is illustrated in Figure 5-13, and again in section 5.17 Appendix A. In the present case, readily available functions were deemed sufficient, but future work might benefit from an algorithm streamlining this aspect (further discussion in section 5.18 Appendix B).

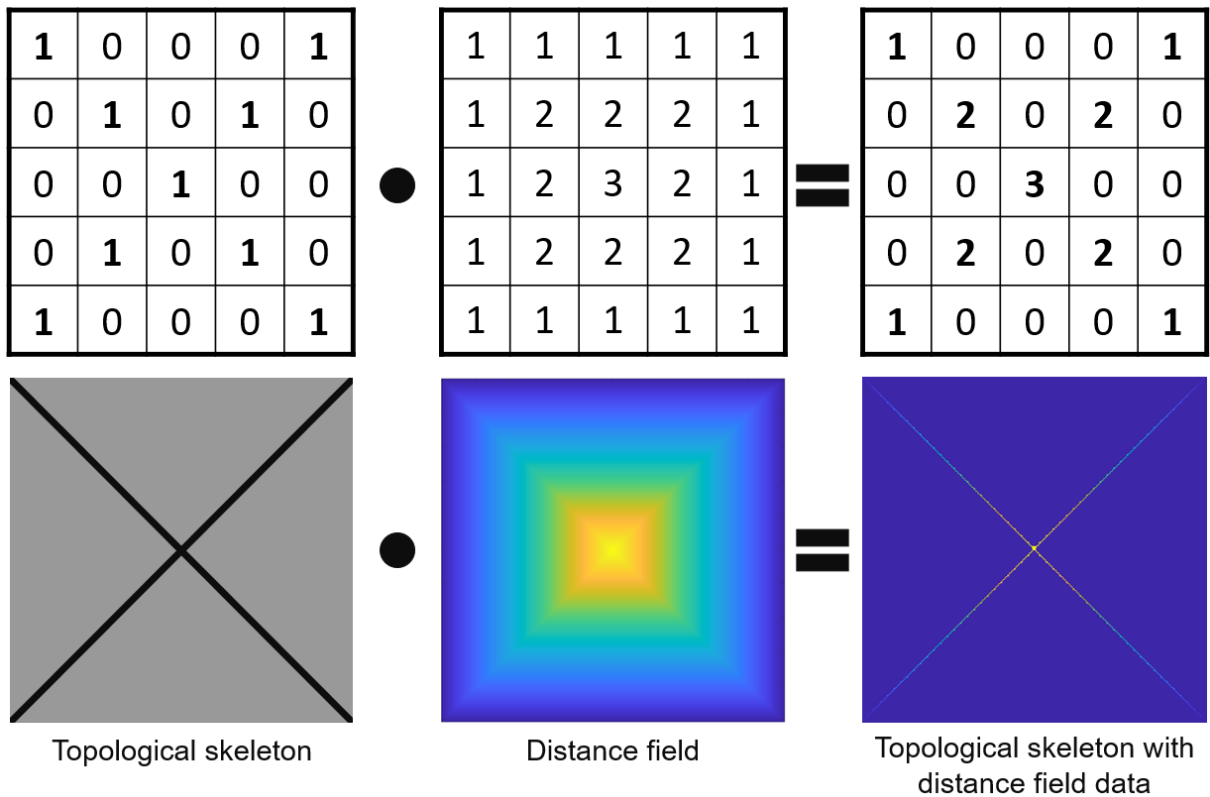


Figure 5-13 – Process of combining the topological skeleton with its distance field data (a square is used as example). Above are the discretized matrices. Below are the visual representations of the matrices.

The original shape reconstruction process requires a circle to be drawn for every point on the skeleton, with the radius of each circle defined by distance field data, reversing the process depicted in Figure 5-10. With minor modification, this reverse process can be used to generate HPZ regions for any contact area shape.

The modification in the reconstruction of the original shape involves assigning a reasonable width to a HPZ at each point of its topological skeleton. That is, the radius of each circle (as in Figure 5-10) is fractionalized by a constant that defines the relative size of HPZ with respect to the contact area. In this work, this fraction is defined such as to obtain an

idealized HPZ area coverage of the contact area. This modifier is used to represent the influence of the crushed ice confining back pressure, which allows the characterization of HPZs in different confinement scenarios. As discussed by Kim (2014), Sopper et al. (2016), and Gagnon and Bugden (2022) confinement pressures will increase when crushed-ice flow is restricted, and measured loads will also increase. The confining crushed ice enables the HPZ to increase in area thus supporting more load, and furthermore the restricted crushed ice flow itself generates direct load increases in the LPZ area acting on the structure. For example, Figure 5-14(a) shows the results for 5% HPZ area coverage of a square contact area, Figure 5-14(b) for 10%, and Figure 5-14(c) for 20% (and if that value was 100%, then the original square shape would be re-constructed).

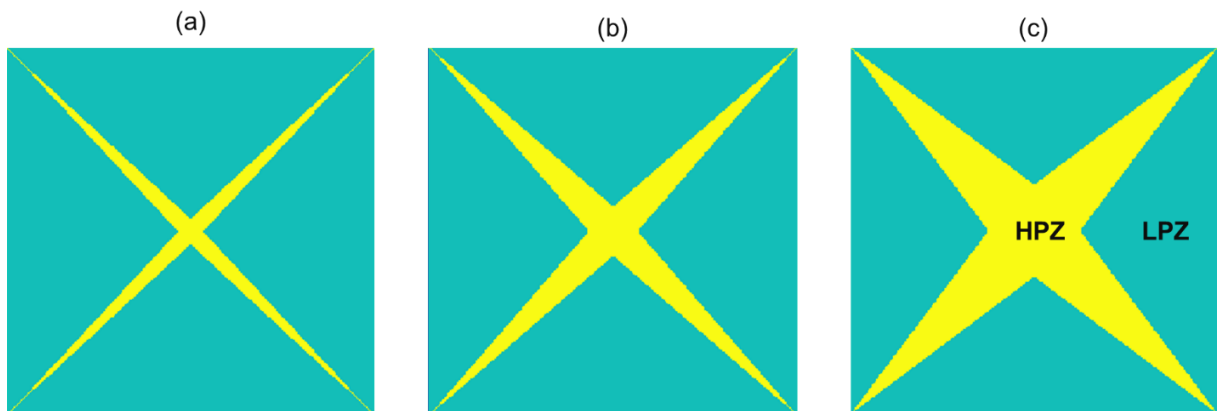


Figure 5-14 – Examples of HPZ (yellow) and LPZ (cyan) representation of a square shape using the topological skeleton method. Different HPZ/Total area ratios are shown: (a) shows a HPZ coverage of 5% of the square area, (b) 10%, and (c) 20%.

There are many factors that influence the crushed ice flow, from ice geometry to boundary conditions (like the presence of water or snow). This work does not study all the possible values that the area ratio constant can have, but based on the few cases where (HPZ Area)/(Total Contact Area) ratio was measured (e.g., R. Gagnon et al. 2020; R. Frederking

2004), HPZs cover around 10-15% of the contact area for cases where the indenter is flat and rigid. The following Figure 5-15 is a summary of the methodology. The implementation of each step is further discussed in greater detail in section 5.17 Appendix A, including the algorithm used for its implementation.

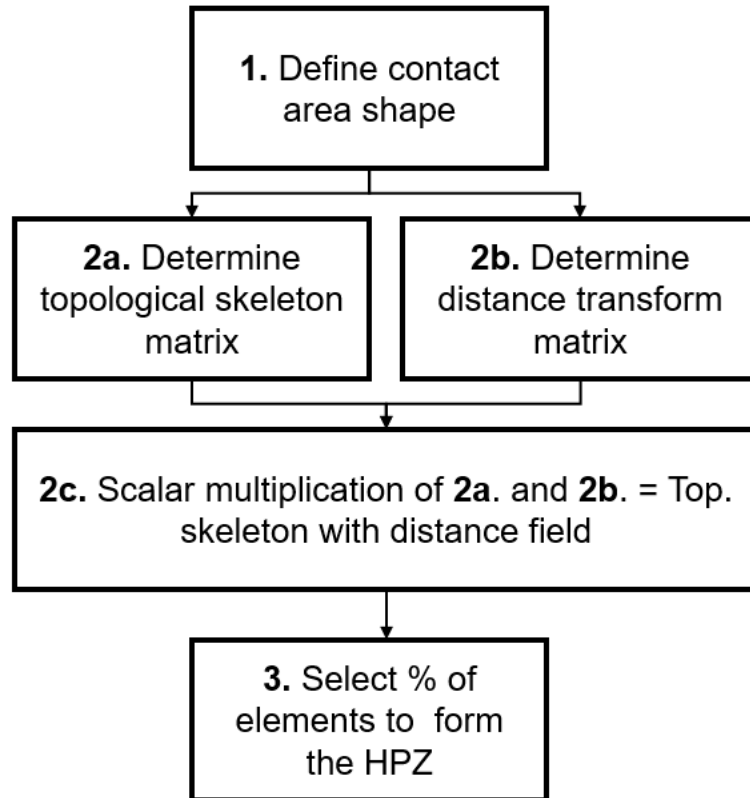


Figure 5-15 – HPZ generation methodology diagram.

The model methodology is exemplified by applying the process on a square contact area. The resulting HPZ distribution generally agrees with the visual data from Hobson’s Choice Ice Island and the proposed model by Spencer and Masterson (1993). This is illustrated in Figure 5-16.

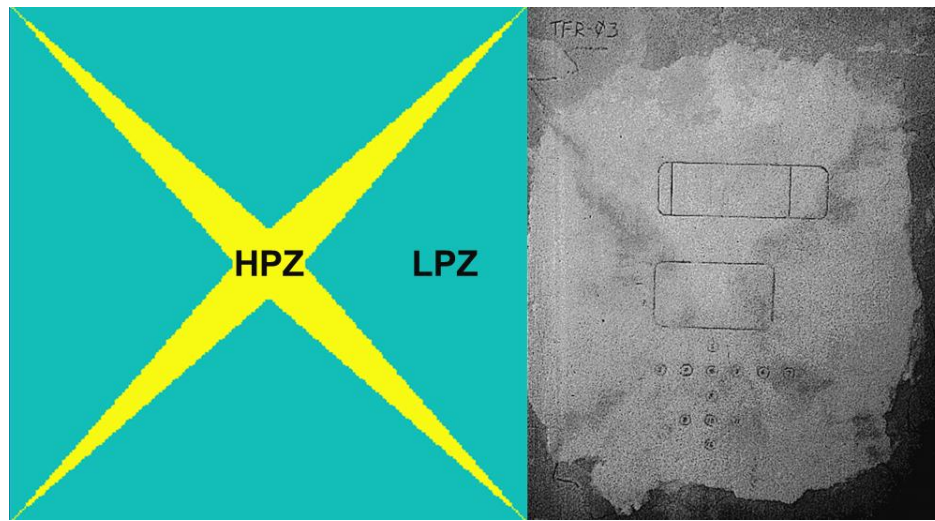


Figure 5-16 – Hobson’s Choice Ice Island indented ice test face (right) (Gagnon, 1998; Spencer and Masterson, 1993) compared with the idealized HPZ distribution (HPZ is yellow and LPZ is cyan) of a square nominal contact area predicted by the topological skeleton methodology (left).

The following Figure 5-17 shows the predicted HPZ distribution for other idealized geometric shapes, with HPZs covering 10% of the shapes’ areas.

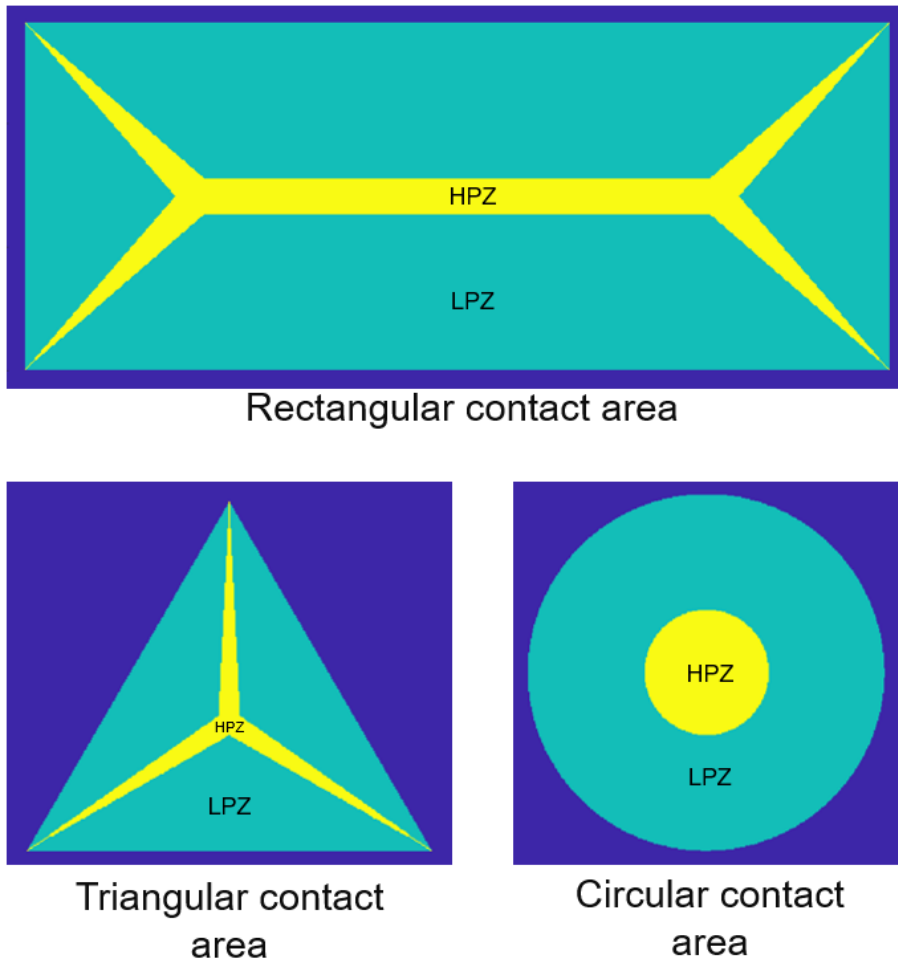


Figure 5-17 – Examples of HPZ distribution patterns (HPZ is yellow, LPZ is cyan, background is dark blue) for idealized nominal contact area shapes. HPZ is assumed to cover 10% of the contact area.

These are idealized models. The effect of possible crushed-ice non-uniform confinement is not included. This may explain some of the variations observed in the following sections when real experiments are studied. Catastrophic spalling events, which change the geometry of the contact area, are not part of this modelling, but assuming that the pre and post spall contact geometries can be described or modelled, then this methodology can be used to predict the corresponding HPZ distributions.

5.11 Comparison with experimental pressure distribution data

This section shows the application of the above topological skeleton methodology for real cases. These cases have comparable HPZ distribution data available, either from pressure sensors or visual observation. The algorithm was set to generate HPZs targeting 10% contact area coverage, the value is based on HPZ area coverage observed experimentally (Frederking et al., 1990; Gagnon et al., 2020). Figure 5-18 shows the resulting test face of one of the large pendulum impacts (Sopper et al., 2015). More specifically, it is the October16_2014 test, as presented in (Gagnon et al., 2020). The picture on the left shows the extracted shape and the resulting HPZ/LPZ distribution. The result generally predicts the observed relatively-intact ice distribution, as the directions and extent of the dendritic arms are similar.

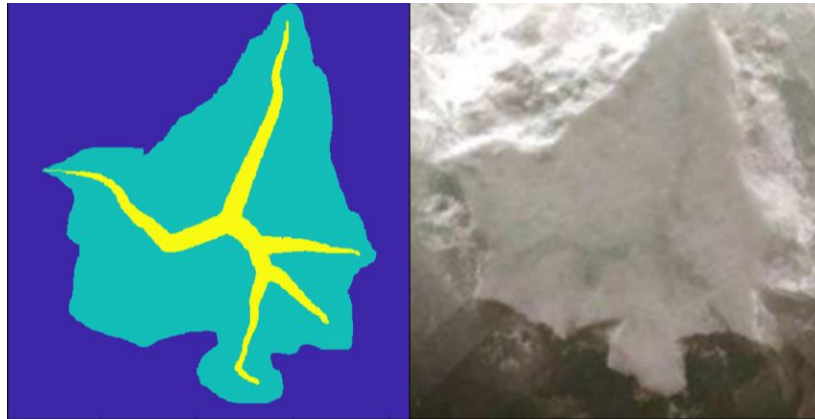


Figure 5-18 – Oct_16 2014 Large pendulum’s impact ice test face (right) (Sopper et al., 2015) compared with the HPZ distribution predicted by the topological skeleton methodology (left). HPZ is yellow, LPZ is green, and the background is blue.

Pressure distribution data are also available for the aforementioned experiment reported in Gagnon et al. (2020) and it is included in Figure 5-19. This data illustrates an issue that can

arise in visual images of the ice contact zones. Part of the local crushed ice, created by initial sintering of shattered spall debris and freezing of a small melt fraction, may only loosely remain in the peripheral contact area, and does not provide confinement or load. A small force might easily remove such material, even by hand at the end of a test. The remaining crushed material, however, is much more robust and is fixed in position. The pressure map data shows that some crushed-ice regions that are visually present in the post impact picture (Figure 5-19) are seemingly not contributing to the contact pressure at the sensor, indicated by arrows.

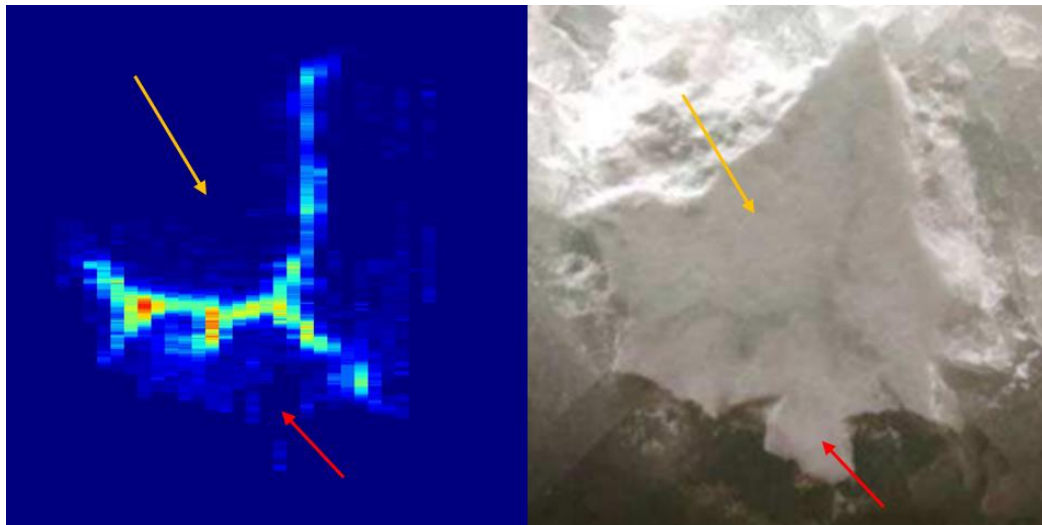


Figure 5-19 – Large pendulum impact ice test face (right) and corresponding pressure map (left), October_16 2014. Red and Yellow arrows show regions of the contact area that have negligible measured contact pressure.

A new contact region is drawn such as to exclude the influence of the regions indicated in Figure 5-19. The resulting HPZ distribution is shown in Figure 5-20, (right). It compares more favourably with the pressure data recorded by the pressure sensing apparatus (left), and with the visual information from the picture taken from the post-impact ice-face

(middle). This treatment was only applied for this special case. The other studied cases have the contact area matching the test face of the experiments.



Figure 5-20 – Large pendulum’s ice impact October16_2014 test face (centre) compared with experimental pressure distribution data, and the HPZ distribution predicted by the topological skeleton methodology (left). Images are not on the same scale.

The following Figure 5-21 to Figure 5-24 show results for 4 Large Pendulum Impacts: Dec15_2014, Jan20_2015, Dec10_2015, Feb25_2016 (Gagnon et al., 2020). Together with the previously presented experiment October16 2014 (Figure 5-20), the results from these experiments show quite good agreement between measured and predicted HPZs. For the particular case of Dec15_2014, the results roughly predict the HPZ shape, but its location differs from what is shown in the pressure map. This is probably related to a HPZ that is still developing after a recent spalling.

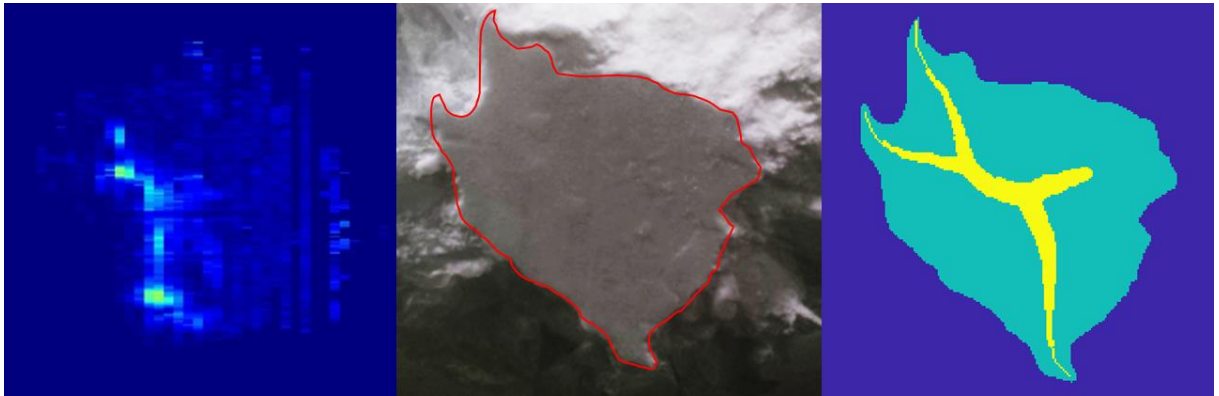


Figure 5-21 – Generated HPZ distribution for Dec15_2014 (Gagnon et al., 2020) test face (centre) using the topological skeleton method (right). It is compared to the pressure map (left). The pressure map is not on the same scale.



Figure 5-22 – Generated HPZ distribution for Jan20_2015 (Gagnon et al., 2020) test face (centre) using the topological skeleton method (right). It is compared to the pressure map (left). The pressure map is not on the same scale.



Figure 5-23 – Generated HPZ distribution for Dec10_2015 (Gagnon et al., 2020) test face (centre) using the topological skeleton method (right). It is compared to the pressure map (left). The pressure map is not on the same scale.



Figure 5-24 – Generated HPZ distribution for Feb25_2016 (Gagnon et al., 2020) test face (centre) using the topological skeleton method (right). It is compared to the pressure map (left). The pressure map is not on the same scale.

Four experiments from Hobson’s Choice Ice Island were compared, TFR01, TFR02, TFR04, TFR05 (Muhonen, 1991), and the results are shown in Figure 5-25 to Figure 5-28 (TFR 03 was discussed in the previous section). For all cases, the methodology shows good agreement with the photos. It is important to note that extruded crushed ice that accumulated above the specimens should not be considered as part of the studied contact area, since it is only loosely attached to the bulk ice feature, and in those regions, HPZs

cannot be formed. The relevant contact-area perimeter selected is shown as a continuous red line.

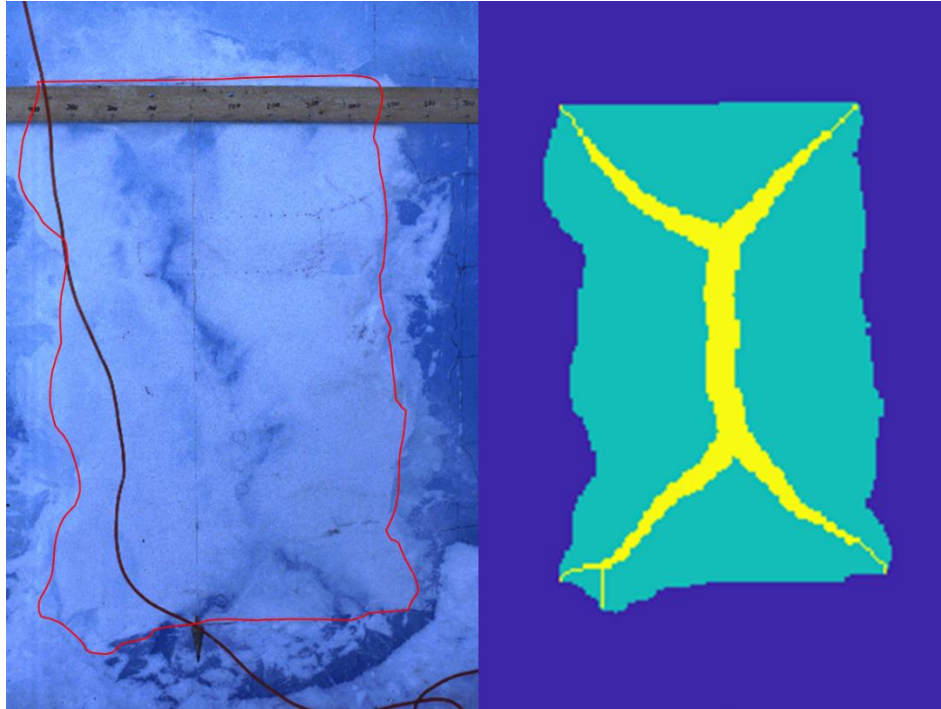


Figure 5-25 – TFR 01 (Muhonen, 1991) test face (left). Generated HPZ distribution using the topological skeleton method (right). The original ice-feature shape was a vertical wedge.

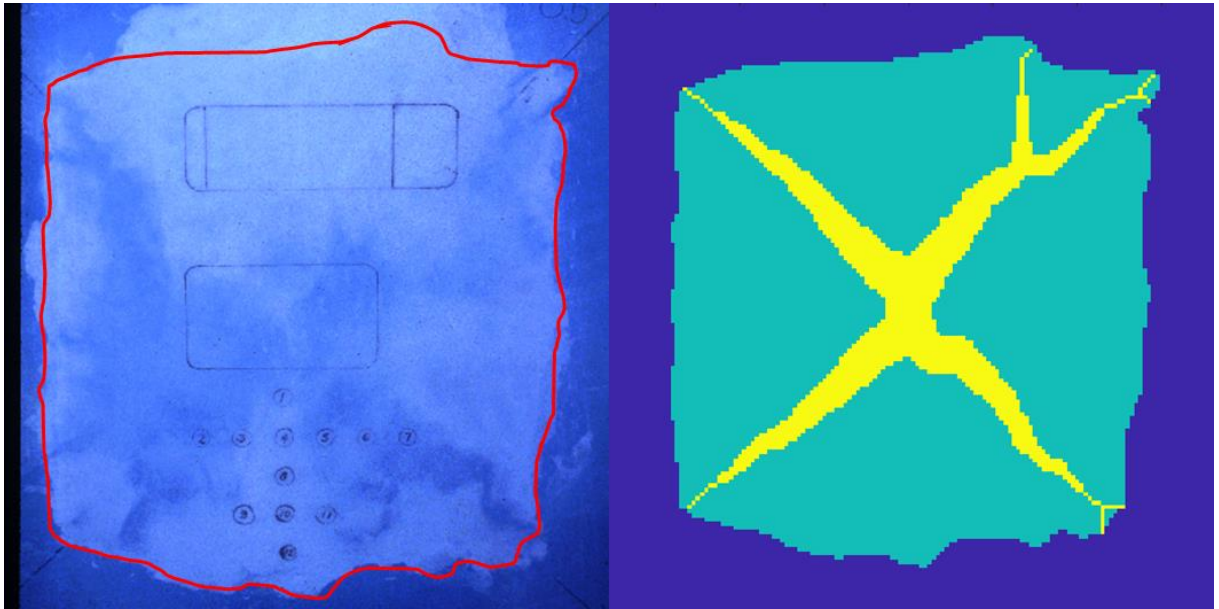


Figure 5-26 – TFR 02 (Muhonen, 1991) test face and also region selected for HPZ generation (left). Generated HPZ distribution using the topological skeleton method (right). The original ice-feature shape was a truncated square pyramid.

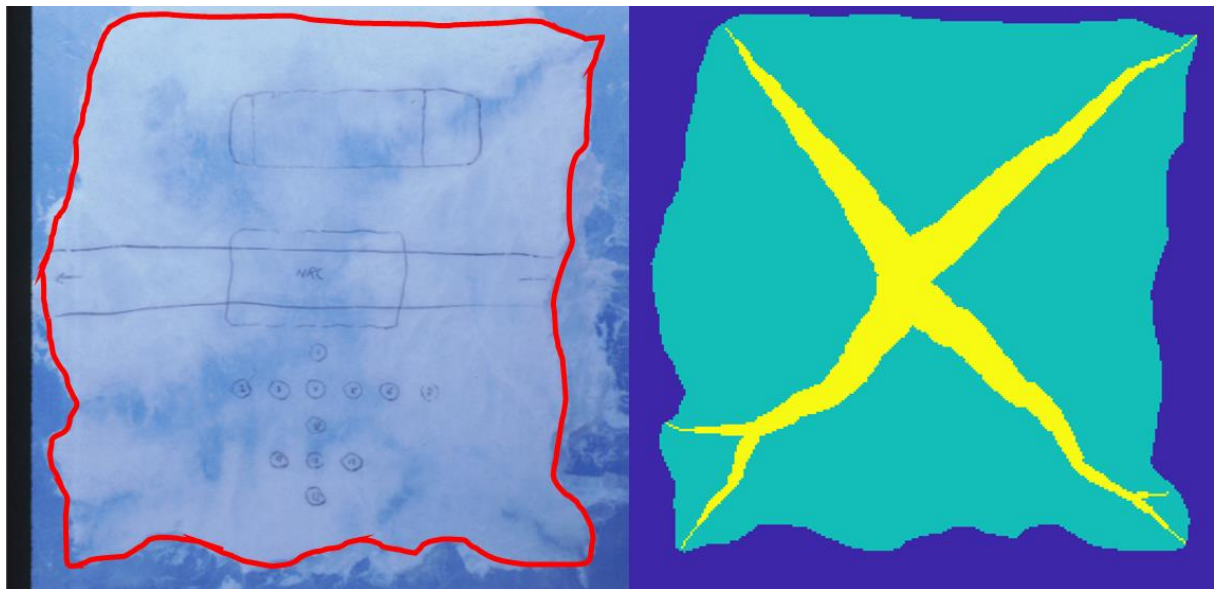


Figure 5-27 – TFR 04 (Muhonen, 1991) test face and also region selected for HPZ generation (left). Generated HPZ distribution using the topological skeleton method (right). The original ice-feature shape was a truncated square pyramid.

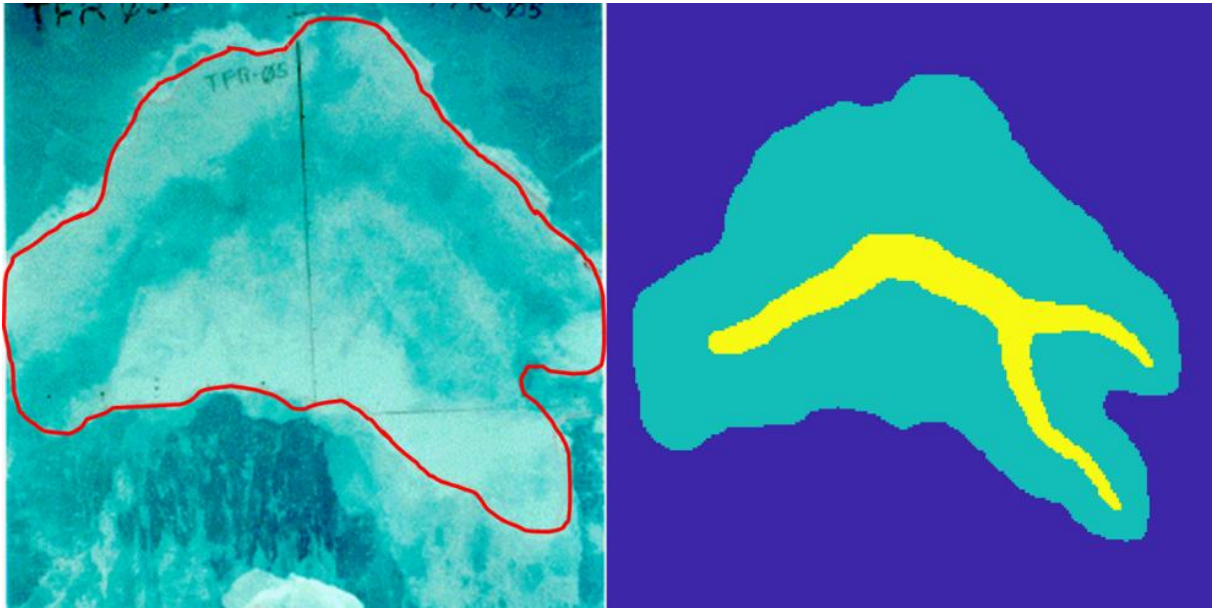


Figure 5-28 – TFR 05 (Muhonen, 1991) test face and also region selected for HPZ generation (left). Generated HPZ distribution using the topological skeleton method (right). The original ice-feature shape was a truncated square pyramid with base rotated 45 degrees w.r.t TRF 04.

Additionally, the procedure was applied to two small-scale indentation experiments. The indented test faces and HPZ prediction results are shown in Figure 5-29 and Figure 5-30. The ice samples used in these small-scale ice-crushing tests (Gagnon and Bugden, 2022) were cut from blocks of freshwater granular ice grown in the lab, where the grain diameter was about 4 mm and the sample dimensions were approximately 7 cm x 7 cm x 7 cm. The samples were square-columnar in shape with a truncated-pyramid top, where the sides of the pyramid were sloped at $\sim 39^\circ$ to horizontal. High-speed-video (HSV) was used to record visual data, viewed through transparent acrylic crushing platens, at one of two rates (1000

images/s and 15000 images/s). The ice-crushing penetration speed was 16 mm/s for all tests.

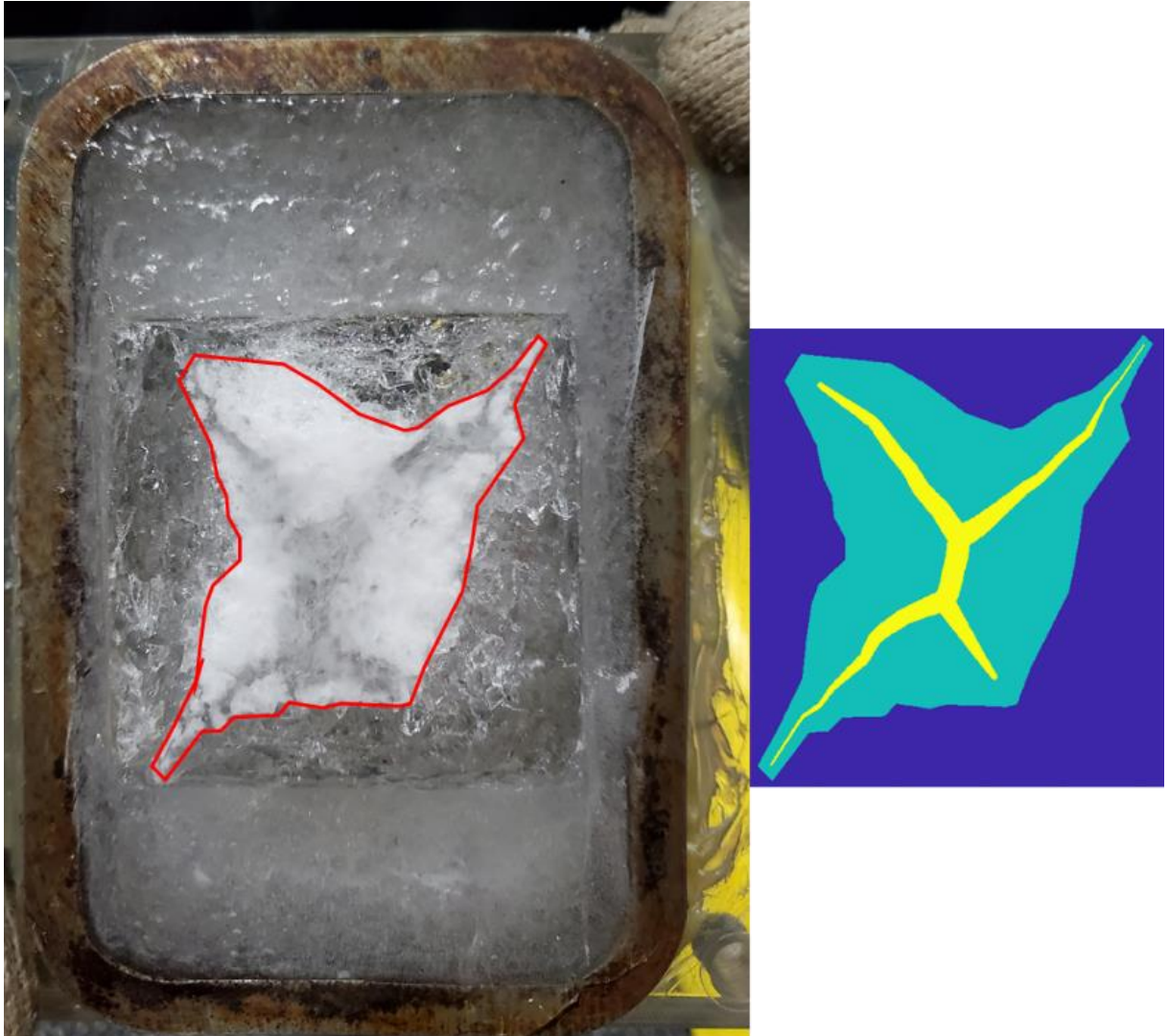


Figure 5-29 – On the left, picture of the post-indentation test face of a small-scale indentation experiment (reported in Gagnon and Bugden (2022)). In this image it is possible to see relatively-intact ice as translucent grey, which is associated with the HPZ, and crushed ice as a milky white region, which is associated with the LPZ. The test-face contact geometry (outlined in red) is used to predict the HPZ distribution using the present methodology. On the right, the predicted HPZ distribution of the region.

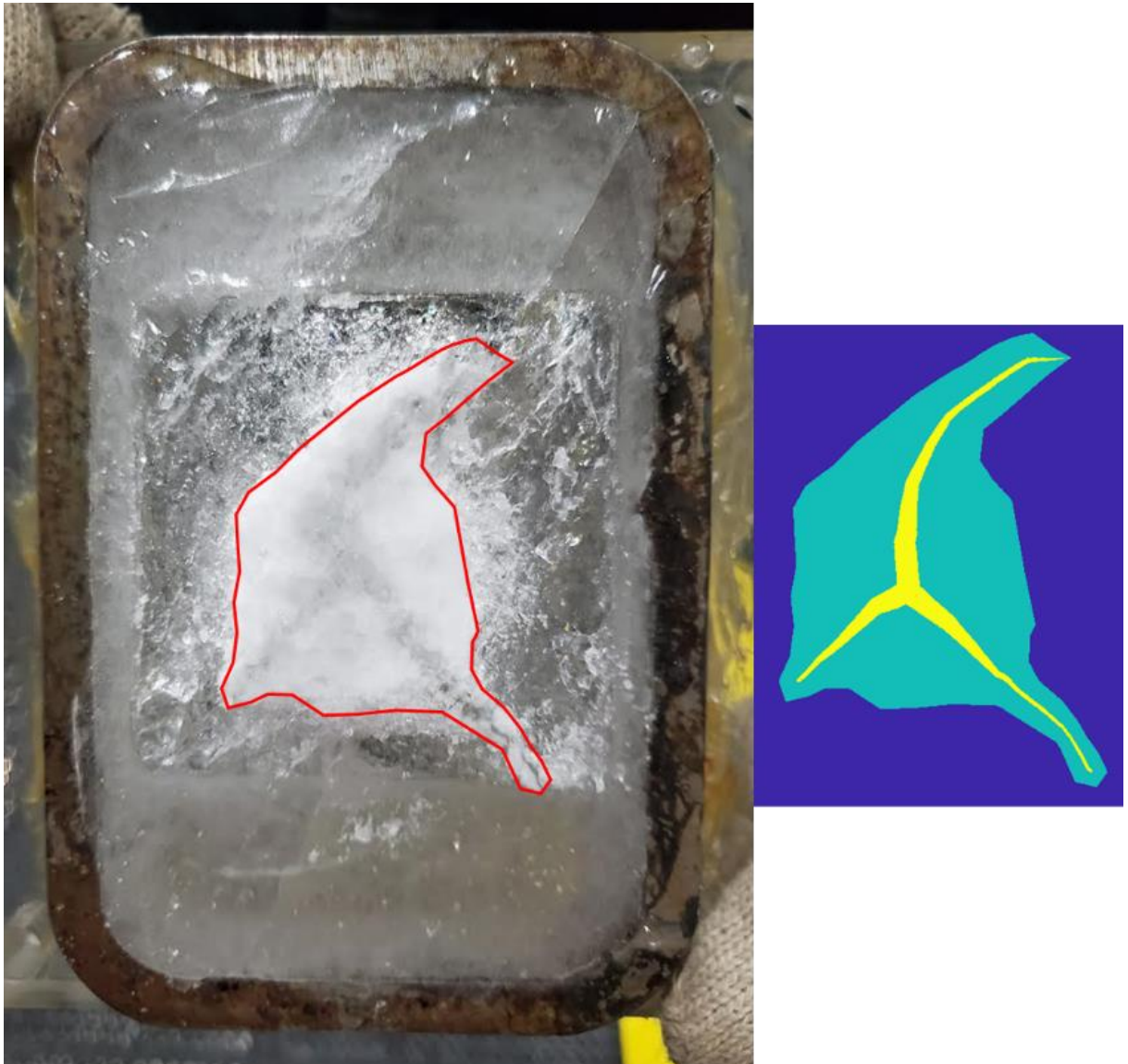


Figure 5-30 – On the left, picture of the post-indentation test face of a second small-scale indentation experiment. In this image it is possible to see relatively-intact ice as translucent grey, which is associated with the HPZ, and crushed ice as the milky-white region, which is associated with the LPZ. The test-face contact perimeter (outlined in red) is used to predict the HPZ distribution using the present methodology. On the right, the predicted HPZ distribution of the region.

Figure 5-30 shows the post-test image of a polycrystalline ice sample that was crushed by a platen similar to the smooth flat platen that had crushed the ice specimen shown in Figure

5-29. The platen had a slightly rough surface that yielded similar ice-crushing behavior and loads during crushing tests as the smooth flat platen, but those data were not included in Gagnon and Bugden (2022). In both cases the methodology was able to reasonably predict the observed HPZ pattern. The set of results in Figures 20-30 show that the proposed use of the topological skeleton to represent HPZ distribution and patterns works reasonably well for small-scale experiments in addition to medium (Large Pendulum Impacts, (Gagnon et al., 2020)) and large scale experiments (Hobson's Choice Ice Island Indentation Experiments, (Muhonen, 1991)).

The cone-section shape illustration in the bottom image of Figure 5-17 (the circular cross-section) is a fundamentally unstable shape with respect hard-zone formation locations because there are no preferential confinement directions, that is, the lateral confinement from the bulk-ice shape is uniform. That is why the pendulum ice impact tests discussed above were more subject to catastrophic spallation events and generally presented contact areas during most of any particular test where the hard zones had dendritic random shapes rather than shapes like those in Figure 5-25. This progression from roughly circular to dendritic HPZ distribution for conic ice shapes can be seen in Figure 5-5, with more examples available in Gagnon et al. (2020). The ice features at the Ice Island, and also the small-scale indentation tests shown in Figure 5-29 and Figure 5-30, however, had well-defined confinement directions that ultimately determined, in most cases, the post-test locations and shapes of HPZs and LPZs. Figure 5-28 shows one of the exceptions, where a catastrophic spallation event differentiated the end result from those of the other tests at the Ice Island (Figure 5-25 to Figure 5-27). Even though there is inherent lack of predictability

of HPZ and LPZ development for a cone-shaped ice feature, this is really a feature of the inability to maintain a circular contact shape and not an indication that the HPZ predicted for a circular shape is incorrect. In all cases the hard-zone size and shape can be ideally predicted with good fidelity if the full contact area shape and size are known at particular points throughout a test, or at the end of a test (e.g. Figure 5-20 to Figure 5-24).

The main conclusion is that the model can generate a reasonable prediction of the observed HPZ size and shape even in complex-shaped contact zones. This representation might be further improved with the addition of a model that describes 3D geometric changes of the bulk ice that arise from large scale spalling during indentation. For example, a 3-dimensional update of current 2D spalling models, such as the models described by Daley (1991) or Taylor and Jordaan (2015) may integrate with this method.

5.12 Discussion on limitations of the geometric method for HPZ representation

The method presented is purely geometry based, thus it cannot directly account for ice related factors such as ice type, temperature, impurities, and grain size. The results presented in this work are only strictly valid for experiments with granular freshwater ice or the multi-year ice from Hobson's Choice Ice Island experiments. In this sense, the effect of crystal lattice orientation with relation to the indentation direction on the development of the HPZs was not studied in this work. Another important aspect is that all cases studied were that of a flat indenter which was indenting in the normal direction of the base of the ice samples. All of these samples are of finite height, but the effect of the ice holder (in laboratory experiments) is not explored. It is assumed that the ice holder functions as a

much larger ice mass that is supporting the indented ice feature. In the large pendulum experiments, the maximum indentation depth (~13 cm) was always less than half the ice cone height (~30 cm), so we speculate that ice-holder effects may not have been very significant in those cases. On the other hand, cracks were often observed to extend to the ice-holder rim, but it is uncertain how that may have affected the outcome of the tests with respect to spallation generation (of the regular type or catastrophic type).

Regarding the surface roughness of the flat indenters, there is evidence that it does not have a significant effect on the HPZ size and shape. Gagnon (2018, 2016) studied friction during brittle ice crushing on flat indenters with smooth and rough surfaces and reported that roughness of the plates (even when significant) did not cause much (or any) friction at the ice-indenter interface, and the general shape/size of the HPZ was not affected. Gagnon (2018, 2016) observed that the high-roughness surfaces would significantly reduce the size (and associated load drop) of most individual spallations and greatly increase their number. This was due to the roughness prominences acting as nucleation sites for the small spallations, whereas a smooth surface would create fewer (but larger) spallations and associated load drops. The net result was that the time-averaged ice loads on the smooth and rough indenter plates were similar. Another study (Dragt and Bruneau, 2013) indicates that there is an increase in peak compressive load as surface roughness increases at the transition between ductile and brittle ice failure regimes. This effect, however, becomes less evident during brittle regime failure.

Spalling is not modelled in this work, thus it would be beneficial to develop a spalling model component (or integrate an existing model) to allow the prediction of the full ice-

crushing process. The topological skeleton method, as presented here, is limited to the prediction of what the HPZ distribution would be at points in time based on the assumption that ‘nominal contact area’ and ‘contact area’ remain relatively similar. However, if the process surface undergoes a radical shape change due to catastrophic spallation, then ‘nominal contact area’ and ‘contact area’ will be significantly different, and that information is necessary to model what happens to the HPZ distribution as penetration continues after such an event.

This method cannot directly account for the effects of external boundary conditions (e.g., the presence of water, snow, and/or rubble enveloping the ice feature) on the confinement due to crushed ice. This is done indirectly by assuming that the final HPZ size is a pre-defined percentage of the total contact area. If external confinement is assumed uniform (which is never truly the case, but it is an assumption required at this stage), then this percentage value can be adjusted to account for the level of confinement. The definition of its value, however, requires further research.

The method shows generally consistent results for different ranges of indentation speeds and impact energies, however there is an appreciable improvement in quality for the small-scale experiments shown in Figure 5-29 and Figure 5-30. Also, regarding these images, the test face pictures were taken during the development of the topological skeleton methodology presented in this work. The test faces were cleared of loose crushed-ice rubble to improve visibility, lighting quality was improved, and pictures were taken in a direction approximately normal to the surface. Note that HPZs are related to the intact-ice region and thus cannot develop outside of the nominal contact areas, as is evident in the

aforementioned figures. This also implies that the method will only represent a full contact area with LPZs that are contained within the nominal contact area.

The method defines HPZ and LPZ regions under the assumption that these zones represent different ice types, i.e., intact and crushed ice respectively. This work does not study the pressure distribution variations within these zones, and furthermore this work is not proposing pressure values that can be assigned to these regions. One could refer to the literature for such average values, for example, the pressure data presented in Gagnon et al. (2020), but note that values from the literature are only strictly valid within the parameters of the particular studies themselves.

Finally, further testing would be necessary to single out the most relevant parameters after geometry, such as indentation speed, indentation direction, non-flat indenters, boundary conditions confinement, and ice characteristics.

5.13 Application for idealized ice load patches

The methodology developed here describes output data for a single contact area, which can be imagined as an instantaneous representation of the interface-contact between ice and the structure. The contact-zone HPZ/LPZ size and pattern at any given instant is a function of indentation depth and nominal contact area geometry. For illustration purposes, Figure 5-31 shows an ice feature similar to the Hobson's Choice experiments presented previously (TRF 01, 02, 03, 04, and 05). It is an ice feature of square pyramidal shape being acted on by a flat indenter, and the pressure distribution is determined at three different indentation depths.

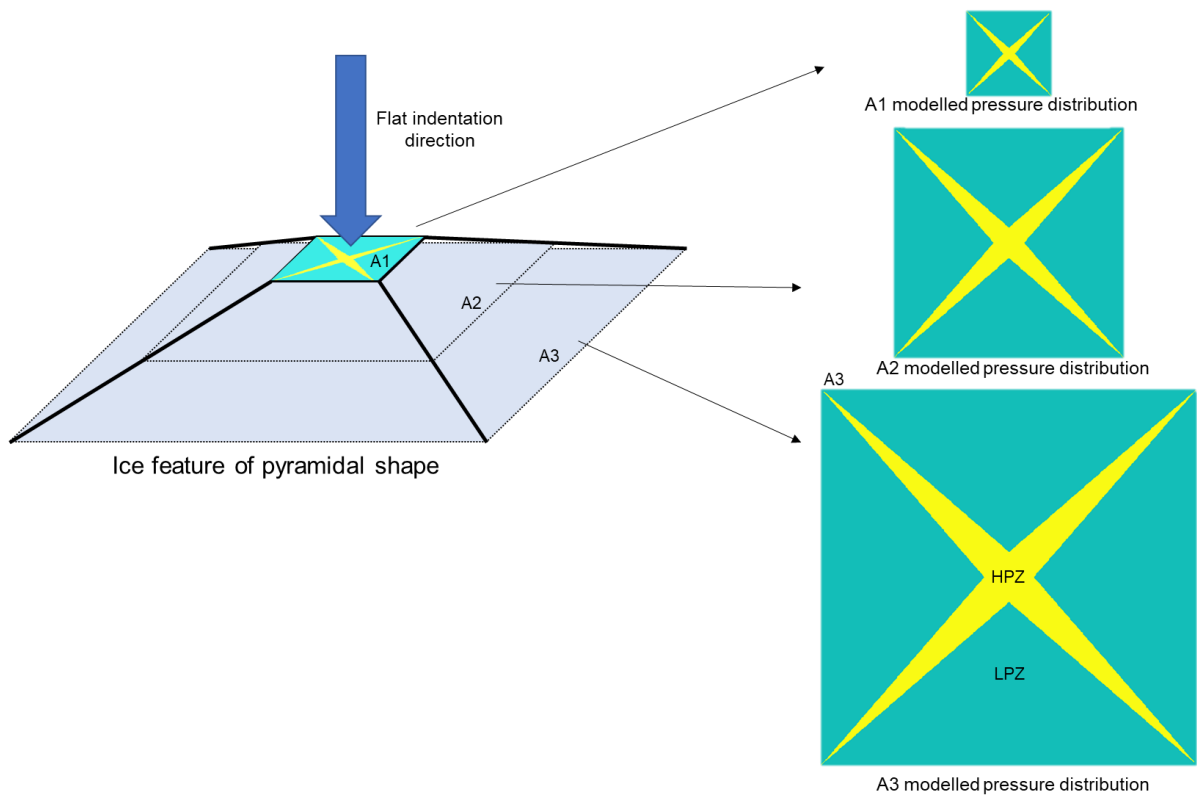


Figure 5-31 – Idealized example of an ice-structure indentation. The contact area progression is represented on the left. The contact areas (CA's) are represented as idealized squares and the modelled pressure distribution is shown on the right.

As indentation progresses, contact area increases, and the arms of the HPZ increase in length. The HPZ arms relative thickness also increases with penetration depth, while maintaining the same shape characteristics. This example shows how the methodology can be used to determine load patches for structural numerical simulations. A consecutive series of pressure-distribution patterns, generated by the methodology, could be applied in a suitable time-step manner to a structure in order to simulate an ice indentation event. The structure could be rigid or elastically/plastically deformable.

5.14 Discussion and Conclusions

In this work a geometry-based methodology is presented for modelling ice pressure distribution during ice impact/indentation. HPZs are regions where ice remains relatively intact at the contact zone between ice and structure, and the interface pressure is high. LPZs represent the regions where crushed ice is in contact with the structure, and the interface pressure is lower. It has been observed that HPZs can exhibit contact pressure almost an order of magnitude greater than LPZs. Therefore, the distribution of HPZs and LPZs affects the structural response.

HPZs tend to form where confinement is the greatest since this reduces the intact ice's susceptibility to fracture and spallation. Confinement arises from the geometrical shape of the bulk-ice feature, and from pressurized crushed ice, which originates from the HPZs and consequently tends to surround them and provide further support. Hence, as observed in various studies, the level of confinement at the ice/structure interface will vary over the indentation interface contact area and is reflected in the locations of the HPZs and LPZs at any instant in time. The present methodology uses the topological skeleton and distance field information of the ice contact area's shape to approximately define the shapes and sizes of the associated HPZs and LPZs, as shown in section 5.11.

The model can describe the HPZ distribution for actual contact area shapes. If the bulk ice feature geometry is known initially, then the methodology will produce reasonable descriptors of HPZ/LPZ distribution during the steps of an indentation, assuming no catastrophic spallation events. This capability makes it useful for numerical structural simulations where ice load patches are applied to a structure.

The model would greatly benefit from the development of a spallation model that predicts ice feature geometric changes. This prediction of evolving contact area shape could then be used to re-predict the HPZ/LPZ distribution as an indentation proceeds using the methodology developed here.

On a final note, pressure values and the percentage of HPZ coverage of the contact area are parameters that depend on the ice characteristics, external boundary conditions, and spallation events. These aspects were not studied in depth in the current work, and the values used for HPZ relative coverage over the contact area were based on average values reported in the literature.

5.15 Acknowledgments

The authors graciously acknowledge the financial support from the Natural Sciences and Engineering Research Council of Canada DND/CRD [grant number DNDPJ 520471-17] ‘Operational Capabilities of Low- and Non-ice-class Structures in Ice’ grant, and the following contributing project partners: Defence Research and Development Canada (Atlantic), Vard Marine Inc., the American Bureau of Shipping (ABS), and the Newfoundland and Labrador Provincial Government [grant number 5404-1984-102].

5.16 References

Blum, H., 1973. Biological shape and visual science (part I). *J. Theor. Biol.* 38, 205–287.

[https://doi.org/10.1016/0022-5193\(73\)90175-6](https://doi.org/10.1016/0022-5193(73)90175-6)

Blum, H., 1967. A Transformation for Extracting New Descriptors of Shape, in: Wathen-Dunn, W. (Ed.), *Models for the Perception of Speech and Visual Form*. MIT Press,

- Cambridge, pp. 362–380.
- Croasdale, K., 2001. Local Ice Load Data Relevant to Grand Banks Structures, PERD/CHC Report 20-61. <https://doi.org/10.4224/12328497>
- Daley, C., 2020. Sea Ice Engineering for ships and offshore structures, 10th ed.
- Daley, C., 1994. Compilation of Medium Scale Ice Indentation Test Results and Comparison to ASPPR. Nepean, Canada.
- Daley, C., 1992. Ice edge contact and failure. Cold Reg. Sci. Technol. 21, 1–23. [https://doi.org/10.1016/0165-232X\(92\)90002-C](https://doi.org/10.1016/0165-232X(92)90002-C)
- Daley, C.G., 1991. Ice edge contact a brittle failure process model, Acta Polytechnica Scandinavica, Mechanical Engineering Series. <https://doi.org/10.13140/RG.2.1.2974.7602>
- Dragt, R.C., Bruneau, S.E., 2013. The collision of cone shape ice samples against steel plates of varying surface roughness, in: Proceedings of the International Conference on Port and Ocean Engineering under Arctic Conditions, POAC. Lulea University of Technology.
- Frederking, R., 2004. Ice pressure variations during indentation, in: International Association of Hydraulic Engineering and Research Proceedings IAHR'04, Vol.2. Saint Petersburg, Russia, Russia, pp. 307–314.
- Frederking, R.M.W., Jordaan, I.J., McCallum, J.S., 1990. Field Tests of Ice Indentation at Medium Scale Hobson's Choice Ice Island, 1989, in: IAHR. Espoo, Finland, pp. 931–

944.

Frisken, S.F., Perry, R.N., Rockwood, A.P., Jones, T.R., 2000. Adaptively Sampled Distance Fields: A General Representation of Shape for Computer Graphics, in: ACM SIGGRAPH. pp. 249–254.

Gagnon, R., Andrade, S.L., Quinton, B.W., Daley, C., Colbourne, B., 2020. Pressure distribution data from large double-pendulum ice impact tests. *Cold Reg. Sci. Technol.* 175, 103033. <https://doi.org/10.1016/j.coldregions.2020.103033>

Gagnon, R., Bugden, A., 2022. A Study of the Effect of Crushing-platen Surface Shape on Ice-crushing Behavior, in: *Proceedings of the 26th IAHR International Symposium on Ice*. Montreal, Canada, pp. 1–10.

Gagnon, R., Daley, C.G., Colbourne, B., 2015. A large double-pendulum device to study load, pressure distribution and structure damage during ice impact tests in the lab, in: *Proceedings of the 23rd International Conference on Port and Ocean Engineering under Arctic Conditions, POAC*. Trondheim, Norway, pp. 1–10.

Gagnon, R.E., 2018. New insights about ice friction obtained from crushing-friction tests on smooth and high-roughness surfaces. *Int. J. Nav. Archit. Ocean Eng.* 10, 361–366. <https://doi.org/10.1016/j.ijnaoe.2018.02.002>

Gagnon, R.E., 2016. New friction mechanisms revealed by ice crushing-friction tests on high-roughness surfaces. *Cold Reg. Sci. Technol.* 131, 1–9. <https://doi.org/10.1016/j.coldregions.2016.08.002>

Gagnon, R.E., 2008. High-Speed Imaging of Mechanisms Responsible for Sawtooth Cyclic

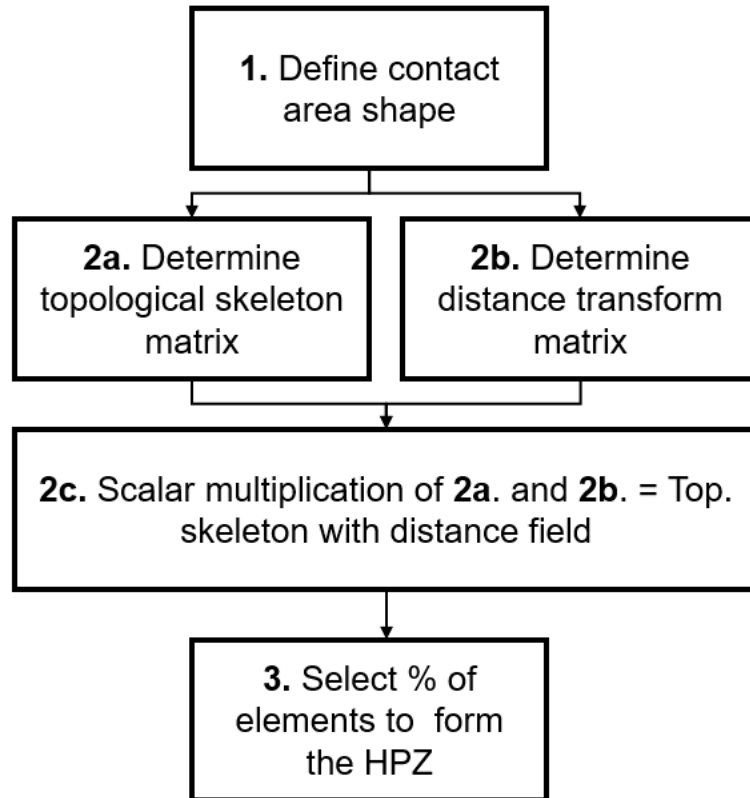
- Loading During Ice Crushing, in: Proceedings of IAHR 2008. Vancouver, Canada, pp. 983–991.
- Gagnon, R.E., 1998. Analysis of visual data from medium scale indentation experiments at Hobson's Choice Ice Island. *Cold Reg. Sci. Technol.* 28, 45–58. [https://doi.org/10.1016/S0165-232X\(98\)00012-3](https://doi.org/10.1016/S0165-232X(98)00012-3)
- Gagnon, R.E., Daley, C., 2005. Dual-axis video observations of ice crushing utilizing high-speed video for one perspective, in: 18th International Conference on Port and Ocean Engineering Under Arctic Conditions. Potsdam, NY, pp. 271–281.
- Gagnon, R.E., Gammon, P.H., 1995. Triaxial experiments on iceberg and glacier ice. *J. Glaciol.* 41, 528–540. <https://doi.org/10.1017/S0022143000034869>
- Glen, I.F., Blount, H., 1984. Measurement of Ice Impact Pressures and Loads Onboard CCGS Louis S. St. Laurent., in: Proceedings of the International Offshore Mechanics and Arctic Engineering Symposium. New Orleans, LA, pp. 246–252.
- Glen, I.F., Blount, H., Comfort, G., Tam, G., 1981. Results of Full Scale Measurements Aboard CCGS LOUIS S. ST. LAURENT During a 1980 Fall Arctic Probe. Ottawa, Canada.
- Iliescu, D., Schulson, E.M., 2004. The brittle compressive failure of fresh-water columnar ice loaded biaxially. *Acta Mater.* 52, 5723–5735. <https://doi.org/10.1016/j.actamat.2004.07.027>
- Joensuu, A., Riska, K., 1989. Structure/ice contact, measurement results from the joint tests with Wärtsilä Arctic Research Centre in spring 1988 [in Finnish]. Espoo, Finland.

- Kamio, Z., Takawaki, T., Matsushita, H., Takeuchi, T., Sakai, M., Terashima, T., Akagawa, S., Nakazawa, N., Saeki, H., 2000. Medium scale field indentation tests: physical characteristics of first-year sea ice at Notoro Lagoon, Hokkaido. Proc. Int. Offshore Polar Eng. Conf. 1, 562–568.
- Kim, H., 2014. Ice Crushing Pressure on Non-Planar Surface. Memorial University of Newfoundland.
- Muhonen, A., 1991. Medium scale indentation tests—PVDF pressure measurements, ice face measurements and interpretation of crushing video. Client Report to National Research Council of Canada, Canadian Hydraulics Center by Helsinki University of Technology, Ship Laboratory.
- Riska, K., Rantala, H., Joensuu, A., 1990. FULL SCALE OBSERVATIONS OF SHIP-ICE CONTACT: RESULTS FROM TESTS SERIES ONBOARD IB SAMPO, WINTER, 1989.
- Sanderson, T.J.O., 1988. Ice mechanics: Risks to offshore structures, First. ed. Graham & Trotman, London, UK.
- Siddiqi, K., Bouix, S., Tannenbaum, A., Zucker, S.W., 2002. Hamilton-Jacobi Skeletons. Int. J. Comput. Vis. 48, 215–231. <https://doi.org/10.1023/A:1016376116653>
- Sopper, R., Daley, C., Colbourne, B., Bruneau, S., 2016. The influence of external boundary conditions on ice loads in ice-structure interactions, in: Proceedings of the International Conference on Offshore Mechanics and Arctic Engineering - OMAE. ASME, Busan, South Korea, pp. 1–11. <https://doi.org/10.1115/OMAE2016-54277>

- Sopper, R., Gagnon, R., Daley, C., Colbourne, B., 2015. Measurements of spatial and temporal variations in ice impact pressures, in: Proceedings of the International Conference on Port and Ocean Engineering under Arctic Conditions, POAC. Trondheim, Norway.
- Spencer, P.A., Masterson, D.M., 1993. A Geometrical Model for Pressure Aspect-Ratio Effects in Ice-Structure Interaction, in: Proceedings of the International Conference on Ocean, Offshore Mechanics and Arctic Engineering - OMAE. Glasgow (United Kingdom), pp. 113–117.
- St. John, J., Daley, C.G., Blount, H., 1984. Ice Loads and Ship Response to Ice. Washington, DC.
- Strutz, T., 2021. The Distance Transform and its Computation.
- Taylor, R.S., Jordaan, I.J., 2015. Probabilistic fracture mechanics analysis of spalling during edge indentation in ice. *Eng. Fract. Mech.* 134, 242–266. <https://doi.org/10.1016/j.engfracmech.2014.10.021>
- Timco, G.W., Weeks, W.F., 2010. A review of the engineering properties of sea ice. *Cold Reg. Sci. Technol.* 60, 107–129. <https://doi.org/10.1016/j.coldregions.2009.10.003>
- Tuhkuri, J., 1995. Experimental observations of the brittle failure process of ice and ice-structure contact. *Cold Reg. Sci. Technol.* 23, 265–278. [https://doi.org/10.1016/0165-232X\(94\)00018-S](https://doi.org/10.1016/0165-232X(94)00018-S)

5.17 Appendix A

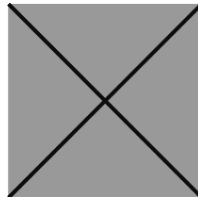
Developed explanation of the methodology presented in Figure 5-15, which is also shown in the sequence:



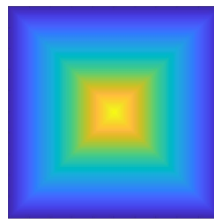
1. Define the 2D shape of the contact area: A black and white image of the shape is imported into MATLAB. It is stored as a binary matrix. Ones represent the contact area (black), Zeros represent the background (white). The functions used in the next steps require this representation format.

2. Obtain the topological skeleton containing the distance field information of the shape:

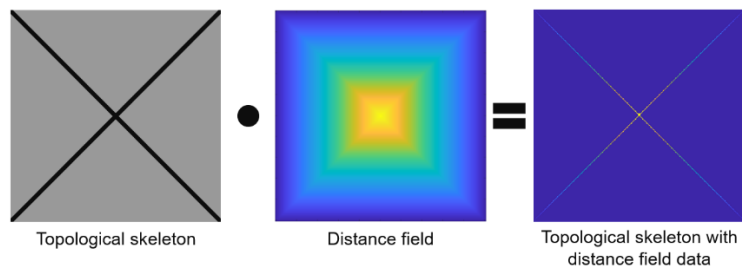
- a. This can be calculated using MATLAB library functions. The functions *bwskel* or *bwmorph* determine the topological skeleton of the shape. Both functions output a logical matrix containing the topological skeleton. Ones represent the skeleton. The two routines use different algorithms, so their output values might differ (this is discussed further in 5.18 Appendix B).



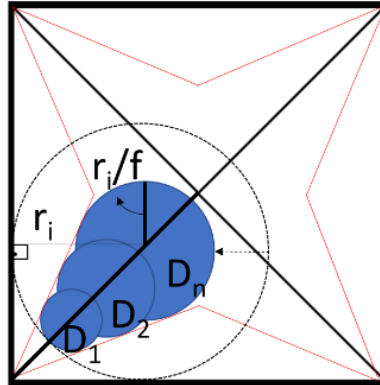
- b. The distance transform of the shape can be calculated using the function *bwdist*.



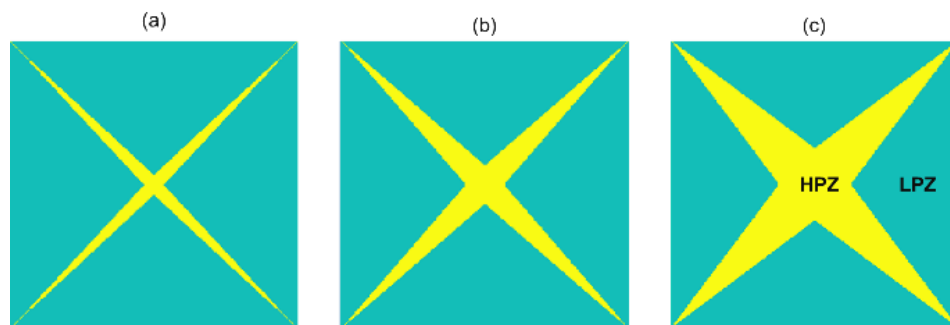
- c. Perform a scalar multiplication of the topological skeleton matrix and the distance transform matrix to obtain the topological skeleton with distance field.



3. Draw discs centred in all points that belong to the topological skeleton. The circumference radii (r_i) are defined as a fixed ratio ($1/f$) of the distance field value obtained in step 2c.



The percentage is a function of the expected HPZ coverage of the area. This is a user defined value. The combined overlapping area of the discs (D_n) define the HPZs, while the area exterior to the discs and interior to the original shape borders defines the LPZs. Images a, b, and c show different percentage values for the same shape.



The code used in MATLAB to generate all the images with HPZs in the current work is presented:

```

LPZ_Ratio=0.9; % target LPZ coverage of the contact area
HPZ_Percent=(1-LPZ_Ratio)*100; % target HPZ coverage of the contact area
%open black and white image file (black image / white background)
baseFileName = sprintf('Image.png');
img=imread(baseFileName);
CA_borders=logical(img(:,:,1)); %transform image into binary matrix
CA_borders2=CA_borders;
%Calculate distance field
CA_dist=bwdist(~CA_borders);
%Calculate top skeleton
%( Conversely, bwmorph(CA_borders,'skel',inf) function can be used)
CA_skel = bwskel(CA_borders);
%Scalar mult. of top. skel. with dist. field
CA=CA_dist.*CA_skel;
CA_dist_skel=CA;
% CA is the topological skeleton with distance field information - this
%defines the largest radius of discs that can be used to approximately
%recreate the original shape

%% Generate HPZ
Total_Area=sum(CA_borders())>0,'all'); %Area of the contact area
% prepare information for the loop
[columnsInImage      rowsInImage]      =      meshgrid(1:width(CA_dist),
1:height(CA_dist));
A=zeros(height(CA_dist),width(CA_dist));
HPZ_image_percent=0;
t=0;
while HPZ_image_percent<HPZ_Percent
t=t+0.01; %t increases at each iteration to slowly increase the HPZ
region
    % until it reaches the desired contact area coverage
    for m=2:height(CA_dist)-1
        for n=2:width(CA_dist)-1
            if CA_dist_skel(m,n)>0
                % selection of elements of CA_dist_skel that are inside a circle whose
                % radius is defined by (CA_dist_skel(m,n)*(t)).
                circlePixels = (rowsInImage - m).^2 + (columnsInImage - n).^2 <=
(CA_dist_skel(m,n)*(t)).^2;
                A=A+circlePixels;
            else
                end
            end
        end
    end

HPZ_Area=sum(A())>=1,'all');
HPZ_image_percent=HPZ_Area/Total_Area*100
end

A=A>=1;
A=A+CA_borders;
figure,imagesc(A)
axis equal

```

5.18 Appendix B

A few considerations are necessary regarding the implementation of the algorithm proposed in this work. As commented, *bwskel* and *bwmorph* functions yield different outputs. This is exemplified in Figure 5-32, which shows a thicker version of the skeleton for better visualization. In that example *bwskel* output skeleton has less “branches”, while *bwmorph* incorporates many branching patterns emanating from the main skeleton structure. Still the core structure (“trunk”) of the skeleton is almost the same in both cases.

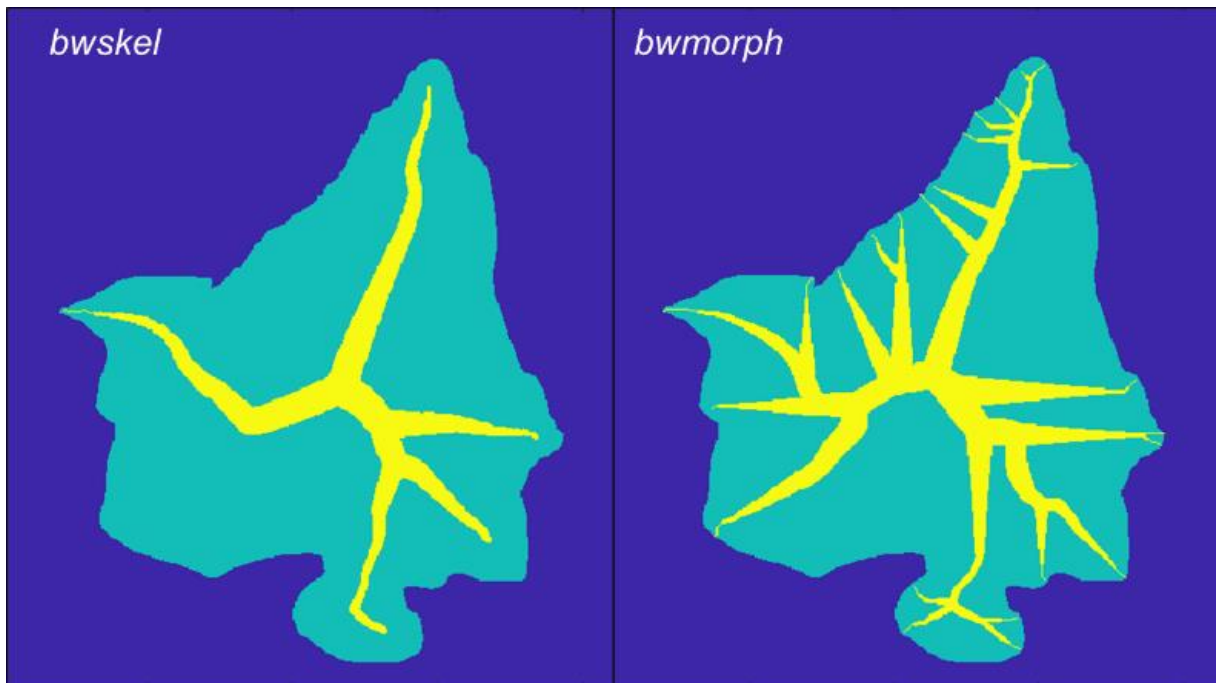


Figure 5-32 – Topological skeleton generation using different MATLAB algorithms: *bwskel* (left), and *bwmorph* (right).

Generally, the *bwskel* function works better for the representation of HPZs in complex shapes with curved perimeter because its algorithm generates only the most significant (i.e., longest) branches of the skeleton. The *bwmorph* function works better for simpler shapes

with straight edges (e.g., squares, triangles, rectangles, etc.). The study of different algorithms for topological skeleton generation would be beneficial, but this is considered out of the scope of the current work.

Another aspect that should be included in this discussion is the fact that the contact area shapes extracted from experiments are hand-drawn in this work. This means that, if two different people with the same training were to define the perimeter of the contact area, it would be almost impossible to obtain the exact same exact shape. The authors tried to simulate this by drawing the perimeter for the same image twice, once more carefully, the second time in a more careless way. The final HPZ distribution results do not show significant divergence even if the drawn shapes are not the same, as it is illustrated in Figure 5-33, which compares two versions of the contact area selection for the same test face.

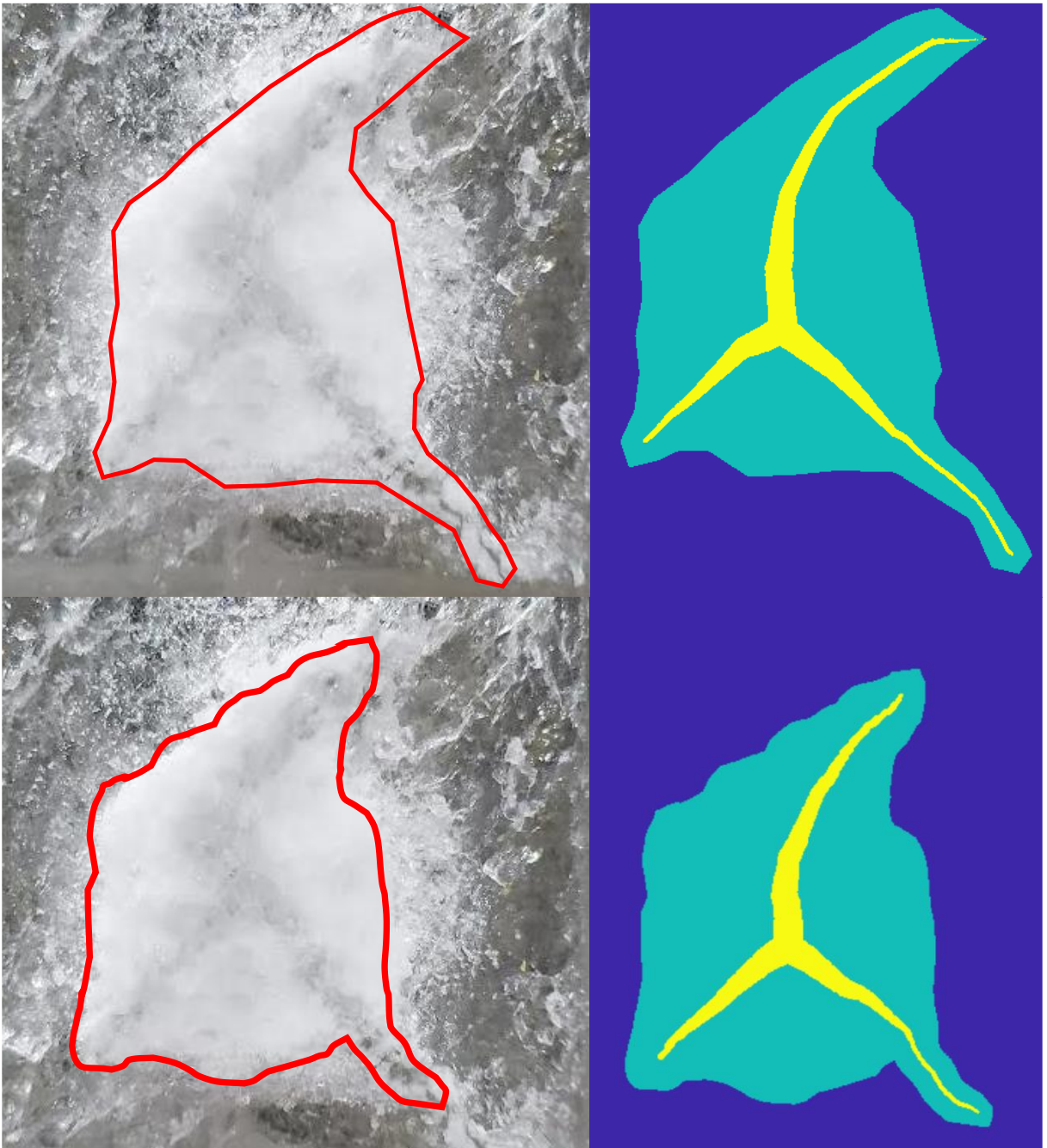


Figure 5-33 – In this image two different contact areas are selected from a test face, the top image shows a more careful selection (the same as the one shown in Figure 5-30), while the second one was drawn more crudely. In both cases the general shape of the HPZs remain very similar.

Chapter 6 The Non-uniform Ice Load Application System (NILAS) and its use in numerical structural analyses of ice impact

6.1 Co-authorship statement

This chapter will be submitted for review to the journal *Marine Structures*. The paper was authored by S. L. Andrade, A. Elruby, C. Daley, and B. Quinton.

S. L. Andrade proposed and developed the ice load methodologies presented in this work, both for coupling ice loads to structural deformation and generating non-uniform pressure distribution. A. Elruby wrote the base code for coupling ice load patches in numerical structural simulations. S. L. Andrade edited and updated the base code to include HPZs and LPZs generation. S. L. Andrade performed the numerical simulations and the data analysis. S. L. Andrade wrote the manuscript. S. L. Andrade, A. Elruby, C. Daley, and B. Quinton were responsible for the paper editing and revisions.

6.2 Abstract

It is challenging to study ice load damage in ships. One important reason for this is the difficulty in properly representing the highly non-uniform pressure distribution as observed at the ice-ship structure interface. This non-uniformity significantly affects the way the structure responds to loads especially as the response exceeds the yield limit. To allow for the representation of complex pressure distributions, this work presents the Non-uniform Ice Loads Application System (NILAS) with the intent of improving ice contact loads representation in numerical simulations. NILAS also couples the ice load to the structure by accounting for the energy losses during the deformation process.

6.3 Introduction

In recent years the Arctic has seen an increase in ship traffic, due to the opening of new shipping routes, mineral exploration, an increase in tourism, and sovereignty assertion. Some of the ships navigating in polar waters are non-polar class ships and even non-ice-strengthened vessels. Even though they operate in ice free water or very light pack ice conditions, there is always a risk of accidental impact against multi-year ice floes, which are capable of causing large plastic deformation to the local structure of such vessels. Current design requirements for ice going vessels do not include any formal evaluation of accidental loads. This is unfortunate because a vessel that transits polar waters should be prepared to sustain unanticipated ice loads without loss of function, even during the summer season. This work's objective is to present a method for assessing the effects of ice loads in ship structures that are expected to operate in Arctic and may be subjected to ice loads beyond their design point, deforming well into the plastic regime. This includes non-ice class ships that are subjected to ice loads and overloaded ice class ships.

In the circumstances discussed, it is expected that the structure will become a significant energy sink for the system. Previous work by Andrade et al. (2022a) presented a coupled-energy ice load model, where IACS type ice load are coupled with structural deformation. The IACS UR I (International Association of Classification Societies Unified Requirements I – Polar Class) design rules for ships that operate in polar waters is based on a limited energy impact scenario, where the ship structure is assumed to have an “icebreaker bow shape”, to be rigid, and the impact kinetic energy is exclusively absorbed by the ice crushing process, but Andrade et al. (2022a) and the current work show that it is

possible to include structural deformation losses in the energy balance equation for the ice load determination procedure. The current work further develops and updates the coupled-energy ice load approach discussed in Andrade et al. (2022a). This work also proposes a new Non-uniform Ice Load Application System (NILAS), which models high- and low-pressure zones in the load patch.

6.4 A summary of the Popov-Daley (PD) method for ice load patch determination.

The underlying methodology behind IACS UR I ice load determination method is based on the method originally proposed by Popov et al. (1967) and later adapted by Daley (1999). Popov et al. (1967) proposed a method to simplify a 3-dimensional ice-ship impact problem, Figure 6-1, to an equivalent 1-dimensional impact in terms of kinetic energy, while Daley (2000, 1999) proposed the use of pressure-area curves to characterize the ice crushing energy. In the current work this methodology is referred to as Popov-Daley method, or PD for short.

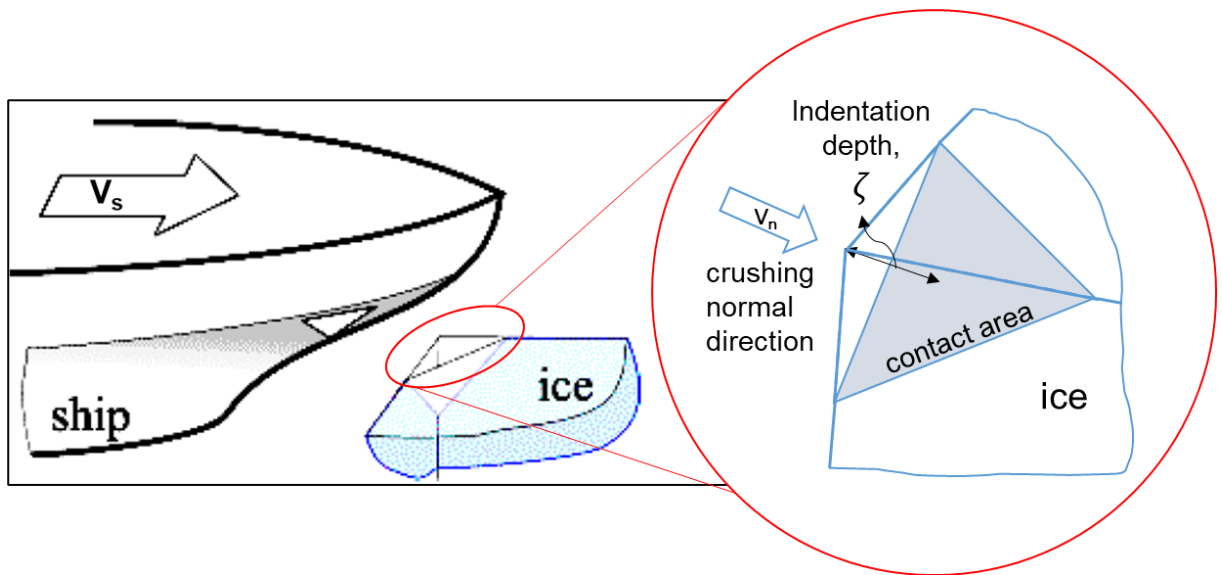


Figure 6-1. Representation of design scenario behind IACS UR I ice load determination method: A ship of speed V_s has a glancing impact against an ice floe causing ice to be crushed. V_n is component of the ship speed normal to the crushing direction. In this work ice is assumed stationary w.r.t the ship and of infinite mass. (Image modified from Daley (1999))

The 1-D system's equivalent kinetic energy is termed KE_e . The PD method results in a normal velocity component, V_n and an equivalent body mass, m_e . The equivalent mass accounts for all interacting masses, rotational inertias, and hydrodynamic additional masses. The equivalent kinetic energy is assumed equal to the ice crushing energy, IE . This assumes that all energy losses come from the ice crushing process, ignoring other recoverable energy losses (e.g., ship structure's elastic deformation) and non-recoverable losses (e.g., ship structure's plastic deformation), as shown in Equation (6.1).

$$KE_e = \frac{m_e V_n^2}{2} = IE \quad (6.1)$$

The equivalent mass is described by Equation (6.2) in terms of the ship displacement, ∇ , and the mass reduction coefficient, C_o .

$$m_e = \frac{\nabla}{C_o} \quad (6.2)$$

Readers are referred to Daley (2000, 1999) for the derivation of the mass reduction coefficient C_o . Note that, as explained in Daley (2000), C_o determination is unnecessarily complex for a codified approach, so a simplification is used in IACS UR I. Despite it having very good comparison for different hull shapes, the final force values will slightly differ between the IACS UR I approach and the direct application of the PD method.

In this glancing ice impact scenario, force is described as pressure applied over a well-defined contact region. The contact area, $A(\zeta)$, is a function of the geometric properties of the bulk ice and ship hull at the studied impact location. Under this assumption, force magnitude, F , is a function of ice penetration, ζ , as illustrated in Equation (6.3).

$$F = PA(\zeta) \quad (6.3)$$

For the determination of the pressure, the PD method uses the concept of a pressure – area curve, whose inclusion is proposed by Daley (2000, 1999). The concept of pressure area-curve, as proposed in Sanderson (1988), relates ice contact pressure to the nominal contact area using a power curve as show in Equation (6.4).

$$P = P_0 A(\zeta)^{ex} \quad (6.4)$$

In Equation (6.4) P_0 is the pressure of the ice at 1m^2 and ex is a constant. Equation (6.4) is combined with Equation (6.1) to define the design load as function of the equivalent kinetic energy. This is shown in Equation (6.5).

$$IE = P_0 \int A(\zeta)^{1+ex} d\zeta \quad (6.5)$$

Equation (6.6) is obtained by combining Equation (6.1) and (6.5).

$$\frac{m_e V_n^2}{2} = P_0 \int A(\zeta)^{1+ex} d\zeta \quad (6.6)$$

As described, the contact area is a function of the ship's structure and the ice feature's geometry at a given penetration depth. The ship structure is assumed flat and uniform at the contact area, with normal frame angle with relation to the water plane, β' . The normal frame angle is a function of the hull waterline angle, α , and the frame angle, β . This can be visualized in Figure 6-2.

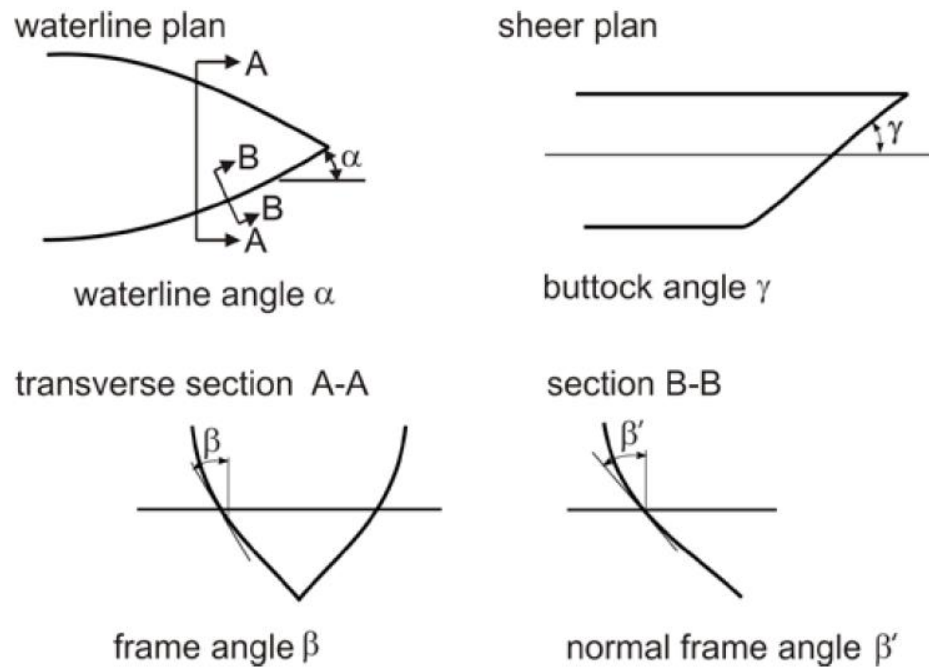


Figure 6-2. Definition of hull angles used in the IACS UR I and PD for ice load determination. (International Association of Classification Societies, 2011)

The ice geometry is that of a wedge with opening angle, ϕ . The normal penetration ζ_n describes the crushing depth of the ice edge in the normal direction of the impact. This is illustrated in Figure 6-3.

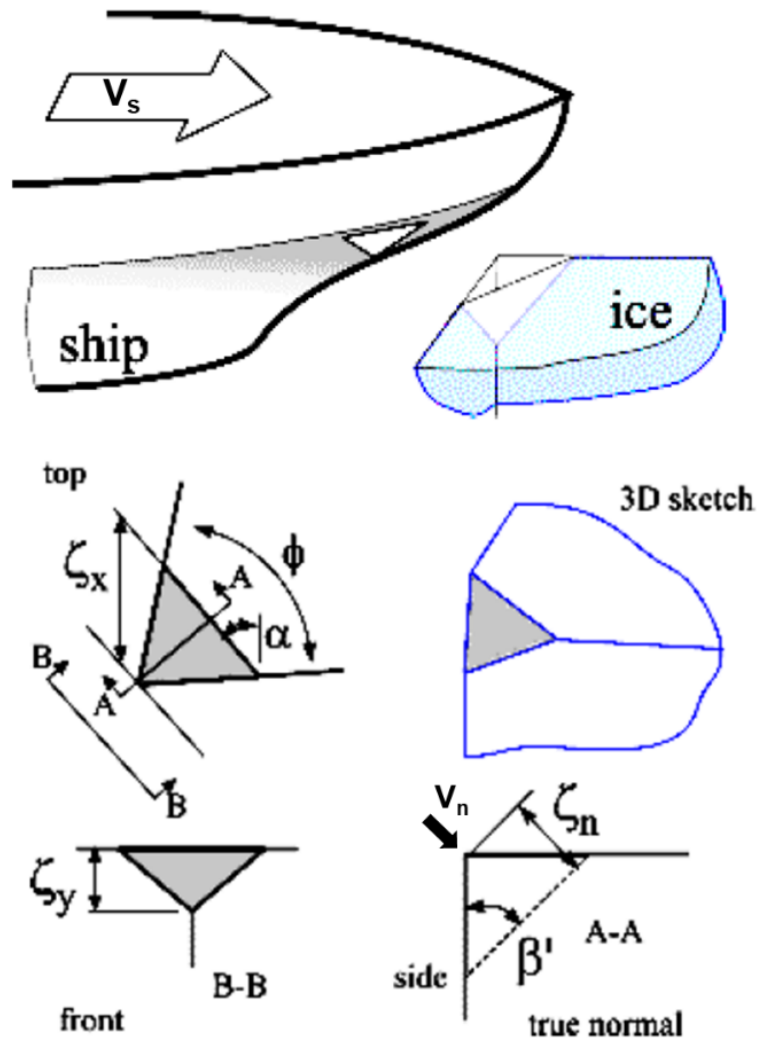


Figure 6-3. General wedge-shaped edge normal to hull. (Daley, 1999)

The derived solution for the contact area, A_n (shown shaded in Figure 6-3), normal force, F_n , and ice crushing energy, IE , are presented in Equations (6.7), (6.8), and (6.9). The normal frame angle calculation is presented in Equation (6.10).

$$A_n = \frac{\zeta_n^2 \cdot \tan(\phi/2)}{\sin(\beta') \cos^2(\beta')} \quad (6.7)$$

$$F_n = P_0 \left(\frac{\tan\left(\frac{\phi}{2}\right)}{\sin(\beta') \cos^2(\beta')} \right)^{1+ex} \cdot \zeta_n^{2+2ex} \quad (6.8)$$

$$IE = \frac{P_0}{(3 + 2ex)} \left(\frac{\tan\left(\frac{\phi}{2}\right)}{\sin(\beta') \cos^2(\beta')} \right)^{1+ex} \cdot \zeta_n^{3+2ex} \quad (6.9)$$

$$\beta' = \text{atan}(\tan(\beta) \cos(\alpha)) \quad (6.10)$$

Normal velocity, V_n , as function of the ship speed, V_s , is determined by Equation (6.11).

$$V_n = V_s \cdot \sin(\alpha) \cos(\beta') \quad (6.11)$$

The IACS UR I load patch is not directly defined by the shape shown in Figure 6-3. The nominal contact area is normalized to a rectangular shape of height, H_{nom} , width, W_{nom} , and aspect ratio, AR (Daley, 2000). This is described by Equations (6.12), (6.13), and (6.14).

$$H_{nom} = \left(\frac{F_n}{P_0 * AR^{1+ex}} \right)^{\frac{1}{2+2ex}} \quad (6.12)$$

$$W_{nom} = H_{nom} * AR \quad (6.13)$$

$$AR = 2 \cdot \tan\left(\frac{\phi}{2}\right) \sin(\beta') \quad (6.14)$$

The load patch dimensions are then reduced to account for observed load concentration as the ice edges spall off. The final design load patch dimensions are determined by Equations

(6.15) and (6.16), where h and w are the design height and width of the design load patch, respectively. Note that the Equation (6.15) only reduces patches with width larger than 1 m. This fact will become relevant in the future sections, and an alternative will be presented.

$$w = W_{nom}^{0.7} \quad (6.15)$$

$$h = w/AR \quad (6.16)$$

The design pressure, p_{design} , can be calculated with Equation (6.17). The force value is independent of the contact area, Equation (6.8), thus the design pressure, p_{design} , is larger than the nominal pressure, P , from Equation (6.4).

$$p_{design} = \frac{F_n}{w \cdot h} \quad (6.17)$$

In summary, the PD method assumes that all available impact kinetic energy is absorbed by ice crushing. The ship structure's deformation energy is not considered in the energy balance. The resulting ice pressure load patch has rectangular shape with height h , width w , and uniform pressure p_{design} .

6.5 A discrete method for the ice load patch creation. Progressive ice load patches

The methodology described in the previous section (PD) generates a single ice load patch determined at the point of maximum ice penetration. Andrade et al. (2022a) present an alternative approach to simulate the ice crushing process progression using load patches in

numerical structural simulations. Their method will be described as Progressive method, or PRO for short. Instead of determining the single load patch determined at the point of maximum ice penetration (and total system energy depletion), the method includes intermediary load patches determined at different ice indentation depths. The PRO method discretizes the ice crushing process into a series of increasingly larger contact area patches. The objective is to simulate the ice crushing process progression in numerical structural simulations with pressure load patches. Figure 6-4 illustrates the difference between the PD and PRO methods for ice load patch generation.

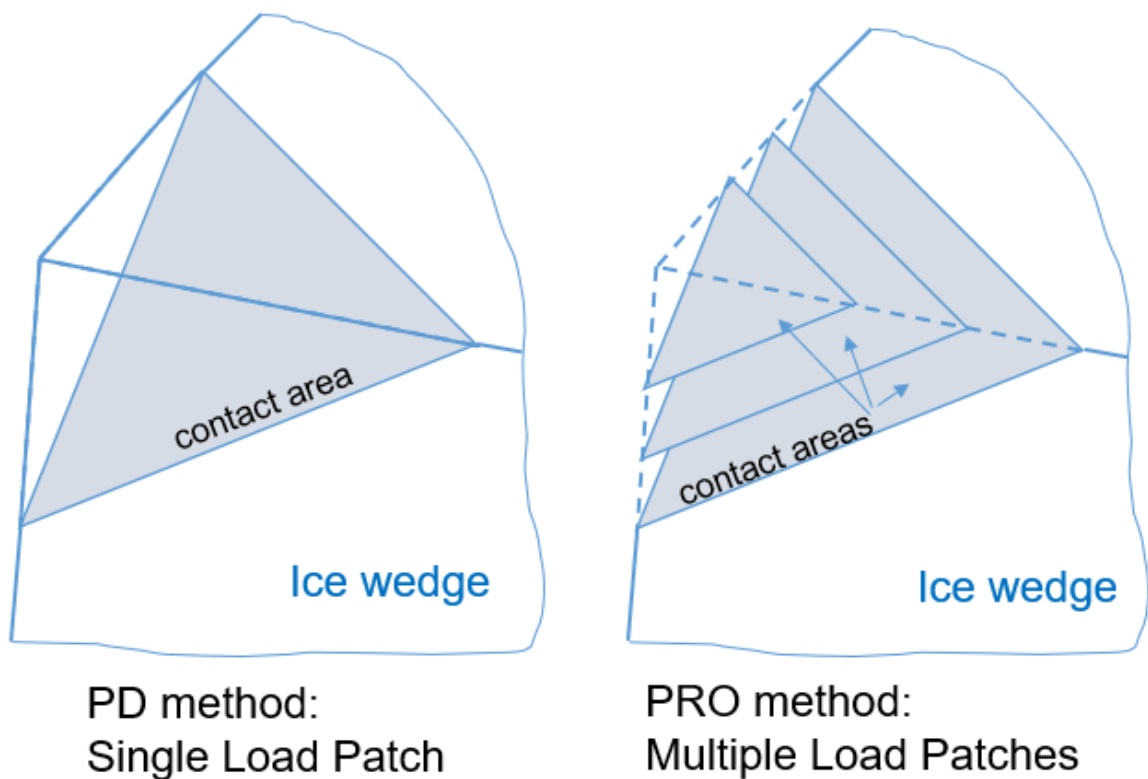


Figure 6-4. Image on the left illustrates the underlying assumption behind the PD method: only the load patch at the point of maximum penetration is considered in the structural design. The right image illustrates the PRO method, which includes the intermediary contact areas before maximum penetration is achieved.

As per Equations (6.7) and (6.8), the load patch parameters are function of the indentation depth. The progressive ice load method discretizes the indentation process into a series of loadsteps. The discretized indentation, ζ_i , is the normal velocity at the current step, v_i , multiplied by a user-defined time interval, t_{step} , see Equation (6.18).

$$\zeta_i = v_i * t_{step} \quad (6.18)$$

Indentation depth is then used to determine the contact patch nominal area, shape, and normal force, Equations (6.7), (6.12 to 6.16) and (6.8) respectively. Finally, the normal velocity, v_i , is updated at the end of each step by subtracting the total energy loss from the initial equivalent kinetic energy, Equation (6.19). Figure 6-5 depicts the progressive load application method load patches for sequential loadsteps in an implicit numerical structural simulation.

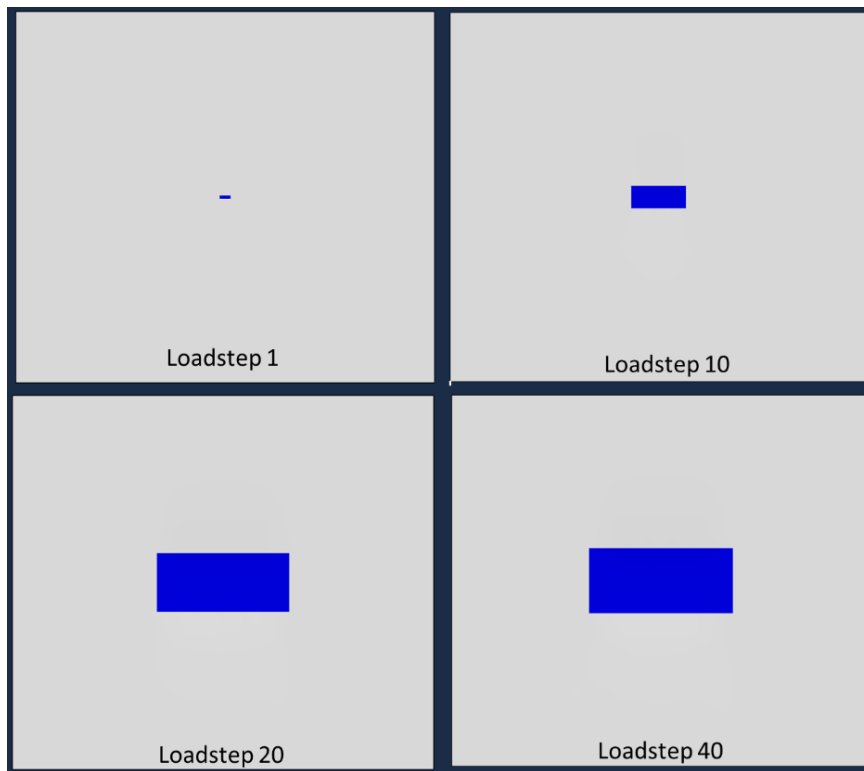


Figure 6-5. Example of load patch sizes at different loadsteps of the same simulation. As expected, load patch size increases during the simulation progression. Loadstep #1 is the first loadstep and loadstep #40 is the last. The simulation is implicit with 40 loadsteps.

If exclusively under IACS UR I, PD, and PRO methods assumptions, the only energy sink for the system is the ice crushing energy, IE_{i-1} , while structural deformation, $E_{S_{i-1}}$, is assumed negligible. Andrade et al (2022a) propose a method to include the structural deformation energy into the PRO method. This approach is used to study structural behaviour of non-ice class ships under ice load, or polar class ships under overload. The method includes the structural deformation energy, E_s , into the energy balance Equation (6.19). The method presented in Andrade et al (2022a) is referred as Progressive approach With Structural Energy, or PROWiSE for short, in the current work.

$$KE_{e_i} = KE_{e_{i-1}} - (E_{s_{i-1}} + IE_{i-1}) \quad (6.19)$$

In the PROWiSE approach, each loadstep is a function of the remaining kinetic energy, which is re-calculated accounting for structural deformation and ice crushing energy losses at the end of each loadstep. This process is illustrated in Figure 6-6.

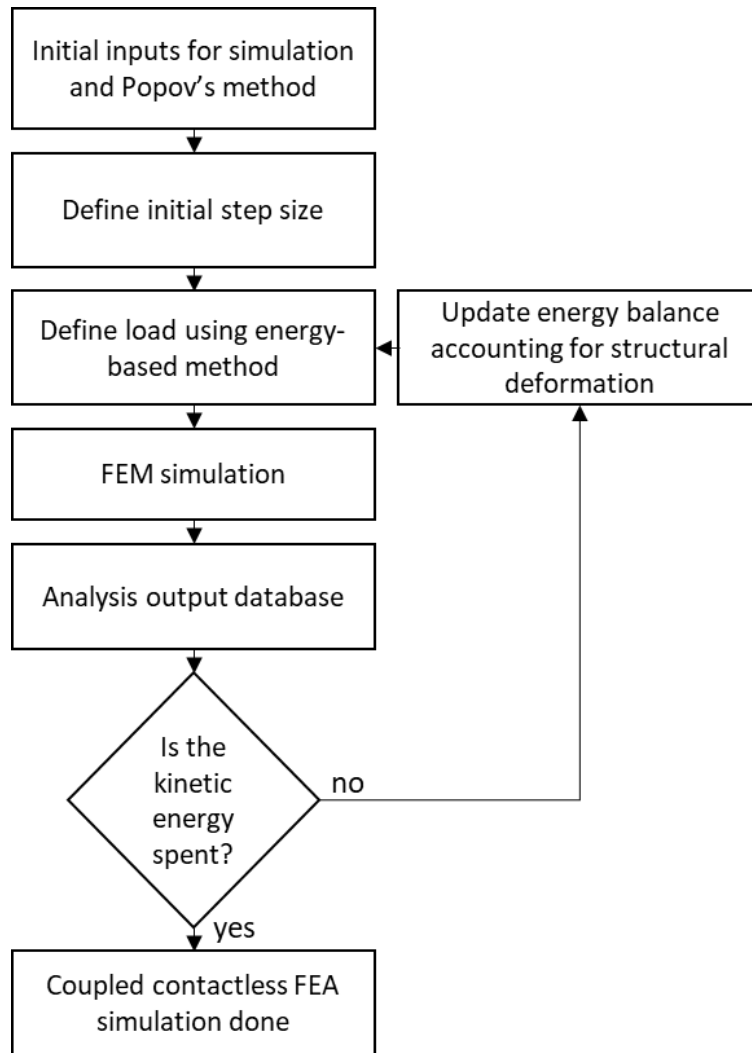


Figure 6-6. Methodology framework for numerical structural simulations with coupled progressive ice loads, or PROWiSE approach (Andrade et al., 2022a)

Both in the present work and in Andrade et.al (2022a) the PROWiSE approach is implemented in Python to be solved in ABAQUS using implicit time integration. Simulations with explicit time integration are also possible, but the simulations are more time consuming. The Python routine runs a series of FEA simulations with incrementally larger number of loadsteps. Each subsequent simulation adds a new loadstep that is determined based on the energy output from the previous simulation. The process is iterated until all initial equivalent kinetic energy, KE_e , is spent. A loadstep interval sensitivity analysis is required if this method. The sensitivity analysis objective is to minimize the energy error (Energy Available minus Energy Spent) at the end of the simulation. This work aimed (and achieved) an error of less than -0.5% at second to last loadstep, and less than +0.5% at the last loadstep for all simulations.

When following the methodology presented in section 6.4, the PROWiSE approach can have initial nominal contact area with width smaller than 1 m. In that case Equation (6.15) would yield a design contact patch that is larger than the nominal patch. This disagrees with the assumption that the actual contact area is smaller than the nominal contact area due to spallation of the edges. Thus, instead of using Equation (6.15) for all loadsteps, a single area reduction factor, ARF , is defined based on the design load patch dimensions for the maximum indentation depth. The resulting ARF is then used to re-dimension all pressure patches for every loadsteps in the discrete simulations, as per Equations (6.20) and (6.21).

$$ARF = \sqrt{\frac{H_{nom} \cdot W_{nom}}{h \cdot w}} \quad (6.20)$$

$$w_{new} = W_{nom} * ARF \quad (6.21)$$

The results from Andrade et al. (2022a) show that the load progression can have significant effects on the structural behaviour in overload cases. The authors observed that the method can capture the effects of propagation of the plastic damage as the load evolves in time. In this work the same approach will be used in many simulations, but the authors will expand the analysis to include a non-coupled progressive load model, where $E_s = 0$. The objective is to separate the effects of progressively applying the load on the structure from the effects of coupling the structural deformation. For this purpose, three load generation methodologies are compared in the current work:

- PD: Single loadstep approach determined as per the procedure described in section 6.4, where the ice load patch is only determined at the point of maximum indentation under the assumption that $E_s = 0$;
- PRO: Non-coupled progressive loadsteps: load patches are determined as per the procedure described in this section while under the assumption that $E_s = 0$;
- PROWiSE: Coupled progressive loadsteps: load patches are determined as per the procedure described in this section while under the assumption of coupled structural deformation energy, i.e., $E_s \neq 0$, for load patch creation purposes. The structural energy E_s is determined from the numerical structural simulation at each loadstep and used to calculate the load patch at the subsequent loadstep.

6.6 Pressure distribution during ice-structure interaction

Another aspect studied in this work is the effect of pressure distribution patterns on the structural response to ice loads. This is important because two different types of ice interact with the structure at the interface region during the ice crushing process: crushed ice and relatively intact ice (Daley, 1994; Gagnon, 1998; Joensuu and Riska, 1989). The first is the crushed ice that is extruded from the contact region. The other type is relatively intact ice in direct contact with the structure. These different ice types impart different contact pressures to the structure. The average pressures in the relatively intact ice region are almost an order of magnitude larger than in the crushed ice region (Gagnon et al. 2020). For this reason, it is common to designate these regions of distinct ice types by their observed relative contact pressure. Intact ice regions are described as high-pressure zones (HPZs), and crushed ice regions as low-pressure zones (LPZs). In Figure 6-7 it is possible to observe how relatively intact ice (dark region in the contact zone) correlates with the corresponding pressure map for that contact area.

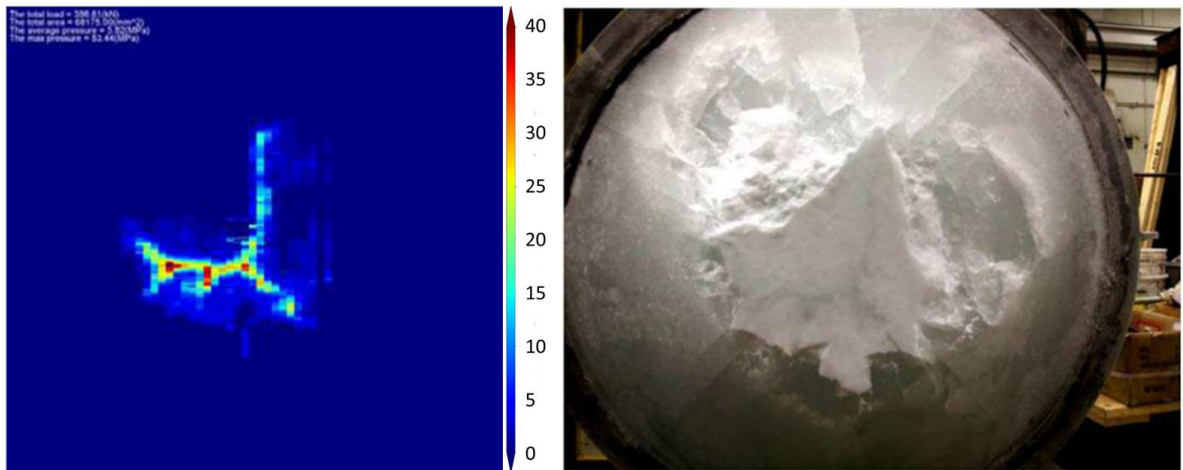


Figure 6-7. Pressure distribution map (left) and the equivalent ice damage (right) (modified from Sopper et. al (2015)). The colored-pressure scale is in MPa on the left image, which shows that HPZs (warmer colors) directly correlate with the observed relatively intact ice observed on the image on the right (the darker grey dendritic features in the contact zone, completely enveloped by milky crushed ice).

The presence of HPZs and LPZs has been documented not only in laboratory experiments (Daley, 1992; Gagnon et al., 2020; Gagnon and Daley, 2005; Riska et al., 1990) but also field experiments (Frederking, 2004; Frederking et al., 1990; Gagnon, 1998; Kamio et al., 2000; St. John et al., 1984). Until Andrade et al. (2022b) proposed a geometry method to describe HPZ distributions, there was no general model to describe their distribution over non-rectangular contact areas. The application of their work in this study is explained in the next section.

6.7 A Non-uniform Ice Load Application System – NILAS

In this section the authors describe an approach to represent non-uniform pressure distribution for the simulation of ice loads in a numerical environment, which will be referenced as Non-uniform Ice Load Application System, NILAS.

6.7.1 How HPZs can be integrated into IACS pressure patches for FEA analyses.

Andrade et al. (2022b) propose a novel geometric method to model HPZ/LPZ contact areas of any shape. Their proposed model uses the topological skeleton and distance field information of the ice contact area's shape to predict the shapes and sizes of the HPZs and LPZs for that contact area patch. The topological skeleton is a discrete representation of the set of medial axes of an object. A medial axis is a geometric descriptor that contains all points of the object that have more than one closest point belonging to its perimeter (Blum, 1973). In Andrade et al. (2022b) a numerical solution is used to determine the topological skeleton of any discrete shape. The contact areas that will be studied in this work, of rectangular and triangular shape, have a closed form solution for their topological skeletons.

For a rectangle with sides ABCD, the bisectors of the corners will form the wings of the skeleton. The intersection points of the bisectors, named I_1 and I_2 , are connected to form the central portion of the skeleton. The topological skeleton is formed by the segments $\overline{AI_{p1}}$, $\overline{BI_{p1}}$, $\overline{CI_{p2}}$, $\overline{DI_{p2}}$, and $\overline{I_{p1}I_{p2}}$. This process is illustrated in Figure 6-8.

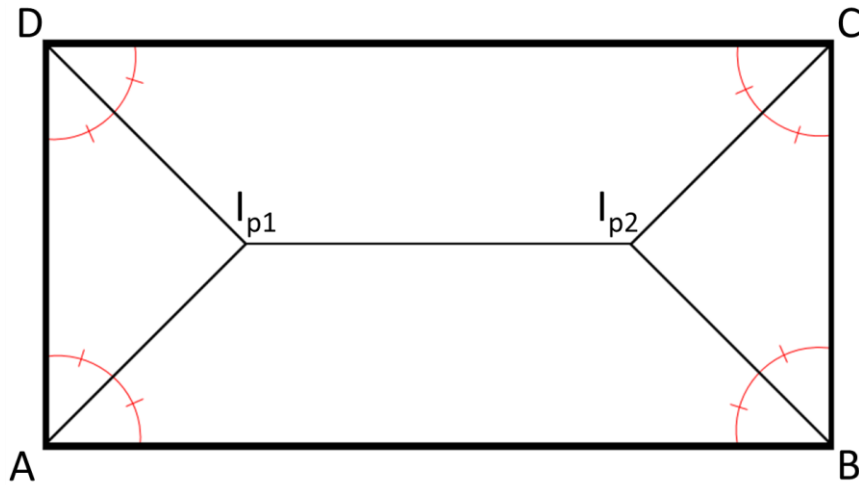


Figure 6-8. Topological skeleton representation for a rectangular shape. The skeleton is formed by the segments $\overline{AI_{p1}}$, $\overline{BI_{p1}}$, $\overline{CI_{p2}}$, $\overline{DI_{p2}}$, and $\overline{I_{p1}I_{p2}}$.

For a triangle of sides ABC, the intersection point of the 3 bisectors is named I . It is used to form the triangle's skeleton by defining the segments \overline{AI} , \overline{BI} , and \overline{CI} . This process is illustrated in Figure 6-8.

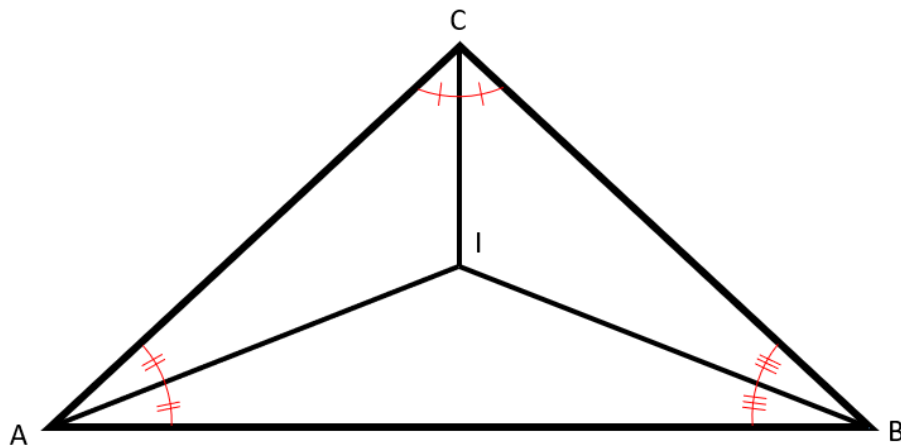


Figure 6-9. Topological skeleton representation for a triangular shape. The skeleton is formed by the segments \overline{AI} , \overline{BI} , and \overline{CI} .

In a 2D object, a topological skeleton can be described as the set of all points that are also the centres of fully enclosed discs that are tangent to at least 2 different points of the object's perimeter. Discs centred at the topological skeleton have their radii, r_i , defined as the shortest distance to the closest edge. This is illustrated in Figure 6-10 for both shapes.

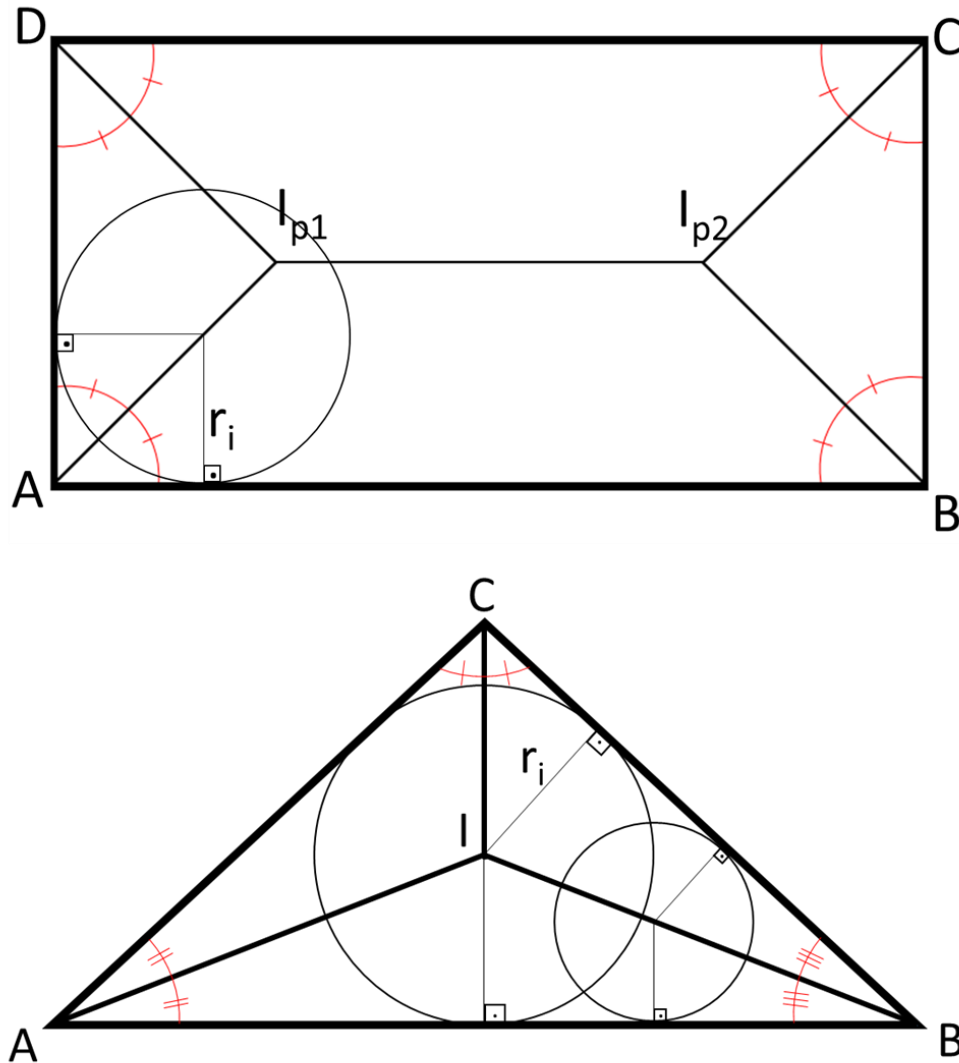


Figure 6-10. Representation of the discs enclosed in a triangle (bottom) and rectangle (top) that are tangent to the closest two sides, and that are centred along the topological skeleton.

A topological skeleton is the discrete representation of a set of segments. Each point of the topological skeleton matrix must be assigned information regarding its distance to the perimeter of the object. This distance is the radius of a disc centred at that point, that if drawn for all points of the skeleton, is capable of recreating the original shape (Blum, 1967; Siddiqi et al., 2002). To represent the HPZs one may uniformly scale down the discs' radii by multiplying them by a ratio f ($0 \leq f \leq 1$). Then the Boolean union of all discs, D_n , will compose the desired HPZ region, as exemplified in Figure 6-11. In the current work this step is done numerically. This will be discussed in the next section.

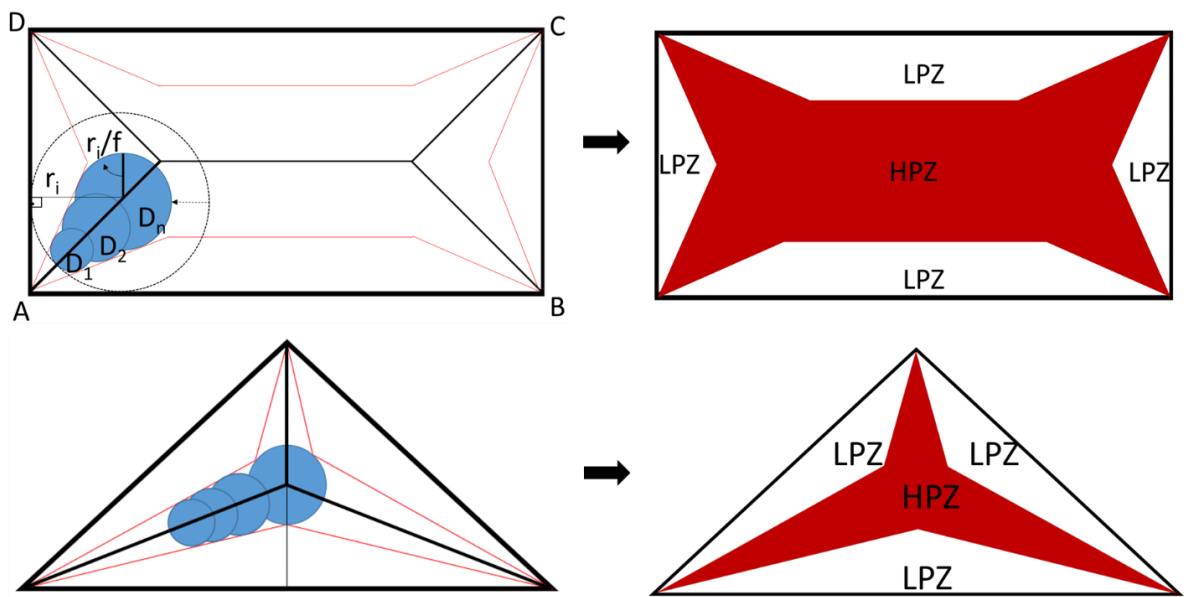


Figure 6-11. Illustration for the process of HPZ zone generation for triangles and rectangles. Discs centred at the topological skeleton have their radii as the shortest distance to the closest edge. These radii are fractionized equally for all discs, and the union of discs will form the HPZ. The HPZ sizes in this image are for illustration purposes only.

6.7.2 Defining LPZ and HPZ size and average pressure for the FEA simulations

The HPZ creation procedure requires discretizing enough discs to approximate the HPZ region. In this procedure, the radii r_i of all the discs D_i are multiplied by the same ratio f , which will vary from 0 to 1. The union of the discs forms the HPZ, $\bigcup_{i=1}^n D_i(\text{radius}_i = r_i * f)$.

When $f = 1$, the HPZ region has the same size and shape of the original contact area. When $f = 0$, there is no HPZ. Figure 6-12 illustrates the effect varying f values in the HPZ size/shape. In Figure 6-12 $f_{\text{bottom triangle}} > f_{\text{top triangle}}$, and thus the bottom contact area has a larger HPZ region than the top one. This illustrates how the variation of the ratio f defines the size of the HPZ region.

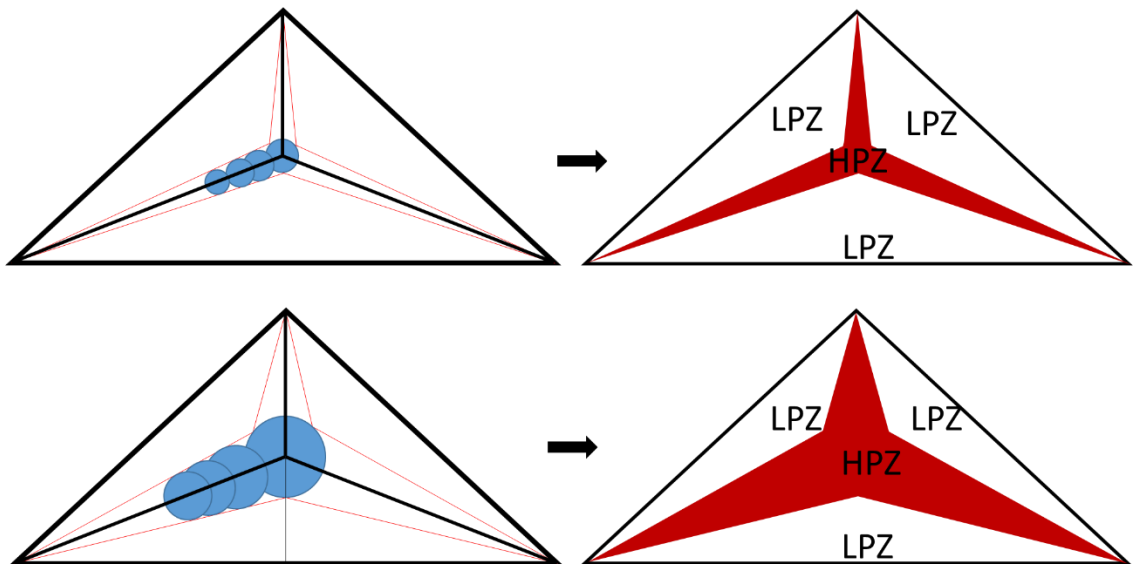


Figure 6-12. The same triangular contact area can be represented with different HPZ regions. In this example the ratio, f , is different for the top and bottom figures, with $f_{\text{bottom}} > f_{\text{top}}$. This causes the bottom contact area to have a larger HPZ region than the top contact area.

In the context of an FEA mesh, each disc selects elements of the mesh that are fully contained within its area. Changing the disc radius will change how many elements are considered as part of the HPZ. In this work, the ratio f is increased iteratively until the number of selected elements that form the HPZ area reaches a desired value.

From the results shown in Gagnon et al. (2020) it can also be determined that HPZs occupy, on average, approximately 13% of the total contact area. Those experiments were performed with polycrystalline freshwater ice. Frederking (2004) reports that HPZs occupy approximately 10% of the contact area in their observations, but for relatively thin first year ice formed in a saltwater lagoon. In this sense, the HPZ and LPZ relative distribution seems to be somewhat ice type independent. Likewise, HPZs and LPZs will both bear a significant portion of the contact load each. Gagnon et al. (2020) report that in the great majority of the experiments performed the HPZs were responsible for approximately half of the measured total load. Since ice compressive strength shows large variation in measured values, even in laboratory settings (Timco and Weeks, 2010), the authors assumed more reasonable to characterize HPZ and LPZ pressures as function of the total load, as defined by the PD method, rather than a fixed pressure value determined experimentally.

The authors recommend further research in this area and for different ice types, but, for the purpose of this work, NILAS will produce HPZ regions of approximately 13% of the contact area. Additionally, HPZ and LPZ regions will each be responsible for half of the total load F_n , which is defined by Equation (6.8). The parameters of each zone within a non-uniform load patch are described by Equations (6.22) to (6.26).

$$A_{hpz} = 13\% * A_{total} \quad (6.22)$$

$$A_{lpz} = A_{total} - A_{hpz} \quad (6.23)$$

$$F_{hpz} = F_{lpz} = F_n/2 \quad (6.24)$$

$$P_{hpz} = F_{hpz}/A_{hpz} \quad (6.25)$$

$$P_{lpz} = F_{lpz}/A_{lpz} \quad (6.26)$$

Where A_{hpz} is the HPZ area, A_{lpz} is the LPZ area, A_{total} is the load patch total area. F_{hpz} and F_{lpz} are the force applied by HPZ and LPZ regions of the contact area, respectively. Finally, P_{hpz} and P_{lpz} are the average pressures in the HPZ and LPZ regions of the contact area respectively. An example of the triangular non-uniform contact area with HPZ and LPZ regions is presented in Figure 6-13. The load patch shown is defined on the mesh of the studied structure.

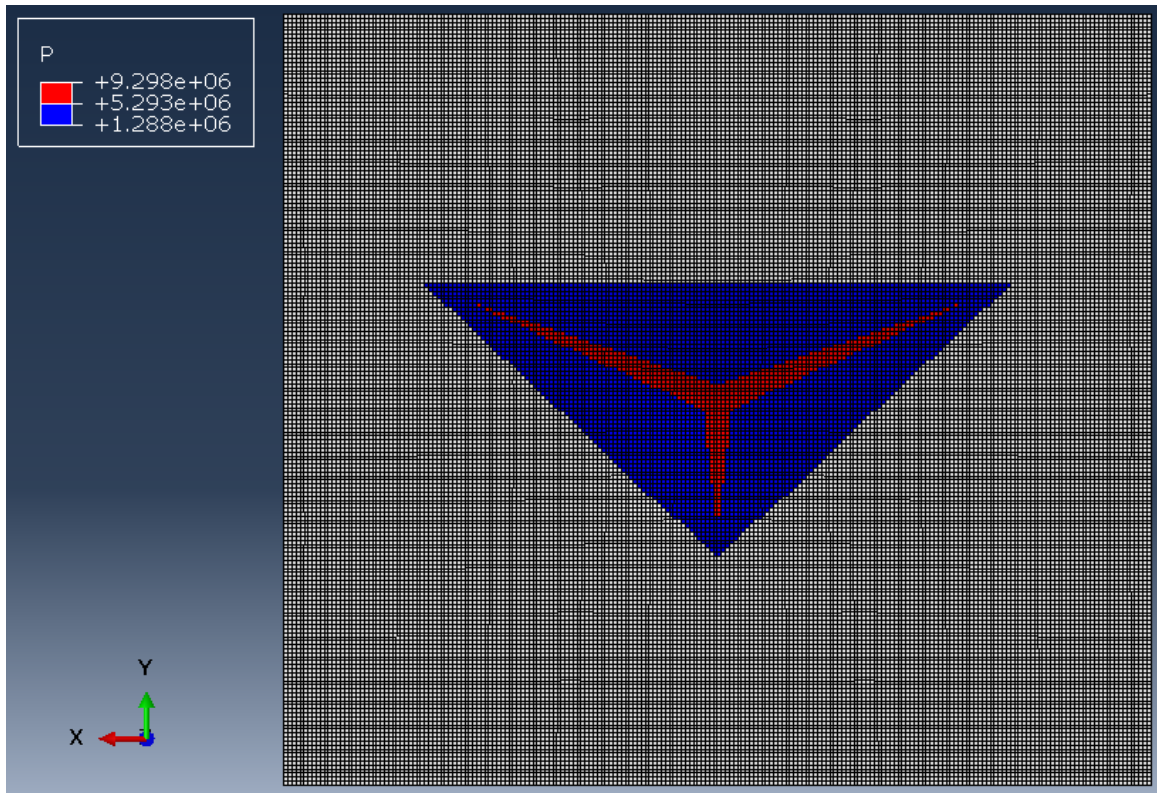


Figure 6-13. Example of a non-uniform load that is used in a number of the numerical structural simulations performed in this work. Red regions are HPZ, blue regions LPZ, and the pressure scale bar is in Pa.

Approaches for HPZ generation in both rectangular and triangular contact areas are presented in this section. The rectangular contact area patch is an adaptation allowing for the codification of the load patch (analytical solution for plate collapse under a triangular load would not necessarily be easily codifiable). Because of this, the authors will only apply the NILAS method to simulation cases with triangular contact areas, so a variation of the PROWiSE method, but combined with NILAS method for pressure distribution. This combination is simply referenced as NILAS method. Additionally, the IACS UR I patch has the nominal contact area reduced by the ARF (area reduction factor), which is an empirical solution for the observed fact that spalling in ice-structure interaction leads to the

formation of HPZs and LPZs. The ARF concentrates the load while maintaining a uniform pressure patch. In the approach presented here (NILAS), the load patches include both high- and low- pressure zones, so there is no need for an Area Reduction Factor.

6.8 The numerical simulation setup

This work studies the effects of different ice load application models in numerical structural simulations. The main parameters varied are the average pressure (i.e., average pressure load magnitude), number of loadsteps, inclusion or not of the structural energy loss in the ice load calculation, load patch shape/size, and pressure distribution over the contact area. The structure chosen for these analyses is a PC7 type structure.

6.8.1 Structural design of the panel

The PC7 structure is designed according to IACS UR I. The principal particulars for a PSV (Platform Supply Vessel) type vessel used to design the test structure are summarized in Table 6-1. The impact is considered to occur at the bow shoulder region. The IACS design load parameters are summarized in the following Table 6-2.

Table 6-1. PC7 PSV type ship parameters.

Ship Particulars	
Length between perpendiculars	88.4 m
Breadth	18.8 m
Draft	6.5 m
Displacement	6100 tonnes
Block coef.	0.55

Waterplane coef.	0.9
Midship coef.	0.9
Geometric properties at impact location (bow)	
Coordinates w.r.t. the centre of gravity	33.7 m; 6.0 m; 0 m
Waterline angle (α)	22 degrees
Frame angle (β)	18 degrees
Ice wedge angle (ϕ)	150 degrees

Table 6-2. IACS PC7 (bow) design load patch for the studied case.

Force	3.019 MN
Line load	1.647 MN/m
Pressure	2.031 MPa
Load patch width	1.832 m
Load patch height	0.811 m

The main frames, webframes, plate, and stringers are designed according to IACS UR I guidelines. The panel's final dimensions are 5.4 m in length and 4.8 m in height. Note that the design was simplified to a flat structure. Large stringers and webframes are designed such as to remain within the elastic regime when directly loaded by the load patch described in Table 6-2. The members' scantlings are listed in Table 6-3 and the resulting grillage structure (i.e., panel) is shown in Figure 6-14.

Table 6-3. Scantlings of the designed PC7 bow panel.

Main frame (transversal)	
type	Built flatbar
net dimensions (mm)	200x14
spacing (mm)	300
span (mm)	1600
Web frame	
type	Built T
net dimensions	700x300x18
spacing (mm)	1800
span (mm)	4800
Stringer	
type	Built T
net dimensions (mm)	500x200x15
spacing (mm)	1600
span (mm)	1800
Plating	
net thickness (mm)	15

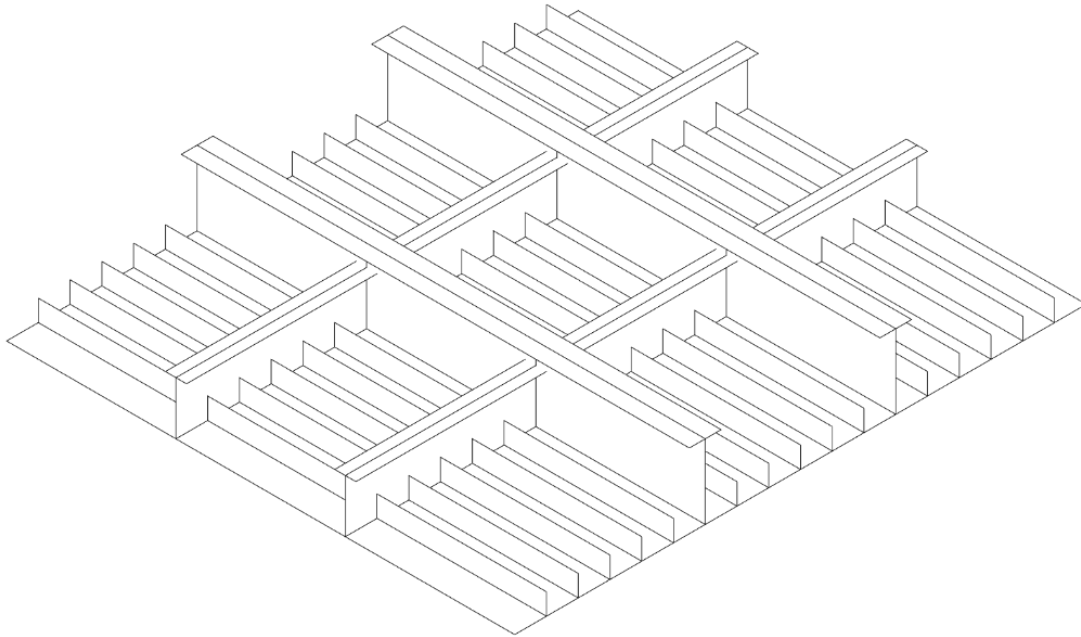


Figure 6-14. Illustrative drawing of the designed PC7 panel structure.

The structure described is modelled and meshed for use in finite elements analyses.

6.8.2 Boundary conditions

The grillage is considered clamped around the perimeter under the assumption that it is bound by the main deck, double bottom and other webframes, as illustrated in Figure 6-15.

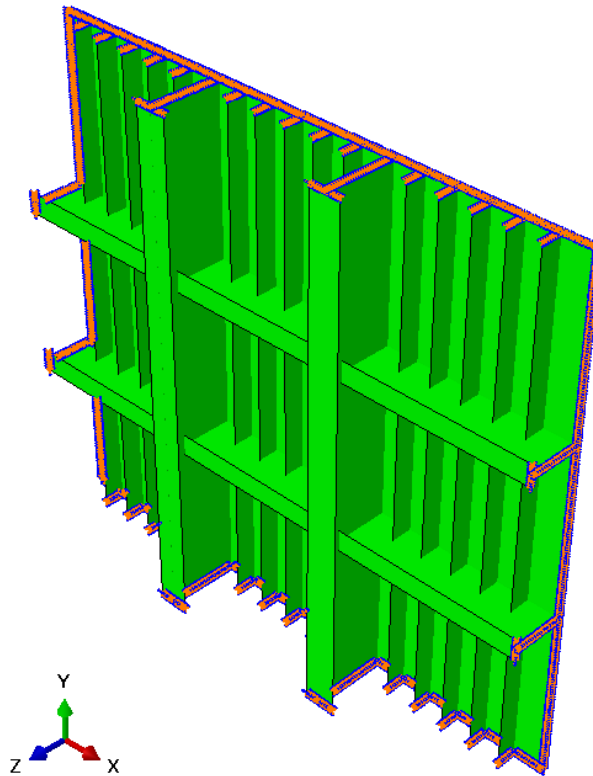


Figure 6-15. Meshed panel showing clamped BC around its perimeter.

The structure has 2-way symmetry, and the geometric centre of the pressure load patch coincides with the geometric centre of the panel in all load cases, this allows the use of symmetry boundary conditions in the coupled-energy simulations, which are more computationally intensive. For triangular load patches a symmetry boundary condition can be used in the YZ plane, Figure 6-16. For rectangular load patches a doubly symmetric boundary condition can be used (in the XZ and YZ planes), Figure 6-17.

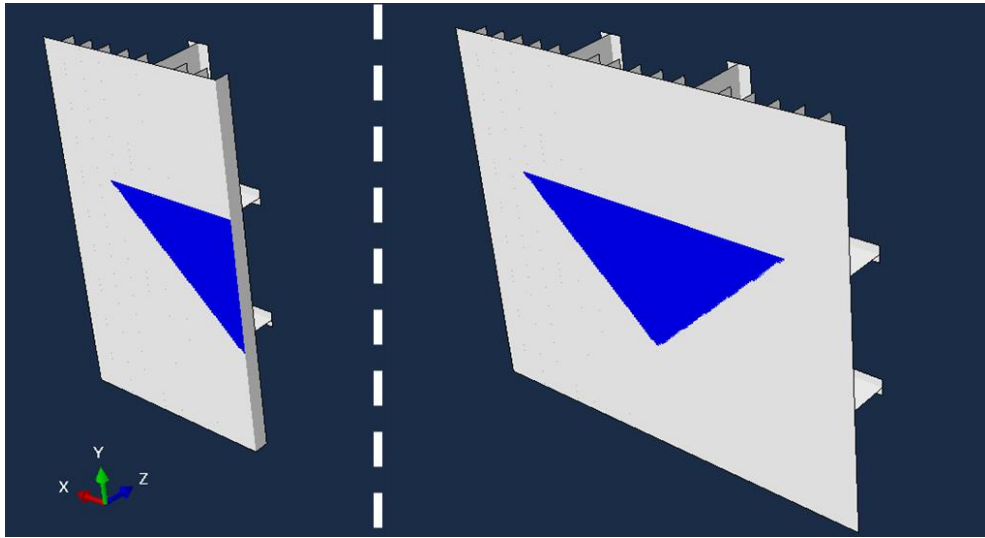


Figure 6-16. Full structural model (right) and halved structural model (left). Symmetric boundary condition (along YZ plane at the geometric centre of the plate) can be used for triangular load patches (exemplified in blue) to approximately half the number of elements in the model.

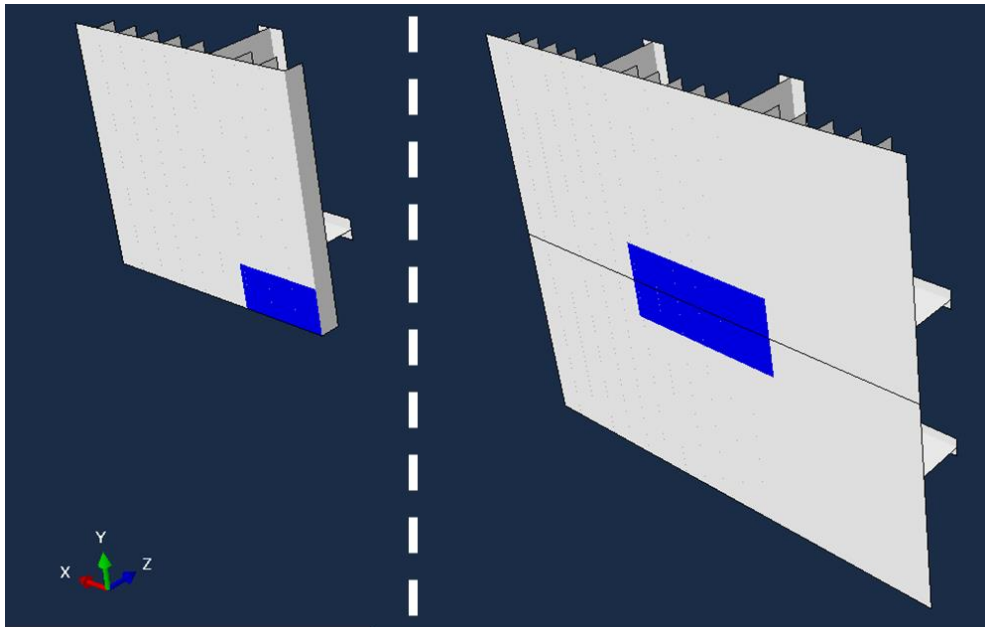


Figure 6-17. Full structural model (right) and quartered structural model (left). Doubly symmetric boundary condition (along XZ & YZ planes at the geometric centre of the plate) can be used for rectangular load patches (exemplified in blue) to approximately quarter the number of elements in the model.

As it is observed in Figure 6-16 and Figure 6-17, the YZ symmetry plane coincides with a main frame element. That frame in particular has its thickness halved (from 14mm to 7mm) to account for the reflected structure added by the symmetry boundary condition. Note that because symmetry is used, the frame may not buckle, however this was not considered an issue for this study, since structural instability was not observed on the central main frame in the cases that use the full structural model.

6.8.3 Meshing

The mesh is composed of S4R (4-node reduced-integration) shell elements with an average edge length of 25 mm. Special attention is observed for the mesh uniformity of the plate region, because that is where the load patch is applied. The structure is imported to ABAQUS as an orphan mesh, so it cannot be re-meshed between loadsteps. Figure 6-18 illustrates the meshed structure, with a close-up to show mesh density relative to the structure size and its members.

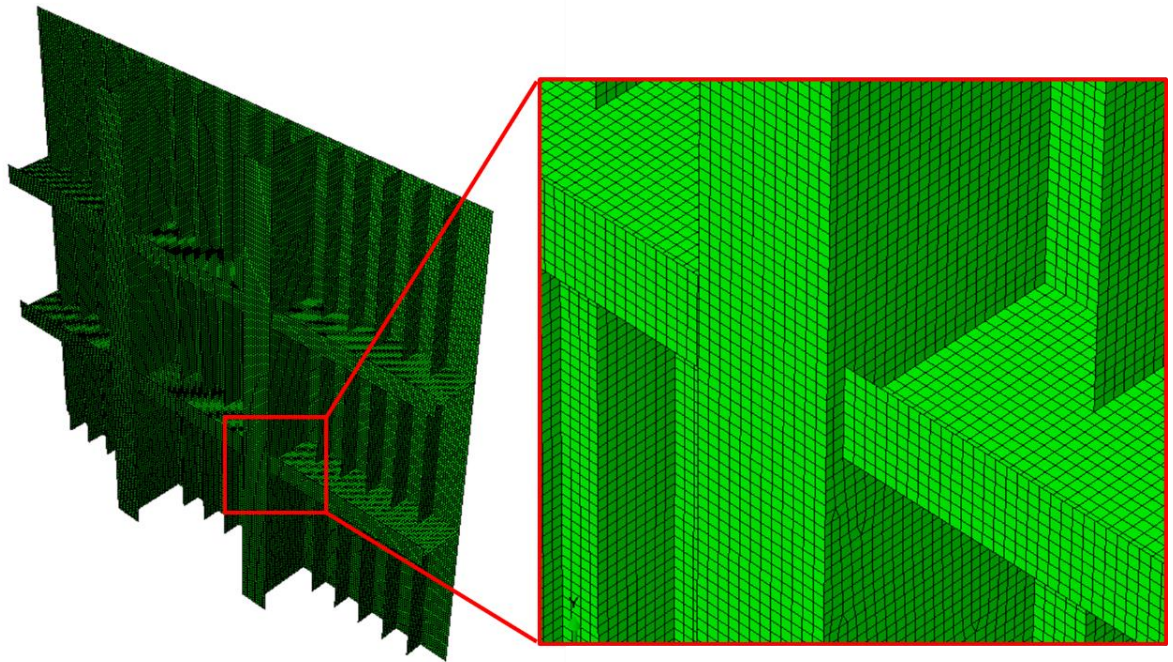


Figure 6-18. Meshed model with a close-up to show element density.

The ideal element size for this study was determined to be 25 mm. The element size is a common multiple of the stringers, frame and webframe spacing, i.e., 1.6 m, 0.3 m, and 1.8m respectively. This guarantees that the mesh is consistently uniform over the load patch region (the centre of the plate) with perfectly square elements. Additionally, the results from the mesh convergence analysis, Figure 6-19, show that this element size is small enough to accurately capture the deformations expected for the worst load case studied (PC4 type load patch with HPZ regions).

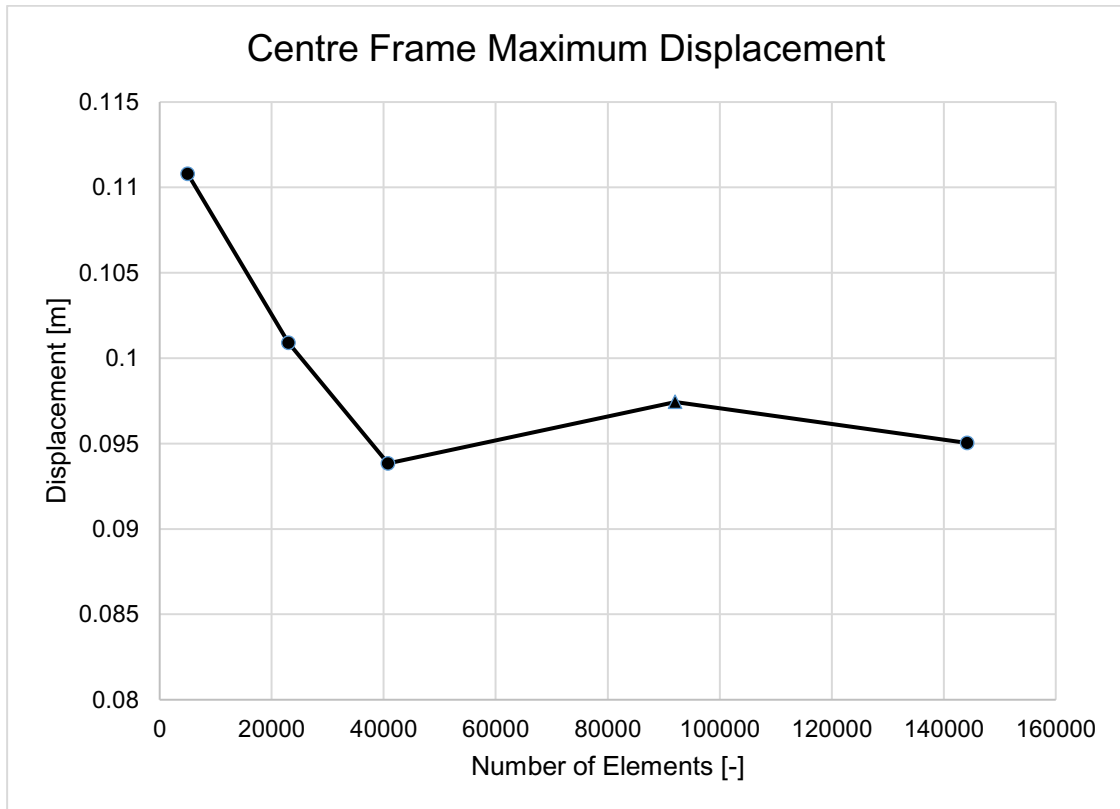


Figure 6-19. Measured displacement for 5 meshes with decreasing element size (from left to right: 100 mm, 50 mm, 37 mm, 25 mm, and 20 mm). The point shown as a red triangle shows the mesh size for the chosen element (25 mm) for this study. The load applied is also the largest load in this study, both in force magnitude (7.61 MN) and pressure concentration (HPZs are present).

6.8.4 Material model

The model's mechanical behaviour is defined with multilinear material model for AH36 steel. The AH36 true stress-strain data provided by ABS's nonlinear FEA guidance (American Bureau of Shipping, 2021) is shown in Figure 6-20.

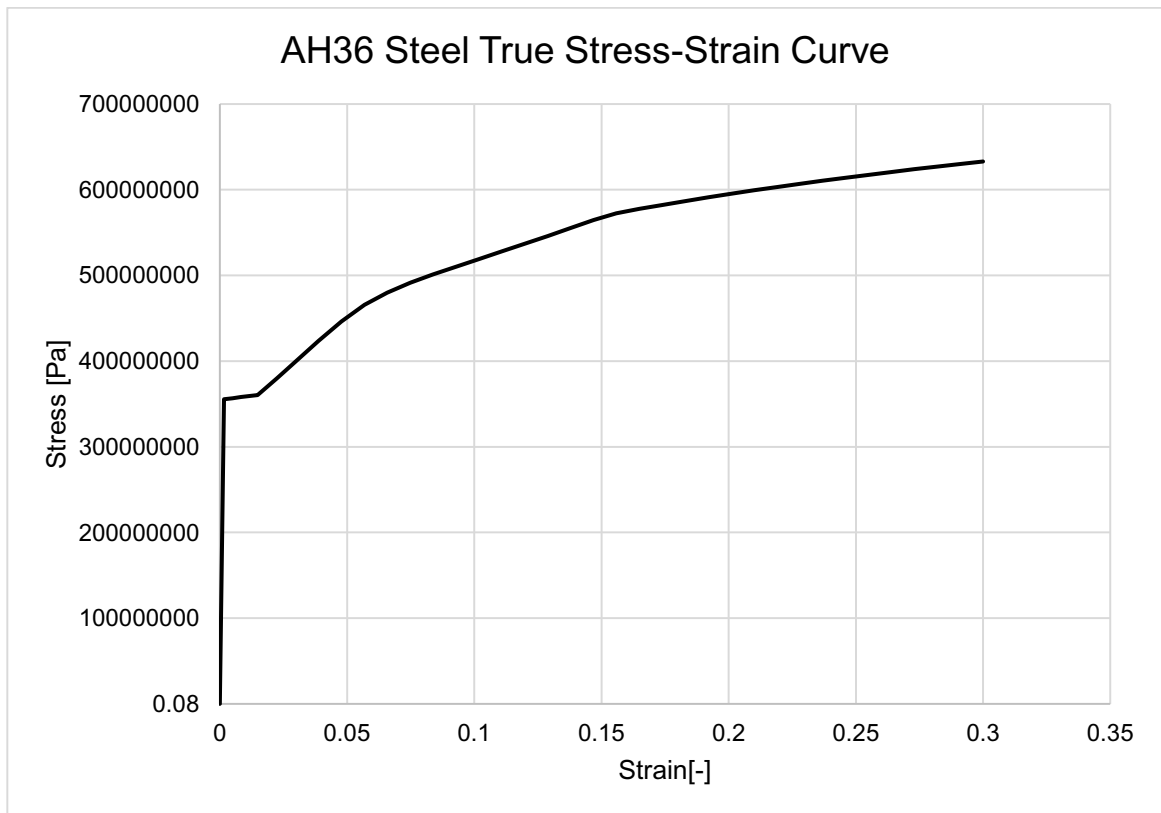


Figure 6-20. AH36 Steel true stress-strain curve (American Bureau of Shipping, 2021).

6.9 Variable parameters of the studied cases

As discussed previously, the structural model is based on a PSV type vessel that was designed under the IACS UR I PC7 requirements. The current work's focus is to study the effects of different ice load parameters as: load magnitude (P_o and V_s variation), loadstep methodologies (single loadstep & multi-loadsteps), inclusion or not of the structural energy loss in the ice load calculation (coupled & not-coupled), load patch geometry (rectangular & triangular), and pressure distribution patterns (uniform & non-uniform). These cases are described as follows in Table 6-4:

Table 6-4. Table describing the different ice load patch parameters that are studied in this work.

Variable Changed	Explanation	Variations studied
Load Magnitude	IACS methodology varies P_0 and V_s to adjust the load magnitude for the class structural requirements. In this work the PC7 Load is the baseline/design case, and the others are overload cases, as the structure is designed to comply with PC7 ice loads.	<ul style="list-style-type: none"> • PC7 Load: $P_0 = 1.3MPa$ and $V_s = 1.5 m/s$ • PC6 Load: $P_0 = 1.5MPa$ and $V_s = 1.75 m/s$ • PC5 Load: $P_0 = 2.0$ and $V_s = 2.0 m/s$ • PC4 Load: $P_0 = 2.45MPa$ and $V_s = 2.5 m/s$
Loadstep Methodology	PD method assumes the application of a single load patch when designing the structure. In FEA simulations it is possible to apply the PRO method, which creates a series of ice load patches that aim to represent the ice crushing process progression in terms of increasing contact area size.	<ul style="list-style-type: none"> • Single Load Patch approach (PD) • Progressive Load Patches approach (PRO)
Load Coupling	Simulations that use the PRO method update the normal velocity V_n by balancing the energy Equation (6.19) between loadsteps. For these cases, the structural energy losses can be used to couple the load patch to the structural deformation. This is done using the PROWiSE method	<ul style="list-style-type: none"> • Coupled Load, $E_{si} \neq 0$ (PROWiSE) • Non-coupled Load, $E_{si} = 0$
Load Patch Geometry	The IACS rules perform a geometric change from the nominal triangular area (wedge cross-section) to a rectangular shape. In FEA this step is not strictly necessary.	<ul style="list-style-type: none"> • Triangular Load Patch • Rectangular Load Patch
Area Reduction Factor	In the IACS method this factor increases average pressure with the objective of accounting for load concentration due to HPZ. This factor is not required, if HPZs are directly included in the load patch pressure distribution.	<ul style="list-style-type: none"> • ARF is applied • ARF is not applied (NILAS)
Pressure Distribution	The effect of the presence of HPZs and LPZs in load patches is compared to uniform pressure distribution.	<ul style="list-style-type: none"> • Uniform Pressure Distribution • Non-uniform Pressure Distribution (NILAS)

Not all possible combinations are necessarily of interest at this stage of the work, thus not all possible required combinations are studied. The following simulations methods with their parameter variations are presented and discussed in this work, Table 6-5.

Table 6-5. Simulations methods used and parameter variations studied.

Simulation Method	Parameter Variations Studied
PD	<ul style="list-style-type: none"> • PC7 to PC4 • Single Loadstep/Contact Area • Non-coupled • Rectangular Patch • ARF used • Uniform pressure distribution
PRO	<ul style="list-style-type: none"> • PC7 to PC4 • Progressive load patches approach • Non-coupled • Rectangular Patch • ARF used • Uniform pressure distribution
PROWiSE	<ul style="list-style-type: none"> • PC7 to PC4 • Progressive load patches approach • Coupled • Rectangular Patch • ARF used • Uniform pressure distribution
NILAS	<ul style="list-style-type: none"> • PC7 to PC4 • Progressive load patches approach • Coupled • Triangular Patch • ARF not used • Non-uniform pressure distribution

6.10 Results and discussion for the simulations

Previous work (Andrade et al., 2022a) presented a progressive coupled ice load model, where ice load determination is coupled with structural deformation. Their motivation is that the maximum force applied to the structure should be smaller if the structural deformation becomes a significant energy sink for the system. On the other hand, that study observed that the reduction in force does not necessarily correlate to a reduction in total

plastic damage on the structure. In fact, some simulations showed an increase in plastic damage. The main reason is that plastic damage is path dependent, thus, to properly understand the differences between coupled and non-coupled approaches requires the analysis of non-coupled progressive simulations. As a final note, the final results from the simulations in the current work, although similar in trend, are not strictly the same to the ones presented in Andrade et al. (2022a), mostly because the mesh size and material models are fundamentally different. In Andrade et al. (2022a) the material model is bilinear, in the current work it is multilinear. In Andrade et al. (2022a) the mesh size is 50mm, in this work it is 25 mm. The mesh size difference affects the patch size accuracy, since HPZs can be very small.

On a final note, all simulations presented here are done with implicit time integration. Although the methods can be solved using explicit time integration, it would be more computationally intensive for the cases presented here, thus, in interest of time, the implicit integration method was preferred.

6.10.1 Cases solved with PD method

This section presents the results for direct application of the PD method. Table 6-6 shows the equivalent kinetic energy for the scenario described for each load case.

Table 6-6. Equivalent kinetic energy for the scenario described for each load case.

	Units	All Load Cases			
		PC7	PC6	PC5	PC4
Equivalent Kinetic Energy (KE_e)	kJ	488.8	665.4	869.0	1357.9

The equivalent kinetic energy is used to determine the load patch force and dimensions, shown in Table 6-7. The load patches applied to the FEA structural model are discrete approximations of the calculated load patch (as per the method described in section 6.4). To maintain force consistency, the load patch pressure values are marginally different. The difference in dimensions between calculated and applied load patch is exemplified in Figure 6-21.

Table 6-7. Load patch parameters for simulations with single loadstep, non-coupled structural energy, rectangular patch, and uniform pressure distribution.

		Units	Simulation method: PD			
			PC7	PC6	PC5	PC4
Calculated Patch ¹	Load	MN	3.1	4.0	5.3	7.6
	Width	m	1.844	1.922	1.912	2.032
	Height	m	0.857	0.893	0.888	0.944
	Pressure	MPa	1.99	2.35	3.13	3.97
FEA Patch ²	Width	m	1.85	1.9	1.9	2.05
	Height	m	0.85	0.9	0.85	0.95
	Pressure	MPa	2	2.36	3.29	3.91

1. The calculated patch dimensions for the non-coupled single loadstep cases at the point of maximum ice penetration.
2. The FEA applied load patch dimensions adjusted to fit the mesh dimensions. The applied patch is a discrete approximation of the calculated load patch. The force is the same in both cases, but pressure is corrected to account for the discrete nature of the contact area.

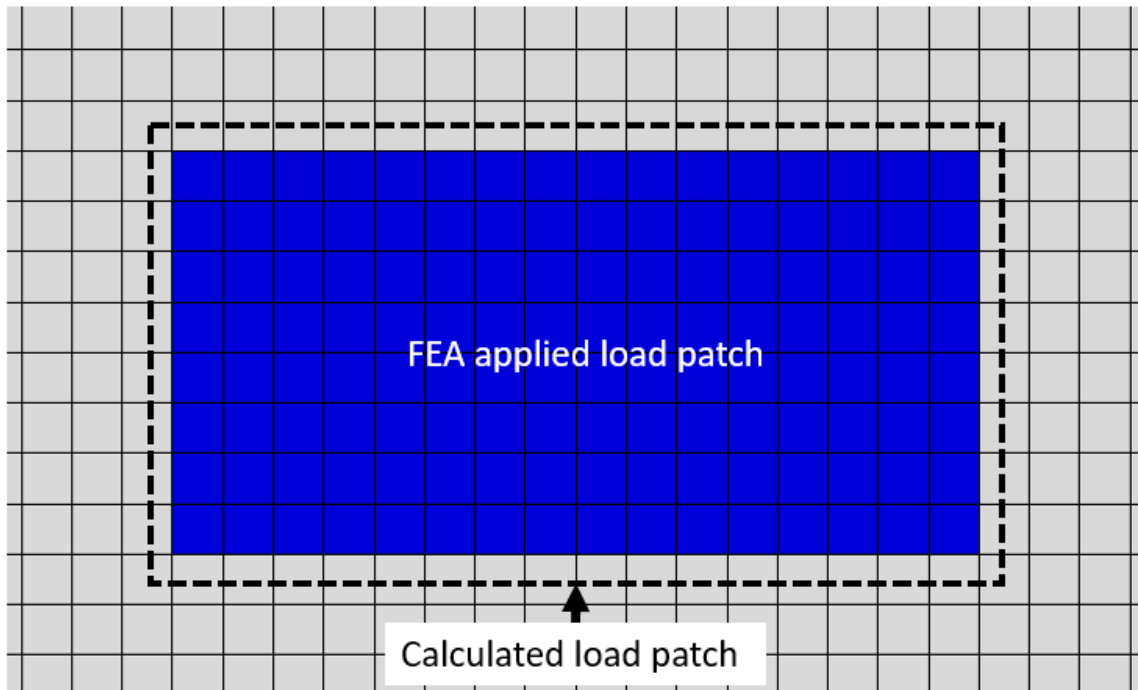


Figure 6-21. Illustration of the conceptual difference between calculated load patch (represented by the dashed rectangle) and applied load patch in FEA meshes (blue region).

The simulation results in Table 6-8 are for the cases with single loadstep and uniform pressure distribution. Total deformation energy increases roughly 2 times from a PC7 load to a PC6 load, 4 times from PC6 to PC5, and 2 times from PC5 to PC4. The plastic deformation differences are even more pronounced, it increases roughly 3 times from PC7 to PC6, 10 times from PC6 to PC5, and 2 times from PC5 to PC4. These results show an interesting aspect of polar ice classes, which is that low ice classes (PC6 and PC7), may be able to survive up to a PC4 type loads without collapsing, but are not prepared to operate normally in the same conditions of heavy ice, as the damage to the local structure can be extensive.

Table 6-8. Deformation energy parameters and maximum plastic strain for the cases: single loadstep, non-coupled, rectangular patch, and uniform pressure.

Indicators	Units	Simulation method: PD			
		PC7	PC6	PC5	PC4
Total Structural Deformation Energy	kJ	12.8	23.7	88.2	184.5
Elastic Deformation Energy	kJ	11.2	18.3	36.4	63.9
Plastic Deformation Energy	kJ	1.6	5.3	51.8	120.6
Peak Plastic Strain	%	0.43%	1.09%	5.06%	9.42%

For the PC7 load case, the maximum observed plastic strain is 0.4%. Additionally, the total deformation energy is 12.8kJ, which is 2.6% of the initial available kinetic energy, while the plastic energy is 0.3% of the kinetic energy. These three facts combined indicate that the design load for a PC7 ship structure (at the bow shoulder region) causes negligible permanent deformation. Even in the PC4 overload case the maximum plastic strain does not come close to exceeding the ultimate strain of the material (30%), even though deformations are large.

Table 6-9 shows the displacement and plastic deformation done to the main frames of the model. The location where the main frame indentation information is collected is depicted in Figure 6-22. This is where the centre of the load patch coincides with the centre of the panel. In this location the largest out-of-plane displacement is observed for a stiffened region of the structure (at transversal framing location).

Table 6-9. Damage done to the framing elements of the structure (not included webframes). Cases: single loadstep, non-coupled, rectangular patch, and uniform pressure

Indicators	Units	Simulation method: PD			
		PC7	PC6	PC5	PC4
Main Frames Plastic Damage	kJ	1.6	5.3	48.2	97.3
Main Frames Damage / Total Damage Ratio ¹	%	99.80%	98.90%	93.00%	80.70%
Central Main Frame Plastic Damage	kJ	0.4	1.4	12.8	23.8
Centre Node displacement	m	0.01	0.015	0.041	0.065
Displacement / Frame span	%	0.60%	1.00%	2.60%	4.10%

1. Note that, it was observed that the rest of the plastic damage is absorbed exclusively by the plate. The plastic damage done the heavy members (webframes and stringers) is negligible in all cases in this and the other sections of this work.

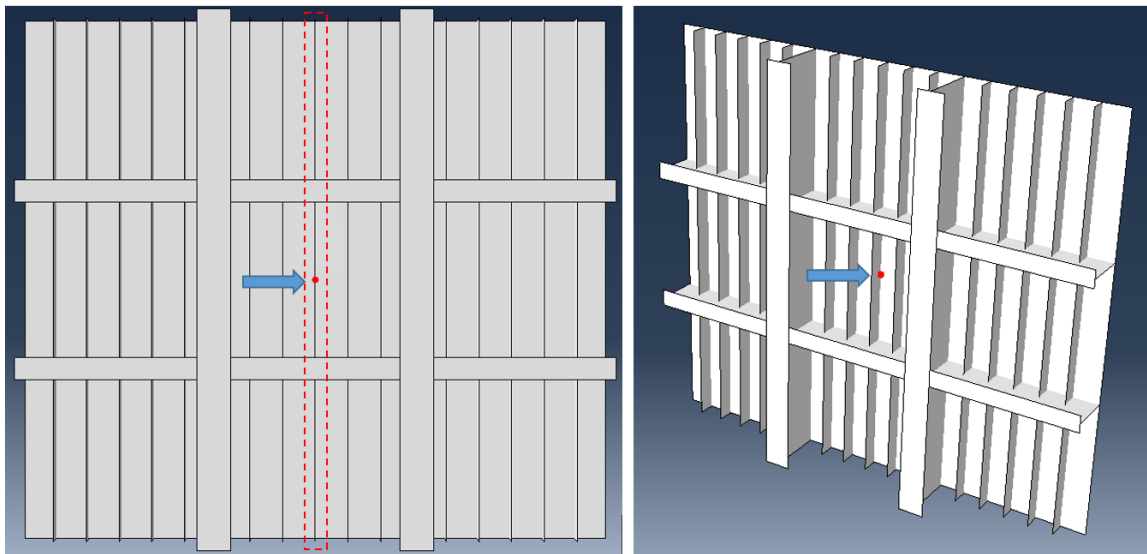


Figure 6-22. Location of the plate's geometric centre, shown by the red dot indicated by the arrow. It is located behind a main frame, located inside the dashed rectangle. The out-of-plane nodal displacement data depicted in this work were collected from the node coincident to that region.

Table 6-9 shows that the main frames absorb the great majority of the plastic damage in all cases. On the other hand, as the load increases, so does the percentage of plastic energy absorbed by the plate, as the structure is starting to use its reserve strength. Also, Figure 6-23 shows no apparent plastic deformation done to stringers and webframes. In fact, damage to these members is either non-existent or negligible in all cases presented in this work (which is the desired effect, as discussed above).

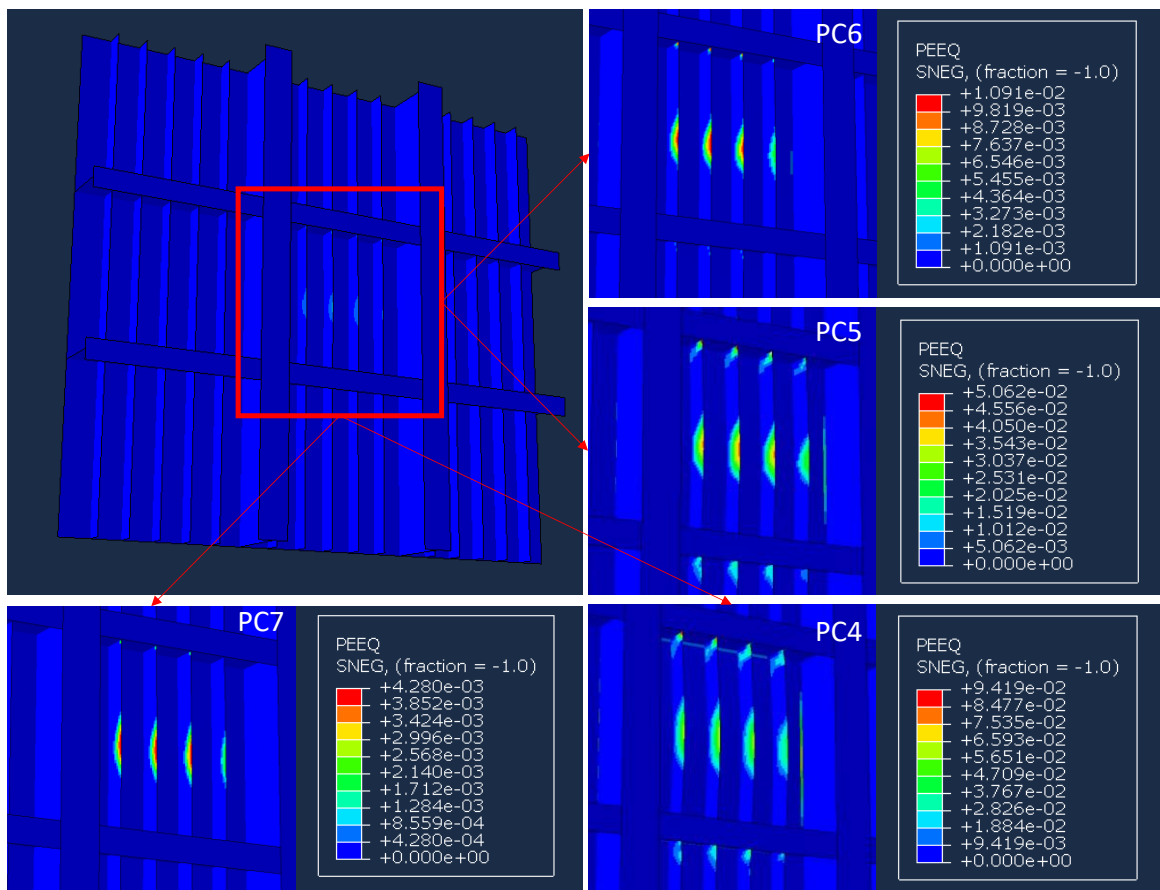


Figure 6-23. Sequence of images showing the difference in equivalent plastic strain for the PD load cases. The colour scale for each load case is shown to its right. The top left image shows the entire structure, and square indicates the region where plastic damage is observed.

The results presented here show that the damage is not linear between the different load cases with a drastic increase in the observed damage parameters occurring when the load changes from PC6 to PC5. The most damaged elements are the main frames in all cases, but as the load increases, so does the relative damage of the plate. The results in this section form a baseline structural response and they are compared with the other studied scenarios in the next sections.

6.10.2 Cases solved with the PRO method

As discussed at start of the previous section (Figure 6-21), applied and design contact area patches may be different. The following curves (Figure 6-24 to Figure 6-27) show the design load patch pressure data (post area reduction factor application) and compare them to the applied average pressure–area information for the progressive load. They show that as contact area increases the applied and design pressures tend to converge and minimize the discretization difference effect.

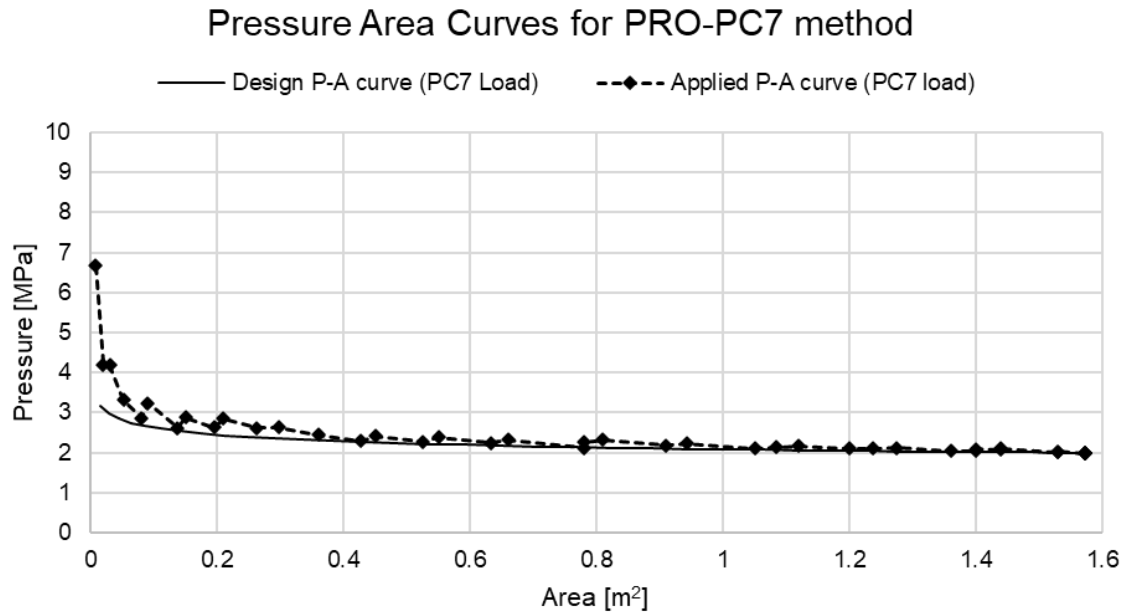


Figure 6-24. Design and applied pressure-area curves for the PC7 case with progressive non-coupled loadsteps, rectangular patch, and uniform pressure distribution.

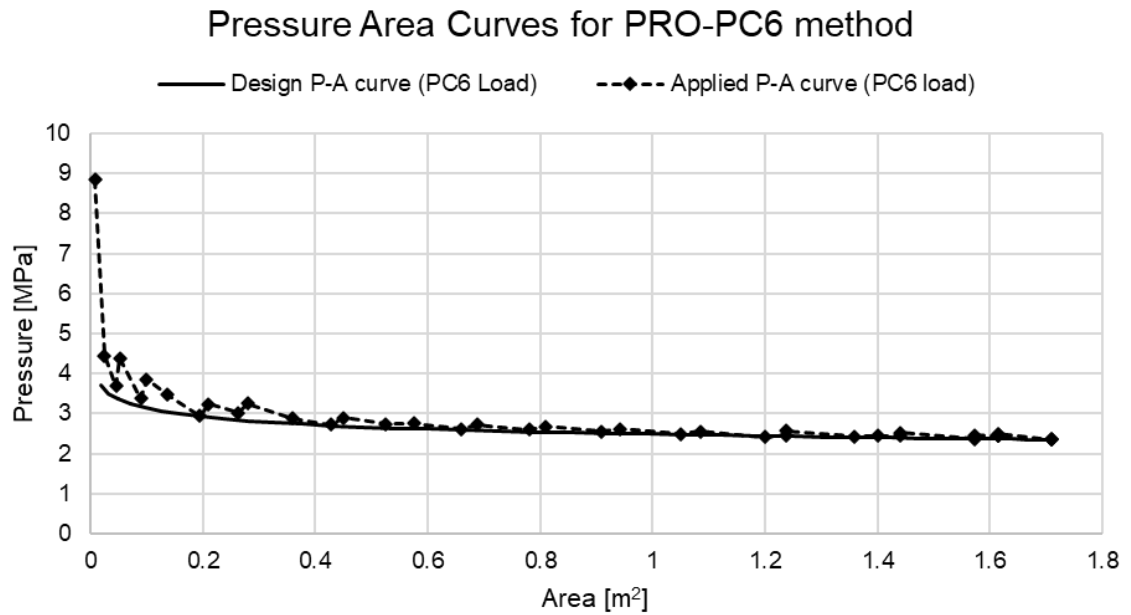


Figure 6-25. Design and applied pressure-area curves for the PC6 case with progressive non-coupled loadsteps, rectangular patch, and uniform pressure distribution.

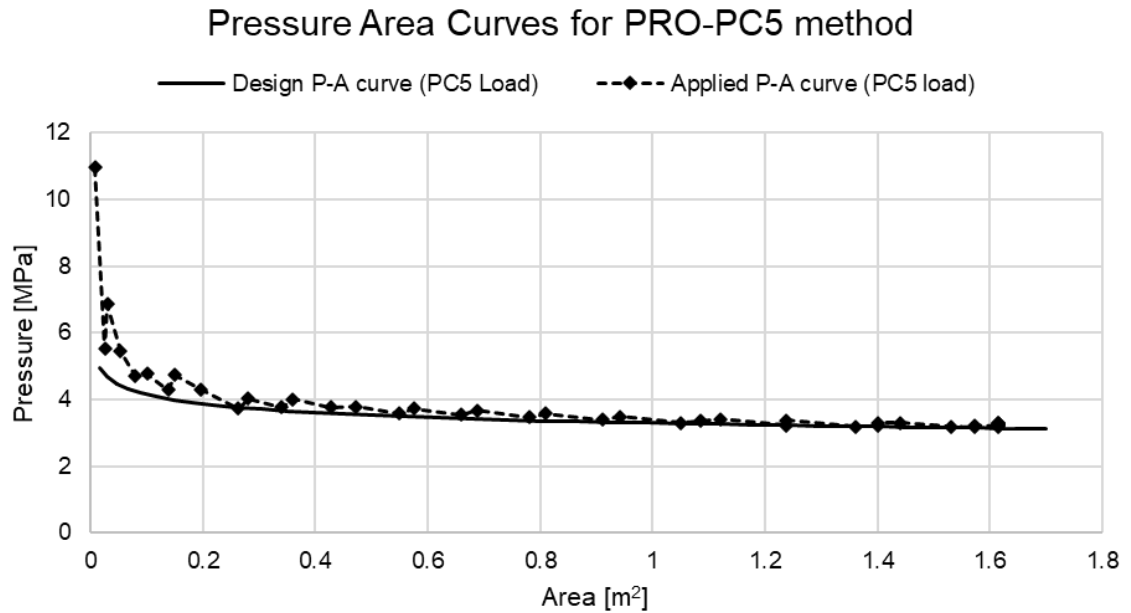


Figure 6-26. Design and applied pressure-area curves for the PC5 case with progressive non-coupled loadsteps, rectangular patch, and uniform pressure distribution.

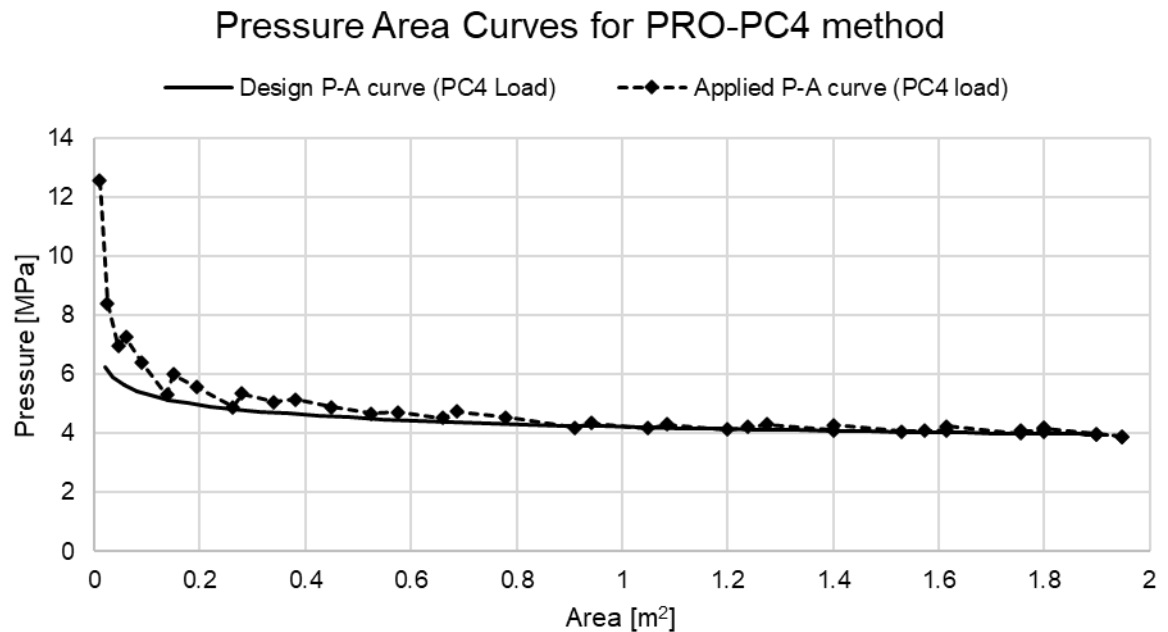


Figure 6-27. Design and applied pressure-area curves for the PC4 case with progressive non-coupled loadsteps, rectangular patch, and uniform pressure distribution.

Figure 6-28 illustrates how the changing pressure area curves relates to the plastic damage progression for PC7 and PC4 load cases. Plastic damage becomes relevant much before the final loadstep. The damage rate seems to decrease at the final loadsteps of the crushing process when indentation rates significantly decrease. Also, the trend is generally similar for both cases, but at different magnitudes of damage. This indicates that the damage progression is relevant for ice impact simulations, possibly even for the design load case, but certainly for overload cases, since plastic deformation is path-dependent, and this invariably changes the way the structure reacts to the load.

Figure 6-29 shows the linear interpolation of the Pressure vs Area vs Plastic Energy data for all four cases discussed so far in this section. The interpolated surface represents the plastic damage as function of the applied pressure-area data. It encapsulates the different IACS class loads in terms of structural damage. It indicates that significant plastic damage occurs at intermediary stages of the impact simulation, since the plastic damage bands are not concentrated at the right side of the surface, when the loads reach their peak.

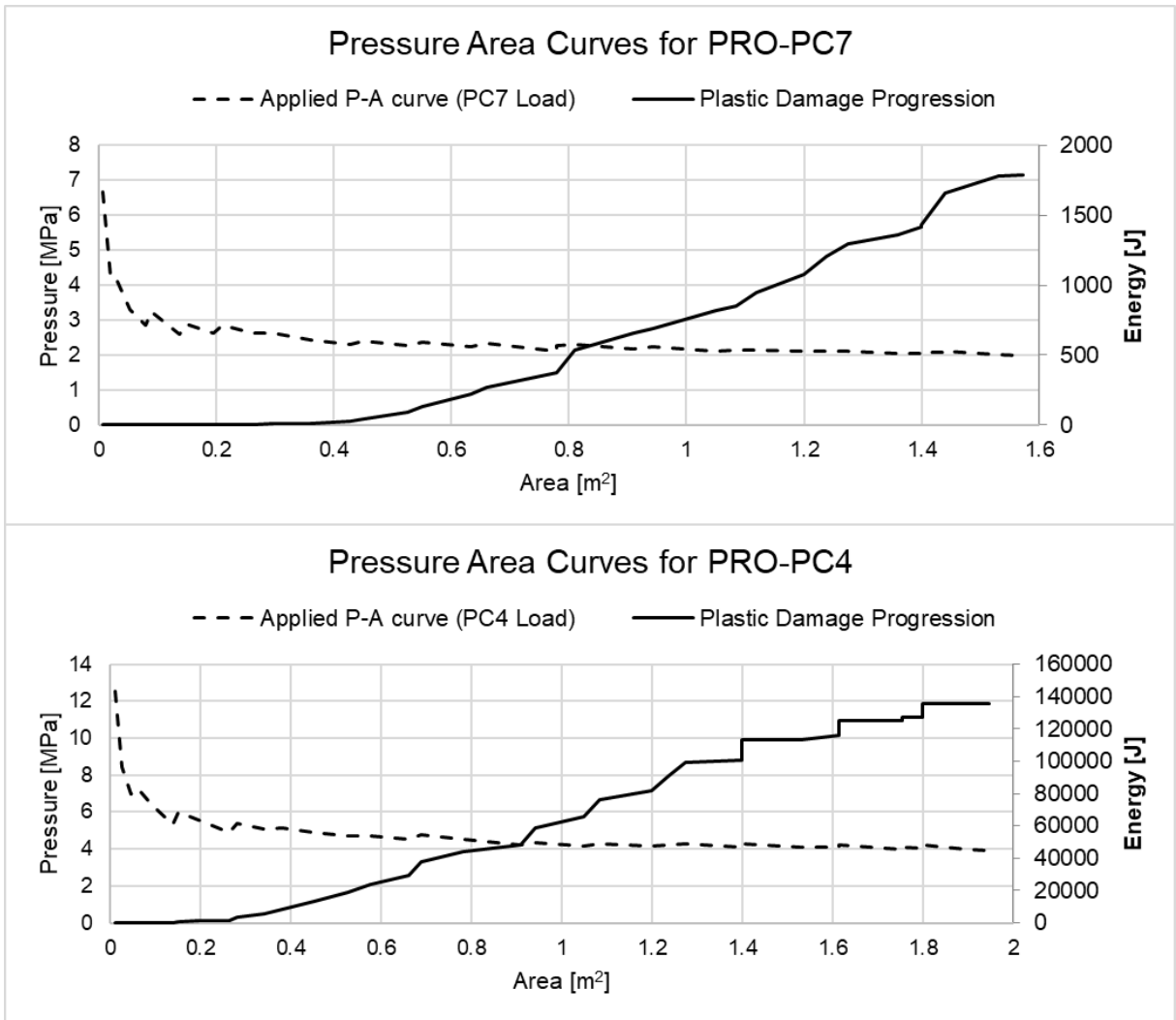


Figure 6-28. Curves showing the progression of plastic damage & applied pressure as function of the applied area for the PRO-PC7- and -PC4 simulations.

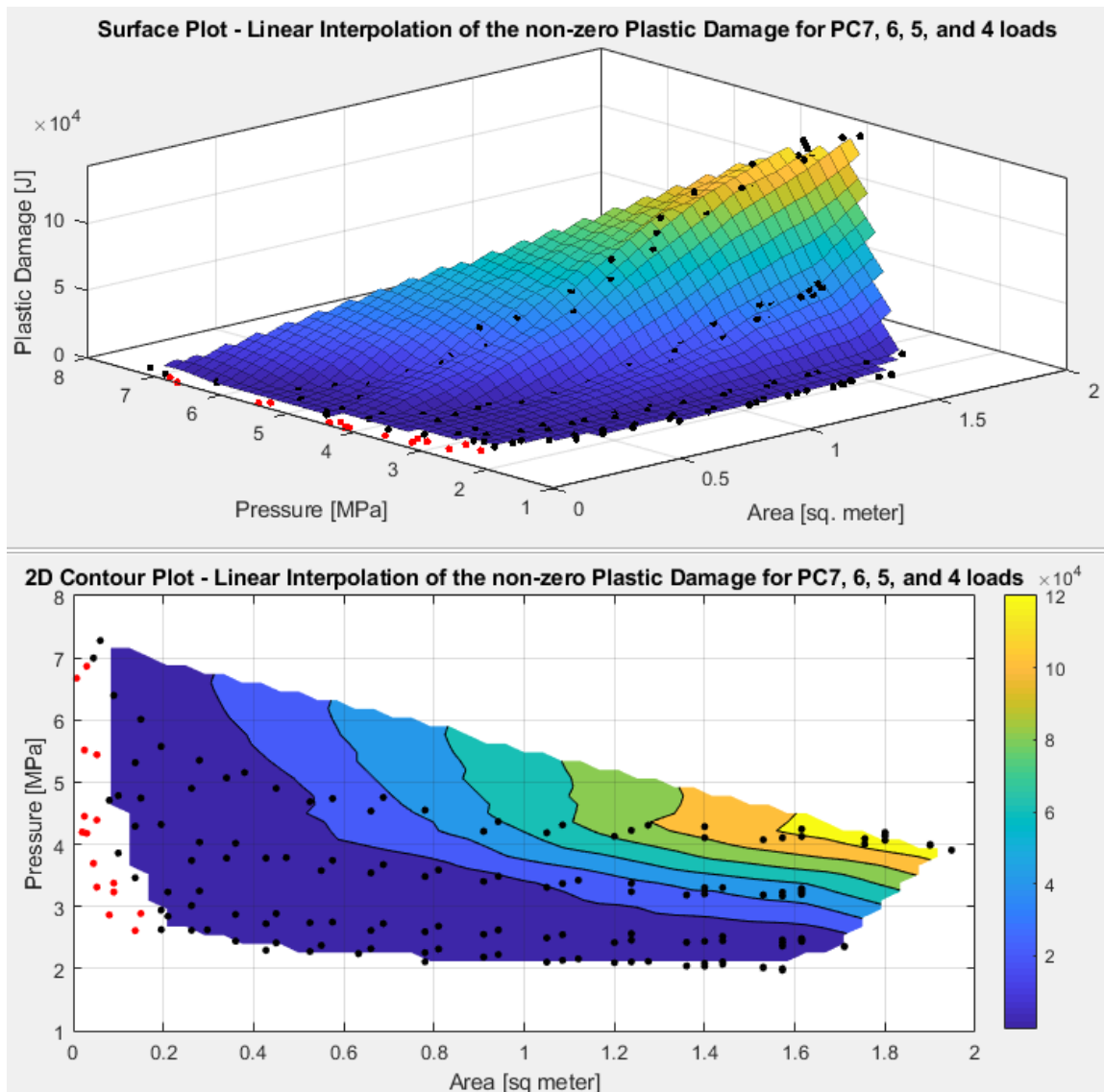


Figure 6-29. Linear interpolation surface for non-zero Plastic Damage vs Pressure-Area from all loadsteps in the PRO-PC7, PC6, PC5, and PC4 cases. Top image shows the 3D surface plot, and the bottom image shows the 2D contour plot. Red dots are the loadsteps with no plastic damage, black dots have non-zero plastic damage. Note that on the bottom image the dots form the four pressure-area curves shown in Figure 6-24 through Figure 6-27. The 2D contour plot shows the plastic deformation energy for the interpolated surface in joules.

Figure 6-30 shows the plastic strain behaviour of the structure at the appropriate loadsteps represented in the 2D contour plot. It is interesting that the loadsteps that fall within the

same plastic energy band show generally similar plastic deformation patterns even under different load patches, like “PC5-Final Step” and “PC4-Step 18”, or “PC6-Final Step” and “PC4-Step 12”.

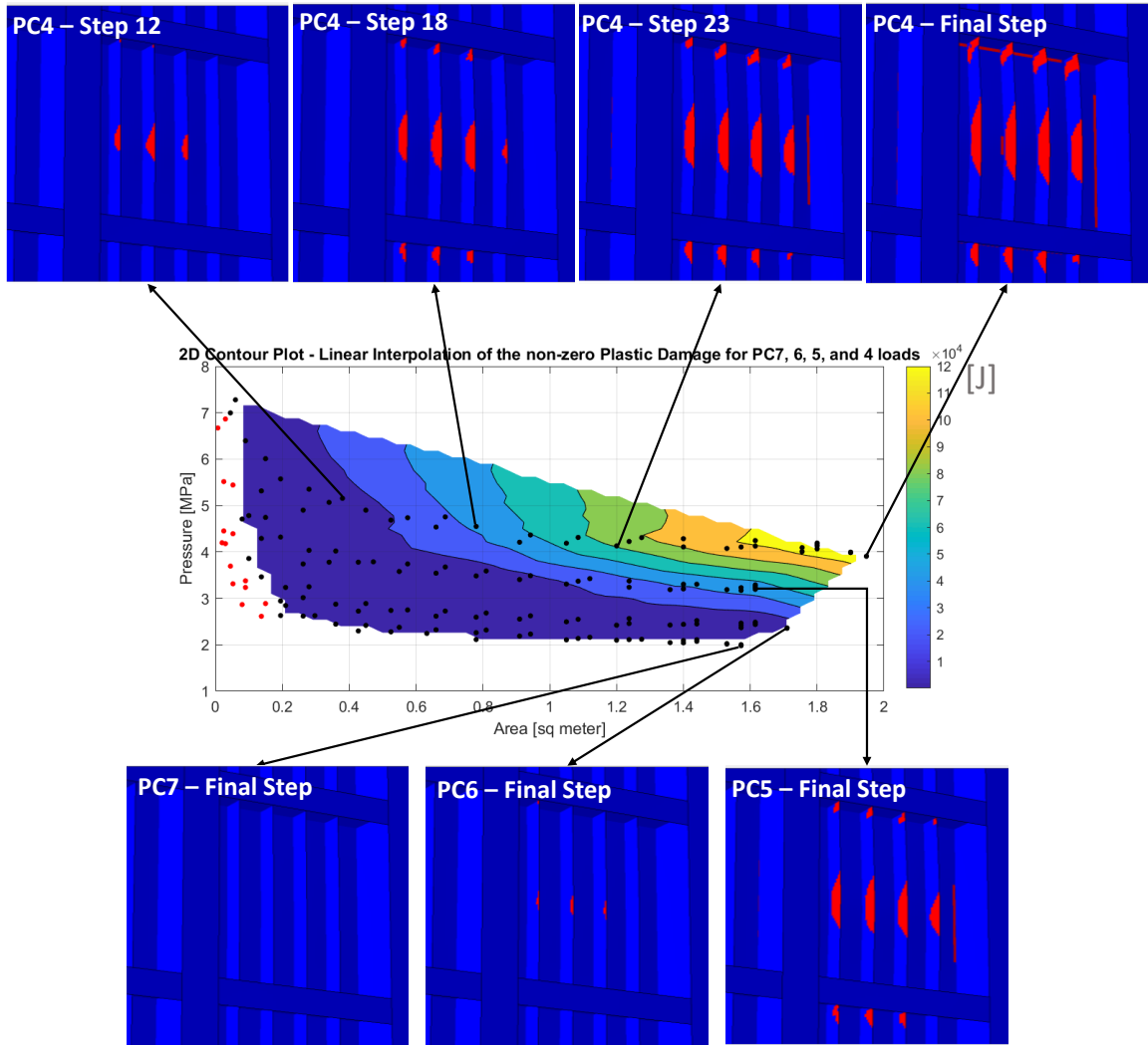


Figure 6-30. Examples of plastic damage of the structure at different simulation stages for different load cases. The images show only the regions where plastic strain is larger or equal 1%. At the centre is the 2D contour plot.

Table 6-10 contains a series of structural response indicator for all cases studied in the non-coupled progressive simulations.

Table 6-10. Summary of the damage done to the structure for the progressive non-coupled simulations with rectangular patch and uniform pressure distribution.

Indicators	Units	Simulation method: PRO			
		PC7	PC6	PC5	PC4
Total Structural Deformation Energy	kJ	13.1	24.7	88.4	199.5
Elastic Deformation Energy	kJ	11.3	18.5	36.2	63.6
Plastic Deformation Energy	kJ	1.8	6.2	52.2	135.9
Main Frames Plastic Damage	kJ	1.8	6.1	48.4	106.1
Main Frames Damage / Total Damage	%	99.7%	98.6%	92.7%	78.1%
Central Main Frame Plastic Damage	kJ	0.475	1.672	12.831	25.702
Centre Node displacement	m	0.010	0.016	0.041	0.068
Displacement / Frame span	%	0.7%	1.0%	2.6%	4.3%
Peak Plastic Strain	%	0.46%	1.21%	5.13%	11.07%

Table 6-11 compares the differences between the progressive and single loadstep approaches by comparing indicators presented in Table 6-10 with the ones presented in Table 6-8 and Table 6-9.

Table 6-11. Table shows the percent change of the damage parameters studied for progressive non couple load cases (PRO, Table 6-10) w.r.t. the base cases (PD, Table 6-8 and Table 6-9)

Percent Change of the Indicators	Units	Simulation methods: PD vs PRO			
		PC7	PC6	PC5	PC4
Total Structural Deformation Energy	%	1.9%	4.4%	0.1%	8.1%
Elastic Deformation Energy	%	0.4%	1.0%	-0.6%	-0.5%
Plastic Deformation Energy	%	12.6%	16.0%	0.7%	12.7%
Main Frames Plastic Damage	%	12.4%	15.7%	0.4%	9.1%
Central Main Frame Plastic Damage	%	11.4%	16.4%	0.2%	8.1%
Centre Node Displacement	%	1.1%	3.2%	-0.6%	4.6%

Table 6-11 results show that in all cases the progressive load application approach (PRO) causes noticeably more plastic damage when compared to the single loadstep cases (PD) and recoverable deformation remains the same. This makes sense since the maximum force is the same in both cases. An interesting observation comes from the PC5 load case. In that case the difference in damage between progressive and single loadstep simulations is very marginal, while the other cases are not. This exception shows the importance of the plastic damage progression analysis, as it is not trivial to extrapolate the structural behaviour based only on the plastic deformation at the point when ice crushing reaches its maximum force. All these observations show the importance of using a load application method, as the PRO method, which can capture the path dependency of the plastic deformation in ice impact simulations, even more so in the overload cases.

6.10.3 Cases solved with the PROWiSE method

The previous section compared the differences between PD and PRO methods. This section compares how the coupled energy approach affects the structural deformation using the PROWiSE method, which is the energy coupled method. Table 6-12 compares the peak force determined by the PRO and PROWiSE approaches. It shows that coupling load to structural deformation will cause a reduction in the maximum force applied to the structure; marginally for the PC7 and PC6 load cases, but noticeably for the PC5 and PC4 cases.

Table 6-12. Peak load comparison for the non-coupled (PRO) and the coupled (PROWiSE) cases.

Indicators	Units	Simulation methods: PRO & PROWiSE			
		PC7	PC6	PC5	PC4
Peak Force: non-coupled cases (PRO)	MN	3.15	4.04	5.31	7.61
Peak Force: coupled cases (PROWiSE)	MN	3.09	3.95	5.00	6.93
Reduction in the total force for coupled cases.	%	-1.7%	-2.3%	-6.0%	-9.0%

Table 6-13 contains a series of structural response indicator for the simulations using the coupled energy approach (i.e., PROWiSE simulations).

Table 6-13. Summary of the damage done to the structure for the progressive coupled simulations with rectangular patch and uniform pressure distribution (PROWiSE).

Indicators	Units	Simulation method: PROWiSE			
		PC7	PC6	PC5	PC4
Total Structural Deformation Energy	kJ	13.1	23.7	79.2	185.4
Elastic Deformation Energy	kJ	11.3	18.0	33.2	59.5
Plastic Deformation Energy	kJ	1.8	5.7	46.0	125.8
Main Frames Plastic Damage	kJ	1.8	5.6	43.0	100.6
Frames Damage / Total Damage	%	99.7%	98.7%	93.5%	80.0%
Central Main Frame Plastic Damage	kJ	0.48	1.53	11.61	24.54
Centre Node Displacement	m	0.010	0.015	0.038	0.065
Displacement / Frame Span	%	0.7%	1.0%	2.4%	4.1%
Peak Plastic Strain	%	0.46%	1.13%	4.79%	10.43%

Table 6-14 compares the relative difference in structural deformation energy and damage between coupled and non-coupled approaches (PRO vs PROWiSE). Note that in all but the PC7 case, there is a reduction in the deformation level when coupled cases are compared with the non-coupled cases. The PC6 case also presents an interesting behaviour, its peak load reduction was marginal at best, but there is a measurable difference in total plastic deformation, with an 8% reduction in plastic energy for just a 2.3% reduction in maximum force.

Table 6-14. Relative difference in structural damage between non-coupled (PRO) and the coupled (PROWiSE) simulation approaches.

Percent Change of the Indicators	Units	Simulation methods: PRO vs PROWiSE			
		PC7	PC6	PC5	PC4
Total Structural Deformation Energy	%	0.3%	-4.3%	-10.4%	-7.1%
Elastic Deformation Energy	%	0.3%	-3.1%	-8.3%	-6.4%
Plastic Deformation Energy	%	0.3%	-7.8%	-11.8%	-7.4%
Main Frames Plastic Damage	%	0.3%	-7.8%	-11.1%	-5.2%
Central Main Frame Plastic Damage	%	0.4%	-8.6%	-9.6%	-4.5%
Centre Node Displacement	%	0.3%	-3.1%	-6.7%	-3.9%

The following figures (Figure 6-31, Figure 6-32, Figure 6-33, and Figure 6-34) compare the deformation and damage done to the structure during the 3 different simulation approaches presented so far cases are solved with PD method, PRO method, and PROWiSE method.

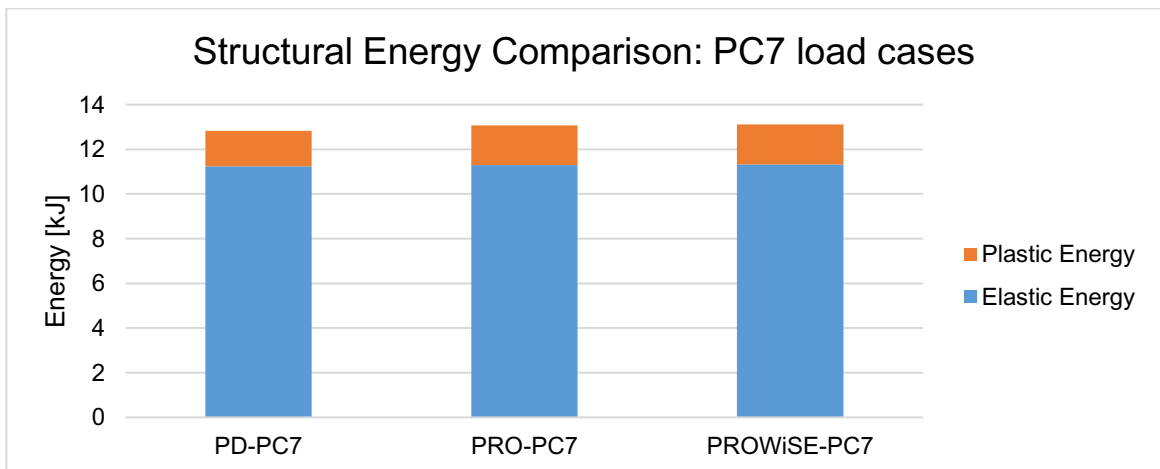


Figure 6-31. Structural energy for the PC7 load cases: single loadstep (PD), progressive non-coupled (PRO), and progressive coupled (PROWiSE).

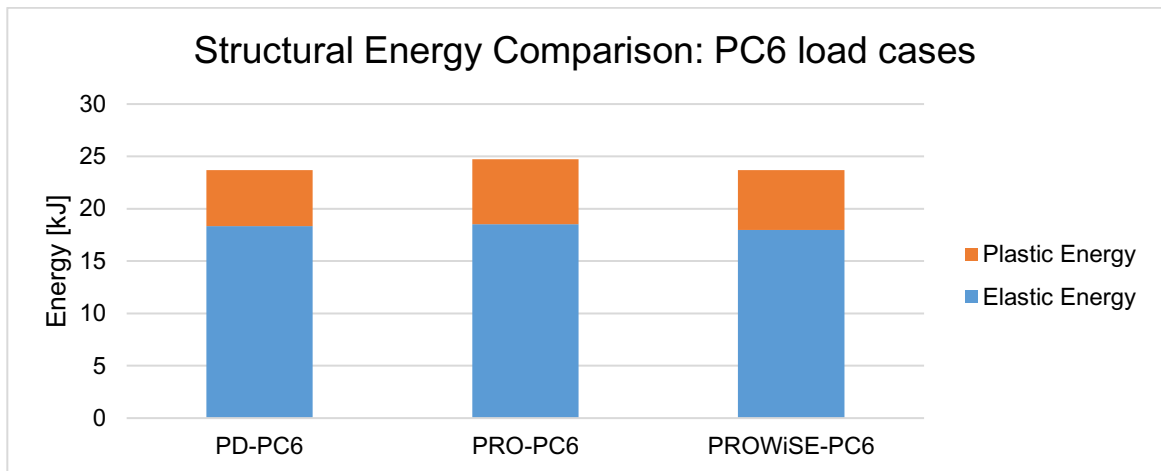


Figure 6-32. Structural energy for the PC6 load cases: single loadstep (PD), progressive non-coupled (PRO), and progressive coupled (PROWiSE).

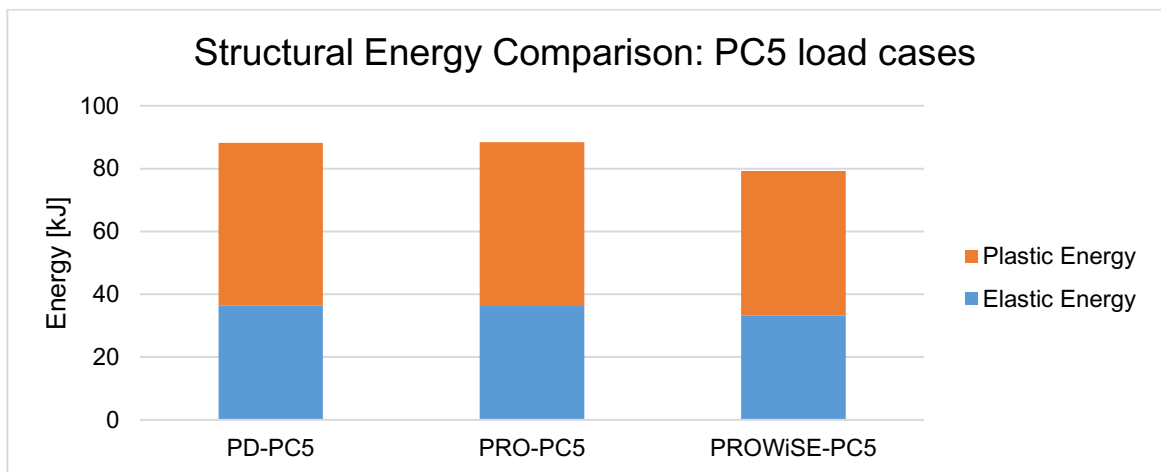


Figure 6-33. Structural energy for the PC5 load cases: single loadstep (PD), progressive non-coupled (PRO), and progressive coupled (PROWiSE).

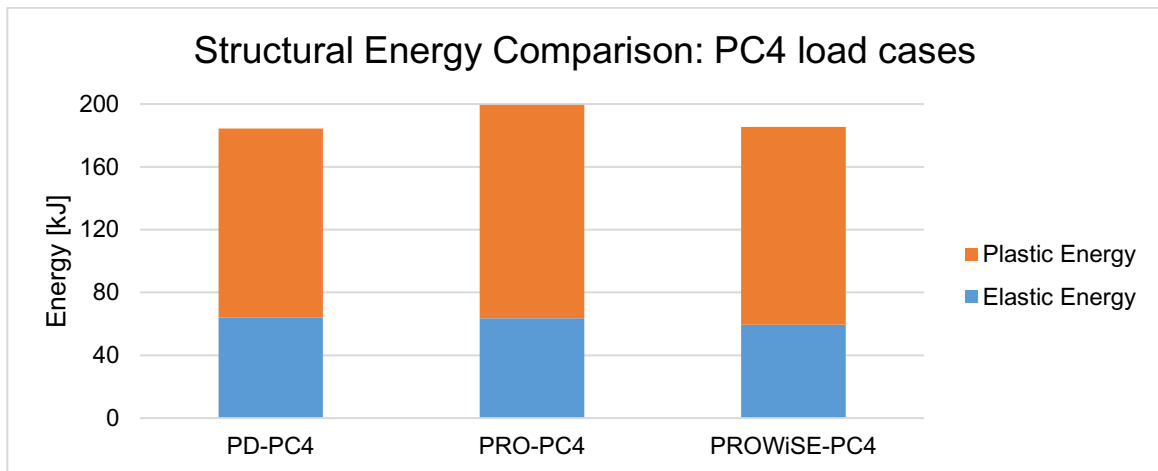


Figure 6-34. Structural energy for the PC4 load cases: single loadstep (PD), progressive non-coupled (PRO), and progressive coupled (PROWiSE).

In general, the results from all the cases studied so far indicate that the PRO method causes noticeably different structural response from the PD method. Coupling the load to structural deformation energy using the PROWiSE method starts to show noticeable difference in the structural behaviour in the PC6, 5, and 4 load cases. Thus, this method is of interest only in overload cases, when deformation energy becomes a significant sink for the initial impact energy, but not for the design load.

6.10.4 Cases solved with the NILAS method.

In this section the authors present the numerical simulations of triangular load patches with non-uniform pressure distribution using the NILAS load generation approach. The NILAS method applies non-uniform pressure distribution and uses the coupled-energy approach. As discussed in the last paragraph of section 6.7.2, the Area Reduction Factor is not required when HPZs are included in the load patch. Both approaches concentrate the ice load, and their effects should not be combined. The inclusion of HPZs and LPZs is expected

to act as an arguably more realistic representation of the observed ice-structure interaction than the Area Reduction Factor.

Figure 6-35 shows how a typical triangular ice load patch progression looks like on the mesh of the studied structure. It shows the discrete representation of the HPZ/LPZ representation in the triangular contact area described in section 6.7.2, but with its geometry adapted to the studied case.

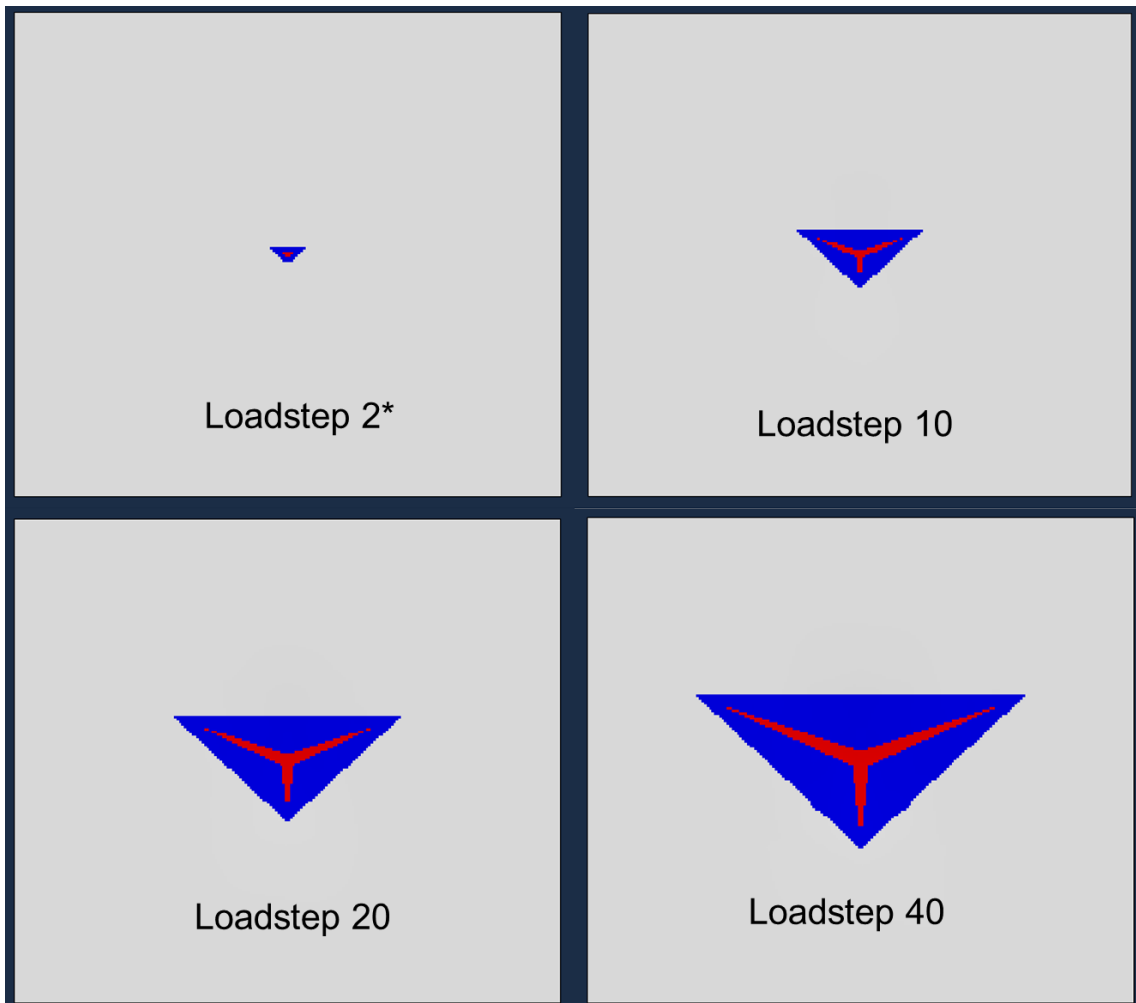


Figure 6-35. Load patches with NILAS method non-uniform pressure distribution. Red regions are HPZs, and blue regions are LPZs. Each image represents a different stage of the ice crushing process (*the top left image shows the second loadstep because the first

loadstep contact area had too few elements to properly define a distinct HPZ). The bottom right image shows the last loadstep.

The triangular patch dimensions are determined from the Equations (6.27) and (6.28) (Daley, 2000), which derive from the scenario presented in Figure 6-3.

$$T_{width} = 2 * \zeta_i * \left(\frac{\tan\left(\frac{\phi}{2}\right)}{\cos(\beta')} \right) \quad (6.27)$$

$$T_{height} = \frac{\zeta_i}{\sin(\beta') * \cos(\beta')} \quad (6.28)$$

As discussed in section 6.4, ζ_i is the normal ice penetration at the current loadstep i , ϕ is the ice wedge angle, and β' is the normal frame angle. In Figure 6-35 it is possible to observe the two distinct regions, HPZs (red, at the centre of the triangle) and LPZs (blue, around the HPZs). The definition of the HPZs and LPZs relative size and pressures follows Equations (6.22) to (6.26), i.e.:

- HPZs and LPZs will apply each half of the total design load F_n ;
- HPZs cover approximately 13% of total nominal contact area A_n ;
- and LPZs cover the rest of the nominal contact area.

The exact HPZ and LPZ area values vary depending on the number of elements selected for each zone. It is the same limitation discussed at the start of sections 6.10.1 and 6.10.2, but applied to more complex shapes. Figure 6-36, Figure 6-37, Figure 6-38, and Figure 6-39 show the nominal- (Equation 6.4), HPZ applied-, and LPZ applied-pressures as function of the respective nominal contact area for all NILAS cases.

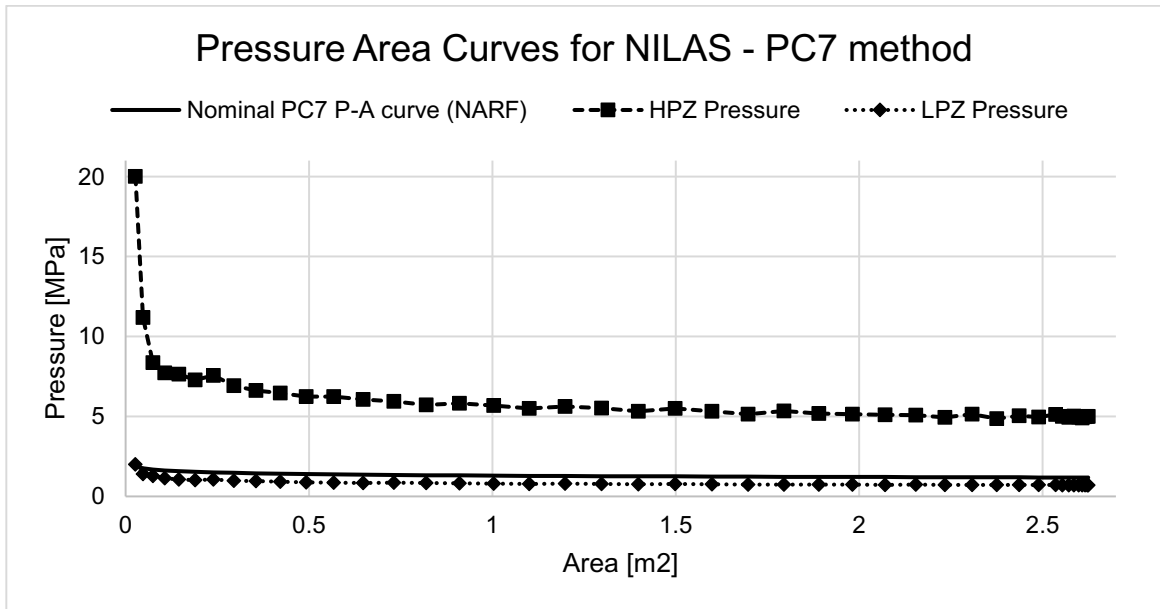


Figure 6-36. HPZs and LPZs pressure values for the load patches applied in the NILAS method for PC7 load. They are compared to the nominal pressure-area curve.

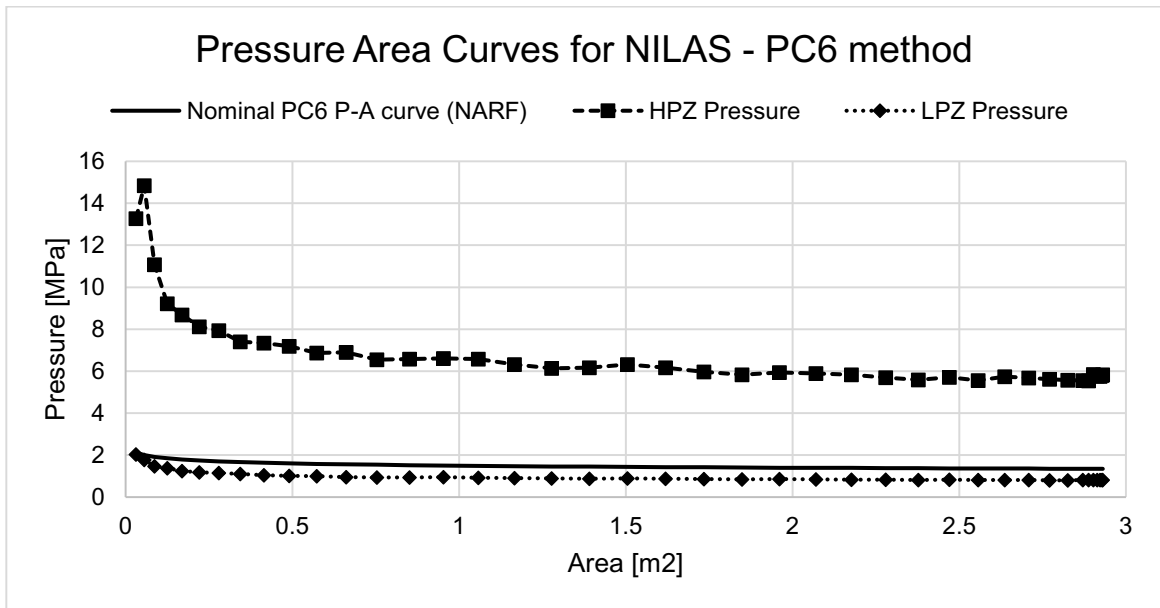


Figure 6-37. HPZs and LPZs pressure values for the load patches applied in the NILAS method for PC6 load. They are compared to the nominal pressure-area curve.

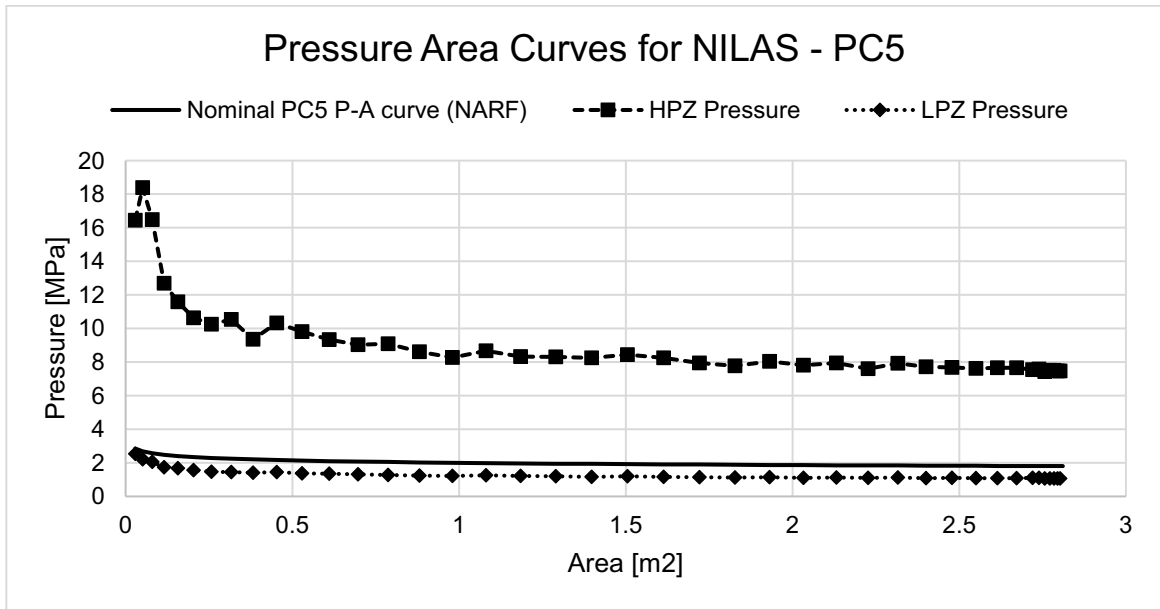


Figure 6-38. HPZs and LPZs pressure values for the load patches applied in the NILAS method for PC5 load. They are compared to the nominal pressure-area curve

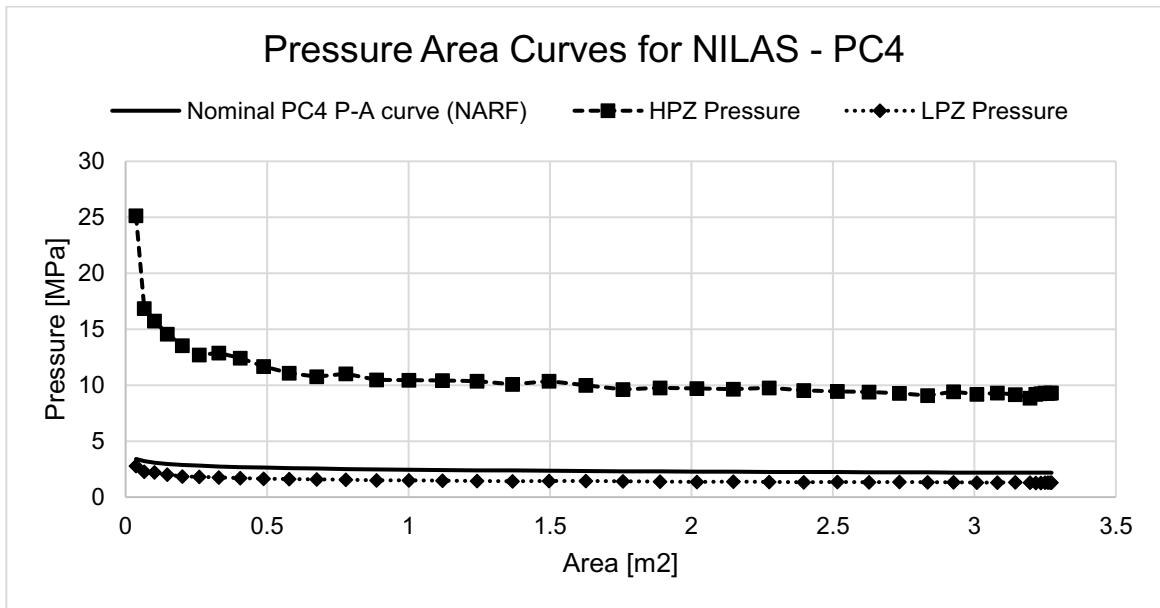


Figure 6-39. HPZs and LPZs pressure values for the load patches applied in the NILAS method for PC4 load. They are compared to the nominal pressure-area curve.

While nominal and LPZ pressures are relatively similar in all cases, the HPZ pressures are significantly higher than the nominal and LPZ pressures. Also, note that the NILAS cases (Figure 6-36 to Figure 6-39) have significantly lower average pressures and larger contact areas than in the PD, PRO, and PROWiSE methods (Figure 6-24 to Figure 6-27). This is because of the Area Reduction Factor is used in these methods.

The triangular load patch geometric centre is coincident with the geometric centre of the panel's plate. This also causes one of the HPZs dendritic arms to coincide with the central main frame location, as shown in Figure 6-40.

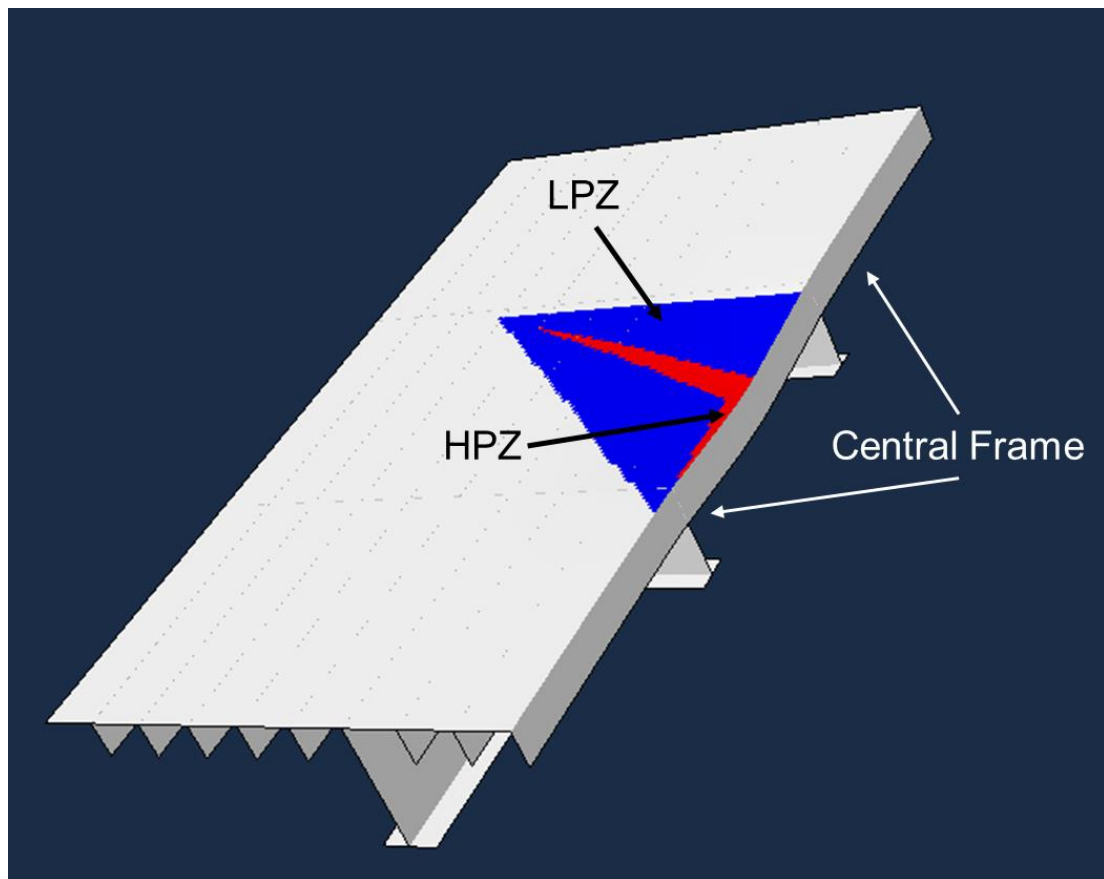


Figure 6-40. Illustration of the location of the load patch and its pressure zones with relation to the structure geometry and its central main frame.

This arrangement reflects the observations that the ice load distribution tends to concentrate around the more rigid structural members (Daley, 2000; Riska and Kämäräinen, 2011). In the IACS codified approach this effect is accounted for with correction factors, i.e., peak pressure factor (International Association of Classification Societies, 2011). In this work this effect is replicated by aligning the HPZ dendritic arm to the central main frame location.

The following figures compare the plastic strain at peak load between the PROWiSE and NILAS methods for the PC4 case at the instant of peak load. Figure 6-41 shows the results for the rectangular uniform load patch (PROWiSE method). Figure 6-42 shows the results for the triangular non-uniform load patch (NILAS method). The figures show generally same level of peak strain, but their pattern is different. In the triangular patch, Figure 6-42, the plastic strain follows the regions of HPZs, while, and in the rectangular patch, Figure 6-41, the plastic strain is relatively uniformly distributed over the 5 main frames.

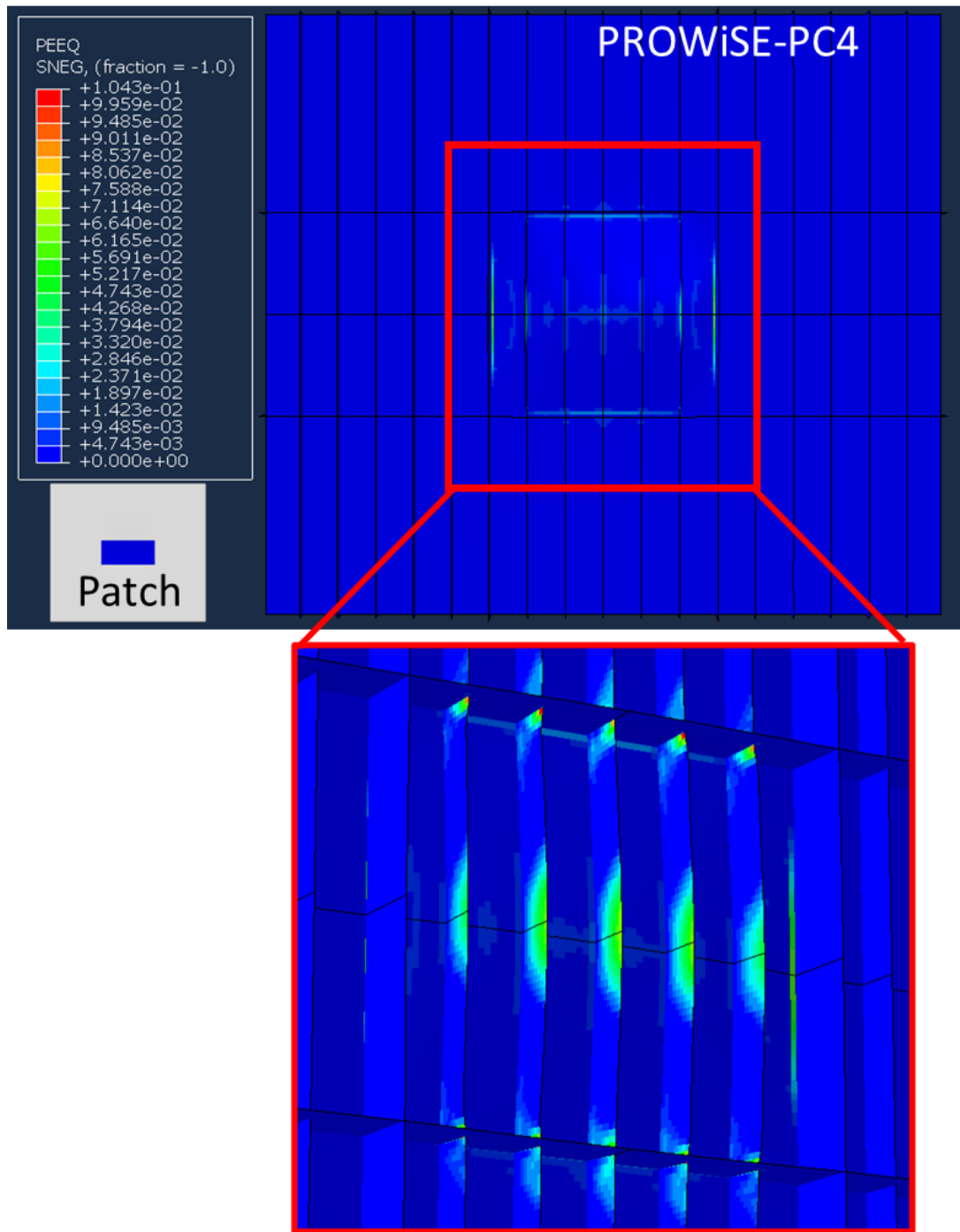


Figure 6-41. Equivalent plastic strain for the PROWiSE-PC4 load case. A cut was performed to hide the top flanges of the stringers and webframes from view. The top image shows the entire structure, and square indicates the region where plastic damage is observed. The small image on the left illustrates the type of load patch applied to the structure.

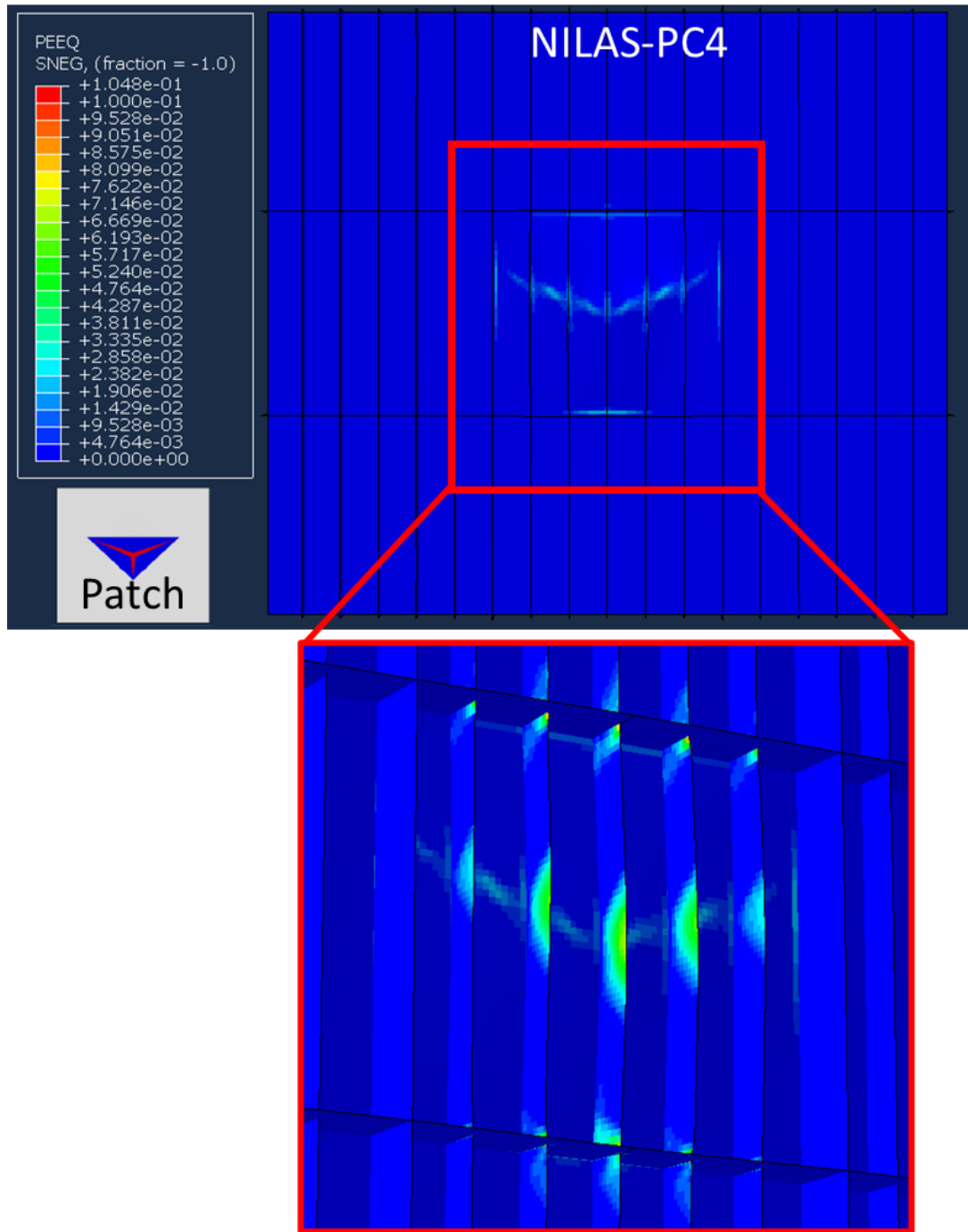


Figure 6-42. Equivalent plastic strain for the NILAS-PC4 load case. A cut was performed to hide the top flanges of the stringers and webframes from view. The top image shows the entire structure, and square indicates the region where plastic damage is observed. The small image on the left illustrates the type of load patch applied to the structure.

Table 6-15 presents the results that describe the total deformation done to the panel when using the NILAS method.

Table 6-15. Summary of the damage done to the structure for the progressive coupled simulations with triangular patch and non-uniform pressure distribution (NILAS).

Indicators	Units	Simulation method: NILAS			
		PC7	PC6	PC5	PC4
Total Structural Deformation Energy	kJ	12.0	23.4	61.6	133.5
Elastic Deformation Energy	kJ	10.0	16.1	29.0	51.8
Plastic Deformation Energy	kJ	2.0	7.3	32.6	81.7
Main Frames Plastic Damage	kJ	2.0	6.9	29.5	67.3
Frames Damage / Total Damage	%	97.8%	94.7%	90.7%	82.3%
Central Main Frame Plastic Damage	kJ	1.26	4.16	13.62	24.19
Centre Node Displacement	m	0.013	0.021	0.041	0.063
Displacement / Frame Span	%	0.8%	1.3%	2.6%	3.9%
Peak Plastic Strain	%	1.16%	3.29%	6.62%	10.48%

Table 6-15 shows that, as with other methods, the main frames are the structural element that are absorbing the great majority of the structural plastic damage. Differently from the PD, PRO, and PROWiSE cases, however, the NILAS simulation is causing more plastic damage to a single frame, the central main frame (same as indicated in Figure 6-40). This is evidenced in Table 6-16, which shows the percentage of the total plastic energy that is absorbed by the central frame in all load cases and methods studied.

Table 6-16. Percentage comparison of the central main frame damage with relation to the total plastic damage done to the structure in all load cases studied.

Load case	Central Main Frame Plastic Damage % w.r.t. Total Plastic Damage. All Load Cases			
	PC7	PC6	PC5	PC4
PD	26.8%	26.8%	24.7%	19.7%
PRO	26.5%	26.9%	24.6%	18.9%
PROWiSE	26.6%	26.7%	25.2%	19.5%
NILAS	62.7%	57.4%	41.8%	29.6%

Table 6-17. Relative difference in structural damage between coupled rectangular patch (PROWiSE) and the coupled triangular patch (NILAS) simulation approaches.

Percent Change of the Indicators:	Units	Methods compared: PROWiSE vs NILAS			
		PC7	PC6	PC5	PC4
Total Structural Deformation Energy	%	-8.6%	-1.2%	-22.3%	-28.0%
Elastic Deformation Energy	%	-11.8%	-10.1%	-12.7%	-13.1%
Plastic Deformation Energy	%	11.9%	26.9%	-29.2%	-35.1%
Main Frames Plastic Damage	%	9.8%	21.8%	-31.3%	-33.1%
Central Main Frame Plastic Damage	%	164.1%	172.5%	17.3%	-1.5%
Centre Node Displacement	%	24.7%	36.9%	7.7%	-4.3%

Table 6-17 compares the results between the NILAS and PROWiSE simulations. The non-uniform load generated using the NILAS method causes more plastic damage in the PC7 and PC6 cases, and less damage for the PC5 and PC4 load cases. On the other hand, elastic deformation is smaller in all cases. Table 6-17 also shows that the deformation done to the

single central main frame is significantly larger for the PC7 (NILAS damage is 164% larger) and PC6 (172.5% larger) load cases, appreciably larger for PC5 (17.3% larger) load case, and marginally smaller for the PC4 case (NILAS damage is 1.5% smaller). An important observation from these results is that simulations done using the NILAS method can significantly change the behaviour and damage done to singular structural elements (e.g., central main frame). This is due to load concentration caused by HPZs.

Figure 6-43 to Figure 6-46 compare the total deformation energy for all methods studied. The NILAS method results are shown in the last column of the set of four.

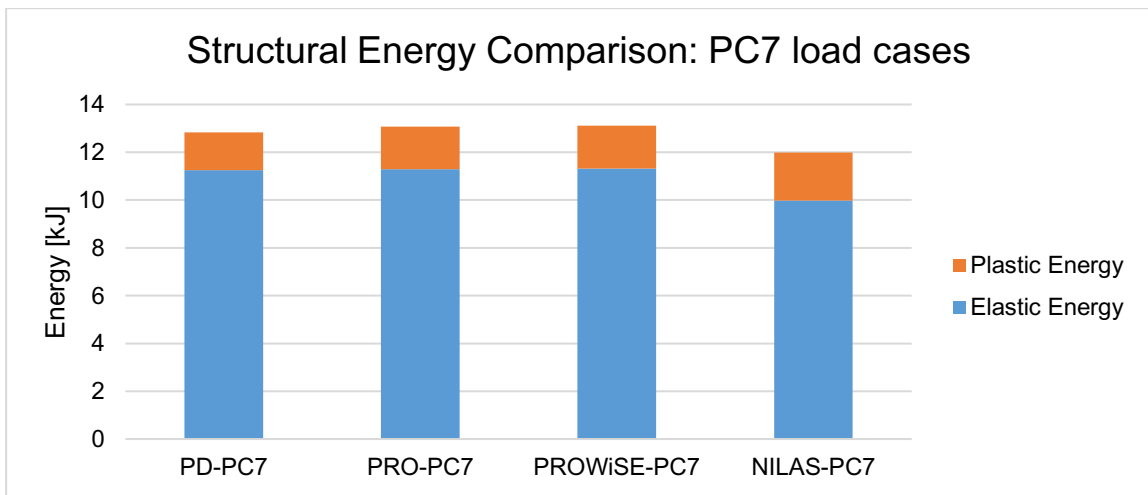


Figure 6-43. Structural energy for the PC7 load cases of all studied simulation approaches. The three on the left use rectangular uniform patches (i.e., PD, PRO, and PROWiSE), the one on the right use the triangular non-uniform patch (i.e., NILAS).

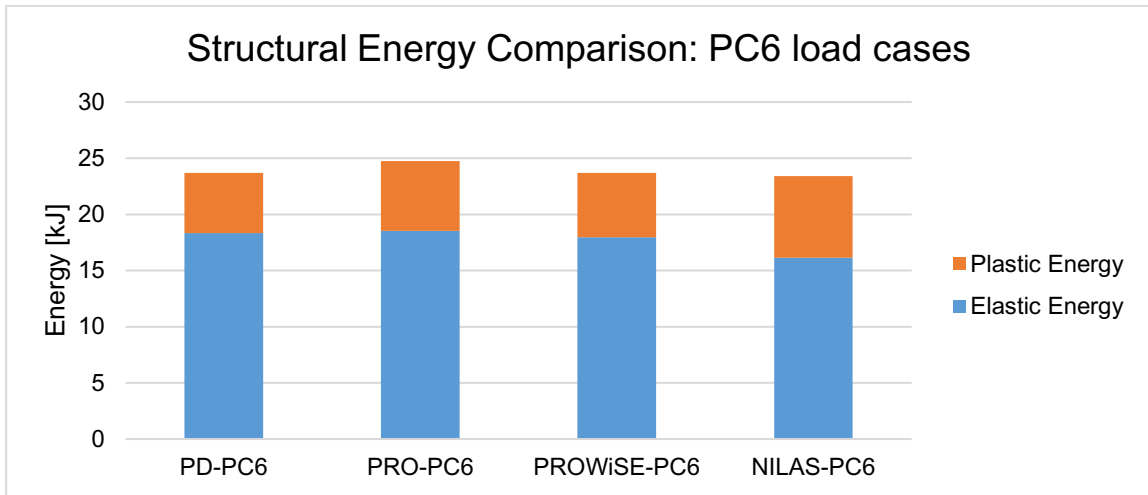


Figure 6-44. Structural energy for the PC6 load cases of all studied simulation approaches. The three on the left use rectangular uniform patches (i.e., PD, PRO, and PROWiSE), the one on the right use the triangular non-uniform patch (i.e., NILAS).

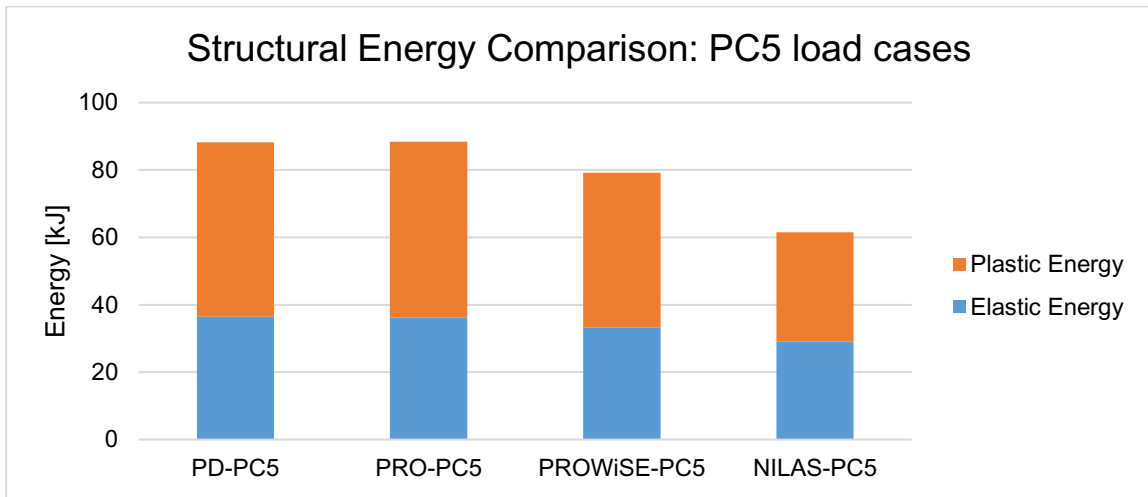


Figure 6-45. Structural energy for the PC5 load cases of all studied simulation approaches. The three on the left use rectangular uniform patches (i.e., PD, PRO, and PROWiSE), the one on the right use the triangular non-uniform patch (i.e., NILAS).

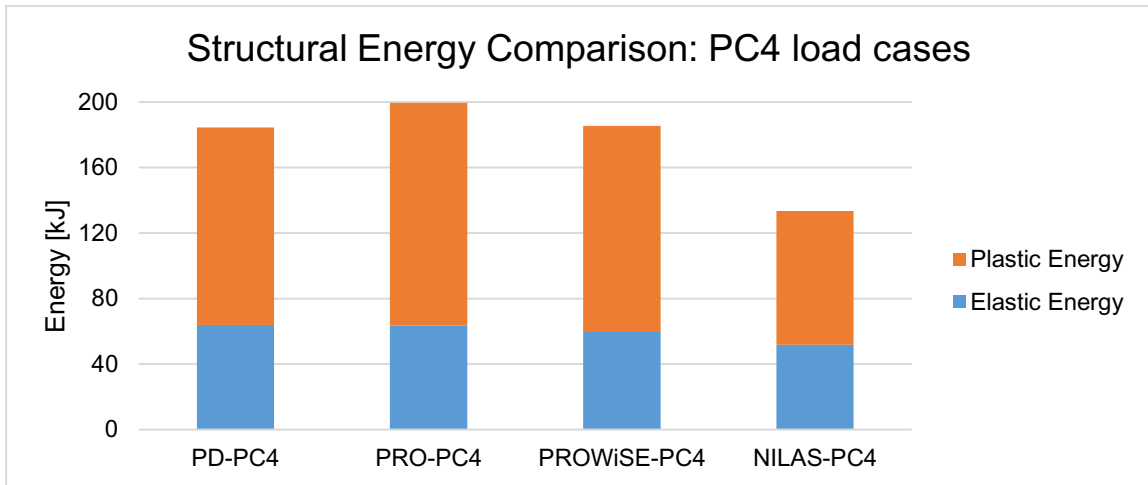


Figure 6-46. Structural energy for the load cases of all studied simulation approaches. The three on the left use rectangular uniform patches (i.e., PD, PRO, and PROWiSE), the one on the right use the triangular non-uniform patch (i.e., NILAS).

When compared to the PD, PRO, and PROWiSE methods, the NILAS method causes less overall structural deformation energy in all cases. The NILAS method causes more plastic damage at the design load, PC7 load, and at a slightly overloaded case, PC6 load. On the other hand, the NILAS method causes less overall plastic damage in larger overload cases, PC5 and PC4 loads, when compared to the PD, PRO, and PROWiSE methods. From the point of view of the central main frame alone, the NILAS method causes significantly more damage in the PC7 and PC6 load cases, appreciably more damage in the PC5 load case, and roughly similar damage in the PC4 load case. Moreover, for the design load (i.e., PC7 load) the change in pressure distribution did not drastically change the overall damage done to the structure. Which means that the studied PC7 structure seems to have a solid design point.

In summary, while the NILAS method leads to less overall deformation energy over the entire structure, it generally causes more concentrated damage in regions where HPZs develop.

On a final note, these observations were only verified for the studied low-polar class structure, it remains to be seen how higher polar classes behave to the non-uniform load patch at their design loads.

6.11 Conclusion

In this work the authors presented and studied a series of different approaches with the intent of improving ice contact loads representation in numerical simulations using load patches. The main parameters studied were:

- Effect of performing a progressive contact simulation that represents the complete ice crushing process and not only the maximum contact area.
- The effect of coupling the load generation by including structural deformation in the energy balance process.
- The development of a non-uniform pressure patch, with HPZs and LPZs that aim to replicate the observed pressure variations in real ice crushing experiments.

For this purpose, a series of simulations are performed on a low-polar class structure, Polar Class 7, and the structural responses for the simulations are compared. The simulations are divided in four sets, three to study the previously described parameters – progressiveness (PRO method), energy coupling (PROWiSE method), and non-uniform pressure (NILAS) - and another set to form the baseline cases based on the Popov-Daley method (PD method),

which apply IACS-like design load patches to the studied structure. For each simulation set, four different load cases are studied with varying nominal pressure and impact velocity (in fact, the parameters values are the same as IACS ones for the following ice classes: PC7, PC6, PC5, PC4). The experimental program is neatly summarized in Table 6-4.

The progressive simulations (PRO) show the importance of the plastic damage progression analysis. Plasticity is a path-dependent process, and the contact area size is continuously changing during ice-ship interaction. It is not possible to obtain the true plastic deformation of the structure based only on a single loadstep load patch. The results show that both total damage (total plastic energy) and localized damage (damage to a particular structural element), can significantly vary if the effects of the changing contact area are accounted for.

The coupled simulations (PROWiSE) show that the IACS design assumption of negligible structural damage is a fair one for the design load. The difference between classic, progressive, and coupled simulations is negligible for the PC7 load case on a PC7 structure. On the other hand, for overload cases, the structural deformation process becomes a significant energy sink for the system, and accounting for that fact will generally reduce the total deformation done the structure.

The proposed approach for the Non-uniform Ice Load application System, the NILAS method, was idealized with the intent of improving ice contact loads representation in simulations that use pressure patches as the load application approach. It is a relatively inexpensive computational way of solving the damage done to a ship panel when under ice crushing load. The pressure distribution over the pressure patch was designed in accordance

with the observations presented in Andrade et. al (2022b). In this sense, NILAS accounts for the ice load concentration due to the presence of HPZs. The method seems to be capable of substituting the IACS UR I defined Area Reduction Factor in numerical structural simulations. The method also allows the expected nominal contact area shape to be used in numerical structural simulations (i.e., there is no need to transform the contact area shape into a rectangle).

Regarding structural behaviour, there are two noteworthy observations that can affect low polar class ships' structural design. The first is that incorporating the ice load progression has produced noticeably different plastic behaviour in the studied scenarios with the only exception being the PC5 load case. The progressive load application approach, even when decoupled, can be considered a superior approach in terms of numerical structural design because it will account for the path dependency of the plasticity while still being simple to implement and it is computationally efficient to solve. The second aspect is that the introduction of non-uniform pressure distribution (NILAS approach) allows for a better assessment of the response of individual structural members when under ice loads (i.e., stiffeners, frames, stringers, and webframes). Since NILAS is capable of replicating the ice load concentration effect observed in real life, it can also be used to assess the effects of single frame 3 hinge collapse failure on the structural integrity of the panel. And, although not the focus of this particular study, the possibility or not of local structural collapse could be assessed with such simulations. In the future this can be used to improve framing design options in low polar class ships.

With all this in mind, the NILAS method is useful for the simulation of the ice load effects in non-polar class ships or overloaded polar class ships.

6.12 Acknowledgements

The authors graciously acknowledge the financial support from the Natural Sciences and Engineering Research Council of Canada DND/CRD [grant number DNDPJ 520471-17] ‘Operational Capabilities of Low- and Non-ice-class Structures in Ice’ grant, and the following contributing project partners: Defence Research and Development Canada (Atlantic), Vard Marine Inc., the American Bureau of Shipping (ABS), and the Newfoundland and Labrador Provincial Government & Labrador Provincial Government [grant number 5404-1984-102].

6.13 References

- American Bureau of Shipping, 2021. Guidance notes on nonlinear finite element analysis of ship and offshore structures.
- Andrade, Sthefano Lande, Elruby, A., Oldford, D., Quinton, B., 2022. Assessing Polar Class Ship Overload and Ice Impact on Low-ice Class Vessels using a “Quasi Real Time” Popov/Daley Approach, in: SNAME Maritime Convention. SNAME, Houston, TX, pp. 1–12. <https://doi.org/10.5957/SMC-2022-108>
- Andrade, Sthéfano Lande, Gagnon, R., Colbourne, B., Quinton, B., 2022. Ice Pressure Distribution Model: A Geometry-Based Solution for High-Pressure Zone Representation. SSRN Electron. J. (under Rev. Cold Reg. <https://doi.org/10.2139/ssrn.4251178>

- Blum, H., 1973. Biological shape and visual science (part I). *J. Theor. Biol.* 38, 205–287.
[https://doi.org/10.1016/0022-5193\(73\)90175-6](https://doi.org/10.1016/0022-5193(73)90175-6)
- Blum, H., 1967. A Transformation for Extracting New Descriptors of Shape, in: Wathen-Dunn, W. (Ed.), *Models for the Perception of Speech and Visual Form*. MIT Press, Cambridge, pp. 362–380.
- Daley, C., 2000. *IACS Unified Requirements for Polar Ships - Background Notes to Design Ice Loads*.
- Daley, C., 1999. Energy Based Ice Collision Forces, in: *Proceedings of the 15th International Conference on Port and Ocean Engineering under Arctic Conditions*. St. John's, Canada, pp. 1–20.
- Daley, C., 1994. *Compilation of Medium Scale Ice Indentation Test Results and Comparison to ASPPR*. Nepean, Canada.
- Daley, C., 1992. Ice edge contact and failure. *Cold Reg. Sci. Technol.* 21, 1–23.
[https://doi.org/10.1016/0165-232X\(92\)90002-C](https://doi.org/10.1016/0165-232X(92)90002-C)
- Frederking, R., 2004. Ice pressure variations during indentation, in: *International Association of Hydraulic Engineering and Research Proceedings IAHR'04, Vol.2*. Saint Petersburg, Russia, Russia, pp. 307–314.
- Frederking, R.M.W., Jordaan, I.J., McCallum, J.S., 1990. Field Tests of Ice Indentation at Medium Scale Hobson's Choice Ice Island, 1989, in: *IAHR*. Espoo, Finland, pp. 931–944.

- Gagnon, R., Andrade, S.L., Quinton, B.W., Daley, C., Colbourne, B., 2020. Pressure distribution data from large double-pendulum ice impact tests. *Cold Reg. Sci. Technol.* 175, 103033. <https://doi.org/10.1016/j.coldregions.2020.103033>
- Gagnon, R.E., 1998. Analysis of visual data from medium scale indentation experiments at Hobson's Choice Ice Island. *Cold Reg. Sci. Technol.* 28, 45–58. [https://doi.org/10.1016/S0165-232X\(98\)00012-3](https://doi.org/10.1016/S0165-232X(98)00012-3)
- Gagnon, R.E., Daley, C., 2005. Dual-axis video observations of ice crushing utilizing high-speed video for one perspective, in: 18th International Conference on Port and Ocean Engineering Under Arctic Conditions. Potsdam, NY, pp. 271–281.
- International Association of Classification Societies, 2011. Requirements concerning Polar Class. IACS Int. Assoc. Class. Soc.
- Joensuu, A., Riska, K., 1989. Structure/ice contact, measurement results from the joint tests with Wärtsilä Arctic Research Centre in spring 1988 [in Finnish]. Espoo, Finland.
- Kamio, Z., Takawaki, T., Matsushita, H., Takeuchi, T., Sakai, M., Terashima, T., Akagawa, S., Nakazawa, N., Saeki, H., 2000. Medium scale field indentation tests: physical characteristics of first-year sea ice at Notoro Lagoon, Hokkaido. *Proc. Int. Offshore Polar Eng. Conf.* 1, 562–568.
- Popov, Y., Faddeyev, O., Kheisin, D., Yalovlev, A., 1967. *Strength of Ships Sailing in Ice.*
- Riska, K., Kämäräinen, J., 2011. A review of ice loading and the evolution of the finnish-swedish ice class rules. *Trans. - Soc. Nav. Archit. Mar. Eng.* 119, 265–298.

- Riska, K., Rantala, H., Joensuu, A., 1990. FULL SCALE OBSERVATIONS OF SHIP-ICE CONTACT: RESULTS FROM TESTS SERIES ONBOARD IB SAMPO, WINTER, 1989.
- Sanderson, T.J.O., 1988. Ice mechanics: Risks to offshore structures, First. ed. Graham & Trotman, London, UK.
- Siddiqi, K., Bouix, S., Tannenbaum, A., Zucker, S.W., 2002. Hamilton-Jacobi Skeletons. *Int. J. Comput. Vis.* 48, 215–231. <https://doi.org/10.1023/A:1016376116653>
- Sopper, R., Gagnon, R., Daley, C., Colbourne, B., 2015. Measurements of spatial and temporal variations in ice impact pressures, in: *Proceedings of the International Conference on Port and Ocean Engineering under Arctic Conditions, POAC*. Trondheim, Norway.
- St. John, J., Daley, C.G., Blount, H., 1984. *Ice Loads and Ship Response to Ice*. Washington, DC.

Chapter 7 Conclusions and recommendations for future work

7.1 Conclusion

The objective of this work was to develop an ice load model to assess possible large structural deformation in non-polar class and overloaded polar class ships.

The first step was the study and measurement of pressure distribution data for ice crushing events (Chapter 2). In this stage the pressure map data was recorded using a novel sensor, the Impact Module, during medium energy (~ 29 kJ) ice crushing impact experiments. The velocity of the impacts reached up to of 4.7 m/s, and loads peaked at 620 kN. The development of high-pressure zones (HPZs) and low-pressure zones (LPZs) over the contact have been recorded and documented at high temporal (500 Hz) and spatial resolution (~ 2 cm²) simultaneously. The study revealed interesting aspects of the ice crushing pressure distribution evolution such as: the consistency of HPZ and LPZ average pressures, 21 MPa and 3.7 MPa respectively, and role of HPZs in defining details of the total load time series. From the results shown in Gagnon et al. (2020) it can also be determined that HPZs occupy, on average, approximately 13% of the total contact area, while HPZs are responsible for approximately half of the total load applied to Impact Module during most of the crushing process duration. The pressure-sensing technology from the Impact Module has been shown to be robust and capable of providing accurate pressure distribution maps during small-to-medium-scale ice impact tests using the large pendulum apparatus. The device also proved capable of performing medium energy ship-ice impact experiments in controlled laboratory conditions with full scale ice and full-scale ship structure.

The next stage was the study of the behaviour of non-polar class structure to ice impact loads using the Large Pendulum Apparatus. At first the pressure loads recorded by the Impact Module were applied to a numerical model of a structure made similar to the ex-HMCS IROQUOIS panel (Chapter 3). The results show that the large pendulum would be potentially capable of causing significant plastic deformation to a non-polar class ship. Later, preliminary impact experiments were performed against actual panels from the ex-HMCS IROQUOIS (Chapter 4). Due to limitations imposed by the Pandemic only preliminary results were available before the completion of this work. Although measurable permanent plastic deformation was observed, it was not possible to use the results from the preliminary experiments for validation of the ice load model developed in this work. A series of adjustments of the experimental procedure were required to improve data collection in future experiments (e.g., increasing sampling rates and changing ballast plate orientation). Similarly, it was not possible to directly compare the response of the panel between the numerical and physical experiments. There were many different variables to allow direct one-to-one comparison. The numerical model grillage had four frames; the physical model tested had three; the maximum kinetic energy of the numerical experiments was 29 kJ, while in the physical experiments it was 46 kJ; and, as commented, the physical experimental procedure needed adjustments; finally, the 2020 Pandemic severely affected the testing program schedule. Nevertheless, the results of both experiments (the numerical and the physical ones) indicate that a method to couple ice load to structural deformation would be required when developing the ice load model for numerical simulations, and that coupling structural deformation energy could be a solution.

The next stage of the research was the development of a geometric model capable of determining pressure distribution in ice contact area patches (Chapter 5). The model was envisioned as a solution that could represent the observed regions of HPZs and LPZs for contact areas of any shape. For this purpose, the test face images, and pressure distribution data provided by the large pendulum impact experiments were used in the development of a geometry-based methodology for modelling ice pressure distribution. The methodology uses topological skeleton and distance field information of the ice contact area's shape to approximately define the shapes and sizes of the associated HPZs and LPZs. If the bulk ice feature geometry is known initially, then the methodology will produce a reasonable descriptor of HPZ/LPZ distribution during indentation, assuming no catastrophic spallation events. This is demonstrated by comparing the prediction with the actual observed HPZs from the large pendulum impacts and also from other indentation experiments available in the literature. This capability makes the topological skeleton method for HPZ/LPZ representation particularly useful in numerical structural simulations where ice load patches are applied to a structure.

The final stage was the development of the non-uniform ice load model for numerical structural simulations. While the IACS UR I ice impact scenario is a limited energy scenario, it assumes that all kinetic energy is absorbed exclusively by the ice crushing process. In the current work's methodology, the Non-uniform Ice Load Application System, or NILAS for short, the losses due to ice crushing and structural deformation are both accounted for. This is done in a procedural manner. NILAS is a progressive method that discretizes the ice crushing process into a series of increasingly larger contact area

patches, which are applied in a numerical simulation as series of loadsteps. The penetration is discretized, and the normal velocity is re-calculated after each load patch is applied to the structure at each loadstep. The deformation energy determined at the end each loadstep is then used to define the load patch applied at the next loadstep. The final step is the implementation of the geometric model for non-uniform pressure distribution (Chapter 5) in the ice load patches.

The NILAS method is a relatively inexpensive computational way of predicting the damage done to a ship panel when under ice crushing load, using ‘contactless’ loads. NILAS provides a relatively more realistic representation of the true pressure progression and distribution when compared to a single uniform load patch methodology. The work conducted over the course of this study clearly shows that the features incorporated into NILAS, namely, coupled-energy contact area progression and HPZ/LPZ pressure distribution, all have significant influence on the predicted load and structural response. Thus, the incorporation of these features provides a significant step in improving predictive capabilities for ice loads on ship structures.

The NILAS is of particular utility for the simulation of the effects of ice loads in non-polar class ships or overloaded polar class ships, as it is a coupled ice load application method that is also able to represent pressure distribution patterns observed in ice crushing experiments.

7.2 Limitations of the current work and suggestions for future work

The method presented in Chapter 5 is purely geometry based, thus it cannot directly account for ice related factors such as ice type, temperature, impurities, grain size, and crystal lattice orientation. Another important aspect is that the method was compared to experiments with flat rigid indenters. The range of experiments studied shows consistency in the importance of contact area geometry, but the individual effect of these parameters remains to be studied.

The topological skeleton method, as it is presented in this work, is limited in that it can only predict the HPZ distribution if the true geometries of the ice feature and indenter were known at all instants of the ice crushing process. Spalling is not modelled, thus it would be beneficial to develop a spalling model (or upgrading an existing 2D spalling model into a full 3D model) to allow the prediction of the full ice crushing process, transforming the geometric method from reactive to predictive.

This method cannot directly account for the effects of external boundary conditions (e.g., water/snow) on the confinement due to crushed ice. This is done indirectly by assuming that the final HPZ size as a pre-defined percentage of the total contact area. If external confinement is assumed uniform (which is hardly ever the case, but it is an assumption required at this stage), then this percentage value can be adjusted to account for the level of confinement. The definition of its value, however, requires further investigation using high temporal and spatial definition pressure sensors.

The geometric method defines HPZs and LPZs regions under the assumption of uniform pressure distribution within those zones, which is not strictly true, and thus there is room for improvement in this aspect of the method. Additionally, the geometric method does not provide values for the average pressures of the HPZs and LPZs, it only defines their expected distribution given a known contact area shape and an assumed coverage percentage of the region. One could refer to the literature, but such detailed pressure and coverage values are limited in number and only strictly valid within the parameters of the study itself. Further research in the average pressure and distribution values of HPZs and LPZs for different ice types and geometries would be beneficial. In the simulations performed in Chapter 6 the authors relied on the pressure-area curve model used in IACS UR I to determine the total load applied at each loadstep and average pressure of the patches. The relative size of HPZs and their contribution to the total load applied on the structure are based on data collected from the experiments in Chapter 2.

The NILAS provides improvements to the commonly used IACS UR I methodology particularly for scenarios that do not fall within its scope, however, it still needs to be validated using experimental data. Such validation could be performed when the ice impact experiment program between non-polar class structures and ice cones is completed at Memorial University of Newfoundland. Ideally the ice features used in these validation experiments would be made of freshwater ice, and they would be shaped into pyramids. Pyramidal shapes have generally well-behaved spallation events, thus maintain a contact area shape that is similar to the nominal contact area. If this remains true during the experiments, then the contact area can be determined by measuring the relative

displacement between the ice holder and panel holder pendulums. This can be done with digital image correlation. The next challenge is determining how the ship structure is deforming while the impact is happening. In Chapter 4 the authors propose the use of accelerometers to integrate the panel's local displacement. This information, combined with load cells measurement, would allow for the nominal pressure to be determined. This would be used to define the HPZ and LPZ pressures using the NILAS method, and then prepare the validation simulations.

Besides that, the NILAS method would benefit from an update in its methodology to account for geometric changes of the impacted ship structure. This would make it possible to correct the contact areas shape as function of the ship structural changes during the numerical simulation. Currently NILAS always assumes a flat ship structure.